Zinc oxide nanowire field effect transistors for sensor applications

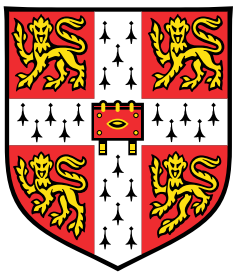

Nikhil Tiwale

Supervisor: Prof Sir Mark Welland

Advisor: Dr Colm Durkan

Department of Engineering
University of Cambridge

This dissertation is submitted for the degree of
Doctor of Philosophy

Downing College November 2017

I would like to dedicate this thesis to my loving family and friends ...

Declaration

I hereby declare that except where specific reference is made to the work of others, the contents of this dissertation are original and have not been submitted in whole or in part for consideration for any other degree or qualification in this, or any other university. This dissertation is my own work and contains nothing which is the outcome of work done in collaboration with others, except as specified in the text and Acknowledgements. This dissertation contains fewer than 65,000 words including appendices, bibliography, footnotes, tables and equations and has fewer than 150 figures.

Nikhil Tiwale
November 2017

Acknowledgements

The gratitude expressed here is sorely inadequate as compared to the role played by these wonderful people in helping me sail through my PhD. Their unwavering patience, kindness and generosity has guided me towards becoming the scientist and the person that I have grown into.

First of all, I would like to express my humble gratitude to my supervisor, Prof Sir Mark Welland for providing me the opportunity to pursue my doctoral studies under his supervision. His constant guidance and encouragement has always been a source of inspiration throughout my doctoral research at Cambridge. Sir Mark directed me towards truly an interesting piece of scientific research while also providing me space to explore diverse ideas, establishing strong foundations for my research career.

From the other side of the world, I wish to thank Prof Prita Pant, my co-supervisor from IIT Bombay. She has been a wonderful mentor ever since my undergraduate studies. Her enthusiasm and wide ranging scientific curiosity has played an inspiring influence on me pursuing career as a researcher. Her support has been pivotal in securing Cambridge-India Partnership Scholarship towards my doctoral studies.

I am eternally grateful to the Cambridge Trusts for their generous financial support, which enabled me to pursue doctoral studies at such a world-renowned university. I would also like to thank all the funding bodies who have provided financial assistance in the form of hardship funds as well as conference travels grants.

I would like to extend my gratitude to Downing College and my tutor Dr Jay Stock for providing me with a welcoming atmosphere in Cambridge. Their unconditional support during the tough periods of my PhD, has been instrumental in successful completion of my doctoral thesis.

The presented work would have been impossible without the guidance of Dr M S M Saifullah, Dr Yury Alaverdyan and Dr Atif Aziz. Since the nascent stages of the project, Dr Saifullah's keen inputs and advice has been invaluable throughout the course of my

PhD research and I would like to present my sincere thanks to him. My heartfelt gratitude to Dr Yury Alaverdyan for his limitless patience in teaching the know-hows of electron beam lithography and cleanroom processing as well as numerous scientific discussions therein. His personal touch and the time spent in training me has been vital in developing my nanofabrication skills. Dr Atif Aziz has been a great support in taking the gas sensing project forward. I would like to offer him my deepest gratitude for day-to-day discussions on device fabrication and characterisation as well as his prompt assistance in experimentation and assimilation.

I would like to thank all the fellow researchers at the Nanoscience Centre, both past and present, with whom I have enjoyed scientific as well as social interactions over the years. In particular, I would like to thank Dr Stanko Nedic for introducing me to cleanroom fabrication and device measurements as well as to Dr Abhinav Prasad and Dr Jerome Charmet for several brain-stimulating discussions. My special thanks to Juan Rubio-Lara for making all the long-work hours rather pleasant as a lab-buddy and a friend. I would also like to acknowledge his keen help with LabVIEW interfacing of the gas sensing setup and with atomic force microscopy. Additionally, it has been wonderful to work alongside the friendly faces around the lab - Alexandra Vaideanu, Zhuocong Xiao and Edward Tan.

I also wish to thank fellow researchers from Cavendish Laboratory and CAPE whose invaluable inputs have helped me further my research. My heartfelt gratitude to Dr Satyaprasad Senanayak for his practical advice related to nuances of processing and testing of the transistor devices. I would also like to extend my thanks to Dr Abhay Sagade, Dr Aditya Sadhanala and Dr Shahab Ahmad whose enthusiasm and dedication towards research has been inspiring and contagious. Many scientific discussions with them have not only introduced me to a range of associated fields but also motivated me to explore broader research avenues and collaborations. Special thanks to Dr Shahab Ahmad for his help with TGA measurements. Also thanks to Dr Sunita Dey for conducting XRD measurements.

I also owe immense gratitude to the support staff at the Nanoscience Centre, who have simplified the logistics around the lab. I would like to acknowledge Dave Roberts, Roger Bourne, Duncan Bulman and Tom Mitchell for the technical support with various instruments and processes around the lab. My special thanks to Ian Ganney for his assistance in building the gas sensing test setup. I also thank Sue Murkett for her diligent support with administrative work and many friendly conversations in the office.

My heartfelt gratitude to all the teachers and mentors who have touched my life and inspired me to become a better learner and aspire for excellence. I certainly would not have reached this far in my academic journey without their help along the way.

During the course of my PhD, I have received support from a host of a friends outside of work. In particular, Jayeta, Nishit, Darshana, Abhinav, Abhijeet, Gautam, Kedar, Vivek, Megha and Rishika have made my time at Cambridge much more enjoyable and memorable with their presence. My warm thanks also to my dear friend and sister Shruti for always being there and standing with me as a huge support through my toughest hours.

Finally, I present my great appreciation to my family for their love and encouragement. I thank both of my parents for cultivating my scientific curiosity ever since a very young age and supporting my endeavours at pursing graduate studies. I would also like to thank my younger brother Girish for being partner in my life-dreams and always being a wonderful friend. I would also like to thank my extended family and friends for their love and enriching my life with their presence as well as encouragements.

Abstract

A wide variety of tunable physio-chemical properties make ZnO nanowires a promising candidate for functional device applications. Although bottom-up grown nanowires are producible in volume, their high-throughput device integration requires control over dimensions and, more importantly, of precise placement. Thus development of top-down fabrication routes with accurate device positioning is imperative and hence pursued in this thesis.

ZnO thin film transistors (TFT) were fabricated using solution based precursor zinc neodecanoate. A range of ZnO thin films were prepared by varying process parameters, such as precursor concentrations and annealing temperatures, and then analysed for their optical and electrical characteristics. ZnO TFTs prepared from a 15% precursor concentration and annealing at 700 °C exhibited best device performance with a saturation mobility of 0.1 cm^2/V.s and an on/off ratio of 10^7. Trap limited conduction (TLC) transport was found to be dominant in these devices.

A direct-write electron beam lithography (EBL) process was developed using zinc naphthenate and zinc neodecanoate precursors for the top-down synthesis of ZnO nanowires. Nanoscale ZnO patterns with a resolution of 50 nm and lengths up to 25 μm were fabricated. A linear mobility of 0.5 cm^2/V.s and an on/off ratio of $\sim 10^5$ was achieved in the micro-FETs with 50 μm channel width. Interestingly, on scaling down the ZnO channel width down to 100 nm, almost two orders of magnitude enhancement in the linear mobility was observed, which reached $\sim$33.75 cm^2/V.s. Such increment in the device performance was attributed to the formation of larger grains and thus reduction in the grain-boundary scattering.

Six volatile organic compounds (VOCs) were sensed at room temperature using the direct-write EBL fabricated ZnO devices under UV sensitisation. As the surface-to-volume ratio increases with the decreasing channel width (from 50 μm to 100 nm), sensing response of the ZnO devices becomes more significant. Ppm level detection of various VOCs was observed; with a 25 ppm level Anisole detection being the lowest concentration. Additionally, using 100 nm device, detection of 10 ppm NO_2 was achieved at room temperature. The

sensing response towards NO_2 was found to be increased with UV illumination and sensor temperature. This led to exhibit $\sim$171 % sensing response for a 2.5 ppm level of NO_2.

Preface

This dissertation is the result of my own work and includes nothing which is the outcome of work done in collaboration except where specifically indicated in the text or acknowledgements. Parts of the findings presented in this thesis have been published or are waiting for submission as manuscripts in preparation.

Publications

1. **N. Tiwale**, "Zinc oxide nanowire gas sensors: fabrication, functionalisation and devices," *Mater. Sci. Technol.* 31(14), 1681–1697 (2015) (Sections from the article are included as parts in Chapter 1, 2, 3 and 5)

2. **N. Tiwale**, S. Senanayak, J. Rubio-Lara, Y. Alaverdyan, M. E. Welland "Charge transport in solution processed ZnO thin film transistors grown from zinc neodecanoate". *(In preparation)* (Chapter 4)

3. **N. Tiwale**, S. Senanayak, J. Rubio-Lara, Y. Alaverdyan, M. E. Welland "Direct Write Electron Beam Lithography for Top-down Fabrication of solution processed ZnO micro/nano FETs". *(In preparation)* (Chapter 5, 6)

4. **N. Tiwale**, A. Aziz, Y. Alaverdyan, M. E. Welland "Volatile organic compound detection using ZnO sensors fabricated by direct-write electron beam lithography" *(In preparation)* (Part of Chapter 7)

5. **N. Tiwale**, A. Aziz, S. Hodge, M. E. Welland "High sensitivity NO_2 detection with direct-write electron beam lithographically patterned polycrystalline ZnO nanowires" *(In preparation)* (Part of Chapter 7)

Additionally, collaborative work carried out during the course of this PhD is also being assimilated into following manuscripts.

1. A. Aziz, **N. Tiwale**, S. Hodge, G Divitini, M. E. Welland "A wool of polycrystalline ZnO nanofibres created using core-shell electrospinning" *(In preparation)*

2. E. K. W. Tan, G. Rughoobur, J. Rubio-Lara, **N. Tiwale**, Z. Xiao, C. A. B. Davidson, C. R. Lowe, L. G. Ochhipinti "Nanofabrication of Conductive Metallic Structures on Elastomers for Gas Sensing Applications" *(Under review)*

Presentations

During my doctoral studies at Cambridge, I have had an opportunity to present my ideas and work on various occasions at conferences and meetings. A selected few are listed here

1. Oral Presentation: "Direct Write Electron Beam Lithography for Top-down Fabrication of sol-gel based ZnO micro-nano FETs", Electron, Ion, and Photon Beam Technology and Nanofabrication (EIPBN) 2016, Pittsburgh *(Jun '16)*

2. Poster Presentation: "Top-down Fabrication of Zinc Oxide Nanowire Field Effect Transistors using Negative Tone Electron Beam Lithography of Zinc Naphthenate" Micro and Nano Engineering (MNE) 2014 Conference *(Sep '14)*

3. Oral Presentation: "Direct Write Electron Beam Lithography for Top-down Fabrication of ZnO Nanowire FETs", Division B (Electrical Engineering) Graduate Conference, University of Cambridge, Duxford *(Sep '14)*

4. Oral Presentation: "Zinc Oxide Nanowire Gas Sensors: Fabrication, Functionalization and Devices", Materials Literature Review Masterclass 2014, Institute of Materials, Minerals and Mining, London *(Apr '14)*

5. Oral Presentation: "ZnO Nanowire FETs for Sensor Applications", Nanoscience Winterschool, Hinterglemm *(Feb '13)*

Table of contents

List of figures

List of tables

Chapter 1

Introduction

1.1 Motivation

The electronic technology industry has taken rapid strides over the past four decades by increasing transistor performance and density, while keeping up the Moore's Law scaling. This geometric scaling has continued in the mainstream complementary metal oxide semiconductor (CMOS) based chip manufacturing. However, equivalent scaling encompassing innovative device design in conjunction with new emerging materials and structures is gaining significance in the semiconductor industry [1]. Currently, semiconductor foundries have reached device scaling down to 10 nm node. At the same time planar architecture has been replaced with vertical FinFET geometry, in order to improve current control. Nanowire-based gate-all-around structure is foreseen for sub-10 nm nodes with possible use of alloyed semiconductors instead of conventional single crystal silicon.

Semiconductor nanowires (NW) have been included among the Emerging Research Devices in the International Technology Roadmap for Semiconductors (ITRS) as a possible downscaling route [2]. Superior electrical, mechanical, optical and thermal properties of semiconductor nanowires open up the possibility of using them as building blocks of futuristic electronic devices such as processors as well as non-volatile memory [3]. Although nanowires have shown superior single device performance, their impact on the post-CMOS technology is dependent on the capability of their integration and scaling up for large hierarchical systems [2].

1.2 User interactivity and sensor integration

While relentless progress has been made in achieving gigantic computational power, the ITRS has also envisioned incorporation of non-digital functionalities under the "More than Moore" (MtM) banner [1]. This trend of combining digital functions and functional diversification can be seen in Fig. 1.1. These functional devices may not follow Moore's Law scaling. Instead they provide digital CMOS world an interactivity with the real world by converting mechanical, thermal, acoustic, chemical, optical and biomedical functions to digital data and vice versa [5]. The "More Moore" and "More than Moore" technologies are perceived as complementary trends. The value addition from MtM devices to the day-to-day lives of end users is immensely widespread. Healthcare, automotive, energy and lightening have been identified as leading markets which have potential to drive the MtM Technology roadmap [1].

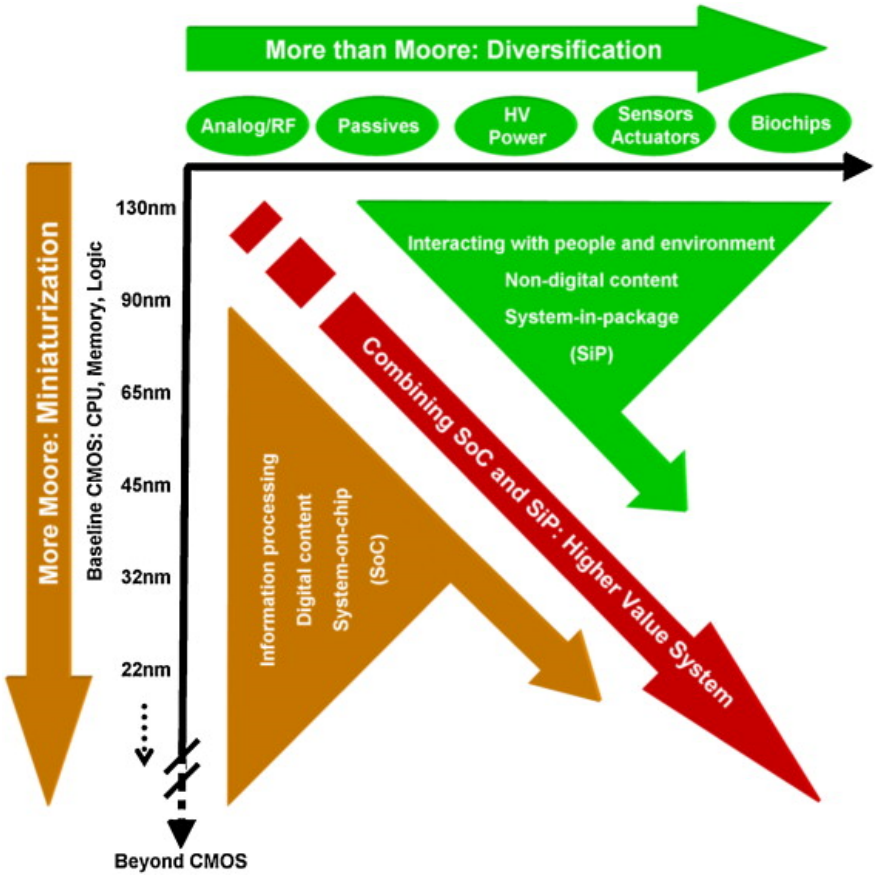

Fig. 1.1 Combined dual trend of digital (More Moore) and nondigital functional diversification (More than Moore) as an integrated system. Reprinted from [4].

Sensors and actuators are at the heart of the MtM devices. Application of nanoscience and nanotechnology opens up a vast range of possibilities because of high surface-to-volume ratios, ultra high sensitivity, higher selectivity, low power consumption and faster response of the nanosensors [4]. Reduction in the sensor size not only makes them cost-effective to manufacture but also enhances their performance. Rigorous demand for cheaper, faster, more sensitive, more selective and more stable nanosensors than their conventional counterparts has been driving the nanosensor research to its new horizons [6].

Over the years the consumer electronics industry has succeeded in imparting a number of "senses" to the electronic world and smartphones are the epitome of their convergence (Fig. 1.2). Speakers and microphone impart speech and hearing ability, whereas, high-resolution embedded cameras provide vision. The tactile sensing in smartphone screens allows it to sense the user's touch. However, one sense that has so far been elusive is that of smell. Utilisation of gas sensors in building an electronic nose is being explored for this purpose and research is being driven to develop integrated gas-sensing platforms.

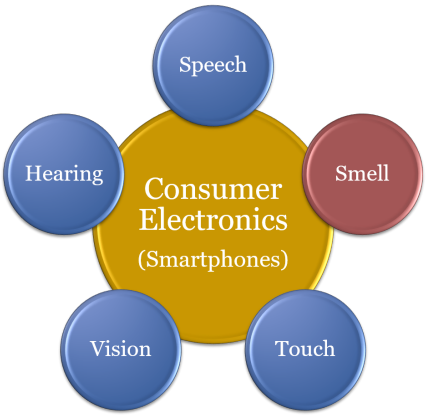

Fig. 1.2 Artificial Senses.

1.3 Electronic nose and breath diagnosis

Smell is one of the primary senses of human beings. Use of sniffer dogs in police forces is well known. The same sense of smell could also be exploited as a diagnostic tool for diseases and health malignancies. This practice of using unusual human odour to diagnose diseases dates back to ancient times and is said to have been in practice since the time of Hippocrates - the father of medicine [7]. One of the obvious examples could be, the fruit-like sweet smell of breath or sweat as an indication of uncontrolled diabetes. On the other hand, urine-like smell indicates towards kidney failure [8].

Since the inception of modern breath diagnosis in 1970, when Linus Pauling detected about 200 volatile organic compounds (VOC) in exhaled air, more than 3000 VOCs have been identified. Breath diagnosis, being a non-invasive, real time and harmless technique, possesses an upper hand over the traditional methods involving blood or urine sampling. However, the lack of insight into the physiological and biochemical origins of these VOCs still presents a major obstacle [8].

In terms of technological perspective, gas chromatography (GC) coupled with a form of mass spectroscopy (MS) has been conventionally used to identify breath biomarkers [9]. Although GC is very accurate, it is also costly, non-portable, time consuming and requires expert interpretation. Alternatively, electronic noses or 'e-noses' have increasingly been used in medical practice for the past 20 years in the diagnosis of renal diseases, diabetes, lung cancer and asthma[10]. In spite of the constructive results provided by e-noses, the highly specific nature of their design limits their utility to diagnosing only a few diseases [9].

Electronic nose is essentially an array of sensors whose responses are analysed using pattern recognition algorithms. A range of sensors based on distinct operating principles

is employed for this purpose: conductive polymers, metal-oxide semiconductor, quartz crystal microbalance and surface acoustic waves, to name a few examples. Another equally indispensable requirement for the e-nose are effective pattern-recognition algorithms that enable identification and discrimination among the mixture of VOC. These algorithms integrate responses of the sensor array and compare them with reference libraries developed by machine learning [11]. With ultra-high sensitive nanosensors on one hand and their CMOS integration for tremendous computational ability on the other, current nanotechnology tools provide unparalleled opportunity to build portable on-chip e-nose systems as never before.

1.4 Opportunities and challenges with multifunctional ZnO

Zinc oxide, due to its versatile material properties, has a unique place in these upcoming novel application domains. It is a wide bandgap semiconductor, imparting transparency to visible light. It is a cheap bio-compatible material already used in sun-screen creams to block the UV rays. It also exhibits piezoelectric properties along with high exciton binding energy, making it suitable for various energy-harvesting and optoelectronic appliations [3].

Doping zinc oxide with a variety of materials can modulate its bandgap and thus electrical conductivity. In, Ga or Sn doping has been widely exploited in thin-film transistor (TFT) applications. Due to higher field effect mobilities, Indium-Gallium doped zinc oxide (IGZO) is poised to replace amorphous silicon in large-area electronics as backpanels in active matrix displays. In this, typically thin film based technology, patterning of the active ZnO based layer is inevitably used to attain a smaller device footprint and hence larger pixel count. However, scaling down to sub-micron size using a conventional etching process is challenging[12, 13].

At the other end of the spectrum are single crystalline ZnO nanowires. They possess a wide variety of physio-chemical properties. Due to the industrial drive for field effect transistors (FET), vast efforts are being applied to nanowire FETs. On the one hand, research is focused on studying individual nanowires that are placed randomly on the substrate to explore their transport properties; on the other, bottom-up grown random network of ZnO nanowires is being extensively explored for gas sensing. Despite such promising capabilities, lack of positional control in device fabrication has been a limiting factor in their large-scale industrial integration.

A typical process flow for the fabrication of semiconductor devices, consists of a stack of many functional layers. Randomly placed nanowires require locating them individually and aligning subsequent layers to fabricate each device. Such a process flow is not only cumbersome but also not suitable for building complex electronic circuits. Without the capability of ramping up towards large-scale integration and high volume manufacturability, cost effective production of the devices, that semiconductor industry boasts upon, cannot be achieved. Although bottom-up growth of random network of nanowires may still be usable for fabricating individual sensors, their wider application in multiplexed sensor platforms would still be unattainable without position control.

A position controlled fabrication process for ZnO nanostructures may alleviate these hurdles. Once ZnO nanowires are fabricated at known predetermined locations, aligned designs for subsequent functional layers and interconnects becomes possible and opens up unparalleled possibilities of integrating sensor and devices platforms. At the same time, easy ramp up to high volume manufacturing of such devices, would lead to making them available at cheap-affordable consumer products.

1.5 Completed project objectives and thesis outline

The aim of this thesis is development of direct write electron beam lithography (EBL) based solution processing route for position-controlled fabrication of ZnO nanowires. This approach consolidates the benefits of polycrystalline thin films and one-dimensional nanostructures. The optimisation of thin film as well as direct write patterned ZnO is investigated with regard to application in FETs. Furthermore, the polycrystallinity of the fabricated ZnO micro/nano structures is exploited for high sensitivity gas sensing application. The following objectives have been accomplished within the framework of this thesis:

1. Characterisation of ZnO thin films synthesised using zinc neodecanoate solution precursor via UV-visible spectroscopy, photoluminiscence (PL) spectroscopy and atomic force microscopy (AFM). Fabrication of ZnO TFT and their electrical characterisation via transfer and output characteristics for optimisation of film thickness and annealing temperature. Investigation of carrier transport mechanism in nano-crystalline ZnO. TFTs with 0.1 cm^2/V.s saturation mobility and 10^7 I_{ON}/I_{OFF} ratio was achieved.

2. Optimisation of direct write electron beam lithography on functional precursors zinc naphthenate and zinc neodecanoate. Optimal dose for fabrication of micro as well as nano patterns was investigated. Electron beam exposure response of both the resists

was assessed using dose curve in order to estimate resist sensitivity ($D_{0.5}$) and contrast (γ). Furthermore, Nano-patterns down to 50 nm resolution and 25 μm length were fabricated.

3. Fabrication and electrical characterisation of direct write EBL based ZnO micro FETs. After optimising ZnO film thickness with both zinc naphthenate and zinc neodecanoate, linear mobility upto 0.5 cm^2/V.s was attained with forming gas post-decomposition annealing. Furthermore, on scaling down ZnO width to 100 nm, almost two orders of magnitude mobility improvement was achieved, reaching up to $\sim$33.7 cm^2/V.s, which was attributed to decreased grain boundary scattering.

4. Designing an in-house measurement setup to characterise the sensing response of direct write ZnO devices towards volatile organic compounds (VOC). Size-dependant improvement in sensing response was observed with decreasing ZnO pattern width. Detection as low as 250 ppm concentrations of ethanol, isopropyl alcohol and toluene while 25 ppm of anisole vapours was demonstrated at room temperature under UV irradiation. At moderate temperature of 100 °C detection of as low as 2.5 ppm NO_2 was also realized with improved response and recovery time.

The thesis is organised in the following manner. In Chapter 2 a brief theoretical background on ZnO semiconductor and working of semiconducting metal-oxide based gas sensors is provided. Chapter 3 reviews conventional bottom-up growth of ZnO nanowires and their application in FETs and gas sensors. Chapter 4 then focuses on process optimisation of ZnO TFT synthesised from zinc neodecanoate. Starting from optical characterisation of fabricated ZnO films, electrical characterisation and brief investigation of carrier transport is presented. After discussing top-down synthesis routes of ZnO nanostructures reported so far, Chapter 5 then introduces a novel concept of direct write patterning of ZnO and demonstrates EBL based ZnO direct writing using zinc naphthenate and zinc neodecanoate. The implementation of direct write ZnO for FET applications is then detailed in Chapter 6. Initially, electrical performance of micro-patterned ZnO FETs is optimized using both precursors followed by the exploration of post-decomposition annealing. The effect of scaling down ZnO FETs to nanoscale is then investigated with electrical and morphological characterisation. In Chapter 7 sensing response of direct write ZnO devices is explored primarily towards range of VOCs with in-house built test setup under UV illumination. In this chapter width-dependant improvement in sensing response is ascertained using ethanol and IPA followed by NO_2 sensing experiments. Finally, in Chapter 8 a summary of the thesis is presented and directions for future work are outlined.

Chapter 2

Theoretical background

2.1 Introduction

Zinc oxide is a versatile material that is being investigated for wide range of functional devices and applications. The work presented in this thesis is focused primarily on transistor and gas sensors applications of solution processed zinc oxide. Thus, it is of paramount importance to gain understanding of its properties, that make it such a multifunctional material. The current chapter explains some of the basic electronic properties of ZnO, followed by outlining working principles of ZnO based gas sensing devices.

2.2 Electronic properties of zinc oxide

ZnO has been studied in bulk form for decades. However, the present renaissance in research related to ZnO started in the mid-1990s, with prospects of epitaxial growth, nanorods, quantum wells and quantum dots [14]. The major stimulus of ZnO research lies in a variety of functional applications such as optoelectronic devices, energy harvesters, transistors, sensors and transparent electronics [15]. The current section will focus on basic properties of ZnO that make it such a versatile material.

ZnO is a II-VI type metal oxide with semiconductor properties. It has wide direct bandgap of around $\sim$3.3-3.4 eV at 300 K[16, 14]. The maxima of the valance band (VB) and minima of the conduction band (CB) lie at the same point in Brillouin zone, k = 0. The lowest CB is formed due to empty 4s states of Zn^{2+} or the antibonding sp^3 hybrid states, while the highest VB originates from filled 2p orbitals of O^{2-} or the bonding sp^3 orbitals. The bandgap energy corresponds to the near ultraviolet (UV) region of the electromagnetic radiation spectrum [14].

ZnO shows high exciton binding energy of about 60 meV, triggering the possibility of lasing action due to excitonic recombination at room temperature, and thus suitability for laser diode [3, 15]. The large bandgap of ZnO provides both insensitivity to light and transparency. Thus ZnO-based thin-film transistors eliminate the need for protective coatings to avoid light exposure. On the other hand, heavy substitutional doping can introduce the possibility of transparent interconnects and electrodes for flat-panel displays [17].

ZnO crystalizes in the form of wurtzite structure at room temperature. It has a hexagonal unit cell with lattice parameters a = b = 0.3296 nm and c = 0.52065 nm [17, 18]. The structure consists of two hexagonal close packed (hcp) sublattices each one with one type of atom. These sublattices are interpenetrating and displaced with respect to each other along

the c-axis by the amount of u = 3/8 = 0.375 [17]. The other way to look at the structure is alternating atomic planes of O^{2-} and Zn^{2+} stacked along c-axis. The lack of central symmetry of the structure in combination with large electrochemical coupling makes ZnO intrinsic piezoelectric material [19].

ZnO has the highest piezoelectric tensor amongst tetrahedrally bonded semiconductors. Of the three independent components of the piezoelectric tensor in wurtzite phase, two are measures of strain-induced polarisation along the c-axis in the absence of electric field. This relationship can be expressed as

$$P_z^{piezo} = e_{33}\varepsilon_z + e_{31}\varepsilon_\perp$$

where ε_z and $\varepsilon_\perp$ are the strains along the c-axis and in the basal plane, respectively, whereas e_{33} and e_{31} are piezoelectric coefficients [20].

In wurtzite ZnO intrinsic defects of O vacancies (V_O) due to the Schottky reaction and Zn interstitials (Zn_i) due to the Frenkel reaction lead to deviation from stoichiometry giving intrinsic n-type conductivity [20, 16]. There is clear experimental evidence that ZnO is n-type; however, the dominating shallow donor is still under discussion. It has been suggested that, due to the much higher ionisation energy of the doubly charged oxygen vacancies, zinc interstitials are major contributors [20, 16]. There are studies suggesting that unintentionally incorporated hydrogen (H) is the major shallow donor [20]. It is indisputable that defects significantly affect grain boundary properties as well as I-V characteristics. However, a large surface area-to-volume ratio at smaller scales indicates that surface defects and adsorbed gases have more impact on the properties of ZnO nanostructures [16].

The hall mobility (μ_H) of electrons in bulk samples is found to be around 200 to 500 cm^2/Vs [21]. The intrinsic processes such as scattering due to Longitudinal Optical (LO) phonons, piezoelectric fields and Froehlich interactions are said to cause this limitation. The mobility value increases with decreasing temperature up to about 2000 cm^2/Vs at 100 K and again drops at even lower temperatures due to scattering with ionized impurities [14, 21]. Values up to 3100 cm^2/Vs have been estimated for nanorods at room temperature [14]. The validity of the value is under question but the results could be explained by quenching of some intrinsic scattering because of smaller lateral dimension [14]. However, one can certainly expect an increase in the mobility in the case of nanorods due to reduced scattering process. A hole mobility of around 5-30 cm^2/Vs has been reported, which is, as expected, considerably lower than the electron mobility [14, 21].

2.3 Working principle of metal oxide gas sensors

A precise understanding of the fundamental mechanism behind the gas-sensitive response of Semiconducting Metal Oxide (SMO) is still unclear. However, it is widely suggested that the ionosorption on the SMO surface is responsible for this response [4]. The process of gas sensing involves two key functions namely reception and transduction. Reception consists of detection of the target gas through gas-SMO interface. On the other hand, transduction involves change in the conduction of the sensor as a result of the surface interaction [22, 23].

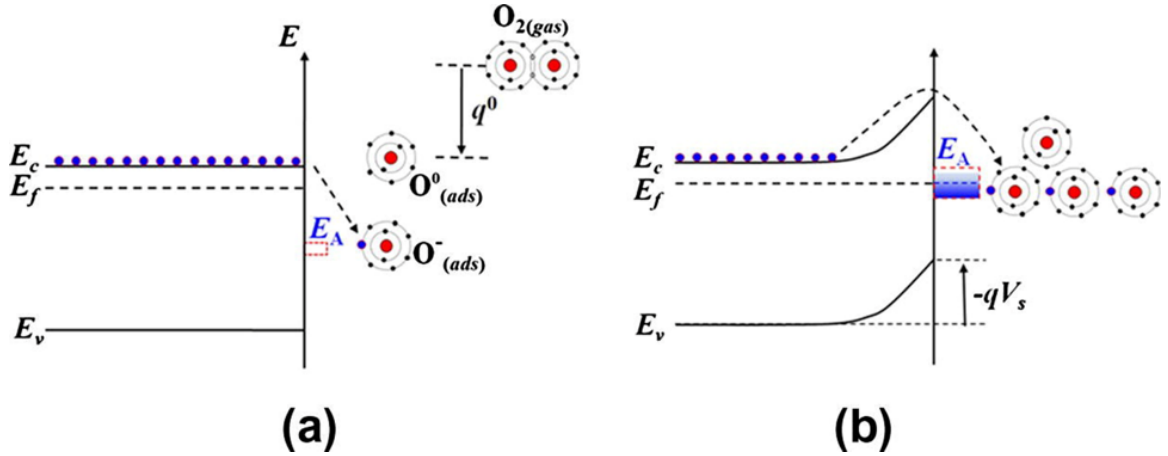

Fig. 2.1 Energy band diagram of the adsorption process of oxygen on n-type semiconductor. (a) Flat band condition (b) after adsorption of oxygen adions. Sourced From [24].

Oxygen in the ambience interacts with the SMO surface forming charged oxygen molecules. These charged oxygen species trap electrons from the conduction band E_C. The trapped negative charge repels other electrons and causes upward band bending forming an electron depletion region on the SMO surface. Fig. 2.1 depicts the process of oxygen adsorption and band bending. The depletion region is also called the space-charge layer. The length of band bending region is the thickness of the space-charge layer. As a result of band bending, conductivity is essentially reduced as compared to the flat band state. In a carefully calibrated system the change in conductivity can be related to the gas concentration. Interaction of this surface with oxidising or reducing gases results in the sensing response [22, 23]. These oxygen reactions can be shown as [25]

$$O + e^- \longleftrightarrow O^- \ (\ between\ 150^\circ C\ and\ 300^\circ C\ )$$

$$2O + e^- \longleftrightarrow O_2^- \ (\ between\ 30^\circ C\ and\ 150^\circ C\ )$$

Sensing of reducing gases

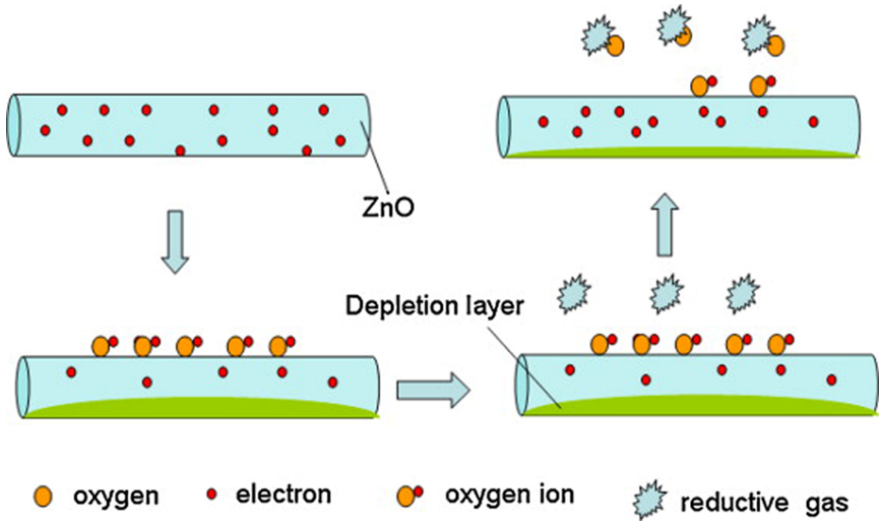

Fig. 2.2 Schematic representation of a reducing gas sensor. Sourced from [26].

In the case of reducing target gas, the gas molecules react with O_2^-, O^- or O_2^- ions and release the electrons back to the conduction band. This leads to an increase in the carrier concentration and therefore the thinning of the depletion layer. The result is a sudden increase in the current which is the sensing signal [26]. The reactions involved in this process can expressed as

$$R + O^- \longleftrightarrow RO + e^-$$

where R is the reducing gas [25]. The whole process is schematically shown in Fig. 2.2. After atmospheric oxygen is adsorbed on SMO surface it captures electrons from SMO and the depletion layer is formed. When the sensor is exposed to the reducing gas it removes the oxygen, electrons are released back to the SMO, and the thickness of the depletion layer is decreased. Gases such as H_2, CO, CO_2, H_2S, NH_3, CH_4 are detected by this mechanism [26].

Sensing of oxidising gases

In the case of oxidising gas the molecules are absorbed onto the surface and the O atoms of the gas capture electrons from the oxide semiconductor. This causes the expansion of the depletion region and decrease in the carrier concentration. This results in the decrease in the conductivity of SMO, which can easily be measured [26]. The whole process is schematically

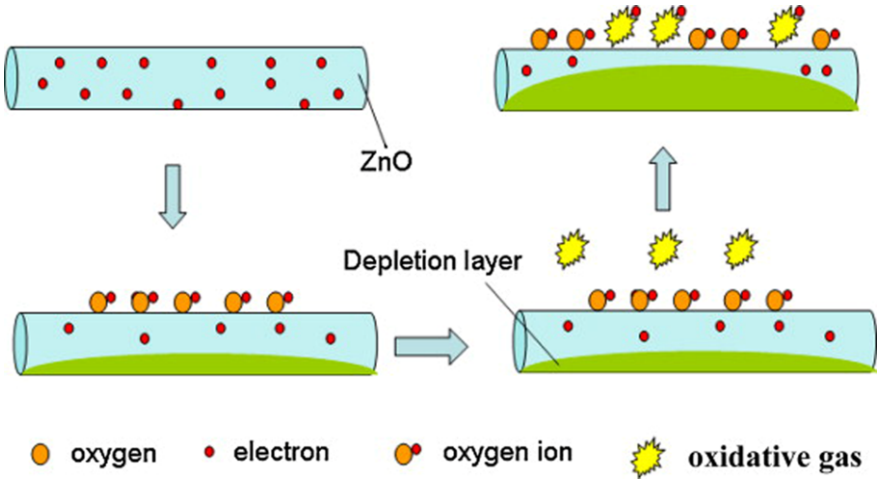

Fig. 2.3 Schematic representation of an oxidising gas sensor. Sourced from [26].

shown in Fig. 2.3. The reactions involved during this process can be expressed as [25]

$$O + e^{-} \longleftrightarrow O_2^{-}$$

2.4 Gas sensor performance parameters

The sensor response, response and recovery time, limit of detection, optimum working temperature, selectivity, stability and reproducibility are the key parameters which define the performance characteristics of the gas sensor. This section outlines these parameters. The definitions are as follows [26, 27].

Sensor response

In general, a sensor response can be defined as the ratio of the change in the sensor signal in the presence of the gas under the test to the original signal without the analyte gas. In the case of semiconducting gas sensors, the signal is either resistance, current, voltage or conductance.

$$Response = \frac{\Delta R}{R} = \frac{|R_{air} - R_{gas}|}{R_{air}}$$

where R_{air} is the sensor signal in ambient air and R_{gas} is the sensor signal in a particular target gas environment. The response is also reported as percent response by multiplying the above equation by 100.

Response and recovery time

Response time signifies how fast the sensor can detect the analyte gas and provides information on how fast the state of the sensor changes in the presence of the analyte gas. It is defined as the time taken to achieve 90 % of the total signal change. On the other hand, recovery time refers to the recovery of the sensor back to its base condition, which is defined as the time taken to reach 90 % of its original state upon removal of the target gas.

Limit of Detection (LOD)

LOD is the lowest amount of target gas for which the sensor could have a response. It is typically calculated as three times the standard deviation corresponding to 0.01 of sensitivity signal [28].

Optimum working temperature

Most of the MOS gas sensors need elevated temperature to accelerate the kinetics of gas adsorption/desorption. Thus it becomes essential to identify the temperature (or range of temperature) at which the sensor gives best response.

Selectivity

The selectivity of the sensor is how well it responds to the target gas as compared with other gases. Although SMO have typically poor selectivity, it can be further enhanced by introducing functional groups in the form of coating, nanoparticle etc.

Stability and reproducibility

The evaluation of stability is based on repetitive cycles of switching between ON state and OFF state. The stability is said to be good if there is very small change in sensor response after numerous tests.

Chapter 3

Review of ZnO nanowire growth, FETs and gas sensors

3.1 Introduction

The previous chapter laid down theoretical insights into the material properties of ZnO and the working of ZnO gas sensors. The present chapter gives an overview of the research carried out on ZnO nanowires and the devices based on the same. In the beginning, a number of widely explored bottom-up growth methodologies for ZnO nanowires are reviewed. The device applications of these nanowires as field effect transistors is then summarised. Subsequently, the final two sections of this chapter report on the sensing applications of ZnO nanowires. At first, functionalisation and device implementation strategies of ZnO nanowire gas sensors are outlined, followed by surveying the reports of electronic nose systems made by using semiconducting metal oxides.

3.2 Bottom up growth of ZnO nanowires

A wide variety of different ZnO nanostructures, such as nanowires, nanorods, nanobelts, nanotubes, nanohelixes, nanorings, nanospirals, nanocombs are being utilized in the semiconductor applications [3, 19]. Growth rates can be controlled to acquire specificity in kinetic parameters of different crystal planes leading to these novel structures [19]. Growth of these nanostructures can in itself be a fascinating area to work on. However, for the purpose of this project, emphasis will be given to growth of ZnO nanowires.

A variety of bottom-up methods have been implemented to synthesize ZnO nanowires. Various groups have attempted to use chemical methods such as Electrodeposition [29, 30], Aqueous Solution Method [31–34], and plasma treatment [35, 36]. Vapour deposition techniques such as chemical vapour deposition (CVD) [37], and pulsed laser deposition (PLD) [38] have also been implemented. More commonly used growth methods will be reviewed in this section followed by a few recently used methods to integrate ZnO NW into the existing semiconductor processing.

Metal-organic Chemical Vapour Deposition

Metal-organic chemical vapour deposition (MOCVD) is a widely used synthesis route for the growth of ZnO nanostructures [3]. Au nanoparticles are used as a catalyst for the MOCVD growth [39–41]. However, there are also reports of catalyst-free aligned growth of ZnO nanowires using MOCVD [42–44]. In spite of a highly orientated nanowire array with good in-plane alignment and the possibility of growing films on top of the NWs for device

fabrication without insulating layer, scalability of the method for mass production is limited [3].

Vapour-phase transport growth

While the chemical approach is generally used at low temperature, vapour-phase growth is carried out at high temperature [18]. Despite the high temperature requirement, this method is widely used due to its simplicity [3]. Perfectly vertical large-scale alignment of ZnO NW using Vapour-Liquid-Solid (VLS) growth was first reported by Huang *et al.* [45] on the a-plane ((1120) crystal surface) orientated single crystal sapphire substrate. Au nanoparticles act as catalysts, which initiate and guide the growth, whereas epitaxial matching between ZnO and sapphire ensures alignment. Maintaining moderate growth rate is necessary and thus lower growth temperature to reduce vapour concentration. Carbon powder was mixed with ZnO to reduce the vaporisation temperature from 1300 °C to 900 °C.

$$ZnO(s) + C(s) \overset{900^{\circ}C}{\longleftrightarrow} Zn(v) + CO(v)$$

Due to the reversibility of the reaction, Zn vapour and CO when transferred to the substrate react back to give ZnO. It is then absorbed by the Au catalyst, resulting in formation of ZnO nanowires. Use of a pre-patterned catalyst layer can lead to patterned distribution of nanowires as seen in Fig. 3.1 [18].

Crystal structure of the substrate plays an important role in orientation of NWs. In the case of sapphire, c-axis of Al_2O_3 and a-axis of ZnO have very small lattice mismatch for a-plane oriented substrate. Hence preferred growth direction is perpendicular to the a-plane of Al_2O_3. GaN, AlN, AlGaN substrates have same wurtzite structure as ZnO. As a result ZnO NWs are allowed to grow only in (0001) direction, following the substrate's crystal orientation [18]. Growth of aligned ZnO NW on GaN, AlN and AlGaN substrates has been reported by Wang *et al.* [46]. The effect of growth conditions such as chamber pressure, oxygen partial pressure [47] and thickness of catalyst layer [48] on alignment quality of the NWs has been systematically investigated by Wang's group. Wang *et al.* have suggested that the thickness of the Au catalyst plays an important role in the VLS growth. It is found that a thinner Au layer creates more energy-favourable sites, due to the wetting situation between Au droplet and the substrate. Thus a thinner layer leads to higher density of nanowires, but width and length distribution of the nanowires was found to be somewhat similar [48] .

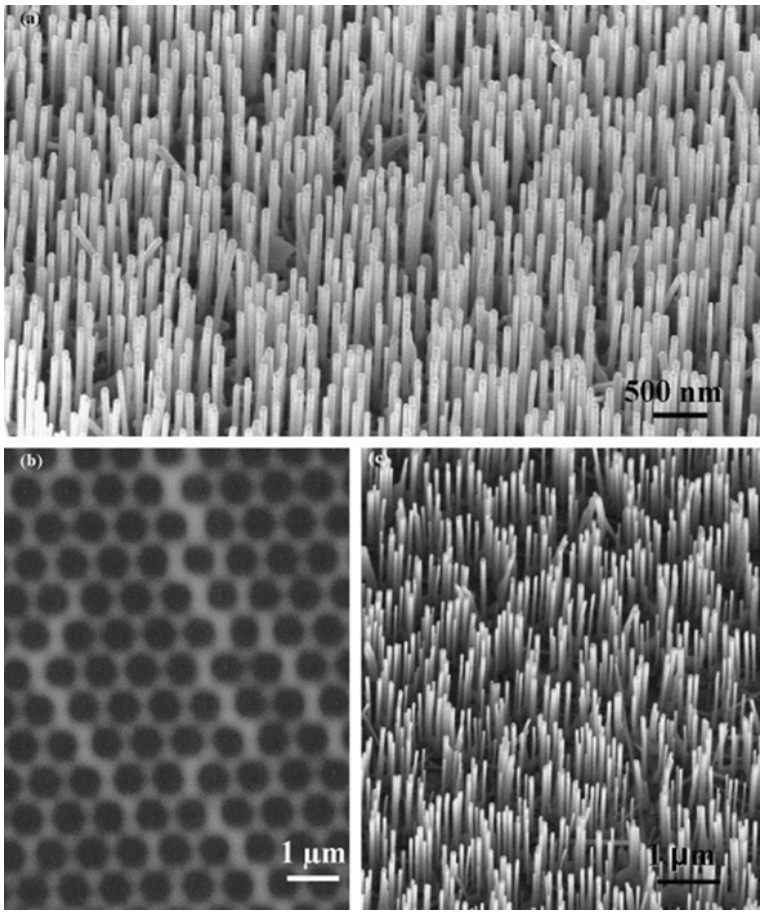

Fig. 3.1 (a) SEM image showing random distribution of aligned ZnO NWs on sapphire substrate with thin Au layer as catalyst. (b) SEM image of pre-patterned Au catalyst layer. (c) SEM image of aligned ZnO NWs following honeycomb distribution as per Au catalyst pattern. Sourced from [18].

Hydrothermal based chemical approach

Hydrothermal is yet another popular method for ZnO NW growth, due to the requirement of relatively low temperature. The method typically involves nutrient solutions of zinc salt (source for Zn^{2+} ions) and a weak base in water (source of O^{2-} ions). Sheng *et al.* [49] have demonstrated one of the approaches of ZnO NW growth using hydrothermal route. 1:1 solution of zinc nitrate and hexamethylenetetramine (HMTA) was used as the nutrient solution. Although the function of HMTA is not very clear, HMTA being a weak base, its slow hydrolysation produces OH− ions gradually. Fast hydrolysation would precipitate Zn^{2+} very fast, leaving a very small amount for ZnO for NW growth. The chemical reactions involved in the growth are as follows:

$$(CH_2)_6N_4 + 6H_2O \longleftrightarrow 4NH_3 + 6HCHO$$

$$NH_3 + H_2O \longleftrightarrow NH_3.H_2O$$

$$NH_3.H_2O \longleftrightarrow NH_4^+ + OH^-$$

$$Zn^{2+} + 2OH^- \longleftrightarrow Zn(OH)_2$$

$$Zn(OH)_2 \xrightarrow{\Delta} ZnO + H_2O$$

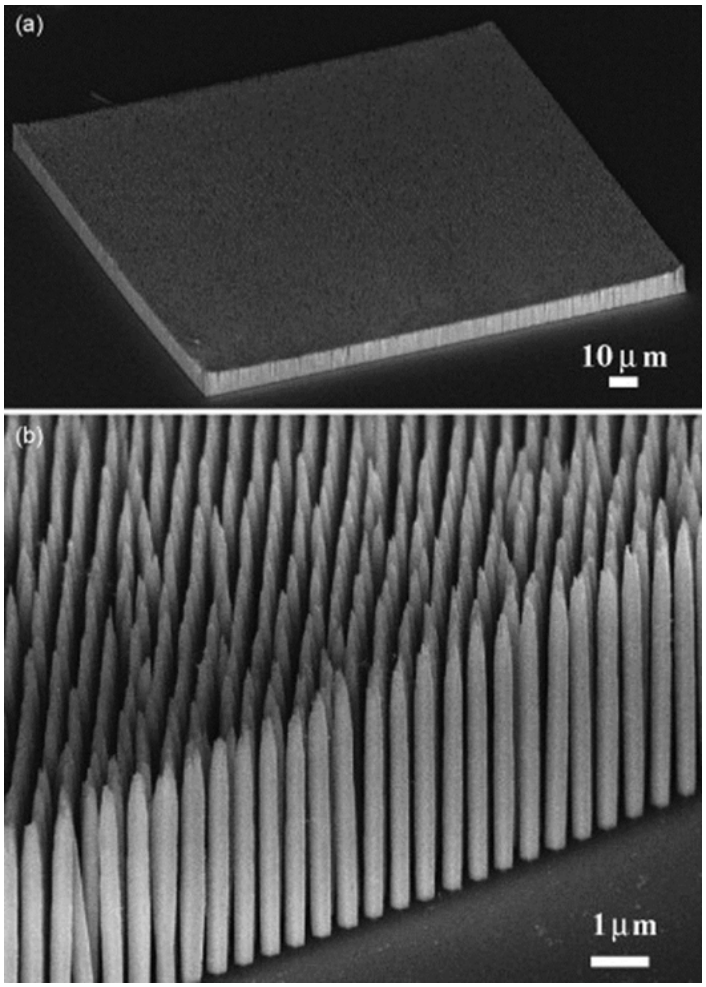

Fig. 3.2 Hydrothermal patterned growth of ZnO NWs on GaN substrate (a) low magnification (b) high magnification SEM image. Sourced from [18].

All the reactions being in equilibrium, reaction parameters such as precursor concentration, growth temperature and growth time can alter the course of the reactions by taking them forward or backward. It has been found that precursor concentration affects density of the NWs, whereas growth temperature and time govern the morphology of the NWs. Sheng *et*

al. have also investigated effect of these parameters on NW growth. Lateral growth is more significant in the initial stage of growth; axial growth dominates in the middle phase and on the other hand in the final stage both axial and lateral growth are found to be significant. Sheng *et al.* found 70 °C to be the optimal growth temperature. Lower temperature was found to form larger nuclei and thus low aspect ratio, whereas higher temperature reflected deviation towards pyramidal growth [18, 49].

Efforts are also made to achieve patterned growth of NWs using the hydrothermal route. For vertically aligned pattern growth, patterns were first created using electron beam lithography (EBL) using PMMA. These patterns act as a mask for ZnO seeds and NW growth was seen in the patterned openings [18, 50]. SEM images of the patterned growth of NWs can be seen in Fig. 3.2. Laterally aligned patterned NW growth has also been reported by Qin *et al.* [51]. Optical lithography was used to create patterns for seed strips. Sputtering of 300 nm of ZnO and 10 nm Cr was carried out in the patterned trenches, followed by lift-off using acetone to get ZnO strips with Cr on top. ZnO strips act as a seed layer for the NW growth, whereas a Cr layer acts as a growth inhibitor, leading to laterally aligned growth of ZnO NWs [51]. Fig. 3.3 shows the laterally grown ZnO NW array.

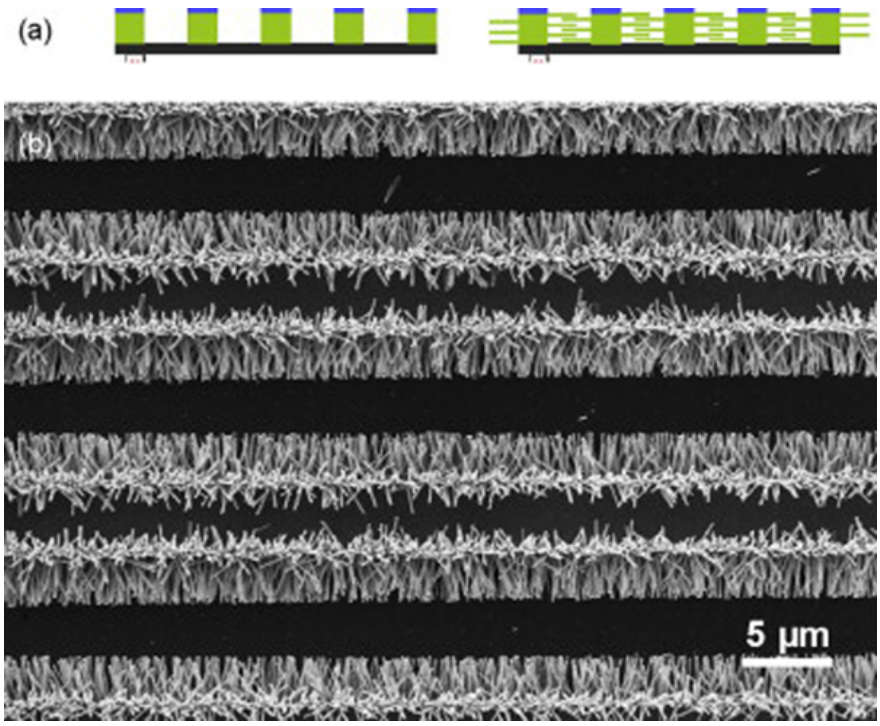

Fig. 3.3 (a) Schematic of ZnO seed strips with Cr on top (b) SEM image of laterally grown ZnO NW array. Sourced from [18].

CMOS integrated NW growth

There is an increasing interest in integrating top-down and bottom-up nanofabrication techniques. Some groups have attempted to achieve on-chip fabrication of ZnO NWs so that the NW arrays could be exploited in functional device application. The hydrothermal approach has been beneficial in this pursuit due to its low processing temperature. Microheaters are used in most cases to selectively heat specific areas on the substrate. Khoang *et al.* [52] have exploited growth inhibitor behaviour of Cr/Pt for selective growth of NWs, as explained in Fig. 3.4.

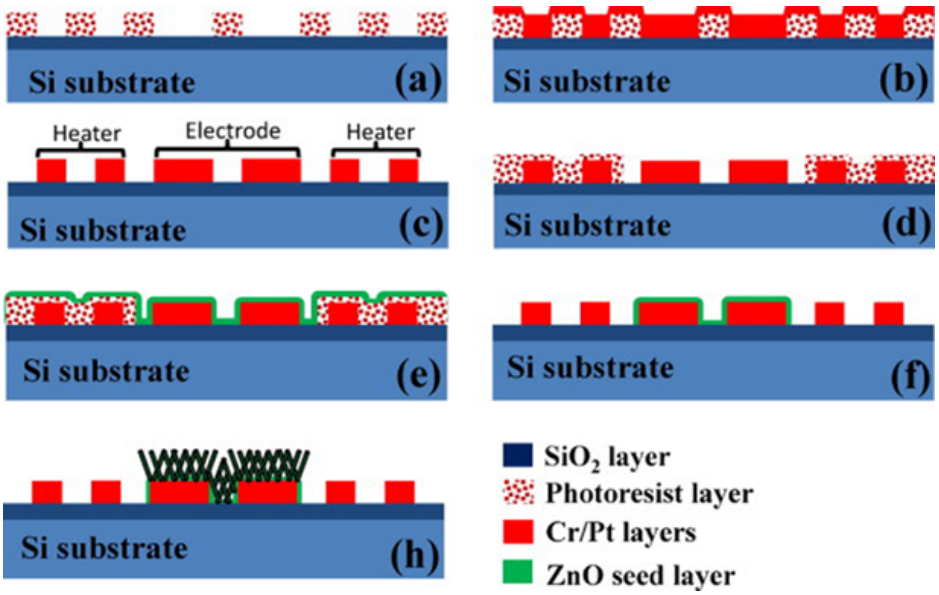

Fig. 3.4 Processing steps for on-chip fabrication of ZnO nanorods (a) spin coating and pattern of photoresist (b) Deposition of Cr/Pt layer for heater or electrode (c) photoresist lift-off (d) second pattern of photoresist layer (e) Deposition of ZnO seed layer (f) photoresist lift-off for ZnO seed layer (g) hydrothermal growth of ZnO NW. Sourced from [52].

Lin and Seshia *et al.* have used bow-tie shaped platinum micro-heaters and oxidation of Zn layer to form various ZnO nanostructures in ambient air. The oxidation area is controlled by applied voltage and ramp rate [53, 54]. This ZnO layer is further used as a seed layer for hydrothermal growth of NWs. Constraining the SiO_2 layer, on the top of the Zn layer, avoids vertical NW growth. It has been reported that a 500 nm thick layer of SiO_2 provoked aligned horizontal growth of NWs under the influence of an electric field [53]. It has later been found that Si_3N_4 shows better constraint on vertical NW growth than SiO_2, and thus a better integrated design has been achieved using Si_3N_4 [53]. Udrea *et al.* have carried out hydrothermal growth on silicon-on-insulator (SOI) based CMOS p+ silicon micro-heaters.

After foundry fabrication of SOI micro-hotplates, a ZnO seed layer was selectively sputtered onto them using shadow-mask, followed by normal hydrothermal growth to achieve ZnO NW sensing layer [55–58].

3.3 ZnO Nanowire Transistors

Field effect transistors (FET) have been the stimulant driving the electronic technology towards smaller, faster and even low-powered devices. Inevitably nanowire-based FETs are the building blocks of nanoelectronic devices. Metal oxide nanowires have emerged as excellent candidates for nanowire FETs, owing to their extraordinary electronic properties such as large bandgap, high electron mobility, controllable one dimensional geometry as well as their suitability for flexible and transparent electronic devices. ZnO NW FETs have been most extensively studied, from the high-performance computing devices, to their various functional capabilities [59, 60]. This section will focus on research progress in the field of ZnO nanowire FETs.

A ZnO nanowire FET device typically consists of source and drain electrodes making ohmic contacts with the nanowire. The third terminal, also called a gate, provides control over the conduction through the nanowire channel by applying a transverse electric field. A dielectric layer is included between the gate metal and semiconducting nanowire. Various configurations of dielectric layer and gate structure have been studied to enhance the device performance.

Due to the simplicity of fabrication, back-gated configuration is very commonly used [61, 62]. Typically native oxide (SiO_2) is exploited as dielectric and heavily doped silicon substrate is connected as gate electrode. One of the earliest ZnO NW FETs was reported by Park *et al.* as showing electron mobility of 75 cm^2/V.s, much higher than the mobility of 0.01-10 cm^2/V.s for ZnO based thin film transistors [62]. In spite of the simplicity in the fabrication, it is not possible to control gating effect on individual FET. Fan *et al.* have found an innovative way to study electrical properties of ZnO nanowire FETs using scanning probe microscopy (SPM) tip. The electrostatic distribution profile across the nanowire channel was measured, leading to calculation of contact resistance at the source and the drain. The significant difference in this contact resistance indicated asymmetric Schottky barriers at the source and drain. Biased scanning tip is used to apply the gate voltage locally to study transport properties of local electrostatic potential.A tapping mode of SPM was also used to induce a periodic switching mode, in turn demonstrating potential use in nano-electromechanical systems (NEMS) [63].

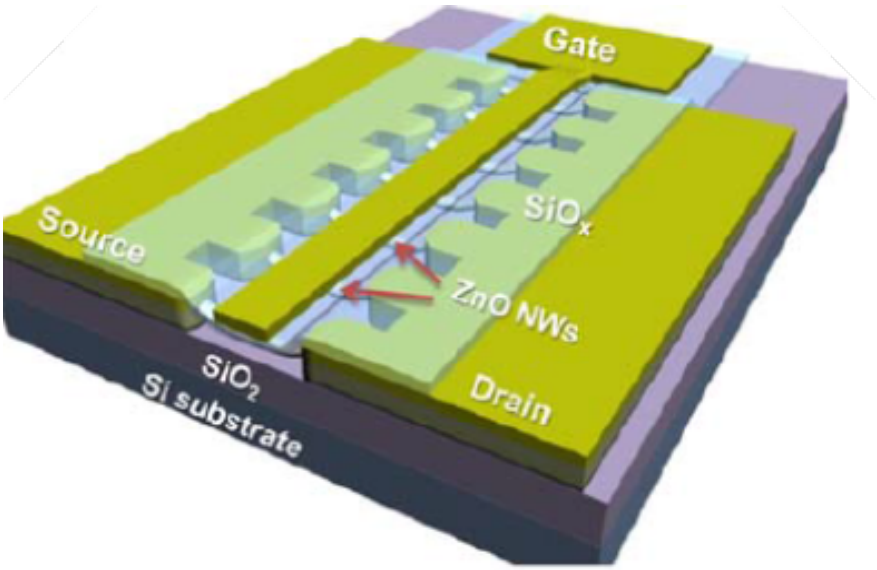

Fig. 3.5 Schematic of DEP-aligned Dual gate multichannel ZnO nanowire FET. Sourced from [64].

LaRoche *et al.* [65] have used top-gate configuration for fabrication of ZnO NW FETs. Keem *et al.* have demonstrated an increase from 19 nS to 248 nS by using top-gate FET instead of back-gate, implying significant gate dependence [66]. Kim *et al.* used dielectrophoresis (DEP) technique to align the ZnO nanowires between two electrodes. The dual (back as well as top) gate multichannel assembly can be seen in Fig. 3.5. The FETs exhibited a four order of magnitude increase in the I_{ON}/I_{OFF} ratio in top-gate configuration as compared with back-gate [64]. The superior electrical performance of top-gate devices is attributed to stronger electrostatic gating [67] as well as higher gate capacitance due to thinner oxide, giving rise to higher transconductance [64]. In another independent study on DEP-aligned multiple ZnO nanowire FET by Suh *et al.* while the drain current was reported to be proportional to the number of nanowires, I_{ON}/I_{OFF} was $\sim 10^6$ times lower in multiple nanowire FET than those of single nanowire FET. This lower ratio could have been caused by an electrostatic screening effect of aligned ZnO nanowires resulting from their infrequent crossing and stacking [68].

Other than conventional back-gate and top-gate configuration, various gate structures have been reported. Ng *et al.* have demonstrated a vertical-surround-gate field-effect-transistor (VSG-FET) based on single crystal ZnO nanowires. The schematic of the VSG-FET is shown in Fig. 3.6. The subthreshold slope (SS) of 170 mV/decade has been reported as higher than MOSFETs at the time. The fabricated devices had at least 10% smaller cell

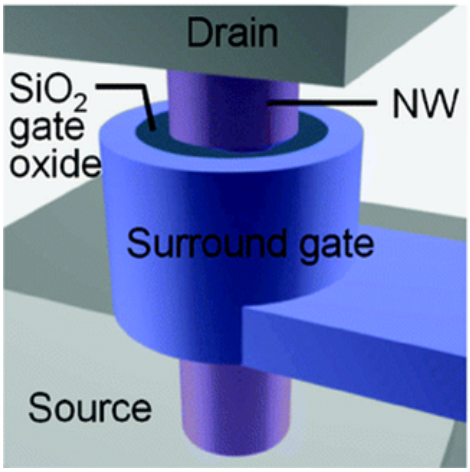

Fig. 3.6 Schematic view of vertical-surround-gate ZnO nanowire FET. Sourced from [69].

size than the state-of-the-art MOSFET. The vertical integration of nanowire FETs could provide a way towards ultrahigh density fabrication of devices [69].

Amartunga and Cha *et al.* have reported a side-gated metal-air gap-semiconductor field effect transistor with ZnO NW as semiconductor channel [70–72]. The devices revealed excellent electrical properties. Transconductance of 3.06 μS was reported, which was an order of magnitude higher than those of earlier studies. The subthreshold slope was measured to be 129 mV/decade, which is at par with any other configuration as well as state-of-the-art MOSFETs. The values of field effect mobility were in the range of 800-1000 cm^2/V.s for all the devices [72]. Lee *et al.* have also reported air-gap FETs based on ZnO nanowire using magnetic field to selectively align Ni-capped ZnO nanowires on a pre-fabricated electrode pattern. Poorer electrical performance was observed with on-off ratio of 10 and field effect mobility of 3 cm^2/V.s and the scattering effect caused by negatively charged surface adsorbates could be the possible reason. However, the device shows prospective application in sensors due to greater surface area availability as well as strong performance dependency on surface interaction [73].

Keem *et al.* have demonstrated fabrication of an omega-shaped-gate (OSG) ZnO nanowire FETs as shon in Fig. 3.7. The transconductance value of 0.4 μS and I_{ON}/I_{OFF} was of 10^7. The enhanced field effect mobility due to the OSG geometry and improved passivation is observed to dominate over reduction due to high-k dielectric Al_2O_3, leading to significantly better electrical performance [74].

The enhancement or depletion working modes of the ZnO nanowire FETs can also be controlled. Heo *et al.* [75] have demonstrated n-channel depletion mode ZnO nanowire

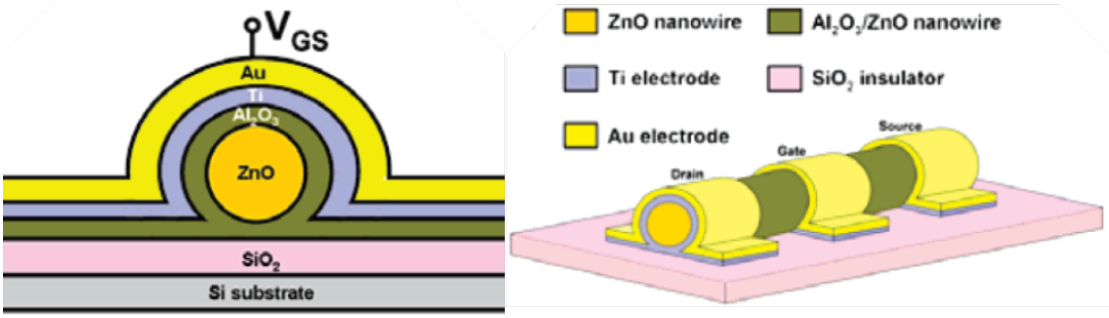

Fig. 3.7 Schematic of omega-shaped-gated ZnO nanowire FET. Sourced from [74].

FETs, at room temperature in the dark with very low gate leakage current as well as excellent saturation and pinch-off characteristics [75]. Hong *et al.* [76] have reported reproducible fabrication of depletion-mode (D-mode) and enhancement-mode (E-mode) nanowire FETs. The authors demonstrated that working modes of the ZnO nanowires can be tuned by manipulating their vapour transport growth. Nanowires grown on Au-coated sapphire substrate showed n-channel D-mode, whereas nanowires grown on Au-catalyst-free ZnO film showed E-mode. Surface defects states acting as scattering and trapping centres are predicted to have caused different modes [76]. Jo *et al.* demonstrated a logic invertor device based on D-mode and E-mode FETs based on ZnO nanowire [77]. Roy and Gao fabricated a logic inverter on a single nanowire using different working modes. The authors achieved E-mode by direct deposition of a Pt gate electrode on the nanowire by focused electron beam (FEB) inducing Schottky barrier; on the other hand D-mode was achieved by encapsulating an insulating layer between the focused ion beam (FIB) deposition of Pt gate electrode and nanowire [78].

Although use of SiO_2 as a gate dielectric is commonly pursued, many groups have also used various other dielectric materials. Yim *et al.* have used 300 nm layer of silicon nitride (Si_3N_4) as gate dielectric [79]. They reported I_{ON}/I_{OFF} ratio of 10^5 and mobility ranging from 1.6 to 8 cm^2/V.s. Cross-linked polyvinylphenol (cPVP) has also been explored as gate dielectric by few groups. Yoon *et al.* have coated DEP aligned ZnO nanowires with 200 nm cPVP. Field effect mobility of back-gated FETs with SiO_2 as gate dielectric was 16 cm^2/V.s, while top-gate measurement with cPVP as gate dielectric revealed mobility of 8 cm^2/V.s [80]. Jo *et al.* have used cPVP as polymer dielectric in a logic inverter based on D-mode and E-mode ZnO nanowire FETs. It was found that smooth nanowire FETs showed transconductance and field effect mobility of 147 nS and 65 cm^2/V.s respectively, whereas corrugated nanowire FETs showed values of 140 nS and 67 cm^2/V.s [77].

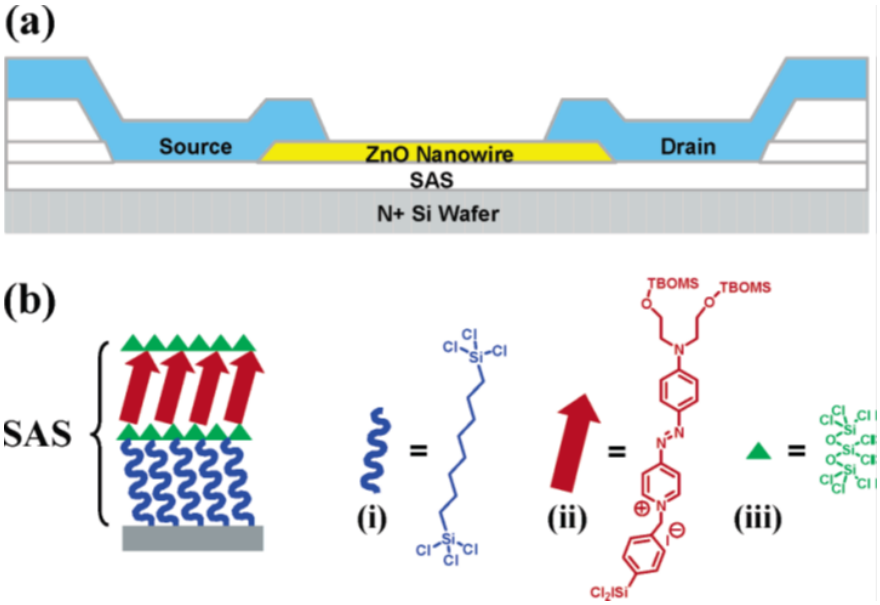

Fig. 3.8 (a) Device structure of ZnO nanowire FET with 15 nm SAS gate dielectric (b) Structure and components of SAS. Sourced from [81].

Ju *et al.* went down the road of self-assembled superlattice (SAS) as gate dielectric. The device structure is shown in Fig. 3.8 In spite of the poorer subthreshold slope (∼400 mV/decade) on-off current ratio (I_{ON}/I_{OFF}) of 10^4, a much improved field effect mobility of ∼196 cm^2/V.s was reported. The devices also showed lower operating voltage of 1.5 V [81]. Furthermore, no significant shift in threshold voltage was observed in these devices after proton irradiation, showing application in space-electronics [82]. Further investigation of the effect of gate-bias-stress resulted in minimization of the off-current and threshold voltage variation [83]. Ozone treatment of the devices revealed improvement in electrical performance with on-off current ratio (I_{ON}/I_{OFF}) of 10^7, subthreshold slope of 130 mV/decade and calculated field effect mobility of ∼1175 cm^2/V.s [84].

There has been significant interest in tuning the electrical properties of ZnO nanowire FETs by controlling surface trapping and scattering states. Park *et al.* have reported a passivation effect due to the polyimide coating on ZnO nanorods leading to mobility increase from 75 cm^2/V.s to ∼1000 cm^2/V.s [85]. Nanowire surface passivation has also been attempted with HfO_2 [86], SiO_2/Si_3N_4 bilayer [87], poly(methyl metahacrylate) (PMMA) [88, 89] Al_2O_3 and parylene C [90]. Chang *et al.* [87] have, in particular, reported much higher mobility of 3118 cm^2/V.s and transconductance of ∼150 mV/decade.

Hong *et al.* have investigated the effect of ZnO nanowire surface interaction on FET performance. Alteration of surface architecture by vapor transport growth of ZnO nanowires

on various ZnO buffer film coated sapphire substrates was demonstrated along with dependency of electrical properties on surface-morphology and nanowire-size [91]. The effect of surface roughness was studied by using smooth-surface nanowires grown on Au-catalysed sapphire and rough-surface nanowires grown on Au-catalysed ZnO/sapphire. Both smooth and rough nanowire FETs demonstrated an increase in mobility from $\sim$ 9.9 cm^2/V.s to $\sim$17.4 cm^2/V.s and from $\sim$11.1 cm^2/V.s to $\sim$ 49.5 cm^2/V.s, respectively, on passivation with PMMA. Threshold voltage shift of 6.7 V and 21.7 V respectively was also observed. Passivated devices also showed larger transconductance indicating stronger electrostatic gating [88]. A positive shift in threshold voltage as well as reduction in undesired hysteresis was also revealed after PMMA passivation [92].

Maeng *et al.* reported a drop in current and positive shift in threshold voltage due to gate-bias sweep. The effect was pronounced in increased oxygen ambient as compared with nitrogen ambient, suggesting oxygen adsorption causing surface depletion [93]. Sohn *et al.* have demonstrated that the positive shift in the threshold voltage can be attributed to adsorption of oxygen on the nanowire surface capturing the conduction electrons and depleting the nanowire channel region [94]. Dependence of threshold voltage and conductivity on measurement procedure in ambient conditions has also been reported by Weissenberger *et al.* [95]. Choe *et al.* investigated threshold voltage shift [96]. The authors have suggested charge trapping in the ZnO NW-dielectric interface as the cause of this effect.

Hong *et al.* [97] and Song *et al.* [98] have used PMMA surface passivation for threshold voltage stabilisation and observed that electrical properties of ZnO nanowire FETs remained unchanged in different oxygen environments or in vacuum. Furthermore, Nedic *et al.* have exploited Al_2O_3 and parylene C to improve the passivation of ZnO nanowire FETs. Parylene C passivated top-gate devices have shown very little variation in threshold voltage, implying reproducibility in the fabrication [90].

In pursuit of achieving threshold voltage control, controlling the diameter of ZnO nanowires opens up another avenue. Kim *et al.* have observed a negative threshold voltage shift from 2.73 V to -3.02 V with increasing diameter from 53.3 nm to 85 nm of silver-doped ZnO nanowire based FETs. This method could be a simple way to control threshold voltage as well as to fabricate both D-mode and E-mode FETs [64]. In another study, nanowire diameter was controlled by varying the thickness of the Au-catalyst layer in vapour-transport growth. A negative shift in the threshold voltage was observed with increasing the nanowire diameter [99]. The diameter dependence of the threshold voltage is possibly due to the change in the number of active charge carriers. A relatively larger depletion region of smaller diameter results from an increase in trap density [99, 64].

Various attempts have been made to control electrical performance and the operating voltage by surface treatment. These techniques include ozone treatment [84], hydrogen plasma [100], electron irradiation [95] and focused ion beam (FIB) treatment [101] where reduction in the surface trapped electrons by removing adsorbed oxygen species resulted in improving device performance. On the other hand, a positive shift in the threshold voltage was observed after oxygen plasma treatment [100] and solvent driven isopropyl alcohol (IPA) treatment [102] due to increased adsorption of oxygen on the nanowire substrate increasing the depletion region. Short time proton irradiation sifted the threshold voltage in a negative direction, whereas long irradiation shifted the threshold voltage in a positive direction [103]. Another study indicated high energy (10 MeV) proton beam irradiation caused a positive shift in threshold voltage with decrease in carrier density [104]. Excimer laser annealing of ZnO nanowires was observed to increase in ON-current and negative shift in threshold voltage [105].

While behaviour of ZnO nanowires is intrinsically n-type [59], efforts have been made to induce p-type conductivity. Xiang *et al.* were the first to report high quality p-type ZnO nanowires. Growth was achieved using chemical vapor deposition on a-plane sapphire, wherein P_2O_5 powder was mixed with ZnO:C mixture. Further annealing at 850 °C in N_2 gas for 1 min was carried out to change the nanowires from n-type to p-type [106]. The p-type conduction was still quite unstable and it reverted to n-type after about two months. Ming *et al.* claimed that, nitrogen could be better suited for p-type doping due to its atomic size being similar to that of oxygen and gaseous dopant source would be more effective. The authors report p-type conduction by annealing in N_2 gas for 2 min at 600 °C [107]. Yuan *et al.* have shown growth of high-quality single crystal p-type ZnO nanowires achieved by reactive CVD method using N_2O as dponat. The FETs based on as-grown nanowires revealed stable electrical properties with hole concentration $\sim 10^{18}$ and field-effect mobility ranging from 10 cm^2/V.s to 17 cm^2/V.s [108].

There have also been a number of reports on ZnO nanowire FETs on flexible and transparent substrate. Kang *et al.* have fabricated ZnO nanowire FETs on polyether sulfone (PES). Along with good electrical performance, less than 3% change was observed on subjecting PES substrate to 0.77% strain [109]. Ju *et al.* have demonstrated fabrication of ZnO nanowire FETs on glass and PET substrate with ∼82% transparency [110]. Noh *et al.* have demonstrated self-aligned ink-jet printing (SAP) of ZnO nanowire FETs, opening new avenues for many solution-dispersible nanowire semiconductor device fabrication [111]. Ko *et al.* have used direct nanoimprinting of metal nanoparticle solution and low-temperature hydrothermal growth of ZnO nanowires together to fabricate a ZnO nanowire transistor on polymer substrate [112]. Liu *et al.* have shown a ZnO nanorod strain driving transistor (SDT)

on Kapton substrate using single-step hydrothermal approach. They have also further used them in complementary manner to realize numerous logic operations [113].

3.4 ZnO nanowires for gas sensing applications

Over the past decade there has been growing demand for chemical and gas sensors for various applications such as environmental monitoring, food safety as well as medical diagnosis [114]. Most common gases of interest are CO, NO, NO_2, NH_3, SO_2, CO_2, CH_4 along with various volatile organic compounds (VOC) such as toluene, acetone, ethanol, methanol and benzene [25]. Some of the gaseous components, even in parts-per-million (ppm) quantities, are hazardous due to their toxicity, corrosive or poisonous effects [24]. Evidently sensitivity is the key requirement for gas sensors. However, the ability to discriminate between gases poses even greater challenges in the development of reliable gas sensors [24]. Lower limit of detection (LOD) and selectivity are key performance metrics of a gas sensor along with low power consumption, fast response and recovery time, stability and sensitivity [25]. The current societal demands require small, portable with wireless connectivity, cheap, fast and easy-to-use sensors. Advances in micro-electromechanical systems (MEMS) have opened up enormous possibilities of integrating gas sensor devices with micro-heaters as well as single conditioning to develop on-chip solutions. Nano-structural materials have further provided unparalleled enhancement in gas-sensing performance owing to their high surface area, effective surface depletion modulation and size matching with analyte particles [114, 24].

Numerous detection mechanisms have been implemented, such as optical absorption, modulation of the field-effect transistor, surface acoustic wave (SAW) resonators, quartz crystal microbalance, current or voltage change and resistive changes. Semiconducting-metal-oxides (SMO) are the most widely used materials in gas sensor production [25]. A vast variety of SMO materials have been put to use in gas sensing. SnO_2 is being pursued most widely for gas sensors, followed by ZnO. However, recent progress in synthesis of high-quality 1D ZnO nanostructures has kindled their widespread use as gas sensors. Different nano-scale geometries are also being tested for this purpose [115].

The work carried out in the past decade has been summarised in numerous review papers on SMO gas sensors [22–24, 114, 116, 117] and SMO nanowire gas sensors [4, 25–27, 115, 118–123]. For the purpose of this project ZnO nanowire based gas sensors will be of primary interest.

Many research groups have attempted to employ ZnO nanostructures for gas sensing applications. Although ZnO nanowire gas sensors have shown superior sensitivity, their selectivity is still an issue. Efforts are also being made to functionalise the ZnO nanowires by various methods such as surface modification, core shell nanowires, changing intrinsic defects in the nanowire, noble metal nanoparticle coating as well as array of nanowires. The work carried out on ZnO nanowire gas sensors is outlined in this section.

Sadek *et al.* have reported optimal temperature ranges for ZnO nanobelt-based gas sensors for H_2, NO_2 and propene sensing [124]. Lee *et al.* have fabricated ZnO nanobarbed fibres based NO_2 sensors with sensitivity up to 30 ppb concentration [125]. Multiple ZnO nanorod based gas sensors with $\sim$18 % sensitivity to 10 % H_2 in N_2 at 200 °C and 21 % sensitivity to ozone at room temperature are reported by Kang et al [126]. Hsueh *et al.* demonstrated the utility of laterally grown ZnO nanowires for ethanol sensing and observed 18 % sensitivity towards 50 ppm ethanol at 300 °C [127]. Zhang *et al.* reported reversible and repeatable CO sensing using ZnO nanowire random network gas sensors [128]. Huh *et al.* reported highly sensitive H_2 detection using ZnO nanorod network [28]. Recently, Yin *et al.* have demonstrated enhanced gas sensing stability and performance towards ethanol sensing by using ethanol as a solvent for solvothermal growth of ZnO nanorods [129]. Well-aligned nanowire arrays have also been used by Liao *et al.* [130], Ra *et al.* [131] and Son *et al.* [132] for gas sensing. Son *et al.* demonstrated sensitivity of 10 even for 0.2 ppm concentration of ethanol [132].

There have been reports of using nanoscale ZnO heterostructures for gas-sensing applications. Park, Choi and Kim have achieved enhancement in gas sensing towards O_2 and NO_2 [133] as well as CO [134] by using SnO_2-ZnO core-shell nanofibres. It has been suggested that a fully depleted shell layer arising due to the ZnO shell-SnO_2 core fibre heterojunction is the reason for this improved performance. Park *et al.* have found enhancement in NO_2 detection of SnO_2-Core/ZnO-Shell nanowires under UV illumination [135].

It has been observed that modification in intrinsic properties of the ZnO nanowire could lead to better sensing performance. Ra *et al.* have found that ZnO nanowires with multiple grain boundaries have a sensing response almost three times that of single crystal nanowires, due to grain boundary modulation. However, they were found to exhibit slower response and recovery times than single crystalline nanowires due to internal diffusion effects [136]. Park *et al.* have also reported dramatically improved sensing response to NO_2 in nano-grained ZnO nanowires [137]. Law *et al.* have found that ZnO nanowire sensors show four times improved sensitivity to NH_3 after oxygen plasma treatment. On the other hand, Chu *et al.* [138] have observed that ZnO nanostructures grown under higher oxygen concentration

show improved H_2 sensing. Both studies suggest that reducing carrier concentration in the nanowires by enforcing higher oxygen amount to adsorb on the surface enhances the gas sensing performance.

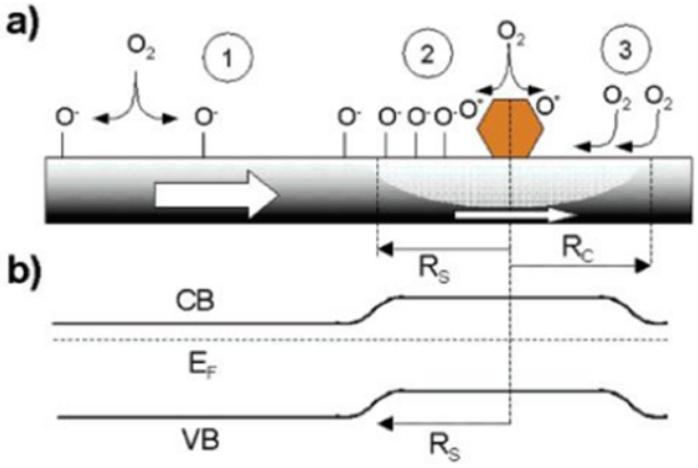

Fig. 3.9 (a) Schematic representation of spillover mechanism of catalysis. 1 denotes adsorption of O_2 on SMO surface, 2 denotes spillover effect and 3 denotes back-spillover effect and R_C is the capture radius (b) band diagram of SMO nanowire with R_S being radius of spillover zone. Sourced from [22].

The gas sensing response is the result of reaction of the target gas with sensor materials' surface. Thus catalytic activity tempering is a measure widely adopted to improve gas-sensing performance. Noble metals are well known for their effective oxidation catalysis. There are a number of reports on various noble metal particles, such as Pt [139–141], Pd [142, 143] [144, 145] and Au [146, 147], being used to increase the gas sensing performance of ZnO nanowires. Improvement of gas-sensing reactions due to a catalyst such as Pd, Pt can be explained by spillover effect. Catalyst dissociates the gas molecule O_2, for example, and then atoms 'spillover' to the SMO surface by diffusion. A 'back-spillover effect' is also observed, wherein a gas molecule resides on the SMO surface but diffuses to the catalyst particle before desorption. The catalyst particle forms a 'collection zone' around it which is denoted by 'capture radius'. An efficient gas adsorption is achieved if the entire SMO surface is covered by collection zones [22, 25]. The entire process is shown in Fig. 3.9.

Specific surface area, temperature and connecting electrodes are the three main factors that influence sensors based on ZnO nanostructures. Different morphologies show different surface-to-volume ratio and thus different sensitivity. Thinner ZnO nano-rod sensors are found to have significantly higher sensitivity due to their larger surface area. The key surface processes involved in gas sensing are temperature dependant. Consequently, sensitivity rises with increasing temperature. However, it drops above the optimum temperature, since

desorption will dominate over adsorption. Thus the temperature at which ZnO nanostructures show highest response varies with target gas. It has also been demonstrated that sensitivity can be increased dramatically if one electrode contact is Ohmic and the other is Schottky, the underlying cause being lowering of Schottky barrier height due to adsorption of O^- thus will produce a jump in the current [26].

Field effect transistor (FET) based gas sensors with ZnO nanowire as channel have also been reported with superior gas-sensing performance as well as selectivity of the sensor [4]. Fan *et al.* have explored gate voltage dependence of oxygen sensitivity and achieved maximum sensitivity of 64% at voltage just above threshold [61]. The authors also found that an electric field applied over the back-gate electrode altered the NO_2 and NH_3 sensitivity significantly [148]. Li *et al.* have observed high sensitivity of ZnO nanowire FETs to oxygen secured by change in drain current along with shift in threshold voltage [149]. Nanowire FETs could be much more sensitive than resistive gas sensors because conductivity of the nanowires can be altered by gate voltage [4]. Multiple channelled nanowire FETs have recently been investigated to achieve uniformity in the gas-sensing properties [24].

Most ZnO gas sensors show maximum sensitivity at elevated temperatures. In order to build an entirely portable gas-sensing device it becomes essential to include micro-heaters along with a sensor device and integrate both with the CMOS technology for signal conditioning. Udrea *et al.* have reported ZnO nanowire-CMOS sensors for ethanol [56, 57], toluene [58] and hydrogen [55] sensing. In order to further decrease the power consumption, optimisation of the microheaters as well as self-heating type SMO gas sensors are also proposed [25, 24].

3.5 Semiconducting metal oxide based electronic nose

Metal oxide gas sensors have shown exceptionally high sensitivity to many chemicals and gases. However, the major hurdle in their practical application is their limited selectivity. An innovative solution to this problem is the Electronic Nose system [150]. The concept is based on identifying a gas mixture by its aroma signature pattern without having to detect its components individually [151]. Electronic nose comprises an array of multiple sensors and a data processing unit. The sensor array contains sensors with distinctively different response to a wide range of gases and volatile organic compounds (VOC). The responses of the individual sensors are collectively studied using statistical and pattern analysis algorithms such as Principle Component Analysis (PCA). The mixture of analytes is identified by its unique electronic fingerprint [151].

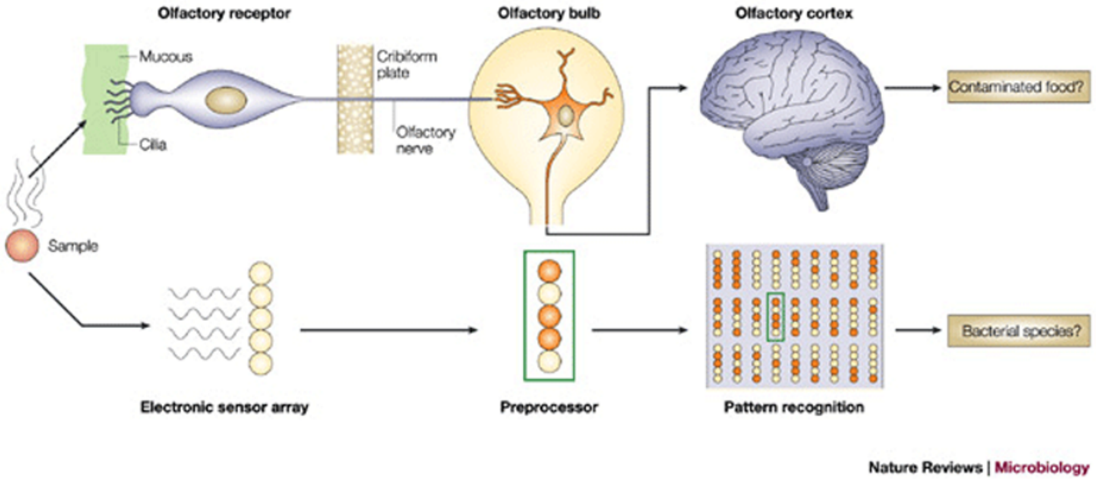

Fig. 3.10 Analogy between human olfactory system and working on electronic nose. Sourced from [152].

Concepts of electronic nose originated while attempting to mimic the ability of the olfactory system to distinguish smells [153]. This analogy between the human olfactory system and an electronic nose is shown in Fig. 3.10. One of the earliest reviews on electronic nose has been provided by Gardner and Barlett [154]. Subsequently, Strike *et al.* have summarised various types of sensor used in building an electronic nose. These include metal-oxide-semiconductor sensors, gas-sensitive field-effect transistors conducting polymers and acoustic wave devices [155]. Electronic nose systems have found application in a wide variety of fields, such as food analysis [156], detection of combustion gases [157] and quality control of alcoholic beverages [158, 159]. Electronic noses based on gas [160] and chemical [161] sensors have been reviewed. This section focuses on electronic noses based on nanowire gas sensors and those implemented in breath diagnosis.

Gerber *et al.* have demonstrated electronic nose systems based on micro-cantilever arrays [162–164]. Use of Karlsruhe Micro Nose (KAMINA) technology to create a thermal gradient on a sensor platform followed by Linear Discrimination analysis (LDA) to enhance discrimination between a number of gases has been reported [150]. Chen *et al.* [165] have built an nanoelectronic nose based on nanowire gas sensors of four materials - In_2O_3, SnO_2, ZnO nanowires and single walled carbon nanotubes (SWNT). The authors emplyed the use of Principle Component Analysis (PCA) to discriminate between H_2, NO_2 and ethanol . The p-type behaviour of SWNT and n-type behaviour of SMO nanowires provided a largely distinctive sensor response leading to great discrimination between hydrogen, ethanol and nitrogen dioxide. Castro *et al.* demonstrated an electronic nose based on five polymers mixed with CNT to distinguish nine organic vapours [166]. Hu *et al.* [167] fabricated a

single-nanowire sensor array of a metal, a semiconductor, and two polymer nanowires on a single chip by selective electrodeposition. The authors reported use of a PCA technique to distinguish four gases with sub-ppm quantities.

Other reports include electronic nose systems based on longitudinal variation of single SnO_2 nanobelt [168] and also with graphene, CNT and copper nanotube [169]. Electronic noses based on ZnO nanowire have also been reported. Ko *et al.* exploited ZnO nanorod patterns of different sizes [170]. Chen *et al.* have designed ZnO nanowire array-based electronic noses using different metal oxide coatings [171, 172] as well as noble metal coatings [173]. The most common trend in all these studies is the use of different materials either for the sensor itself or for sensor coating to prepare the array to achieve a distinct response. It has also been observed that most of the electronic nose systems reported above have used either PCA or LDA to analyse the sensor response.

Recently electronic nose systems have been employed for breath diagnosis of a wide range of diseases. The reason for their popularity is the capability to produce results much faster than by conventional methods and prospects of detecting disease at a much early stage [11]. There have been numerous reports on electronic nose based breath diagnosis for lung and brain cancer [174–177] . Gardener *et al.* have reviewed some of the earliest work carried out at Warwick University on electronic nose to diagnose illness [178]. Wilson and Baietto have provided a comprehensive review of biomedical applications of electronic nose technologies [7]. Chen *et al.* [179] have provided one of the latest reviews of applications of electronic nose in clinical diagnosis. In their brief review, the authors have shed light on components of the electronic nose system and provided a list of actively researched human diseases for electronic nose-based diagnostics and their proposed bio-markers.

Chapter 4

Solution Processed ZnO Thin Film Transistors from Zinc Neodecanoate

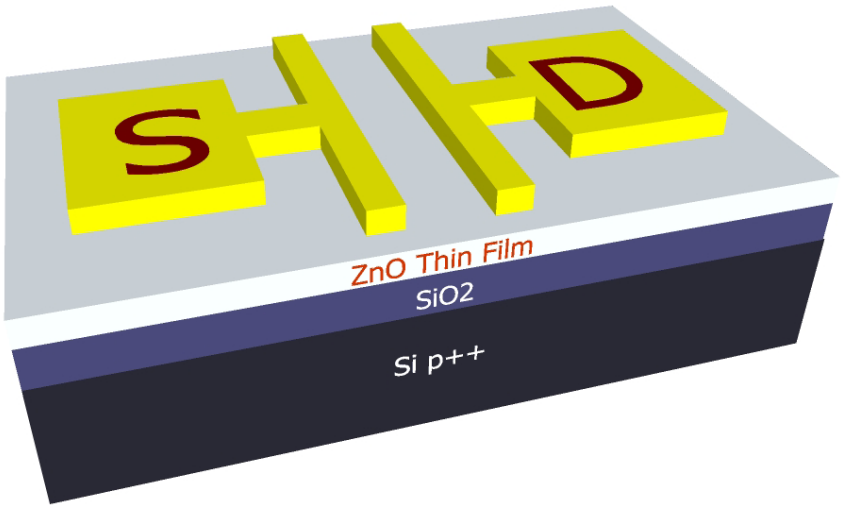

4.1 Introduction

The ZnO-based devices that have shown the most promising prospects and evolved rapidly towards commercial integration are thin-film transistors (TFTs). Over the past 15 years, this area of oxide TFTs has grown exponentially, spanning from vacuum-based processing to cheaper solution-based processing in recent years. An epitome of the growth in the area of oxide electronics is Indium-gallium doped zinc oxide (IGZO) poised to replace a-Si as a channel material among active matrix displays.

Due to their simplicity of fabrication as well as suitability to various optical and electrical characterisation, development of conventional TFT devices was investigated prior to exploring direct-write patterned devices. The current chapter thus focuses on fabrication of ZnO TFTs using zinc neodecanoate as functional precursor. Optical as well as structural characterisation was used to inspect the quality of the zinc oxide formed after thermally decomposing the precursor films. Optimisation of the fabrication process is then carried out by acquiring electrical characteristics of ZnO TFTs. In the final section the carrier transport mechanism is then investigated.

4.2 Fabrication Method

4.2.1 Precursor preparation

ZnO thin films were prepared from zinc neodecanoate precursor obtained from Alfa Aesar (structure shown in Fig. 4.1). Physically the precursor is a pale brown coloured viscous liquid with density of 1.1 g/cm^3. Zinc content in the chemical is typically 17.9-18.2 %. The precursor was observed to be immiscible in water.

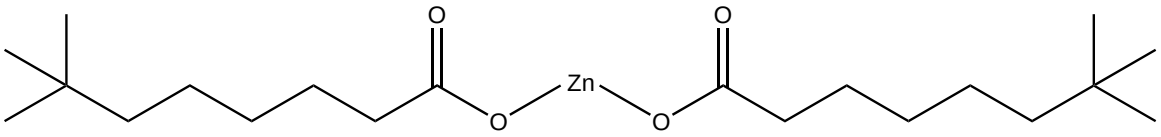

Fig. 4.1 Chemical structure of zinc neodecanoate Molecule.

The precursor material was diluted by dissolution in toluene and, in order to avoid any photodegradation, amber coloured 20 ml glass vials were used to prepare and store the solution. Since toluene aggressively dissolves standard polypropylene caps, PTFE faced

silicone rubber lined caps were used. Owing to the viscous nature of zinc neodecanoate, the required quantity of the material was measured by weight.

The glass vial and cap were cleaned with acetone and isopropyl alcohol and thoroughly dried using compressed nitrogen. Depending on the required precursor concentration, a measured amount of zinc neodecanoate was then added into the vial. The vial was removed from the weighing scale and a proportionate volume of toluene was added. The concentration and quantities of both the chemicals used, are shown in Table 4.1. In order to thoroughly dissolve precursor in toluene the sealed vial was then placed in a water bath under ultrasonic agitation at 80 °C for 3 hours. The vial was then removed from the water bath and allowed to cool down. Once dissolved, the solution was stable for months.

Table 4.1 Dilution of zinc neodecanoate

Concentration	Toluene (ml)	Zinc Neodecanoate (ml)	Zinc Neodecanoate (gm)
5 %	15	0.75	0.83
15 %	15	2.25	2.48
25 %	15	3.75	4.15
50 %	12	6	6.64

4.2.2 Substrate preparation

The substrates used for ZnO TFTs were prime grade boron doped p^{++} Si(100) wafers with 100 nm thermally grown SiO_2. The 4" wafers were diced into 12 mm x 12 mm sized substrates using a diamond tip cutter. Cleaved substrates were thoroughly cleaned with 10 min ultrasonic agitation in acetone and isopropyl alcohol and dried using compressed nitrogen flow. The samples were then placed in a freshly prepared piranha solution (1:3 mixture of hydrogen peroxide and sulphuric acid) for 15 min and then thoroughly rinsed in HPLC grade water. After blow drying with compressed nitrogen, samples were treated with oxygen plasma for 10 min and then dried on a 200 °C hotplate. The precursor solution was then spin coated on the dried substrates. Single crystal quartz substrates were used for the UV-visible spectroscopy measurement and were processed in exactly the same way as the Si-SiO_2 substrates.

4.2.3 Precursor spin coating

Before spin coating, the solution was drawn into a disposable syringe. Syringes with PTFE plunger are used since toluene dissolves standard rubber plungers. The solution was then filtered through 0.2 μm syringe filter with PTFE or nylon membrane. In order to avoid contamination, dried samples were loaded into the spin coater and the solution was filtered directly on to the substrates. The spin coating was performed at 2000 rpm for 60 sec with ramp rate of 2000 rpm/sec. After the spin coating samples were baked at 115 °C for 1 min to dry off the remaining solvent.

4.2.4 Precursor decomposition

Once the precursor is spin coated onto the substrate, a thermal annealing step is required to decompose and form ZnO. In order to choose a suitable temperature range thermogravimetric analysis (TGA) was performed. The temperature vs percent weight loss profile can be seen in Fig. 4.2. The material was held inside the furnace at 100 °C for 30 min to get rid off any adsorbed water molecules and then ramped up to 850 °C with 10 °C/min. Between ∼125 °C and ∼275 °C a low rate of mass loss can be seen due to loss of volatile impurities. After ∼275 °C the final stage of degradation can be observed when a steeper rate of mass loss takes place. The peak at the mass loss rate at ∼350 °C suggests decomposition of neodecanoate molecules. After ∼375 °C no significant mass loss was observed, signifying completion of the precursor conversion.

Given the TGA analysis, annealing temperatures starting from ∼400 °C were chosen for the further optimisation of the ZnO films. Samples with spin-coated precursor were loaded into a Carbolite tube furnace using Haldenwanger alumina combustion boats of 115 mm x 16mm x 9mm dimensions purchased from Fisher Scientific. Haldenwanger impervious aluminous porcelain (IAP) furnace worktubes were used with dimensions of 22 mm bore x 28 mm outer diameter 660 mm length. IAP worktubes were used as a cheaper alternative to standard mullite worktubes, since no aggressive halogen chemistry or extreme high temperatures were required. After loading the samples roughly at the centre of the furnace, the furnace was ramped up at 10 °C/min up to final annealing temperature ranging from 400 °C to 700 °C. Once the set point temperature was reached the furnace was kept at that temperature for 1 hour and then furnace cooled slowly back to room temperature. During the annealing step, one end of the tube was connected to the exhaust line, giving very weak vacuum suction, while the other end of the tube was left open for the annealing to take

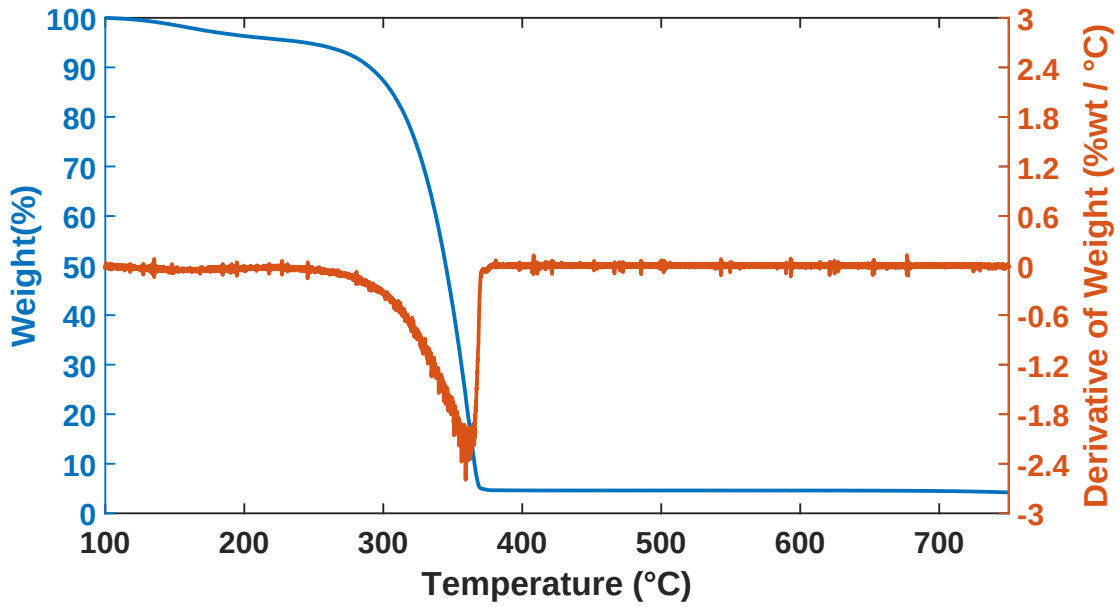

Fig. 4.2 Thermogravimetric analysis (TGA) of zinc neodecanoate with percent weight loss (left axis) and rate of weight loss (right axis). Measurement was performed in nitrogen flow of 20 ml/min with 10 °C/min starting with 11.3 mg zinc neodecanoate.

place in air environment. The precursor decomposition experiments were also carried out under the Ar flow of 100 sccm. However, zinc oxide films were not formed.

4.2.5 Electrode fabrication for TFT structure

The thin film transistors fabricated in this study were Bottom Gate-Top Contact devices. Once the ZnO thin films were prepared on the Si-SiO_2 substrates, the source and drain contacts were formed using photo-lithography and lift-off process. The complete processing flow is shown in Fig. 4.3.

AZ5214E photoresist was spun on top of the ZnO layer at 6000 rpm for 60 sec with ramp rate of 2000 rpm/sec. The thickness of the photoresist formed was $\sim$1 μm. The samples were then baked at 115 °C for 1 min to dry off the solvent. The samples were then exposed with 365 nm UV light in contact mode with SUSS MJB4 mask aligner using negative chrome mask on soda-lime glass. The intensity of the mask aligner UV lamp was maintained at 10 mW/cm^2 and the samples were exposed for 1 sec giving 10 mJ/cm^2 of dose. The samples were then baked for 2 min at 125 °C. This post-exposure bake step, also known as reversal bake, causes cross linking within the exposed region of the resist. A flood exposure of 25 sec

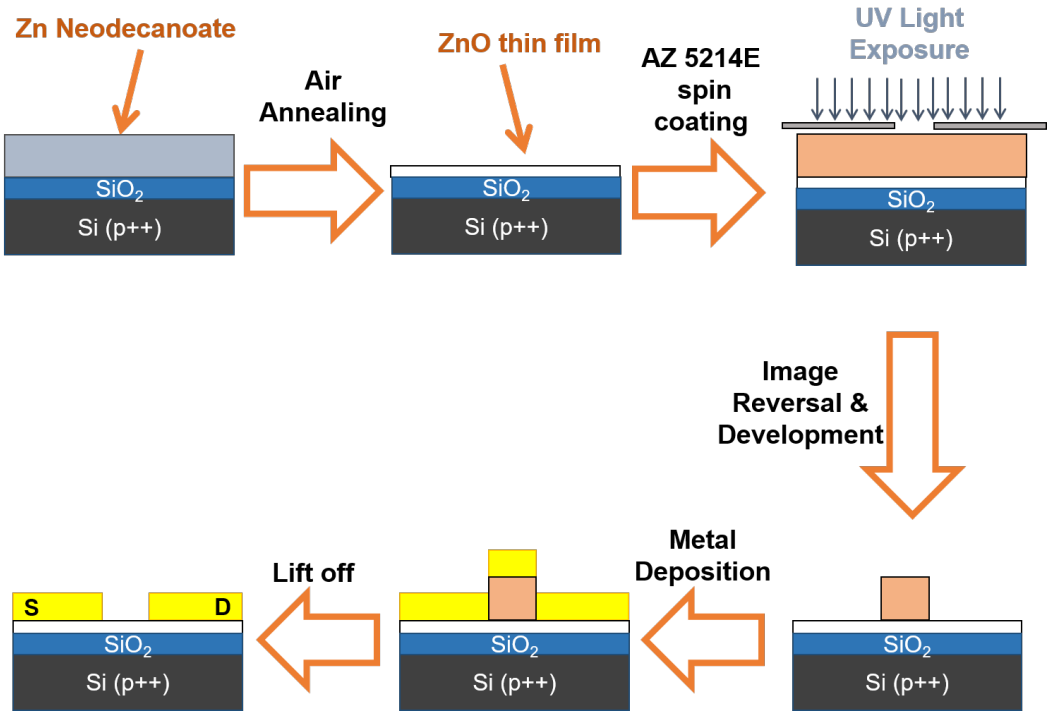

Fig. 4.3 Processing steps for ZnO TFT from zinc neodecanoate precursor.

(250 mJ/cm^2) was then applied to render uncrosslinked regions of the photoresist soluble in developer solution. The samples were then submerged in AZ 726 MIF developer for 25 sec, followed by thorough rinsing in water to remove excess developer and avoid further resist erosion. The undercut profile generated by this image reversal photo-lithography is ideal for the lift-off process.

After development the samples were loaded into a metal evaporation chamber and pumped down to 10^{-6} mbar pressure. Once under vacuum, the metal source is heated using either electron beam bombardment or resistively heating a tungsten boat containing the source material. Due to extremely low pressure inside the chamber, contact metal typically melts and starts to evaporate. Once the steady evaporation rate is achieved, the shutter is opened to allow the contact metal to deposit on the substrate. After $\sim$100 nm metal deposition, the shutter is closed and the source is allowed to cool down. The chamber is then vented to atmospheric pressure and the samples are unloaded from the chuck.

The final step in the fabrication of TFTs is to lift off metal from the regions masked by the photoresist. The samples were submerged in warm acetone ($\sim$40 °C) for a couple of hours and agitated with a stream of solvent using a disposable syringe. Gentle sonication was applied for a few seconds, as necessary. During the lift-off step the photoresist dissolves in acetone solvent and metal that was deposited on top of it gets detached from the substrates.

The samples were then removed from the acetone and rinsed with isopropyl alcohol to remove acetone, then dried under compressed nitrogen flow. Once prepared, the samples were stored in amber coloured desiccators.

4.3 Material Characterisation

4.3.1 Structural characterisation of ZnO thin film

In order to study the effect of decomposition temperature on the conversion to crystalline ZnO phase and the crystal quality, X-ray diffraction measurements were performed on ZnO films prepared by drop casting. A 15 % zinc neodecanoate solution was drop casted on a cleaned Si-SiO_2 substrate and left overnight to evaporate the solvent. The substrates were then calcined at temperatures ranging from 400 °C to 700 °C for 1 hr, followed by XRD characterisation. Fig. 4.4 depicts the evolution of XRD pattern with annealing temperature. The XRD peaks obtained from the measurements were indexed using polycrystalline wurtzite/zincite ZnO JCPDS card No. 36-1451 [180, 181]. The peaks at 2θ angles of 32 °, 34.5 ° and 36.5 ° correspond to (100), (002) and (101) orientation of ZnO, respectively. The peak at 33 ° probably corresponds to contamination peak, as suggested in case of zinc naphthenate [182].

Presence of ZnO crystalline peaks in all the annealing temperature clearly suggests formation of polycrystalline ZnO films [183]. However, with increasing annealing temperature, the corresponding peaks get sharper. At the same time, the peak-width also becomes narrower with increasing decomposition temperature. Such evolution of the XRD measurements can be attributed to improved crystallinity of the converted ZnO phase as well as increase in the ZnO grain size. In order to ascertain the broadening of the most prominent three peaks-(100), (002) and (101), the corresponding XRD peaks were fitted to Gaussian distribution function. The values of full-width-half-maxima (FWHM) thus obtained from the Gaussian fits are illustrated in Fig. 4.5 for different annealing temperatures. A monotonous decrease in the FWHM with increasing calcination temperature can be clearly seen for all three peaks, implicating increase in the average grain size of the ZnO films formed [184].

4.3.2 Optical Characterisation of ZnO Thin Films

Zinc oxide, being a direct bandgap semiconductor with a wide-bandgap of $\sim$3.3 eV[16], is transparent to visible light. However, it starts absorbing light in the near UV region.

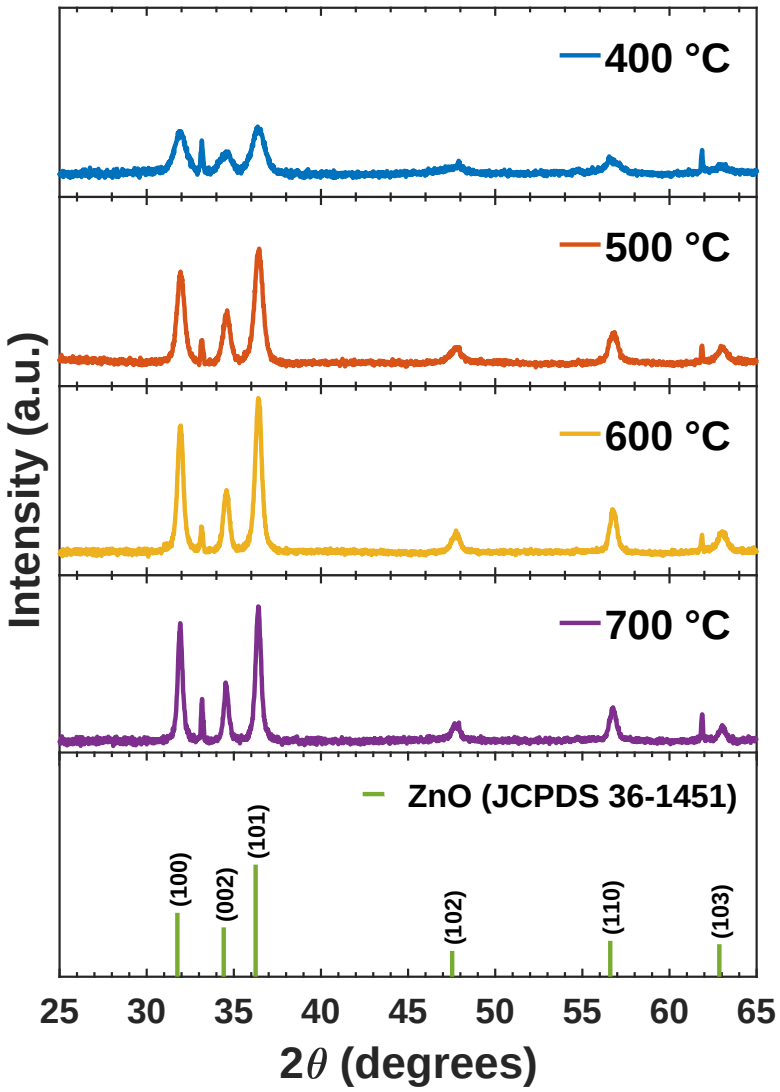

Fig. 4.4 X-ray diffraction measurements of ZnO films prepared by drop casting 15 % zinc neodecanoate and annealed at different temperatures depicting polycrystalline nature of the films. The peaks identified with polycrystalline wurtzite/zincite ZnO JCPDS card No. 36-1451 [180, 181]. As the annealing temperature is increased, the corresponding peaks are seen get sharper while the peak-width gets narrower, suggesting improvement in the crystalline quality of ZnO.

Investigation of absorption and emission properties of ZnO thin films can provide insights into the quality of the thin films as well as defect states residing within the ZnO bandgap.

At first, the thickness of the ZnO thin films, synthesised at different processing conditions, was estimated using ellipsometry measurements. Table 4.2 presents the estimated thickness of the ZnO films prepared using different concentrations of zinc neodecanoate after

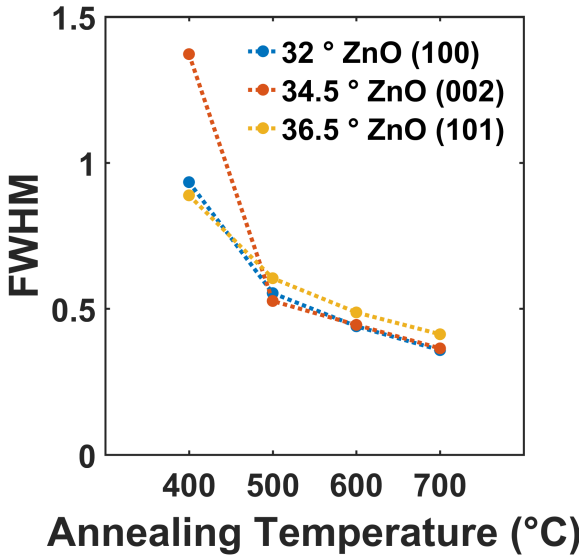

Fig. 4.5 Variation in the full width half maxima (FWHM) of the ZnO XRD peaks (100), (002) and (101) with annealing temperature.

calcined at 500 °C. On the other hand, ZnO thickness achieved from 15 % zinc neodecanoate after annealing at temperatures ranging from 400 °C to 700 °C is shown in Table 4.3.

Table 4.2 ZnO film thickness after annealing different concentrations of zinc neodecanoate at 500 °C

Concentration	ZnO Thickness (nm)
5 %	14.7
15 %	22.4
25 %	30.1
50 %	38.5

Table 4.3 ZnO film thickness after annealing 15 % zinc neodecanoate at different temperatures

Annealing Temperature	ZnO Thickness (nm)
400 °C	23.3
500 °C	22.4
600 °C	21.2
700 °C	20.5

UV-visible spectroscopy was carried out in order to study the absorption properties of the films annealed at different temperatures. A 15 % concentration of zinc neodecanoate was

used to spin-coat pre-cleaned quartz substrates and then annealed at various temperatures ranging from 400 °C to 700 °C. For the UV-visible measurements a blank quartz substrate was used as reference and the system was calibrated before each of the sample films was scanned. The absorbance (A) at wavelengths ranging from 300 nm to 800 nm was then converted to percent transmittance using the following equation,

$$\%T = 10^{(2-A)} \tag{4.1}$$

The plot of % transmittance versus wavelength for films annealed at different temperatures is shown in Fig. 4.6a. Nearly 100 % transmittance across visible range signifies the presence of transparent ZnO phase. A prominent onset in the spectra can be seen between 350 nm and 400 nm. As the annealing temperature increases from 400 °C to 600 °C stronger absorption is observed below $\sim$ 370 nm, which can be attributed to the improvement in the crystal quality of ZnO films, as established by the XRD measurements (Fig. 4.4). Increasing the temperature from 600 °C to 700 °C showed no significant difference in the transmittance.

Tauc plots were used to estimate the bandgap of the ZnO films. The transmittance on the ZnO thin film can be calculated from the optical absorption coefficient α using the equation,

$$T = e^{-\alpha t} \tag{4.2}$$

where T is the transmittance of the light and t is thickness of the thin film. In a direct bandgap semiconductor the optical bandgap of the thin film material can be related to α using the expression [185, 186]

$$(\alpha h\nu)^2 = A(h\nu - E_g) \tag{4.3}$$

where h is Planck's constant and ν is frequency of photons corresponding to incident light and E_g is the bandgap of the semiconductor. Fig. 4.6b shows the Tauc plots for ZnO films annealed at different temperature. Using the linear extrapolation method, the bandgap of ZnO films is calculated for each processing temperature. The thickness of the ZnO films shown in Table 4.3 was used for the bandgap calculation. A decrease in the bandgap is observed as the annealing temperature is raised from 400 °C to 600 °C. A higher bandgap in the films annealed at lower temperature may be associated with the quantum confinement effect of nano-crystalline ZnO phase embedded in an amorphous ZnO matrix, as previously reported by Tan *et al.*[186]. Increasing temperature causes grains to grow bigger leading to a decrease in the optical bandgap [186]. The estimated bandgap values are in agreement with previous reports on solution processed ZnO thin films [187–189]. The deviation from the

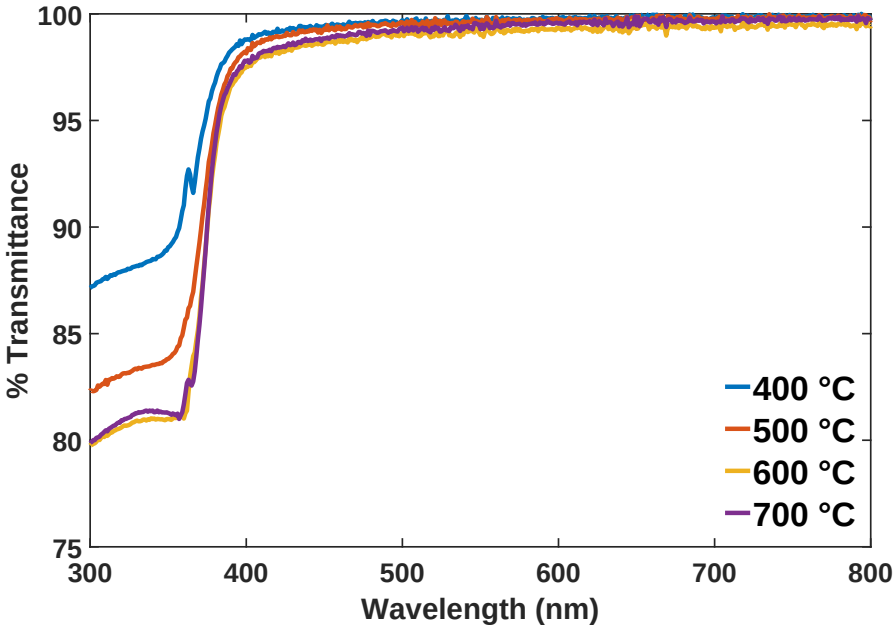

(a)

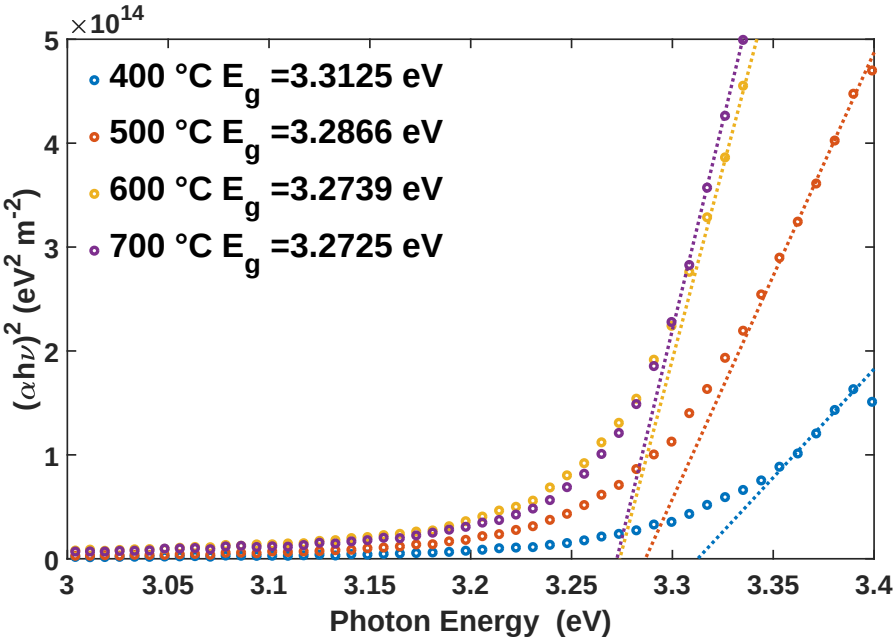

(b)

Fig. 4.6 Optical Characterisation of ZnO films annealed at different temperatures (a) Transmission Spectra of ZnO film prepared from 15 % zinc neodecanoate and annealed at different Temperatures (b) Tauc Plot extracted from Transmission spectra with calculated bandgap E_g.

ZnO bandgap of 3.37 eV has been reported to be due to the absorption at ∼3.15 eV from valence band-donor transition [190, 184].

Photoluminiscence (PL) measurements were also carried out using 266 nm laser with an incident power of 2.2 mW power. The peak at ∼380 nm corresponds to near band edge (NBE) emission and is attributed to recombination of free-exciton [191, 192]. Significant deep-level emission can be seen at all annealing temperatures. The complexity of the deep emission centres in ZnO is not fully understood. However, Kim *et al.* have suggested oxygen vacancies could be a possible source of deep-level emission based on the observation of increased deep-level emission among ZnO films sputtered at a lower oxygen partial pressure [193].

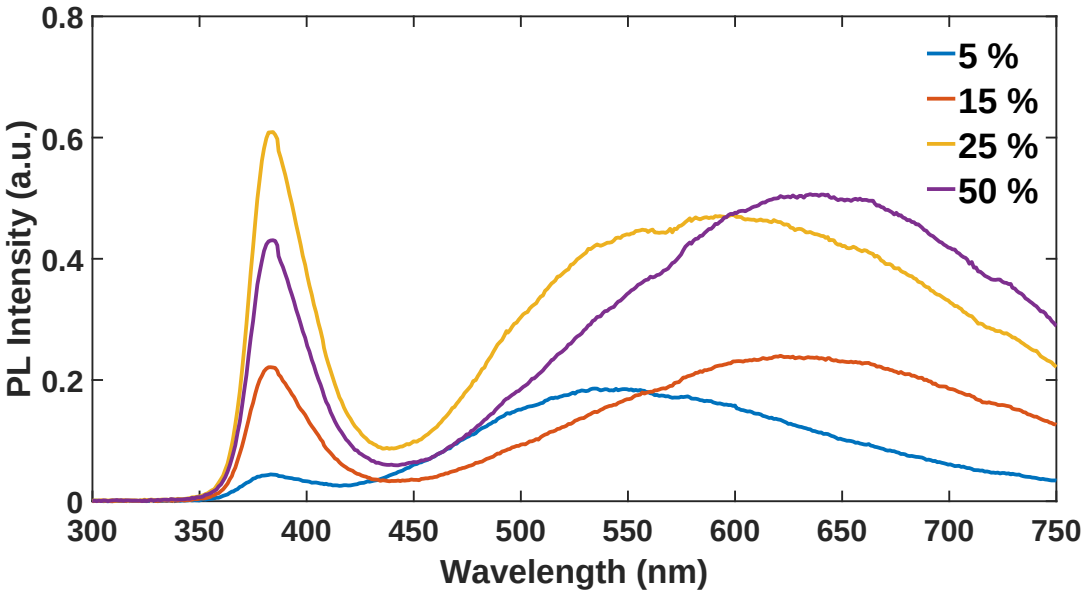

Fig. 4.7 Photoluminiscence Spectra of ZnO films prepared from different concentrations of zinc neodecanoate after annealing at 500 °C.

Fig. 4.7 shows variation of PL spectra of films deposited using four precursor concentrations and annealed at 500 °C. A weak NBE peak with respect to deep-level emission at 5 % concentration may be caused by ultra thin ZnO film with significant disorder. As the precursor concentration is increased, the NBE peak becomes increasingly narrow due to the increasing thickness of the film. Additionally, increase in the relative NBE emission as compared with deep-level emission can be seen as precursor concentration is increased from 5 % to 25 %. However, at 50 % concentration higher relative defect emission points to increased disorder within the film. Such an increase in disorder may be plausibly attributed to the formation of inefficient packing of larger sized particles.

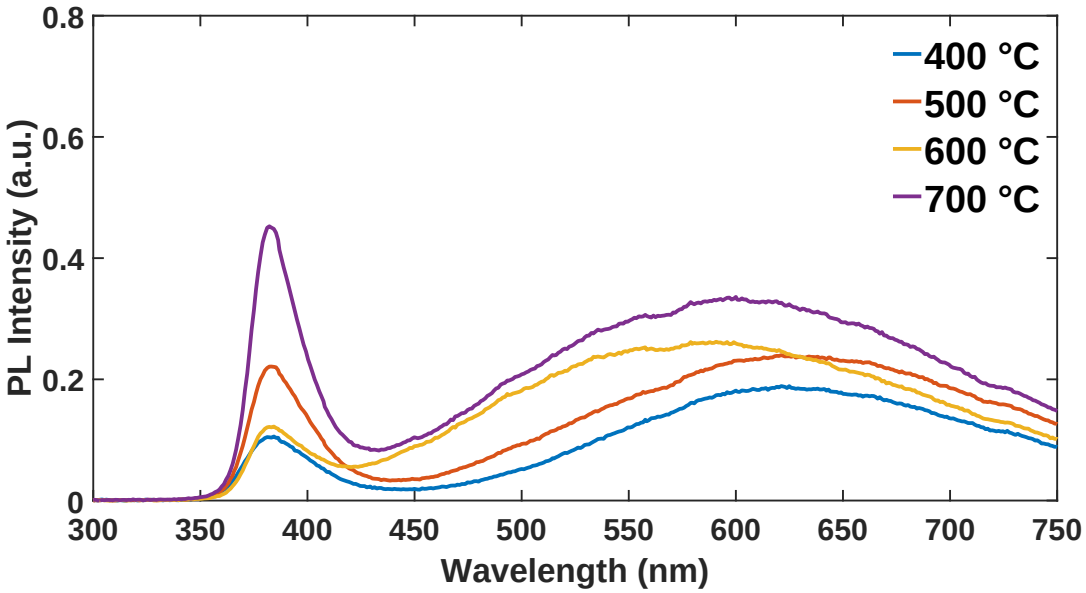

Fig. 4.8 Photoluminiscence Spectra of ZnO films prepared from 15 % zinc neodecanoate after annealing at different temperatures.

Evolution of PL spectra of 15 % concentration films annealed at different temperature was also studied (Fig. 4.8). The relative emission at NBE compared with deep-level can be seen to increase as the annealing temperature is increased from 400 °C to 700 °C. Higher defects emission from films annealed at 400 °C could be caused by smaller sized ZnO particles and presence of disordered grain boundary regions. As the annealing temperature is increased, improvement in the crystallinity makes the NBE peak more and more prominent. Additionally, higher temperature assists with coalescence of smaller grains into the bigger ones, decreasing disordered grain boundary regions as well as non-radiative defects [184, 194].

4.3.3 Surface analysis of ZnO thin films

Atomic force microscopy (AFM) was carried out to understand the morphology of the ZnO films formed after annealing. Fig. 4.9 depicts the evolution of surface characteristics, when precursor concentration was varied from 5 % up to 50 %. The roughness of the synthesised ZnO films was estimated as root mean square (RMS) value using the AFM software. Upon increase in concentration, an increase in thickness is observed (Table 4.2) and correspondingly the roughness increases from 0.917 nm to 1.92 nm with increasing precursor concentration. The trend where surface roughness increases with thickness has

also been reported in the case of ZnO films prepared from zinc acetate [195]. The increasing roughness also points towards increase in ZnO grain size, as the precursor concentration is increased.

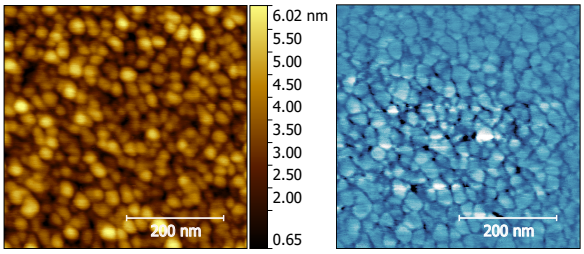

(a) Concentration 5 % R_{rms} = 0.917 nm

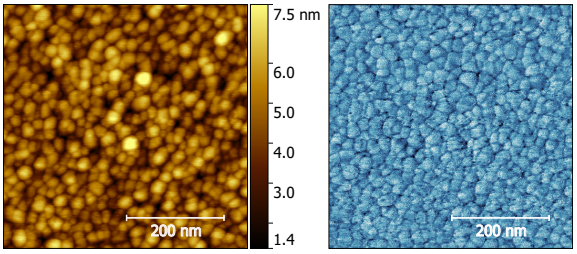

(b) Concentration 15 % R_{rms} =1.02 nm

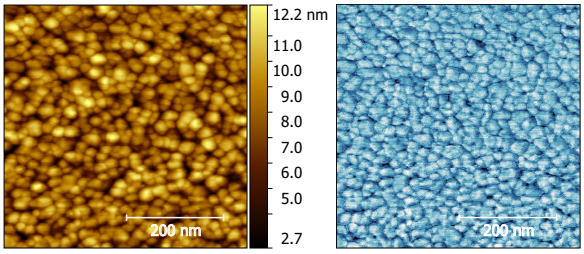

(c) Concentration 25 % R_{rms} = 1.64 nm

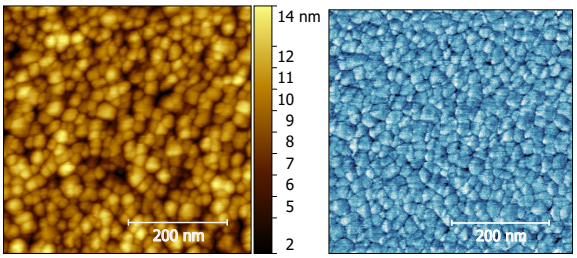

(d) Concentration 50 % R_{rms} = 1.92 nm

Fig. 4.9 AFM images showing Topography (left) and Phase (right) over 500 nm x 500 nm area of ZnO films prepared from different precursor concentrations showing increasing roughness with increasing concentration. All films annealed at 500 °C.

Furthermore, Fig. 4.10 shows AFM images of ZnO films obtained upon annealing at different annealing temperatures. Upon increasing the temperature, the surface morphology evolves and the RMS roughness increases from 0.832 nm to 1.35 nm. In accordance with narrowing of XRD peaks with increasing temperature (shown in Fig. 4.4), the increase

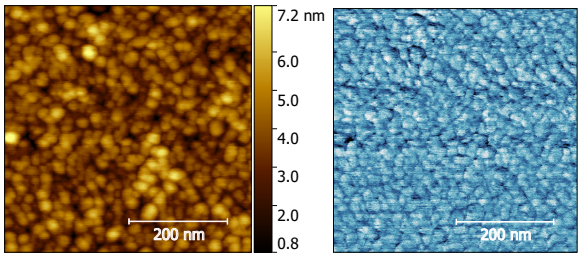

(a) 400 °C R_{rms} = 0.832 nm

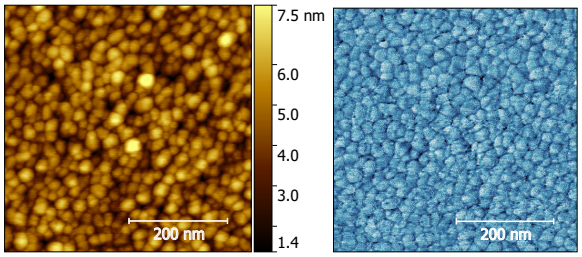

(b) 500 °C R_{rms} = 1.02 nm

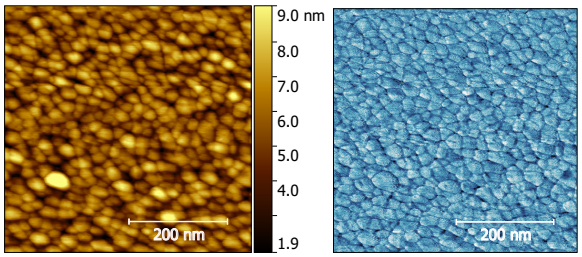

(c) 600 °C R_{rms} = 1.23 nm

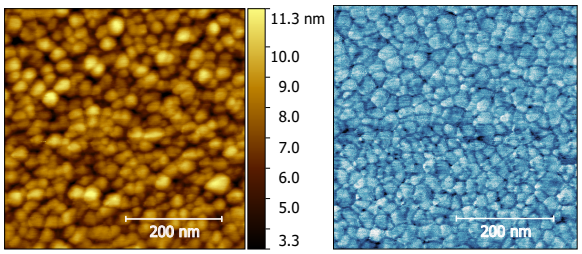

(d) 700 °C R_{rms} = 1.35 nm

Fig. 4.10 AFM images showing Topography (left) and Phase (right) over 500 nm x 500 nm area of ZnO films prepared from 15 % concentration annealed at different temperatures. Estimated roughness increases with increasing annealing temperature.

in roughness also indicates increase in the ZnO grain size. Similarly, evolution in surface characteristics has also been reported by Adamopoulos *et al.*[184]. However, relatively higher temperatures are used in current work possibly due to the longer organic chain of the constituent precursor, leading to higher required temperatures for precursor decomposition.

4.4 Electrical Characterisation

The thin film transistors devices used in this work are of the Bottom Gate-Top Contact type, as shown in Fig. 4.3. Heavily doped p-type (p^{++}) Si substrate was used as bottom gate with a 100 nm thermally grown oxide layer as gate dielectric. After the formation of ZnO thin film with respective processing, source drain regions were prepared using photolithography. For all the devices discussed in this chapter, 100 nm of aluminium was used for source-drain metal contacts. Unless otherwise stated, all the devices had 500 μm channel width and 5μm channel length. The device substrate was attached to the glass piece with conducting coating using silver-epoxy paste. After the paste is well dried it is used to contact the back-gate. All the devices were characterised using SUSS-Microtec Probe station and Keithley 4200 SCS. All the measurements were carried out in the dark under ambient air conditions and at room temperature. Source-to-drain voltage of 50 V was applied and gate voltage was swept from -20 V to 70 V with 2.5 V step in both forward and reversed direction to obtain the I_d-V_g transfer measurements. During the I_d-V_d output measurements a constant gate voltage was applied and source-drain voltage sweep was made from 0 V to 50 V with 1 V step. Gate voltage was varied from 10 V to 70 V with 10 V step.

4.4.1 Parameter extraction

In order to extract various transistor parameters, transfer measurements conducted in a saturation regime were used. The mobility in the saturation regime of a transistor channel is calculated using the following expression:

$$\mu_{sat} = \frac{2L}{WC_O}\left(\frac{\partial\sqrt{I_{DS}}}{\partial V_G}\right)^2$$

where L and W are channel length and width respectively, C_O oxide capacitance per unit area. The value of 3.5 x 10^{-8} F/cm^2 was estimated for C_O, assuming 100 nm thick SiO_2 gate oxide and relative dielectric constant (ε_r) 3.9. A straight-line fit was made where gradient of $\sqrt{I_{DS}}$ is maximum. The slope of the line was used for $\frac{\partial\sqrt{I_{DS}}}{\partial V_G}$ and x-intercept was used to estimate the value of threshold voltage V_{th}. sub-threshold swing was calculated using the expression:

$$S = \frac{\partial V_G}{\partial(log\ I_{DS})}$$

A straight-line fit was made to log(I_{DS}) vs V_G plot where gradient of log(I_{DS}) is maximum. The inverse of the slope of this line was used as sub-threshold swing estimation. The on-off ratio of the transistor, I_{ON}/I_{OFF} was calculated by dividing maximum and minimum values of I_{DS}.

The trap concentration per unit energy (D_T) [196] was calculated using the following expression:

$$D_T = \frac{C_0}{e^2}\left(\frac{eS}{k_b T ln(10)} - 1\right) \tag{4.4}$$

4.4.2 Optimisation of precursor concentration

In order to find optimal thickness of ZnO film, electrical characterisation was performed on devices prepared from different concentrations of precursors annealed at 500 °C . Typical transfer and output curves for these devices are shown in Fig. 4.11 and Fig. 4.12 respectively. It can be clearly seen from the transfer curves (Fig. 4.11) that devices fabricated from all the precursor concentrations show a small amount of hysteresis. The ON current in the device prepared from a 5 % concentration showed the lowest value, while devices fabricated with higher concentrations demonstrate similar magnitude of ON current. Lower ON current in the case of a 5 % concentration, may be attributed to insufficient percolation pathways for the current flow as well as higher carrier scattering due to smaller ZnO grain size. As depicted in Fig. 4.12, output characteristics of all devices show a distinct linear and saturation regime in the I_D-V_D behaviour, suggesting ohmic contact between ZnO and Al source-drain.

Fig. 4.13 displays average trends in the transport parameters as a consequence of variation in precursor concentration. The devices made from a 15 % concentration showed highest mobility as well as On-Off ratio. Mobility was observed to increase from an average of 6.8 x 10^{-4} cm^2/V.s to 2.1 x 10^{-2} cm^2/V.s when precursor concentration was changed from 5 % to 15 % (Fig. 4.13a), which can possibly be explained by an increase in the percolation pathways available for electron carrier transport. At higher precursor concentrations, however, bigger particles may form throughout the thicker precursor film, which may cause inefficient packing. This may lead to limited percolation of charge carriers and contribute to carrier trapping. The later is also evident from the minimum values of sub-threshold swing of 4.1 V/dec and trap concentration per unit energy 1.5 x 10^{13} $eV^{-1}cm^{-2}$ at 15 % concentration. With increased precursor concentration, an increase in the trap concentration is observed as depicted in Fig. 4.13e. The average values of threshold voltage estimated are in the range of 10 V to 30 V, as shown in (Fig. 4.13c). Such a high values of threshold voltage point to significant number of trapping centres within the ZnO film. A decrease in threshold voltage

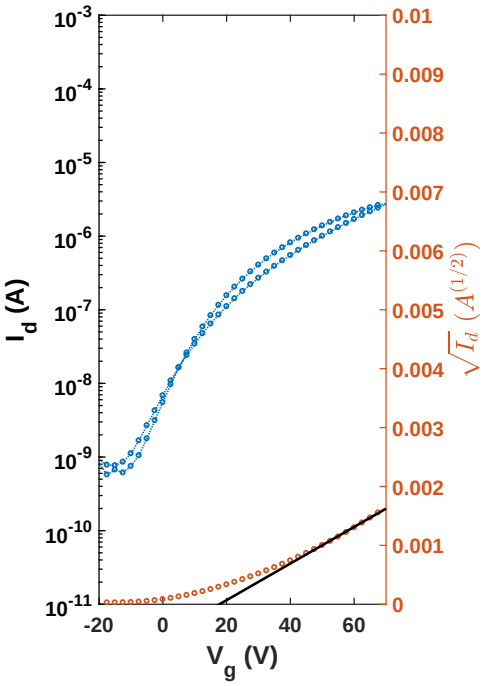

(a) Concentration 5 %

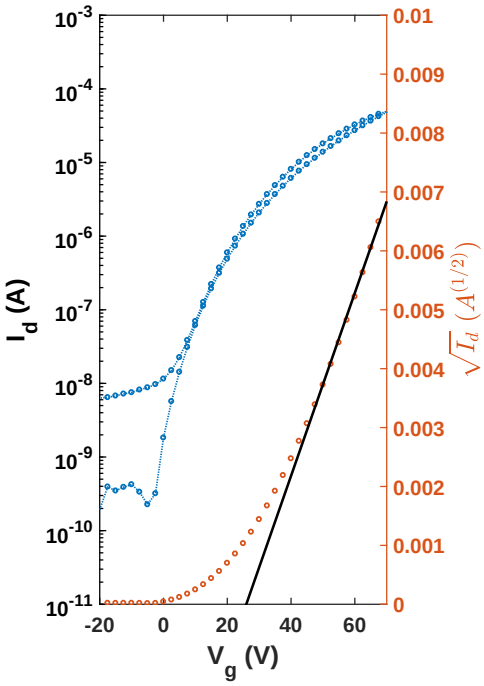

(b) Concentration 15 %

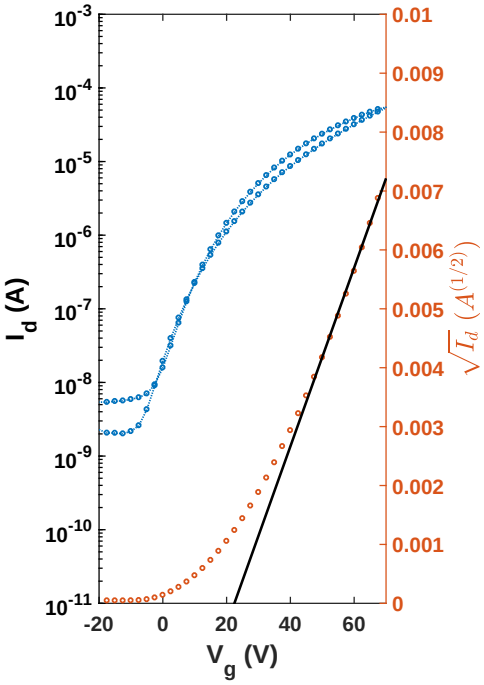

(c) Concentration 25 %

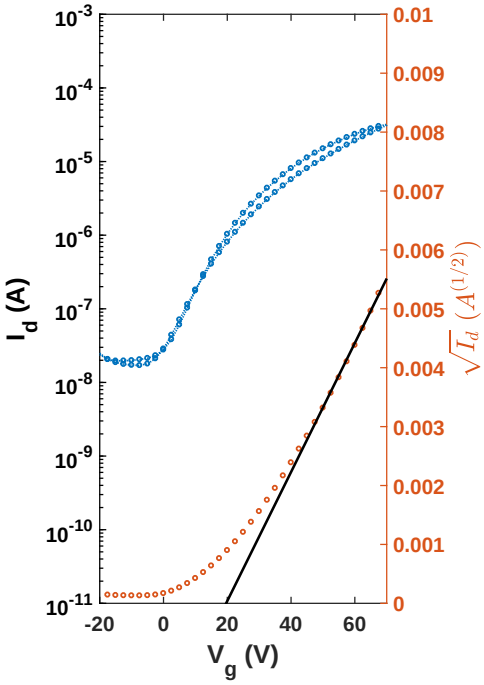

(d) Concentration 50 %

Fig. 4.11 Transfer curves of ZnO thin-film transistors prepared from different concentrations of the precursor.

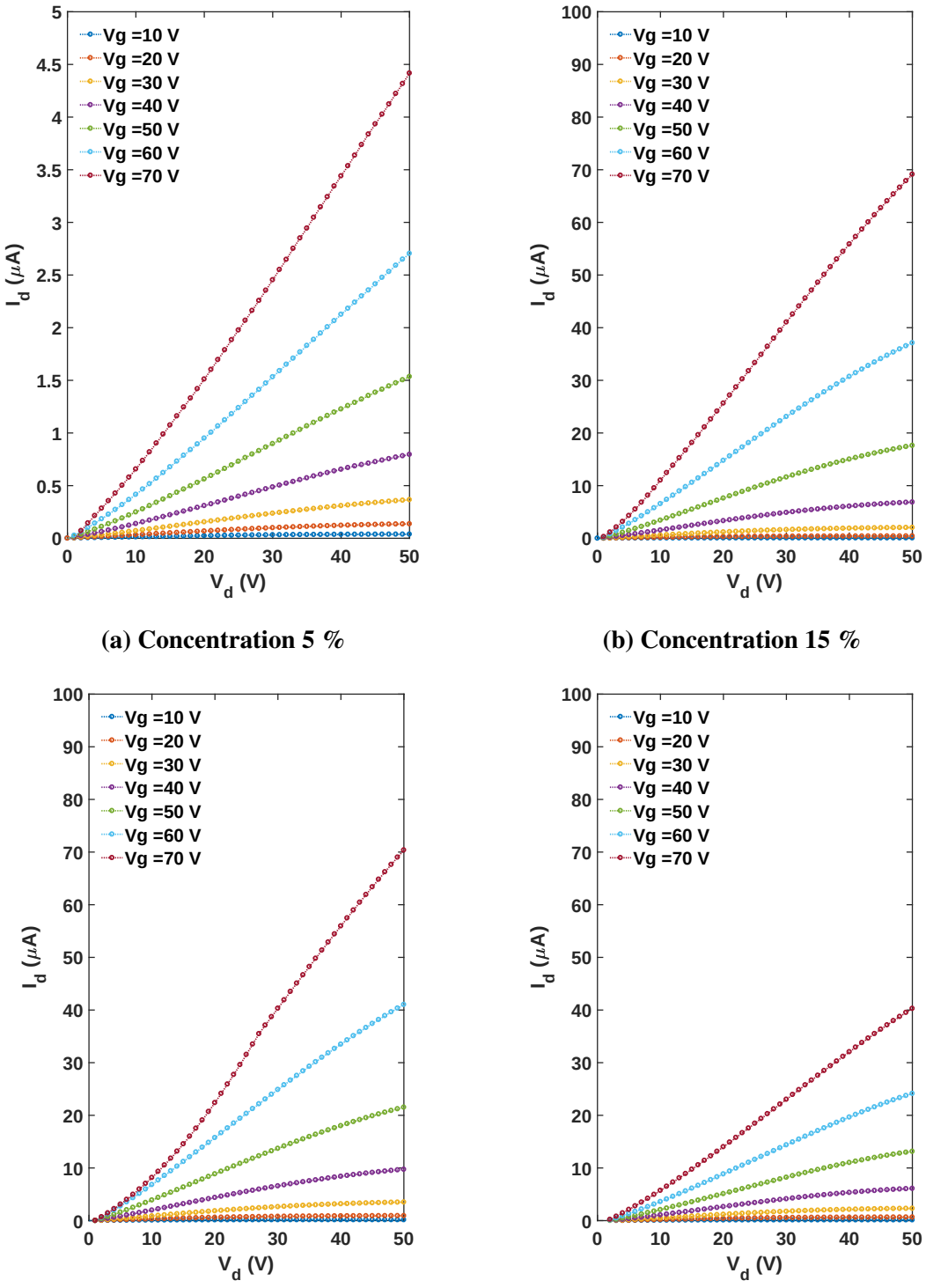

(a) Concentration 5 %

(b) Concentration 15 %

(c) Concentration 25 %

(d) Concentration 50 %

Fig. 4.12 Output curves of ZnO thin-film transistors fabricated with different precursor concentrations.

at higher precursor concentrations may be associated to improved bulk conductivity due to increased ZnO thickness, reflected in higher OFF current (Fig. 4.11).

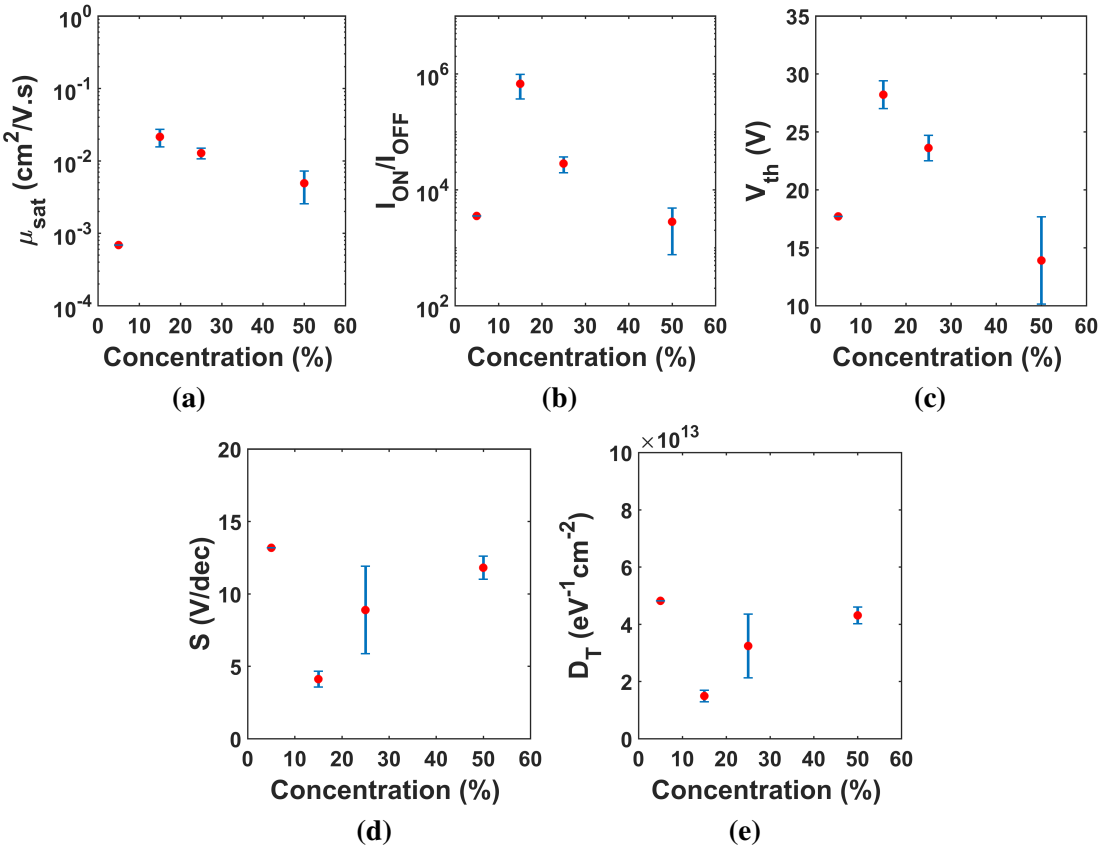

Fig. 4.13 Transistor parameters calculated for ZnO TFTs from different concentrations of zinc neodecanoate.

4.4.3 Optimisation of Annealing Temperature

The impact of precursor annealing temperature was also studied, with films prepared from 15 % concentration of the precursor and then annealed at different temperatures ranging from 400 °C to 700 °C. It is evident from the transfer curves shown in Fig. 4.14 that the ON-current of the devices increases with increasing annealing temperature. At 400 °C the transistor operation can be be seen. However, the lower ON current is possibly due to smaller ZnO grain size and significant grain boundary regions causing carrier scattering. The presence of disordered grain boundaries is associated with trapping centre, which also explains higher hysteresis in these devices. As annealing temperature is increased, the ON current of the transistor increases due to increased degree of crystallinity and ZnO grain size,

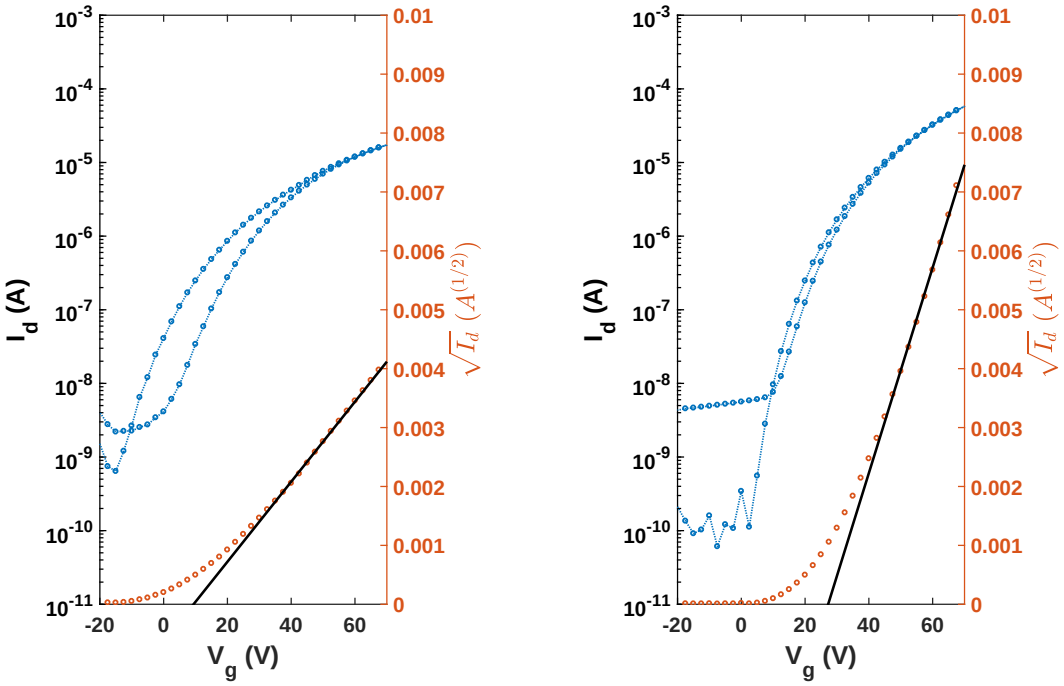

(a) 400 °C

(b) 500 °C

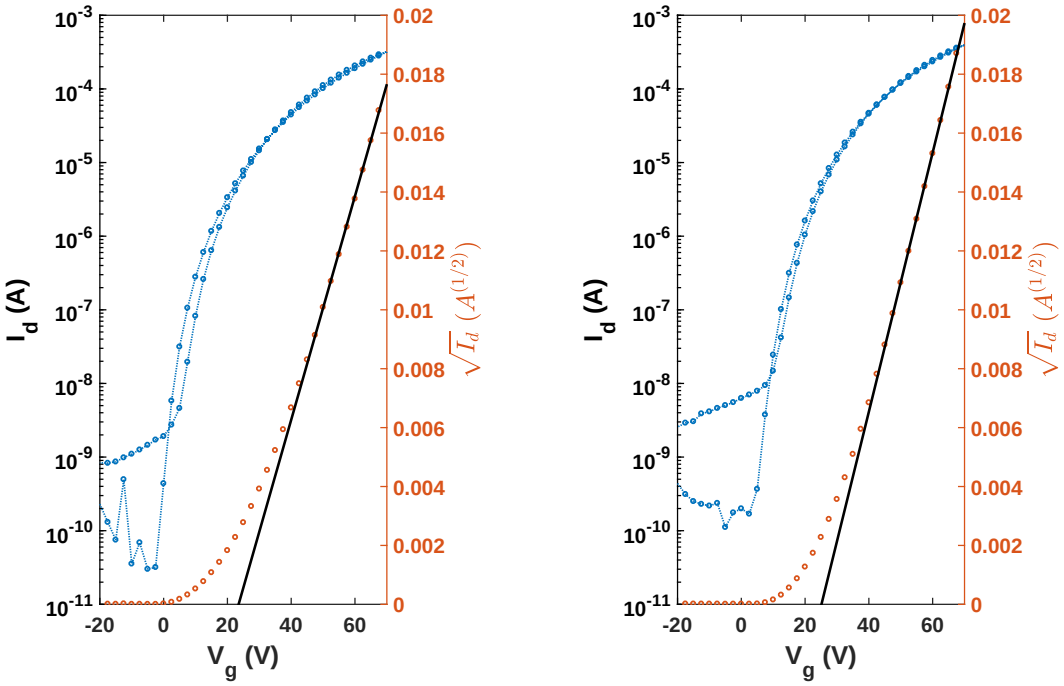

(c) 600 °C

(d) 700 °C

Fig. 4.14 Transfer curves of ZnO thin film transistors annealed at different temperatures.

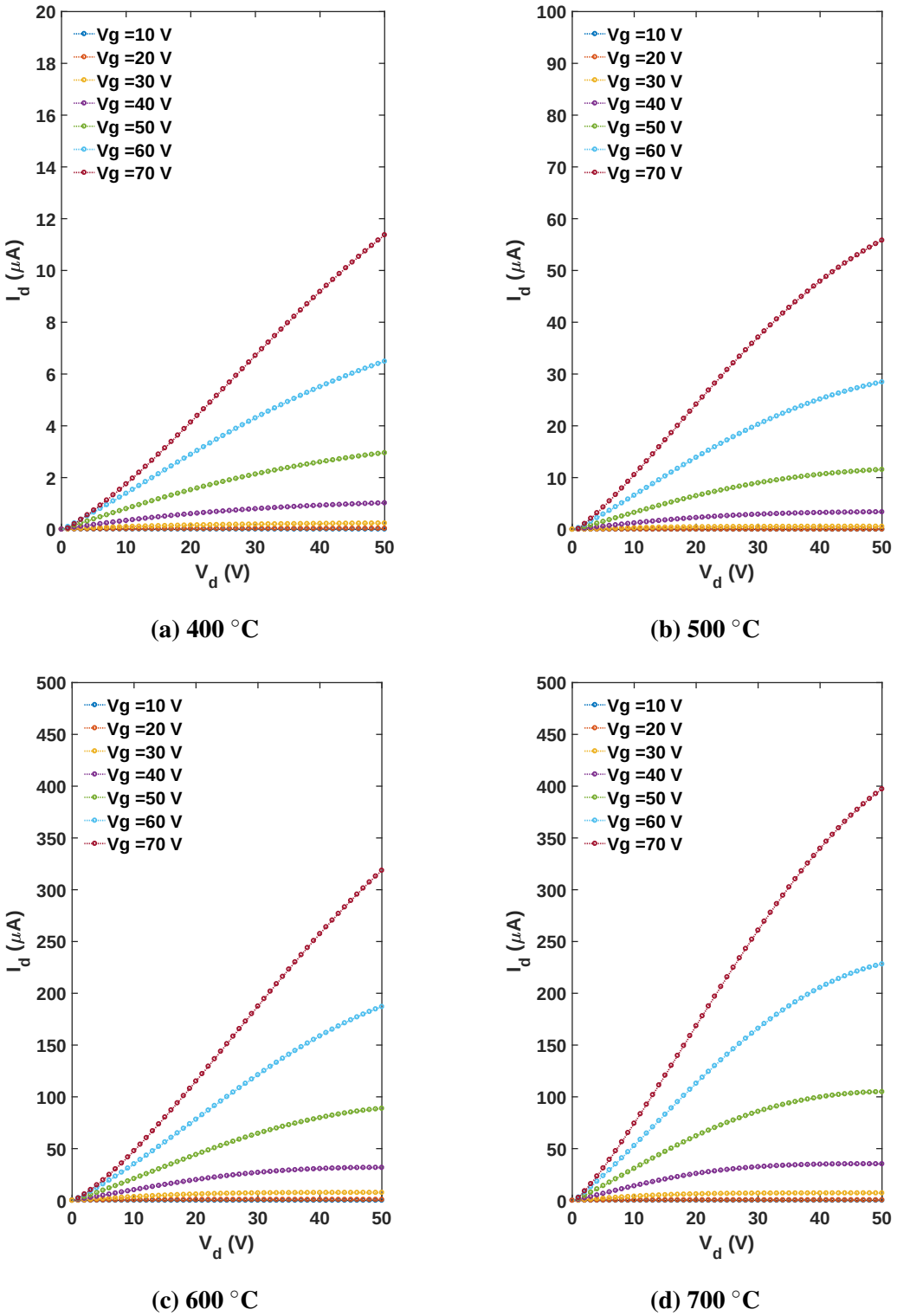

(a) 400 °C

(b) 500 °C

(c) 600 °C

(d) 700 °C

Fig. 4.15 Output curves of ZnO thin film transistors annealed at different temperatures.

in turn reducing carrier scattering. Fig. 4.15 depicts representative output curves of devices from different annealing temperatures. Monotonous increase in the current with annealing temperature can also be seen here. All the devices show good linear behaviour at low drain voltages. A clear evolution of saturation regime in output characteristics can be seen from 400 °C to 700 °C. This indicates that films fabricated from higher annealing temperature have lower contact resistance. A clear saturation can be seen in the device with 700 °C annealed film.

A number of devices were fabricated at each of the annealing temperatures and their performance in saturation regime was measured. Evolution of various transistor parameters with annealing temperature is plotted in Fig. 4.16. Overall, improvement in each of the device parameters is seen as a consequence of increase in annealing temperature.

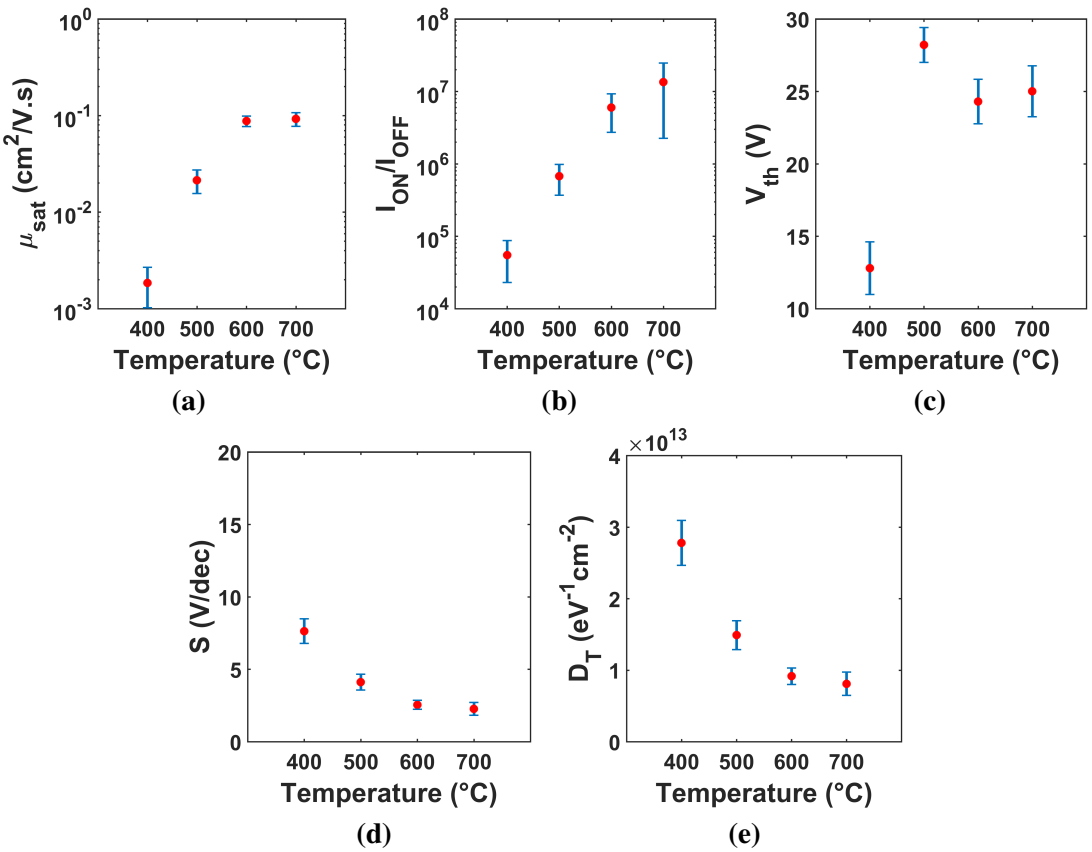

Fig. 4.16 Transistor parameters calculated for different annealing temperatures.

As shown in Fig. 4.16a, the average saturation mobility increased from 1.8 x 10^{-4} cm^2/V.s at 400 °C to 9.22x 10^{-2} cm^2/V.s at 700 °C. Steep increase of an order of magnitude can be seen in the mobility from 400 °C to 2.14 x 10^{-2} cm^2/V.s at 500 °C. Considerable enhancement in mobility is also observed when annealing temperature was raised to 600 °C,

reaching 8.76 x 10^{-2} cm^2/V.s. However, only marginal improvement is seen after 600 °C to 700 °C. A similar trend is also seen in the case of I_{ON}/I_{OFF} which increases from 5.5 x 10^4 at 400 °C to 1.3 x 10^7 at 700 °C. Roughly, an order of magnitude change in I_{ON}/I_{OFF} is seen with every 100 °C increase in annealing temperature, except for only two times increase from 600 °C to 700 °C. Advancement in both of these performance parameters can be attributed primarily to improvement in the crystal quality of the films [197, 198], as evident from XRD measurements (Fig. 4.4). In addition, higher temperature aids grain growth, leading to decrease in grain boundaries, and thus reduction in grain-boundary scattering. Such an effect of processing temperature on improved device performance is similar to what has been shown in various reports [198–201].

A sharp improvement in sub-threshold swing was also seen (Fig. 4.16d). The average sub-threshold swing drops from 7.6 V/dec at 400 °C to less than half the value of 2.3 V/dec at 700 °C. Improvement in the semiconductor-dielectric interface properties with increasing annealing temperature could be the primary cause of this evolution in the transport characteristics which is similar to what has been reported by Jeong *et al.* [199]. Lyu *et al.* [196] have provided a method of estimating interface trap density per unit energy, which is presented in Equation 4.4. We then calculated corresponding trap densities using Equation 4.4 [196] which is shown in Fig. 4.16e, clearly depicting decrease in average trap states from 2.7 x 10^{13} $eV^{-1}cm^{-2}$ at 400 °C to 8.1 x 10^{12} $eV^{-1}cm^{-2}$ at 700 °C. Grain boundary trapping is a dominant mechanism in oxide semiconductors, and thus decrease in grain-boundary regions with increased temperature would explain lower values of trap density.

4.4.4 Investigation of Carrier Transport

Gate dependence of the mobility was investigated to gain deeper insights into the carrier transport in the ZnO films annealed at different temperatures. A model proposed by Lee *et al.* [202] was used to ascertain the conduction mechanism of the charge carrier. According to this model, field effect mobility can be expressed as,

$$\mu_{FE} = K(V_{GS} - V_{th})^{\gamma} \tag{4.5}$$

where K and γ emperical parameters chosen appropriately to fit the data. The value of fitting exponent γ elucidates the type of transport mechanism assumed. If the value is closer to 0.7, then that would imply Trap-limited charge (TLC) transport. On the other hand, a value closer to 0.1 suggests negligible trapping and that other conduction mechanisms such as percolation dominated conduction (PC) may be at play [202, 203].

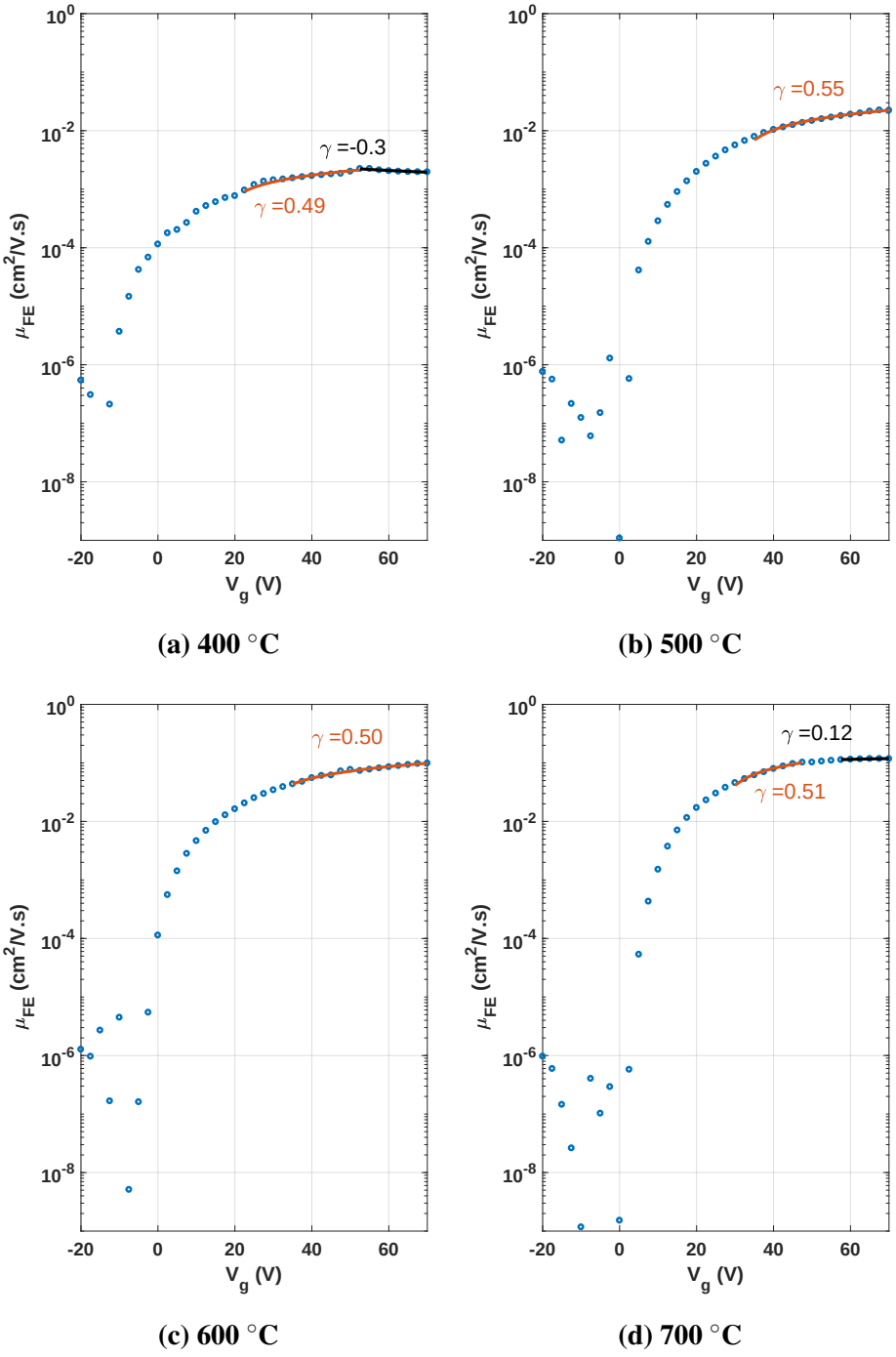

(a) 400 °C (b) 500 °C

(c) 600 °C (d) 700 °C

Fig. 4.17 Mobility vs gate voltage plots of ZnO thin film transistors annealed at different temperatures.

In Fig. 4.17, field effect mobility (μ_{FE}) of representative devices, annealed at different temperatures, is plotted against gate voltage (V_g). In each of the plots, fits to equation 4.5 are

also displayed. It can be seen that for temperatures from 400 °C to 600 °C the exponent γ attains values closer to 0.7, suggesting TLC dominated transport mechanism. In devices with ZnO film annealed at 700 °C (Fig. 4.17d), however, two transport regimes can be identified. At V_g just higher than threshold voltage, γ has value of 0.51, pointing to the transport still dominated by TLC; whereas at higher V_g regime the exponent γ drops to 0.12. This, in turn, implies that in a high gate voltage regime, most of the traps are filled up. Hence all the charge accumulated by the gate voltage thereafter can go directly to the conduction band and can add to the current flow. There might still be other mechanism at play, which limits the mobility.

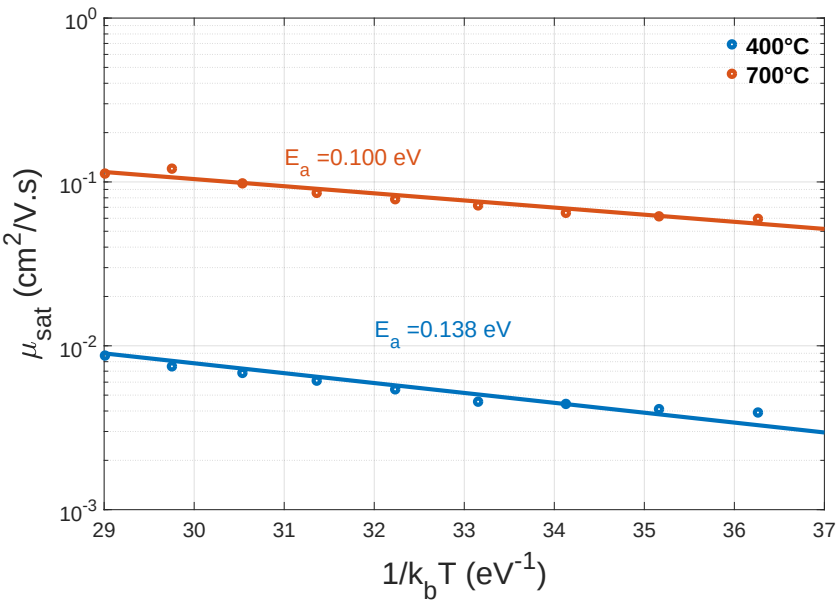

Fig. 4.18 Arrhenius Plots of saturation mobilities extracted from ZnO TFTs with films annealed at 400 °C and 700 °C.

Dependence of saturation mobility on temperature was also investigated for devices annealed at 400 °C and 700 °C. Transfer curves were measured for these devices at temperatures ranging from 300 K to 420 K. Extracted saturation mobility values were plotted against $1/k_bT$ (Fig. 4.18) and fitted to Arrhenius expression,

$$\mu_{sat} = Aexp(\frac{-E_a}{k_bT}) \tag{4.6}$$

As depicted in Fig. 4.18, for the device with ZnO films annealed at 400 °C, activation energy E_a was estimated to be 0.138 eV. Interestingly the value of activation energy is very close to the energetic levels of zinc interstitials (Zn_i) which was suggested by Cordaro *et al.*

to be around 0.17 eV [204]. On the other hand, as shown in Fig. 4.18, the activation energy E_a was lowered to the value of 0.1 eV for 700 °C. The higher activation energy of 400 °C device indicates the existence of deeper traps, while in the case of 700 °C the trap states are shallower. Removal of these deep traps as a consequence of higher annealing temperature may explain the improved performance of the devices.

4.5 Concluding remarks

In conclusion, application of zinc neodecanoate functional precursor was explored for fabricating ZnO thin film transistor. Optical characteristics of the ZnO thin films were investigated using UV-Vis and PL measurements. The films prepared using various precursor concentrations and decomposed at different temperatures showed excellent transmittance in the visible region, making them suitable for transparent electronics applications. The bandgap of $\sim$ 3.2 eV attained in these films was also found to be in agreement with previous reports.

It was found that films prepared with 15 % concentration of zinc neodecanoate in toluene show best performing devices. In agreement with various studies undertaken on solution processed ZnO, increased annealing temperature gives rise to increment in device performance. After optimisation, devices annealed at 700 °C showed highest mobility, reaching upto 0.1 cm^2/V.s with I_{ON}/I_{OFF} ratio $\sim 10^7$ and sub-threshold swing as low as 2.26 V/dec.

Finally, the transport mechanism in the ZnO films prepared from zinc neodecanoate was also briefly investigated. Using analytical models, it was found that TLC conduction dominates in films annealed at low temperatures. However, in 700 °C annealed film, TLC transport could be seen at low gate voltages and the transport deviated from TLC mechanism at high gate voltage bias. Activation energies for saturation mobility, estimated from Arrhenius plot, suggested the presence of deeper traps at low processing temperature, while shallower trap levels exist in high-temperature processed films. The understanding gained with regard to ZnO devices prepared from zinc neodecanoate was further employed in optimising direct-write EBL based nano-FETs discussed in Chapter 5. However, the development of direct-write EBL patterning approach for ZnO is first discussed in the following chapter.

Chapter 5

Top-down fabrication of ZnO nanostructures

5.1 Introduction

During the fabrication of ZnO thin films based devices top-down fabrication methods have quite often been used. In fact such fabrication steps are widely used in large-scale applications such as active-matrix display panels. However, fabricating ZnO structures at nanoscale by top-down route has been particularly challenging. Direct write solution processing based techniques are becoming increasingly popular since they provide cheaper alternatives to vacuum-based techniques, that are heavily dependant on lift-off or plasma etching. In the current chapter an electron beam lithography-based direct-write approach is implemented using zinc naphthenate and zinc neodecanoate precursors.

5.2 Review on top-down synthesis of ZnO nanostructures

Among the ZnO NW fabrication methods, greatest effort is focused on bottom-up growth of ZnO NWs. However, an increasing number of reports of ZnO nanostructure fabrication using top-down approaches have been produced in recent years.

Litho-Etch based Top-Down synthesis

Ra *et al.* reported naanoscale spacer lithography (NSL) technique using inductively coupled plasma (ICP) to etch conformally coated ALD ZnO film into nanowires [131]. Sultan *et al.* [205] have also fabricated ZnO NW using atomic layer deposition (ALD) of ZnO on pre-patterned SiO_2 surfaces, followed by ICP etching to remove unwanted ZnO layer. Lee *et al.*, on the other hand, have used initially sputtered ZnO film. A poly(methyl methacrylate) (PMMA) layer was then spin-coated on ZnO film and patterned either by nanoimprint lithography or electron beam lithography. The patterned PMMA layer was then used as mask for reactive-ion-etching (RIE) to achieve ZnO nano-patterns [206].

Nanoimprint Lithography (NIL) for ZnO nanopatterns

Yang *et al.* used zinc acetate based sol as a imprint resin and nanopatterned PDMS mold to fabricate ZnO-gel nanopatterns followed by thermal annealing at 650 °C to achieve ZnO nanostructures [207]. A combination of UV-NIL and octadecyltrichlorosilane (OTS) self-assembled monolayers (SAMs) was implemented to pattern zinc acetate seed layer for ZnO nanowire growth by Jung *et al.* [208]. Jo *et al.* dispersed ZnO nano-particles into

imprint resin made of benzylmethacrylate and UV-photo-initiator Irgacure 184. The authors exploited a UV-NIL technique with PDMS mold to pattern ZnO nano-particle clustors at room temperature [209]. Kim *et al.* modified the zinc acetate based sol-gel precursor with photosensitive 2-nitrobenzaldehyde for UV-NIL and 300 °C annealing to achieve ZnO nano-patterns [210]. The nano-patterned ZnO was then utilised for graphoexpitaxy of PS-b-PMMA block-copolymer lithography. A similar formulation was also used by Park *et al.* to fabricate nano-patterned ZnO seed for hydrothermal ZnO nanowire growth [181].

Top-down fabrication via direct write patterning of precursors

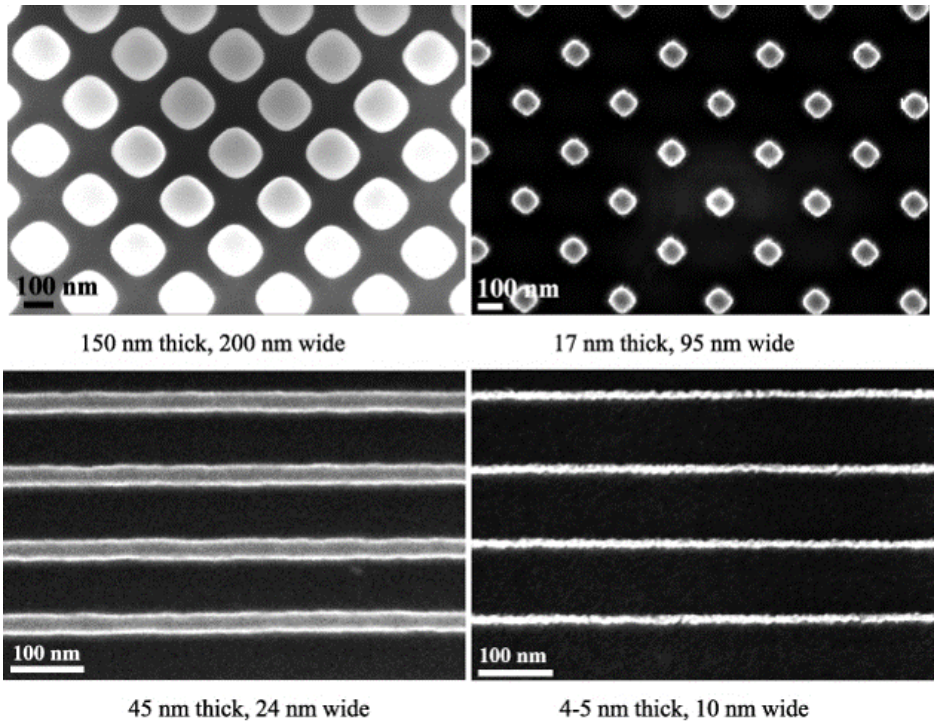

Fig. 5.1 SEM images of zinc naphthenate nanostructures prepared by EUV-IL on the left and corresponding ZnO nanostructures formed after heat treatment on the right. Reprinted from [211].

Saifullah *et al.* have demonstrated direct writing of sub-10 nm ZnO high aspect ratio features using zinc naphthenate and EBL [182, 212]. Zinc naphthenate acts as negative tone resist for electron beam and its low molecular weight makes in suitable for high-resolution EBL. A mixture of 1 ml zinc naphthenate in 20 ml toluene was spin-coated at 4000 rpm for 30 s on Si wafer to achieve 100 nm thick film. 100 kV E-beam with 1.5 nA probe current was used to write the sub-10 nm pattern followed by 10 s development in toluene.

The nano-lines were found to have line edge roughness of ∼2.8 nm, the smallest reported till then for any electron beam resist. Heating of the nano-lines at 500 °C for an hour in air resulted in formation of crystalline ZnO with slight decrease in line edge roughness to 2 nm. Auzelyte *et al.* have further explored the use of zinc naphthenate with extreme ultraviolet-interference lithography (EUV-IL) to achieve nano patterns. It has been reported that, after heat treatment at various temperatures and time, the best quality of ZnO fabrication is achieved after annealing at 850 °C for 1-2 min [211]. ZnO nanostructures formed by this method are shown in Fig. 5.1.

5.3 Direct write electron beam lithography

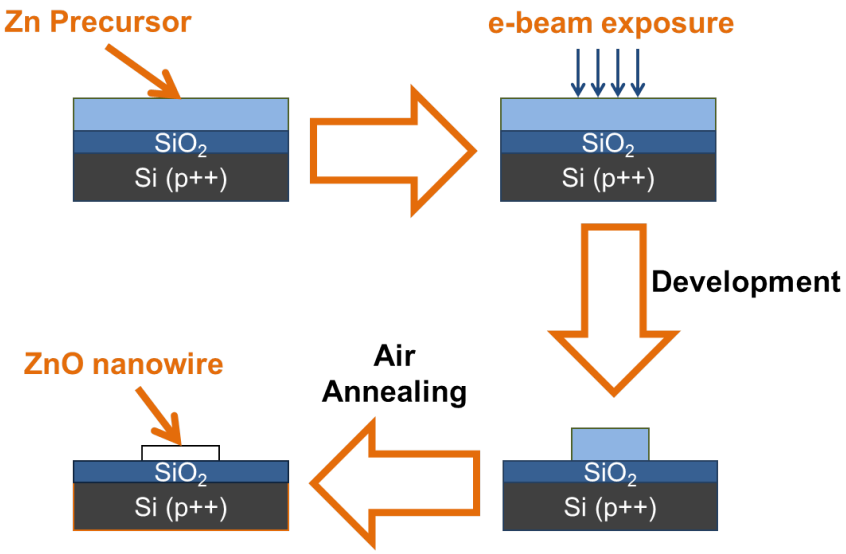

Fig. 5.2 Schmetic representation of direct writing of ZnO nano-patterns using electron beam lithography (a) Spin coated Zinc oxide precursor (naphthenate or neodecanoate) (b) e-beam exposure to crosslink precursor (c) development in toluene (d) annealing heat treatment to form ZnO nanowire.

SiO_2(100 nm)/Si wafers are cut into square pieces and are subjected to ultrasonic agitation in acetone, isopropyl alcohol (IPA) for 10 min each to clean the substrates. Samples are then dried using nitrogen gun and exposed to 10 min oxygen plasma for removal of organic impurities as well as improving hydrophilicity of the substrates. Samples are then baked at 180 °C to dehydrate their surface just before the spin coating. Prediluted toluene solution of zinc precursor is then spin coated on top of the substrate followed by short baking at 115 °C to evaporate remaining toluene. Samples are then exposed with electron beam to write a particular pattern onto the samples. During the e-beam irradiation precursor undergoes

crosslinking reaction within the exposed area. As a result the exposed area becomes insoluble in developer solvent, while rest of the precursor washes away. After the development step the samples are annealed in air to decompose the organic components and convert the patterned area into zinc oxide phase. Typical processing steps during direct write electron beam lithography route are outlined in Fig. 5.2.

The performance of a resist is characterised using the two parameters, Contrast (γ) and Sensitivity ($D_{0.5}$). The contrast of the resist is defined as,

$$\gamma = \frac{1}{log_{10}\left(\frac{D_1}{D_0}\right)} \tag{5.1}$$

where D_0 is onset dose at which the resist starts to crosslink and D_1 is dose at which the entire thickness of the resist is crosslinked and rendered insoluble in developer [213]. D_1 and D_0 are typically estimated as the dose at the intersection of highest and lowest resist thickness respectively to a straight line fit within the transitioning region from uncrosslinked resist to crosslinked resist. On the other hand, sensitivity of the resist is typically defined as the dose at which half the resist thickness is crosslinked ($D_{0.5}$) [182].

During the course of this research, Crestec CABL-9000C Electron Beam Lithography (EBL) system was used for writing the patterns onto the zinc precursors. The system operates at 50 kV and typically a 1-1.5 nA beam current was used to achieve $\sim$ 2-3 nm beam size and a beam step size of 1-10 nm is used for nanoscale patterns. During the device optimisation stage a 20 nA current with up to 60 nm step size was also used to write micron scale large patterns. Unless otherwise stated, an analogue exposure mode was used throughout.

5.4 Electron Beam Lithography of Zinc Naphthenate

Zinc naphthenate ($\sim$ 67 wt.- % in mineral spirits) was purchased from Alfa Aesar. As received zinc naphthenate is a pale brown coloured viscous liquid and needs to be diluted in order to spin coat on substrates. The structure of a zinc naphthenate molecule is shown in Fig. 5.3. During the initial trial, 1 ml of zinc naphthenate was diluted in 20 ml anhydrous toluene to make a 5 % concentration solution and sonicated to ensure uniform mixing.

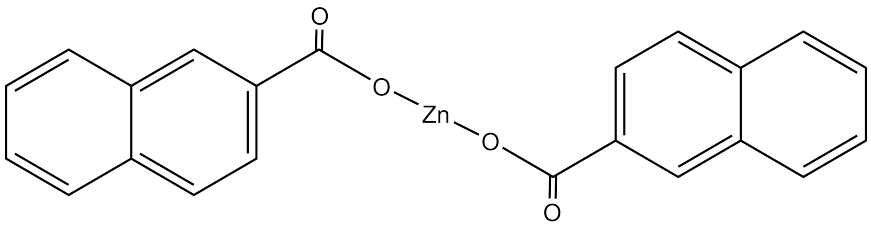

Fig. 5.3 Chemical structure of zinc naphthenate Molecule.

5.4.1 Spin coating of zinc naphthenate

In order to achieve good lithography patterns, a uniform film of zinc naphthenate is required after spin coating. The solution was filtered using a 0.2 μm filter directly on the substrate for spin coating, and then spun at 4000 rpm for 30 sec. Earlier studies on TGA-DTA analysis of metal naphthenates have suggested loss of mineral spirits and toluene between 100 - 200 °C [182]. Accordingly substrates were baked at 115 °C following spin coating to evaporate the toluene solvent. It was observed that initially uniform-looking film degraded in 24 hours. The film showed granulated structure with randomly distributed droplets on the substrate. The micro-sized droplets are shown in Fig. 5.4. The granulation process was observed to have accelerated due to heat treatment at 115 °C and the film degraded within 10 -15 min instead of 24 hours. The granulation of the film is probably caused by aggregation of zinc naphthenate under surface tension.

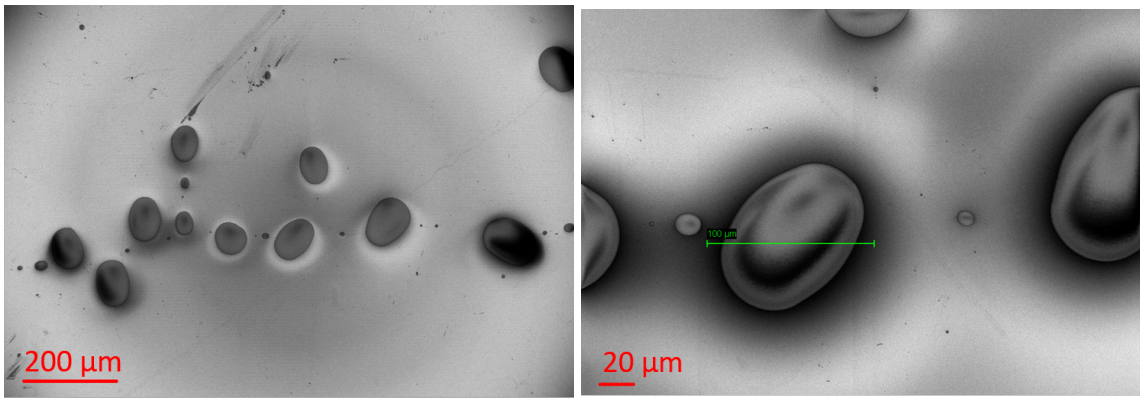

Fig. 5.4 SEM micrographs of globules formed on silicon substrate ∼24 hours after spin coating.

Strong cohesive forces within zinc naphthenate dominate over adhesive forces between zinc naphthenate and SiO_2, thus causing granulation over the period of time. Maintaining extreme cleanliness of the substrates was critically important in delaying the agglomeration by avoiding pinhole formation due to dust particles. Thus piranha cleaning was also often

implemented, followed by 10 min oxygen plasma treatment. Additionally, ultra-thin films of resists are preferred to achieve extreme high resolution in lithography patterning. However, stresses within the ultra-thin resist film may also cause delamination issues. Therefore, various spin-coating rates were tried in order to obtain uniform film thickness without delamination. The spin speed of 2000 rpm for 60 sec was found to be optimal. This was helpful in ensuring a fairly uniform layer of resist and thus decreasing the possibility of delamination while achieving a sufficient processing window for electron beam lithography. As demonstrated in nest section, resolution down to 50 nm was obtained using these processing conditions.

5.4.2 Optimisation of micro patterns

Micron scale patterns, which are easy to characterise, are used for initial optimisation and understanding. In order to optimise micro-patterning various concentrations of zinc naphthenate were spin coated on SiO_2 (100 nm)/Si at 2000 rpm for 60 sec. 1 nA beam current was used for the exposure. A dose test was carried out to write 50 μm square patterns using 1200 μm x 1200 μm field size divided in 20000 dots, making 60 nm beam step during the exposure. An array of 4 x 3 patterns was exposed while varying the electron dose from 2.5 mC/cm^2 to 30 mC/cm^2 in the step of 2.5 mC/cm^2. After the exposure the samples were developed in toluene for 30 sec. After drying the substrates with compressed nitrogen flow, optical microscopy was used to ascertain optimal dose. Fig. 5.5 depicts an example of as developed patterns resulting from the dose test. It can be seen that zinc naphthenate patterns start to form at 5 mC/cm^2 dose, which may be since zinc naphthenate starting to get crosslinked at this dose and thus, rendering insoluble in the developer. The patterns become clearer and sharper until 15 mC/cm^2, which may be attributed to increasing degree of crosslinking in the resist. After 15 mC/cm^2 no significant change is seen, possibly due to fully crosslinked zinc naphthenate. Thus 15 mC/cm^2 was henceforth considered the optimal dose for micro-scale patterns.

As the size of the patterns is decreased, a higher electron dose is required for the crosslinking of resist patterns as well as improving adhesion between the patterns and substrates. However, excessive dose for larger patterns start to cause feature broadening. Such broadening can be attributed to forward as well as backward scattering of the electrons causing proximity effects [214]. Fig. 5.6 illustrates an example of a dose test carried out with different sizes of micron sized patterns. The patterns were exposed using 1.5 nA beam current with 120 μm x 120 μm field size using 60000 dots giving step size of 2 nm. As shown in the Fig. 5.6a, a 3 x 3 array of patterns was exposed starting from 15 mC/cm^2 with

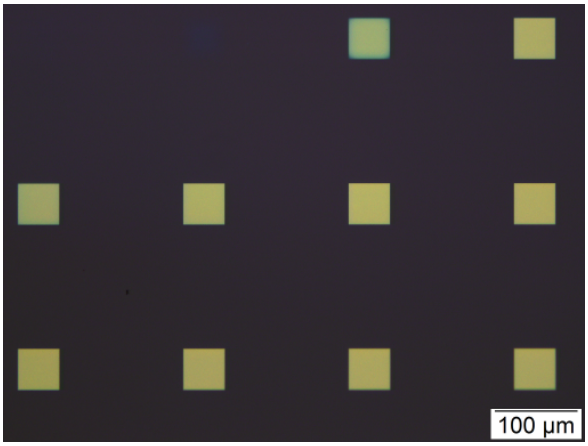

Fig. 5.5 Optical Microscope image of a 4 x 3 array of 50 μm square pattern on 5 % zinc naphthenate exposed to increasing electron dose using 1 nA beam current. Starting from top left, the exposure was incremented in steps of 2.5 mC/cm^2 from left to right and then onto the next row to a maximum of 30 mC/cm^2.

7.5 mC/cm^2 increment. No significant feature broadening is seen up to 30 mC/cm^2, after which larger patterns start to show proximity effects. The smallest feature of 5 μm square shows hardly any broadening even at 75 mC/cm^2.

5.4.3 Electron beam exposure dose response

In order to characterise resist properties of zinc naphthenate a 5 x 5 array of 2.5 μm square pattern was exposed on resist film spun using 5 % concentration at 2000 rpm for 60 sec. The patterns were exposed using 1 nA beam current and 600 μm x 600μm field size divided into 60000 dots. The electron exposure dose was varied from 1.5 mC/cm^2 upto 37.5 mC/cm^2 with increments of 1.5 mC/cm^2. After 30 sec development in toluene the remaining heights of the resist patterns were characterized using AFM measurement. The acquired topography profile is depicted in Fig. 5.7a. The extracted resist pattern thickness was then plotted against the exposure dose and the resulting dose curve is drawn in Fig. 5.7b. Resist Sensitivity ($D_{0.5}$) of $\sim$ 16.7 mC/cm^2 and contrast, γ of 6.2 was estimated from the resist dose curve.

5.4.4 Nano patterning of zinc naphthenate

Typical writing of high-aspect ratio nanostructures requires much higher electron dose to crosslink the resist as well as to improve their adhesion with the underlying substrate. After

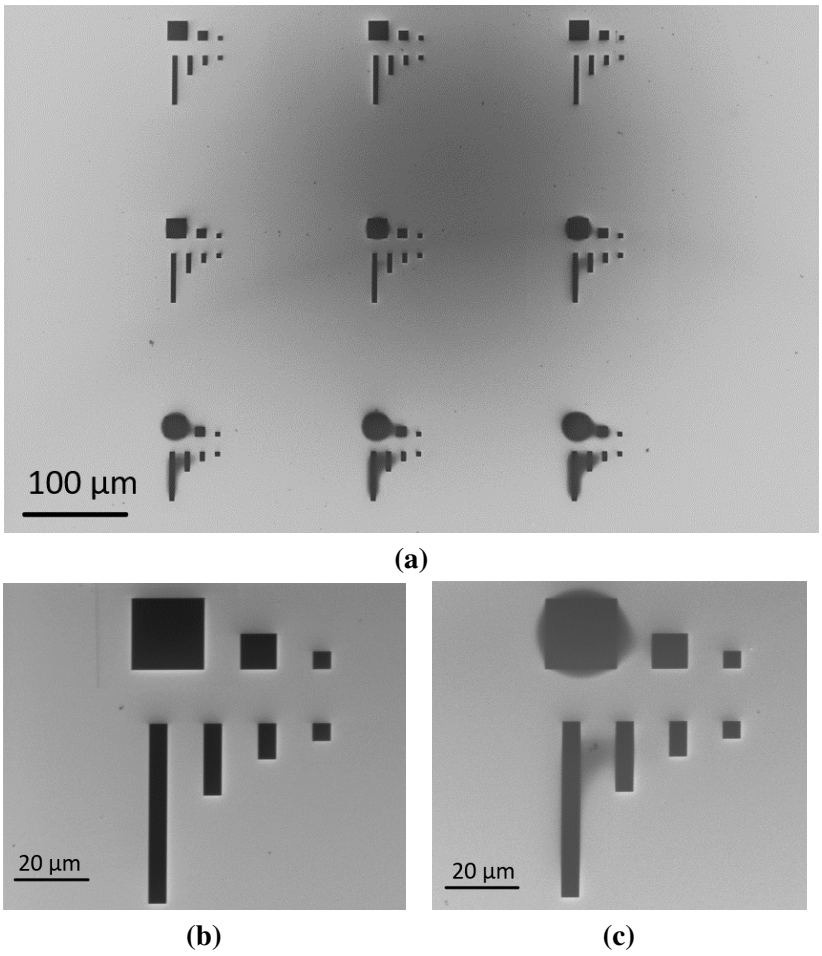

Fig. 5.6 SEM micrographs of (a) 3 x 3 array of various micro scale patterns on a film prepared from 5 % zinc naphthenate using 1.5 nA beam current with increasing electron dose. Starting from top left, the exposure was incremented in steps of 7.5 mC/cm^2 from left to right and then onto the next row to a maximum of 75 mC/cm^2 (b) Patterns with 15 mC/cm^2 exposure dose showing optimal exposure (c) Patterns with 52.5 mC/cm^2 exposure dose showing broadening in bigger pattern while smaller patterns are still not overexposed.

carrying out number of dose tests, in similar manner as reported for micron-sized structures, various linewidths of nano-patterns were successfully fabricated. Zinc naphthenate patterns of 25 μm length and resolution down to 50 nm were prepared using the direct write technique. Representative SEM images of different linewidth nanopatterns and 10 μm length written in zinc naphthenate are illustrated in Fig. 5.8. These nano-patterns were exposed using electron dose of 36 mC/cm^2 with 1.5 nA current and 120 μm square field size divided into 60000 dots giving 2 nm step size.

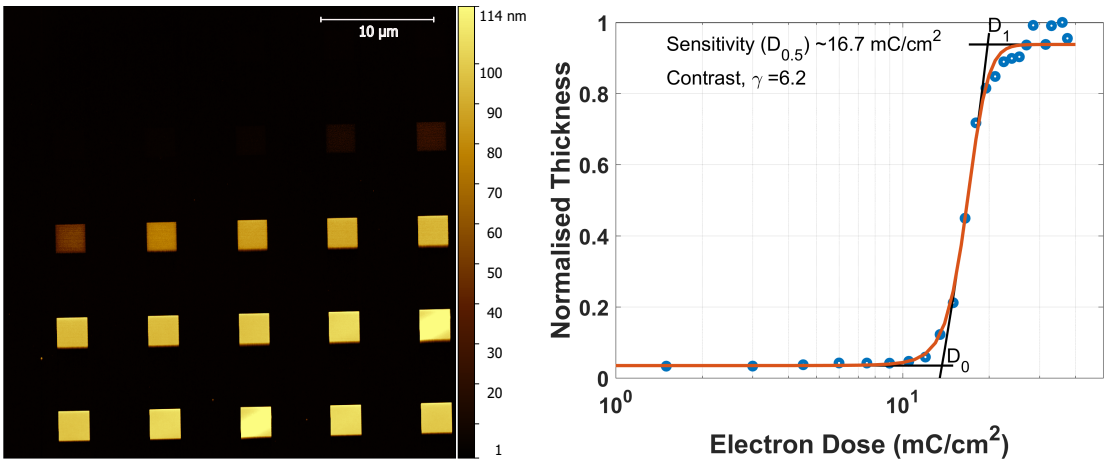

(a) AFM topography **(b) Dose Curve**

Fig. 5.7 Electron exposure response of zinc naphthenate (a) AFM topography image of 5 x 5 array of 2.5 μm x 2.5 μm patterns exposed on 5 % zinc naphthenate with 1 nA current and 10 nm beam step with increasing electron dose. Starting from 1.5 mC/cm^2 at top left, the electron dose was increased in steps of 1.5 mC/cm^2 from left to right and then onto the next row. (b) Post development normalised resist height estimated using AFM and plotted against exposure dose.

Zinc naphthenate nanopatterns were decomposed at 500 °C to convert them to ZnO. SEM images of these nanopatterns before and after decomposition are compared in Fig 5.9. In agreement with previous reports [182, 211, 212], lateral shrinkage within the patterns is clearly seen and can be attributed to mass loss of organic components of the resist during the decomposition.

Grating styled nano-patterns were also exposed using 25 % zinc naphthenate and converted to ZnO by decomposing them at 500 °C. 1 nA beam current and 600 μm x 600 μm field size with 10 nm beam step was exploited for the exposure. 50 lines of 500 nm linewidth and 25 μm length were exposed at 25 mC/cm^2 dose with 1 μm pitch. On the other hand, 100 lines of 100 nm linewidth and 25 μm length were exposed at 50 mC/cm^2 dose with 500 nm pitch. Fig. 5.10 presents AFM topography images of the grating patterns after converting to ZnO. These grating patterns illustrate the capability of high-density ZnO nano-patterning using direct-write EBL on zinc naphthenate.

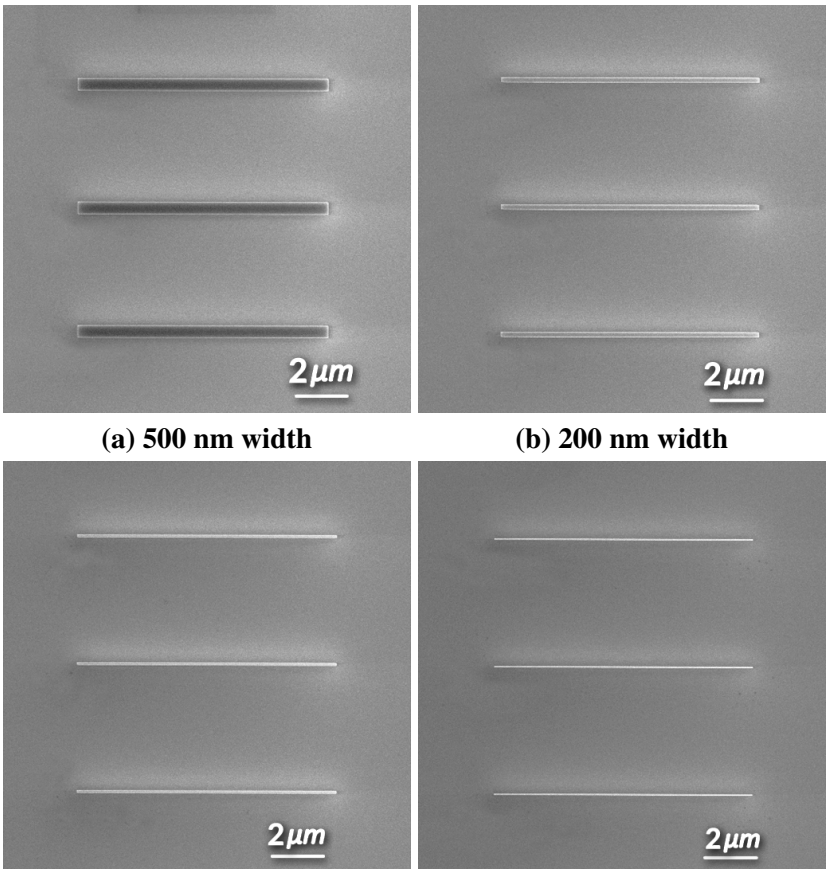

(a) 500 nm width (b) 200 nm width

(c) 100 nm width (d) 50 nm width

Fig. 5.8 SEM micrographs of 10 μm long zinc naphthenate nanopatterns with different linewidth exposed to 51 mC/cm^2 using 1.5 nA beam current 60 μm x 60 μm field size and 1 nm beam step.

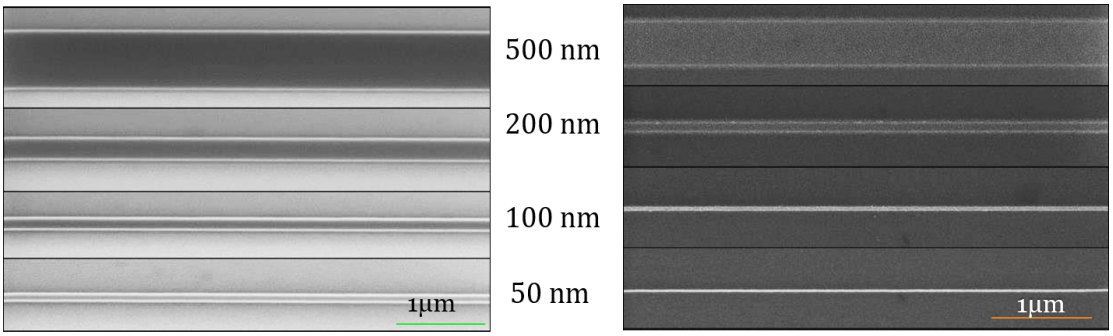

Fig. 5.9 SEM micrographs comparing different linewidth nano-patterns written in zinc naphthenate (left) and resulting ZnO nanowires after decomposition at 500 °C (right) with noticeable lateral shrinkage due to loss of organic components.

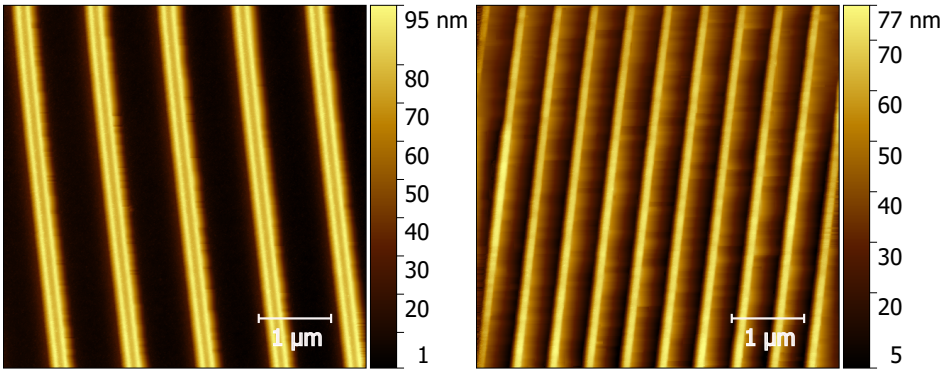

(a) 500 nm width 1 μm pitch **(b) 100 nm width 500 nm pitch**

Fig. 5.10 Nanoscale grating patterns exposed using 25 % zinc naphthenate and decomposed at 500 °C.

5.5 Electron Beam Lithography of Zinc Neodecanoate

As received zinc neodecanoate was also required to be diluted using toluene before use for EBL. The dilution procedure described previously in section 4.2.1 was employed to prepare required concentrations of zinc neodecanoate.

5.5.1 Optimisation of micro patterns

The electron dose required for patterning the micron-sized feature was also estimated at the beginning by carrying out an exposure dose test on 50 μm square patterns. A 5 % concentration of zinc neodecanoate, spin coated at 2000 rpm for 60 sec, was used for this purpose. A beam current of 1 nA was employed on 1200 μm x 1200 μm field size divided in 20000 dots made a 60 nm beam step. A 5 x 4 array of patterns was exposed by varying the electron dose from 0.4 mC/cm^2 to 8 mC/cm^2 in the step of 0.4 mC/cm^2. Development of the samples was then carried out in toluene for 30 sec. The exposed patterns were observed under an optical microscope. The optical image is presented in Fig. 5.11. Zinc neodecanoate begins crosslinking at dose as low as 2 mC/cm^2. Fully crosslinked patterns can be seen from about 4 mC/cm^2. However, small improvement in the patterns was still observed up to $\sim$ 6.8 mC/cm^2.

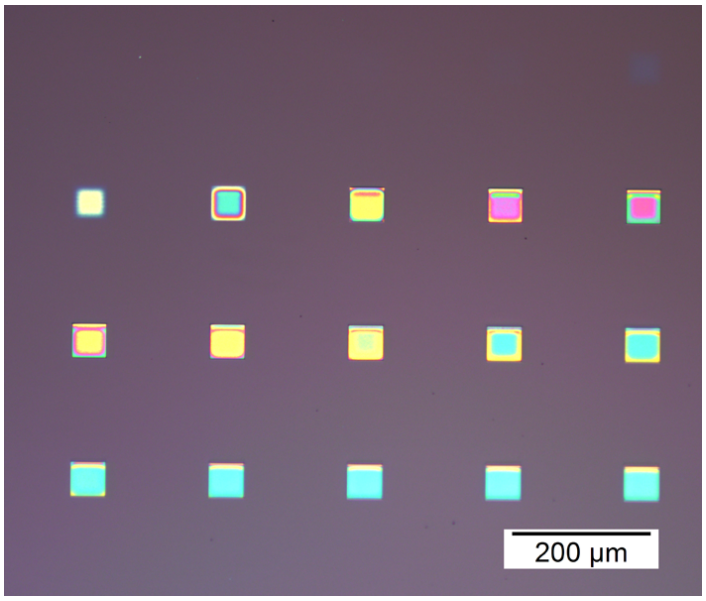

Fig. 5.11 Optical Microscope image of a 5 x 4 array of 50 μm square patterns on 15 % zinc neodecanoate exposed to increasing electron dose using 1 nA beam current. Starting from top left the exposure was incremented in steps of 0.4 mC/cm^2 from left to right and then onto the next row to a maximum of 8 mC/cm^2.

5.5.2 Electron beam exposure dose response

Similar to zinc naphthenate, a 5 x 5 array of 2.5 μm square pattern was exposed on 5 % zinc neodecanoate spin coated at 2000 rpm for 60 sec. A beam current of 1 nA was used to expose onto 600 μm x 600μm field size divided into 60000 dots. The electron exposure dose variation was carried out from 0.5 mC/cm^2 up to 10 mC/cm^2 in steps of of 0.5 mC/cm^2. The samples were then subjected to 30 sec development in toluene, followed by AFM measurement to estimate the thickness of resist patterns. Fig. 5.12a shows the topography profile characterised using AFM scan. The plot of resist pattern thickness against exposure dose and resulting dose curve is drawn in Fig. 5.12b. Resist Sensitivity ($D_{0.5}$) of $\sim$ 4.4 mC/cm^2 and contrast γ of 6.4 was evaluated from the resist dose curve. Zinc neodecanoate being more sensitive as compared with zinc naphthenate, it posses a possibility of faster e-beam exposures requiring less writing times.

5.5.3 Nano patterning of zinc neodecanoate

Zinc neodecanoate was also employed in fabricating high aspect ratio nanopatterns. Due to the higher sensitivity of zinc neodecanoate as compared with zinc naphthenate, nanopatterns were achieved even at dose as low as 5 mC/cm^2. SEM images in Fig. 5.13 show different linewidth nanopatterns with 10 μm length which were exposed at 5 mC/cm^2. 1 nA current

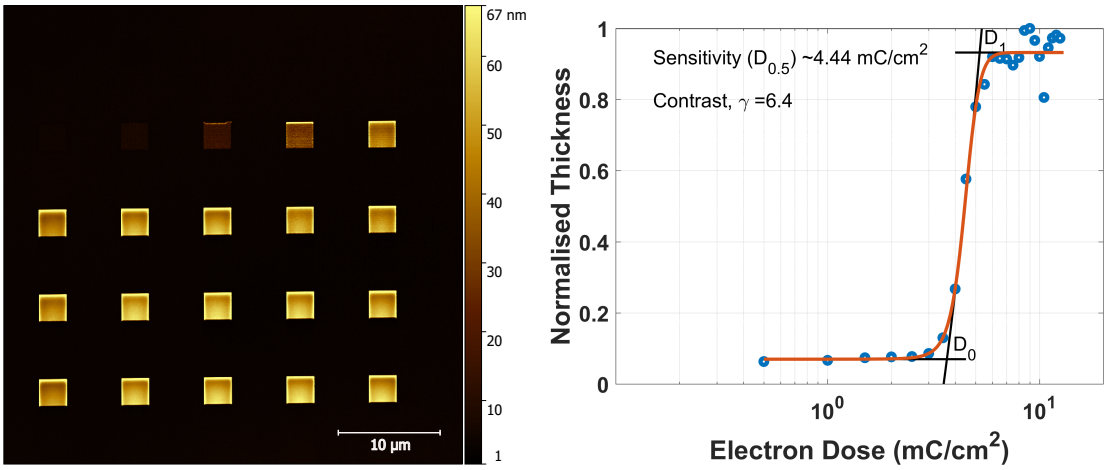

(a) AFM topography **(b) Dose Curve**

Fig. 5.12 Electron exposure response of zinc neodecanoate (a) AFM topography image of 5 x 5 array of 2.5 μm x 2.5 μm patterns exposed on 5 % zinc neodecanoate with 1 nA current and 10 nm beam step with increasing electron dose. Starting from 0.5 mC/cm^2 at top left, the electron dose was increased in steps of 0.5 mC/cm^2 from left to right and then the next row. (b) Post development normalised resist height estimated using AFM and plotted against exposure dose.

and 60 μm square field size divided into 60000 dots was implemented to fabricate these patterns with 30 sec development in toluene. 25 μm long nano-patterns with a resolution of 50 nm were achieved in zinc neodecanoate as well and was used to fabricate devices discussed in next chapter.

Grating styled nano-patterns were exposed using 15 % zinc neodecanoate and converted to ZnO by decomposing them at 500 °C. 1 nA beam current and 600 μm x 600 μm field size with 10 nm beam step was implemented for the exposure. 50 lines of 500 nm linewidth and 25 μm length were exposed at 12.5 mC/cm^2 dose with 1 μm pitch. On the other hand, 100 lines of 100 nm linewidth and 25 μm length were exposed at 25 mC/cm^2 dose with 500 nm pitch. Fig. 5.14 presents AFM topography images of the grating patterns after converting to ZnO. These grating patterns demonstrate capability of fabricating high density ZnO nano-lines by direct-write EBL on zinc neodecanoate. Such a grating style ZnO lines were later utilised in nano-patterned gas sensing devices discussed in Chapter 7.

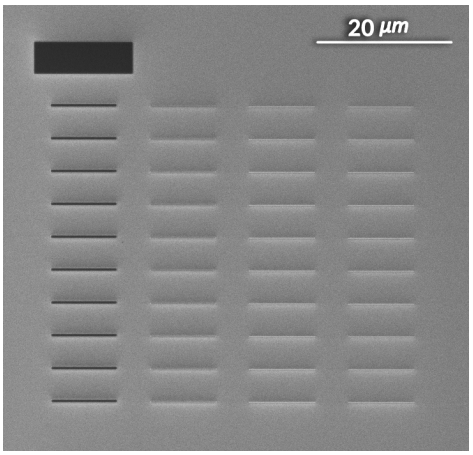

(a) All widths

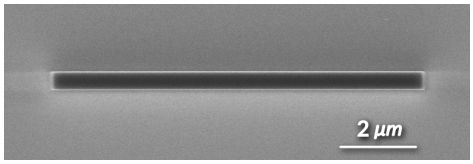

(b) 500 nm width

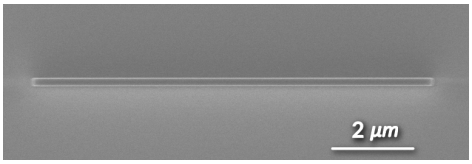

(c) 200 nm width

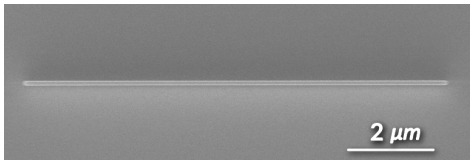

(d) 100 nm width

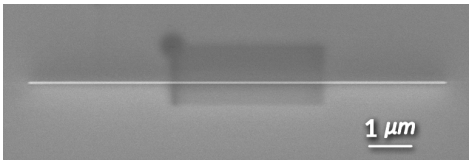

(e) 50 nm width

Fig. 5.13 SEM micrographs of 10 μm long zinc neodecanoate nanopatterns with different linewidth exposed to 5 mC/cm^2 using 1 nA beam current 60 μm x 60 μm field size and 1 nm beam step.

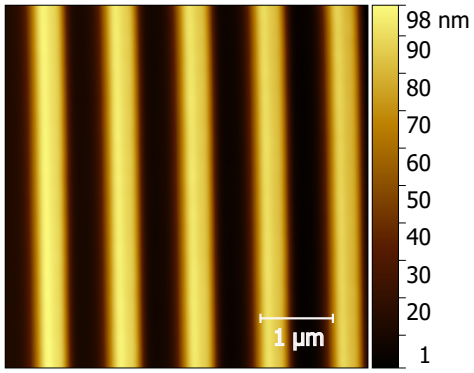

(a) 500 nm width 1 μm pitch

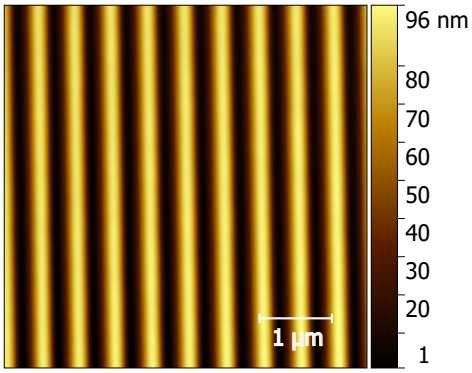

(b) 100 nm width 500 nm pitch

Fig. 5.14 Nanoscale grating patterns exposed using 15 % zinc neodecanoate and decomposed at 500 °C.

5.6 Concluding remarks

Two precursor schemes based on zinc naphthenate and zinc neodecanoate were explored for direct write electron beam lithography for top-down synthesis of ZnO nanowires. Required electron exposure dose was optimized for a number of micron-sized as well as nanoscale patterns with resolution down to 50 nm and length upto 25 μm. A systematic dose test was carried out for 2.5 μm square patterns on both the resists. Thickness at various electron dose values were measured using AFM and used for extracting resist parameters. Zinc naphthenate demonstrated sensitivity of 16.7 mC/cm^2 and contrast of 6.2, whereas zinc neodecanoate showed sensitivity of 4.4 mC/cm^2 and contrast of 6.4.

Chapter 6

Direct-write electron beam lithography for ZnO micro-nano FETs

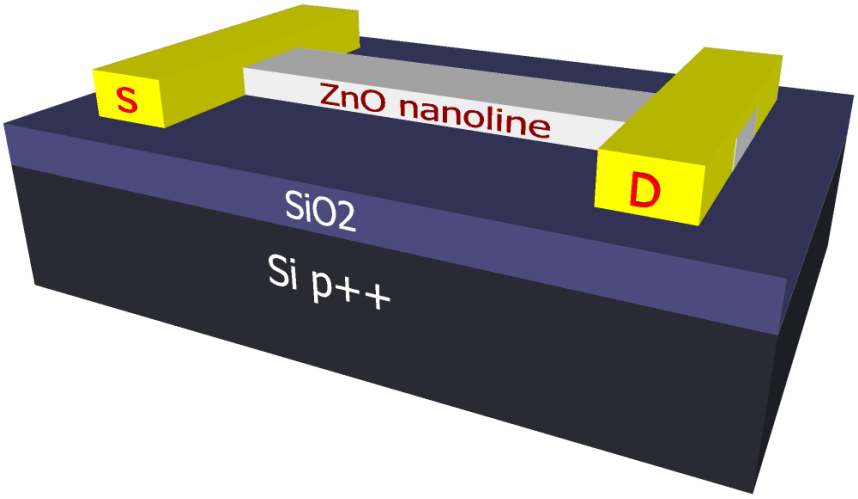

6.1 Introduction

In recent years, the approach of direct write patterning of sol-gel precursors for fabrication of micro/nano-scale oxide structures has been increasingly explored for fabrication of field-effect transistor applications. Since this approach requires fewer processing steps as compared with conventional top-down routes, they are attractive for developing cheaper fabrication protocols for sol-gel based ZnO devices with high device density. In this chapter electron beam lithography (EBL) based direct write approach has been implemented for fabrication of ZnO devices.

6.2 Solution processed Direct patterned oxide transistors

Regardless of the deposition technique employed, be it vacuum based or solution processed, patterning of the oxide channel layer has often been implemented. Such patterning provides device isolation [183] to allow large-scale integration. Additionally, a patterning channel region suppresses gate leakage current by decreasing the overlapping area between gate and source/drain electrodes [215, 13]. Most conventional patterning techniques depend on lift-off [216], wet etching [12, 13] or reactive ion etching (RIE)[217]. However, etching-based techniques often have detrimental effects on device performance due to damage caused to the oxide channel layer [12]. In addition, resist residues left after the stripping process can also cause deterioration of the oxide semiconductor interface properties. Cho *et al.* have recently reported modified wet-chemical etching processes to increase the durability of the oxide channel [13].

At the other end of the spectrum nano-scale oxide devices fabricated using a bottom-up approach lack positional control in device fabrication and limit their large-scale integration. While trying to achieve nanoscale resolution in oxide patterning, wet etching techniques pose particular challenges. On the other hand, delamination issues are difficult to control during lift-off processing. Lee *et al.*[206] have demonstrated a RIE based approach of patterning ZnO nano devices, while the performance they achieved remained poor. Sultan *et al.* have explored remote plasma enhanced ALD process in conjunction with RIE technique to fabricate ZnO TFTs with saturation mobility of 0.33 cm^2/V.s [218]. Later on, using inductively coupled plasma (ICP) based etching of ALD films in conjunction with spacer technique, the authors also reported nanowire FETs with field effect mobility of 10 cm^2/V.s [219]. Ghazali *et al.* further modified this technique using photoresist sidewall smoothing also to report field effect mobility of 7.7 cm^2/V.s[220].

In the past few years direct patterning of sol-gel precursors has been investigated to fabricate a metal-oxide channel for transistor device applications. Direct-write patterning has a number of marked benefits over conventional processing, primarily due to the requirement of fewer steps in fabrication flow while attaining positional control in device placement. Furthermore, direct-patterning of oxide semiconductors evades photoresist residue as well as degradation of the channel layer during etching steps. In addition, direct-write patterning can be easily implemented to achieve nano-scale oxide structures where conventional processing techniques face a number of challenges.

Rim *et al.* adopted benzoylacetone chemical modification to fabricate direct photopatterned IGZO TFTs with field-effect mobility of 1.15 cm^2/V.s at annealing temperature of 350 °C. In the same report, the authors also explored a nitric acid and acetylacetone-based oxidiser-fuel combination to achieve phtopatterned In_2O_3 TFTs at 250 °C. The processing temperature being low enough for processing of flexible substrates, the authors reported TFTs fabricated on polyimide substrate with field effect mobility of 2.24 cm^2/V.s with on-off ratio of 10^8 [215]. Lim *et al.* used a similar chemical modification to achieve fully self-patterned TFT (saturation mobility 0.03 cm^2/V.s) with both ITO contacts as well as a ZTO channel fabricated by direct photopatterning. The authors also demonstrated the capability of this method to pattern ITO and ZTO lines with 55 μm resolution using 365 nm UV lamp [221]. In another report Rim *et al.* further applied 254 nm DUV radiation and ammonium hydroxide additive to realise IGZO TFT with mobility upto 84.4 cm^2/V.s by also using direct-patterned Al_2O_3 as dielectric [222].

Lin *et al.* exploited a zinc methacrylate-based formulation and 193 nm ArF DUV Laser for direct patterning of IGZO TFTs. With annealing temperature of 600 °C, the authors in this study were able to achieve field effect mobility of 9.9 cm^2/V.s [223]. Yeh *et al.* also used zinc methacrylate precursor to fabricate a 300 nm channel width zinc oxide nanowire transistor with mobility 0.45 cm^2/V.s [224]. Jeong *et al.* implemented zinc diacrylate as a photocurable precursor to prepare zinc oxide TFTs achieving mobility of 0.853 cm^2/V.s on SiO_2 dielectric that increased to 7.14 cm^2/V.s in ion-gel gated device [225].

Jones *et al.* have reported ZnO nanowire FET using electron beam lithography direct patterning of ZnO using zinc neodecanoate precursor[226]. An in-depth study is further required to optimize the ZnO devices with this method. Zinc naphthenate is another direct-write electron beam lithography precursor that has been reported for high-resolution ZnO nano-patterning [182, 212]. However, no report was found to have used zinc naphthenate for fabrication of ZnO FETs. In this chapter, process optimisation of ZnO micro/nano FETs using zinc neodecanoate and zinc naphthenate direct-write precursors has been explored.

6.3 Initial Process Development

As in earlier chapters, boron doped p^{++} Si(100) wafers with 100 nm thermally grown SiO_2 were used as substrates for the fabrication of FETs. During the fabrication of ZnO-based FETs using the direct-write EBL approach, two steps of aligned lithography were necessary for ZnO layer and metal electrode layer respectively. In order to ensure precise alignment of these two layers, the use of alignment markers was inevitable. Thus, at the beginning of the device fabrication process a separate lithography step was carried out to lay down $\sim$ 100 nm thick Ti/Au alignment markers at predetermined locations on diced and cleaned substrates.

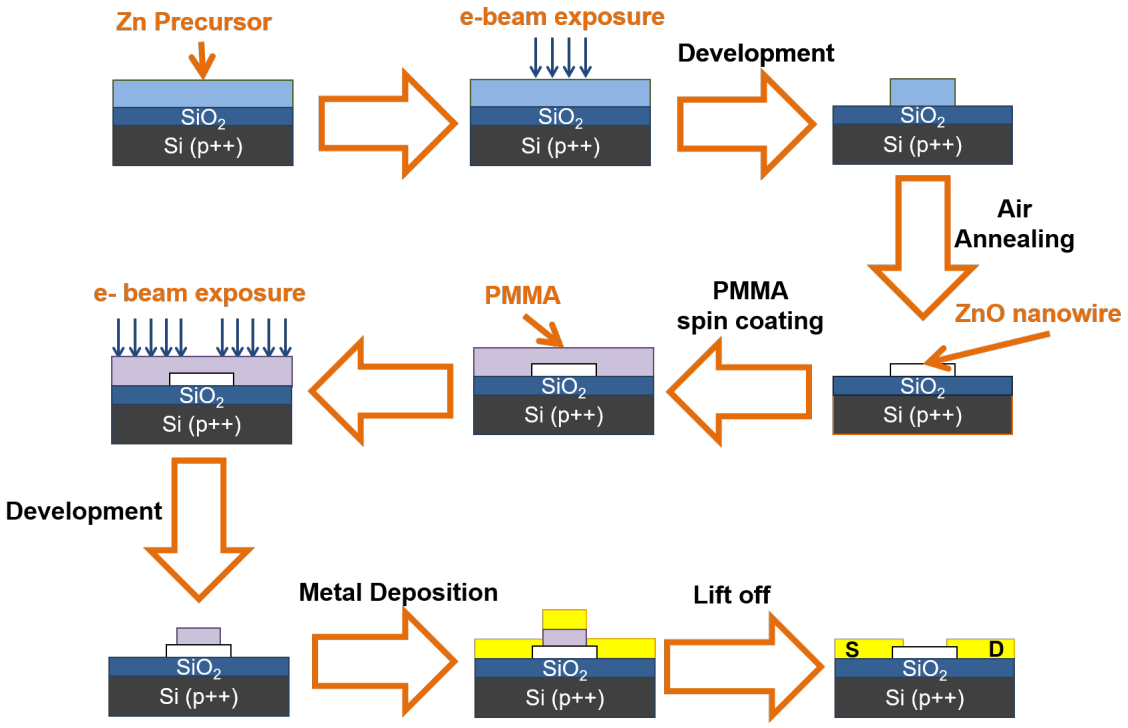

Fig. 6.1 Processing steps for fabrication of ZnO FETs using direct write EBL.

General fabrication flow of FET fabrication, after the deposition of markers, is shown in Fig. 6.1. A pre-diluted solution of zinc naphthenate or zinc neodecanoate in toluene was filtered onto the substrate using a 0.2 μm syringe filter with PTFE or nylon membrane and spin-coated at 2000 rpm for 60 sec. Samples were then placed on a 115 °C hotplate for 1 min to evaporate the solvent. This was followed by loading the samples into the Crestec CABL-9000C Electron Beam Lithography system and exposed with pre-optimised current and dose at 50 kV acceleration voltage. The e-beam exposure forms cross linking within the precursor, rendering the exposed region insoluble in toluene. Samples were developed

in toluene for ∼30 sec to wash off unexposed precursor. Decomposition of the organic component and conversion to zinc oxide was then carried out by annealing the samples in ambient air inside a Carbolite tube furnace at 500 °C, unless otherwise mentioned.

After the formation of ZnO regions PMMA 950 A4 was spin-coated on substrates at 2000 rpm for 60 sec. The samples were then baked at 180 °C for 2 min to crosslink PMMA. Electron beam lithography for the electrode regions was once again carried out using Crestec CABL-9000C. An exposure dose of ∼650-700 μC/cm^2 was used with 1 nA beam current for positive tone lithography on PMMA. Exposure to an electron beam breaks the polymer chains within PMMA, and is thus removed during the development step. Samples were developed in methyl isobutyl ketone (MIBK) diluted with isopropyl alcohol (IPA) in 1:3 ratio for 60 sec followed by 15 sec rinse in IPA. Source and drain electrodes are then deposited using electron beam evaporation. 50 nm Ti followed by 100 nm Au is deposited using the Kurt J. Leskar electron beam evaporation system at a pressure of $\sim 10^{-6}$ mbar. Departing from the general practice of adopting only a few nano-meters of Ti adhesion layer, a much thicker Ti layer is incorporated here to form ohmic contact with the underlying ZnO layer. The lift-off was then carried out by placing the samples in warm (∼40 °C) acetone for a few hours, followed by gentle agitation using a stream of solvent and ultrasonication if required. Samples were then rinsed in IPA and dried using a compressed nitrogen flow. Fig. 6.2 depicts an example of aligned fabrication of zinc oxide nanowires prepared from zinc naphthenate and Ti/Au electrode deposited on top.

In order to investigate electrical characteristics of direct-write EBL patterned ZnO devices, initial study was conducted using zinc neodecanoate as a precursor material. Given the findings discussed in Chapter 4, a 15 % concentration of zinc neodecanoate was used for the device fabrication. Substrates with spin coated precursor were loaded into the EBL system. A 25 μm x 100 μm sized pattern was exposed with 10 mC/cm^2 dose using 5 nA current and 60 nm beam step size. The exposed substrate was then developed in toluene for 30 sec and dried with compressed nitrogen flow. After annealing the substrate at 500 °C for 1 hr, Ti-Au electrodes with 5 μm separation were fabricated using the above-mentioned aligned lithography in PMMA and subsequent lift-off.

6.3.1 Effect of Ambient Atmosphere

During the initial experiments to determine optimal conditions for transistor measurement and study the effect of surrounding conditions on device performance, transfer curve measurements were carried out in different atmospheres using a Lakeshore vacuum probe station.

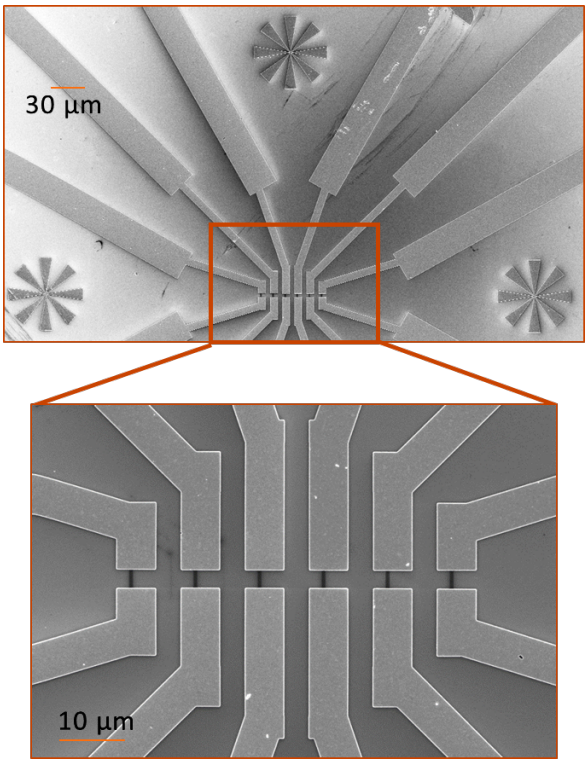

Fig. 6.2 SEM images showing precise positioning of direct-write EBL ZnO nanowire devices along with the alignment markers and Ti/Au electrodes.

The acquired I_D-V_G characteristics at V_D = 1 V are shown in Fig. 6.3. At the beginning of the measurement repeated gate-voltage scans were carried out until the device showed negligible threshold voltage shift. The measurement at this point is shown as "Pre-air". Subsequently the chamber was pumped to 10^{-4} mbar vacuum. The corresponding measurement is depicted as "Vac". When the ZnO device was taken from air to vacuum the surface-adsorbed oxygen species were desorbed releasing trapped electrons for conduction. As a result OFF current was increased drastically, showing less than an order of magnitude on-off.

When nitrogen or dry air was inserted at equilibrium pressure of $\sim 10^{-2}$ mbar, no significant change was observed in transfer curves, suggesting that these conditions were not sufficient to trap electrons and bring the OFF current down. The chamber was then filled with dry air to bring it to atmospheric pressure. Both ON current and OFF current were then seen to have decreased, while transfer curve showed slightly more than one order of on/off ratio. It was only after leaving the device overnight inside the chamber filled with dry air that the device started showing OFF current similar to the original value. While the measurement showed a $\sim 10^3$ on/off ratio, hysteresis decreased significantly. The device was then kept

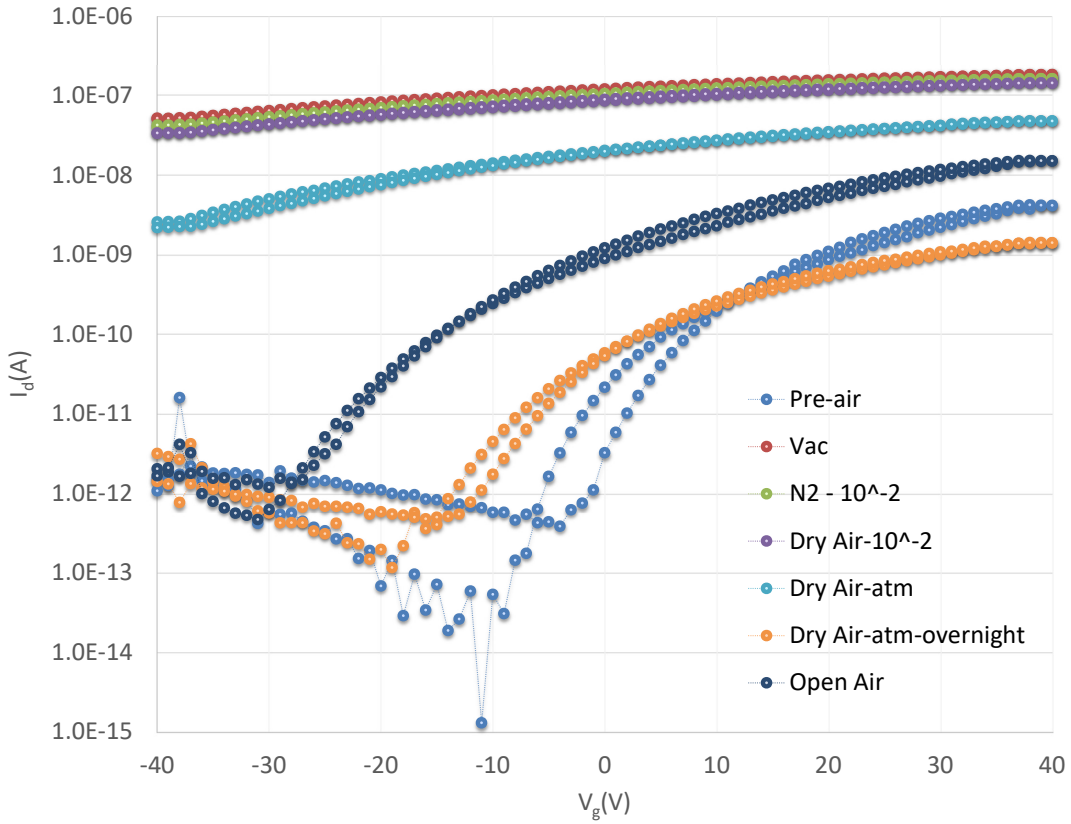

Fig. 6.3 Transfer characteristics of ZnO FET (W/L = 25 μm / 5 μm) fabricated using direct-write EBL on zinc neodecanoate in different ambient atmosphere.

in ambient air conditions (humidity $\sim$50 %) for 3 days and the first transfer curve acquired under that condition is presented as "open air".

6.3.2 Effect of gate voltage sweep-rate

In order to scrutinize electronically active traps present within the ZnO matrix, transfer characteristics were acquired at different gate voltage sweep-rate and in different ambient conditions. During the three different measurements, gate voltage sweep was stepped with 1 V, 0.5 V and 0.05 V respectively. Fig 6.4 presents transfer curves acquired with different scan speeds in open-air ambient, clearly showing increase in the hysteresis at slower sweeping rate. This observation points to deep level traps, since they are activated at slower sweep rates. Interestingly, only a small amount of hysteresis can be seen even at lower sweep rate when the measurements were carried out in vacuum environment ($\sim 10^{-3}$ mbar), as shown in

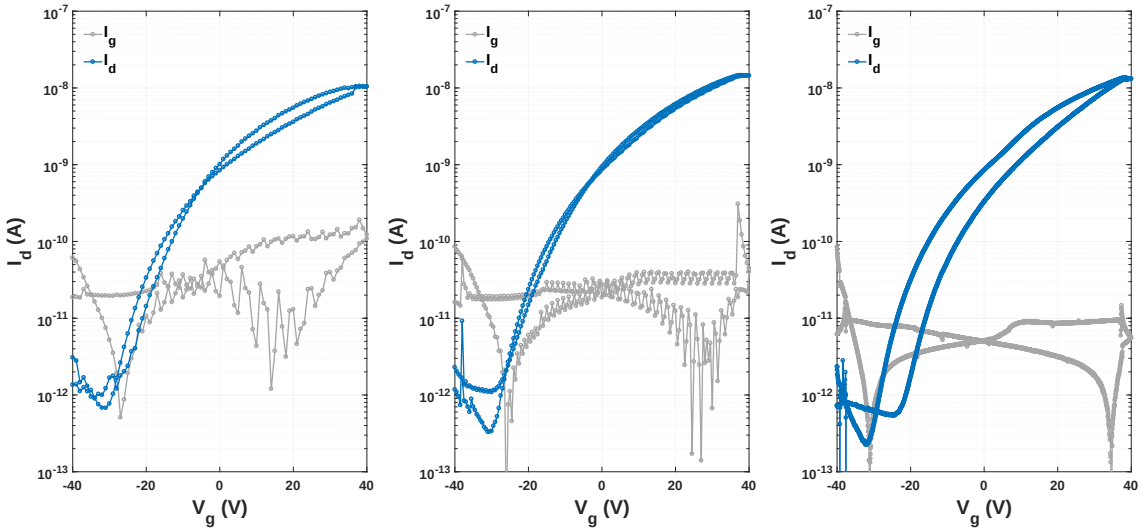

(a) 1 V Step **(b) 0.5 V Step** **(c) 0.05 V Step**

Fig. 6.4 Effect of gate voltage sweep rate in ambient air condition.

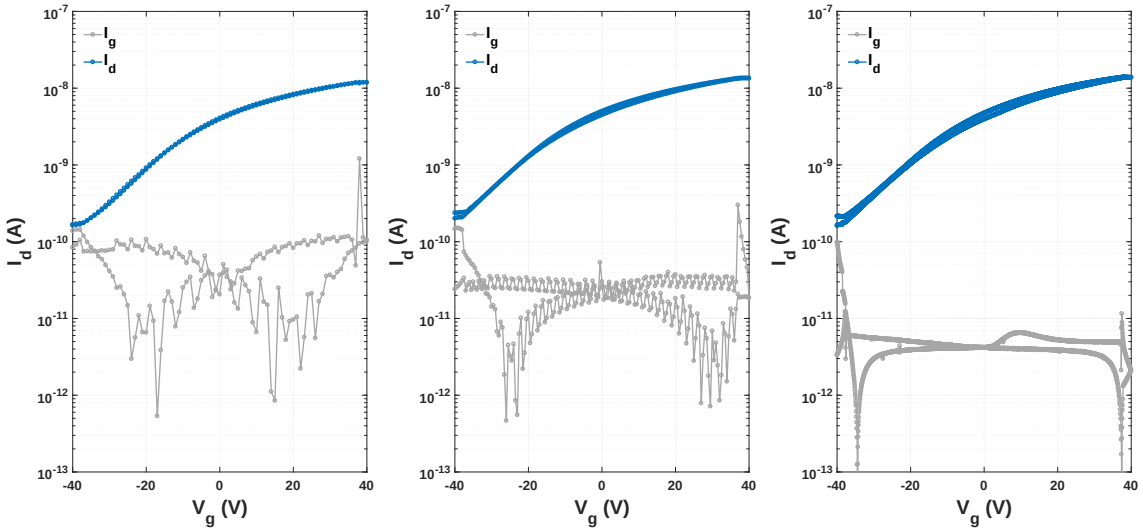

(a) 1 V Step **(b) 0.5 V Step** **(c) 0.05 V Step**

Fig. 6.5 Effect of gate voltage sweep rate in vacuum ($\sim 10^{-3}$ mbar).

Fig. 6.5. The I_{ON}/I_{OFF} ratio of $\sim 10^4$ in ambient air decreased to $\sim 10^2$ in vacuum due to two orders of magnitude increase in the OFF current.

From the above set of measurements, hysteresis in ambient air condition can be attributed to adsorption of oxygen and/or water molecules on the ZnO surface, trapping conduction electrons to surface states. However, when ZnO devices are in vacuum environment, a

higher concentration of oxygen vacancies may arise due to desorption of these species. Since oxygen vacancies in ZnO can act as shallow donors, they generate an excess of conduction electrons, effectively decreasing traps and increasing OFF current. In the ON state, however, the carriers generated due to gate action dominate the transport and hence similar current can be seen in both air and vacuum measurements. There might still be some other defects within ZnO, effectively limiting the ON current.

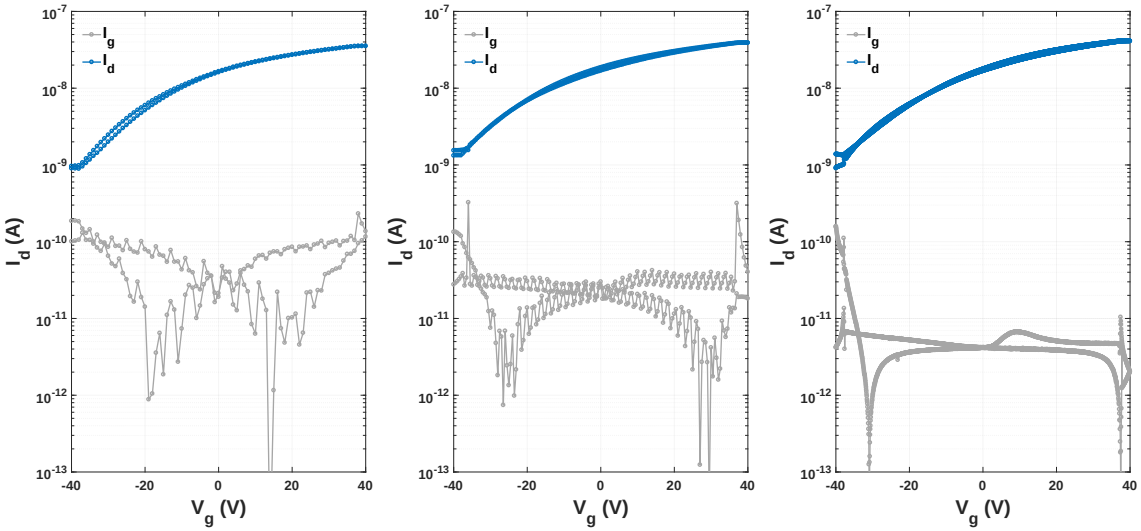

(a) 1 V Step **(b) 0.5 V Step** **(c) 0.05 V Step**

Fig. 6.6 Effect of gate voltage sweep rate after passivation by parylene C.

Measurements with different gate voltage sweep rates were also carried out after deposition of Parylene C (Fig. 6.6). Parylene C not only removes adsorbed oxygen/water molecule species but also passivates ZnO surface. This results in a decreased number of trap states and an increase in electron charge carrier density. Consequently, both ON current and OFF currents were found to be even higher than measurements conducted in vacuum. The presence of a negligible amount of hysteresis even at slower scan speed was consistent with vacuum measurements, signifying removal of traps states from ZnO channel.

6.3.3 Surface Modification

It has been reported that silanol groups, formed due to adsorbed water molecules on SiO_2 surfaces, are efficient traps for n-type conduction [227]. Suspecting that this might be one of the causes of limited mobility in ZnO, various surface treatments were investigated. Vapour deposition of organosilane self-assembled monolayers (SAM) was carried out prior to ZnO

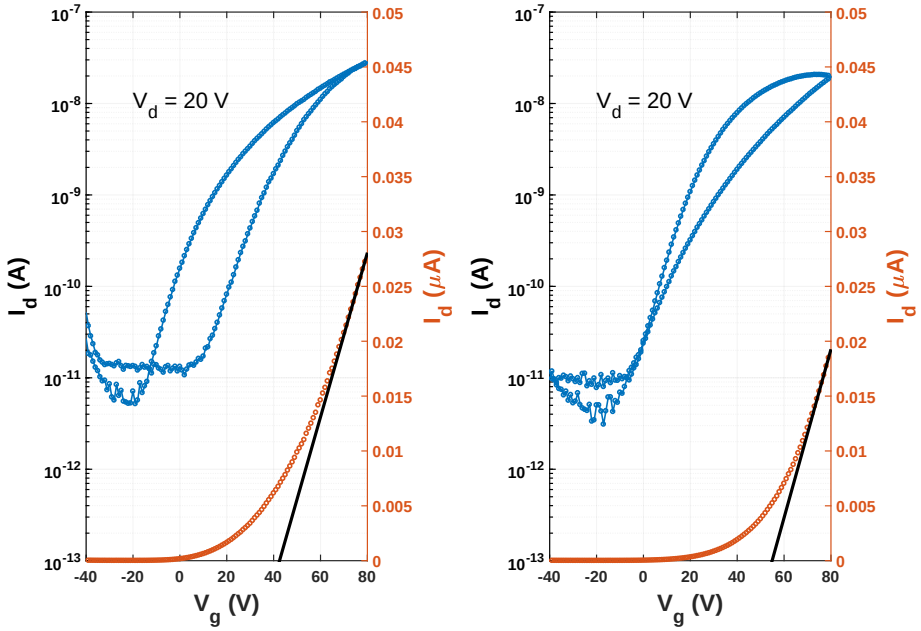

(a) 100 nm SiO_2 **(b) 100 nm SiO_2 + 30 nm Al_2O_3**

Fig. 6.7 Comparing the effect of different dielectric configurations.

channel layer processing, followed by device fabrication. The devices, however, showed either no change or degradation in the performance, as compared with a device without any SAM layer. During the control tests carried out on silanized substrates annealed to 500 °C without the ZnO, the channel showed a decrease in water contact angle, suggesting that the heat treatment caused decomposition of the silane layers and rendered the surface treatment ineffectual.

ALD deposition of 30 nm of Al_2O_3 was then carried out on Piranha solution-cleaned Si-SiO_2 substrates and ZnO devices were then fabricated following the usual method. The comparison of the transfer characteristics with and without the Al_2O_3 layer is shown in Fig. 6.7. As can be clearly seen, no significant change was observed in the on/off currents during the transistor operation. It was then concluded that the oxide interface traps due to Silanol groups are not the major mobility-limiting factor.

6.3.4 Effect of high temperature annealing

In an attempt to improve the crystallinity of e-beam patterned ZnO layer formed, as developed zinc neodecanoate patterns were subjected to higher temperature annealing. During a particular experiment patterned zinc neodecanoate was annealed at 600 °C for 1 hr after

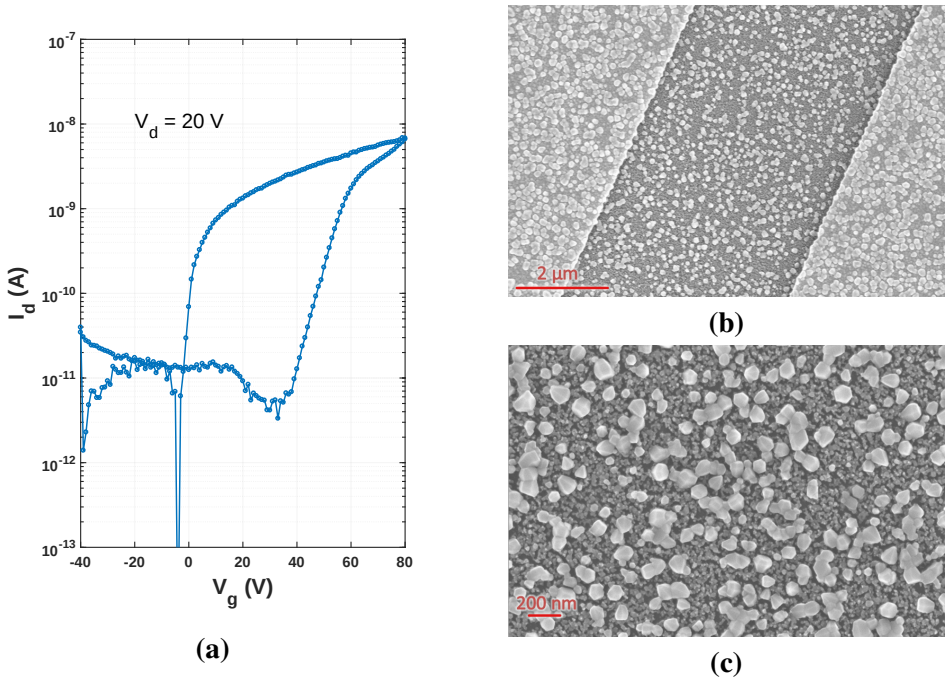

(a) (b) (c)

Fig. 6.8 ZnO device prepared by annealing patterned zinc neodecanoate at 600 °C (a) Transfer characteristic (b),(c) are the SEM images showing large ZnO crystallites.

temperature ramp rate of 10 °C/min followed by routine device fabrication protocol. As illustrated in Fig. 6.8a, the device showed rather decreased ON current with significantly increased hysteresis. After investigating the surface morphology of the ZnO channel using SEM, larger sized crystallites were observed, as shown in Fig. 6.8b and Fig. 6.8c. The higher annealing temperature may have caused coalescence of smaller grains, leading to excessive grain growth. However, formation of porosity in between the crystallites may have led to insufficient percolation pathways causing a drop in channel current.

6.3.5 Effect of contact metal

Typically a metal with work function lower than electron affinity of the n-type semiconductor is employed to achieve ohmic contacts. To this end, Ti and Al with work functions 4.33 eV and 4.28 eV respectively are well suited for n-type ZnO with electron affinity ∼4.2-4.35 eV. However, the presence of defects at the metal-ZnO interface may cause formation of a Schottky barrier and increase in contact resistance [228]. In order to investigate whether the metal contact resistance may be a mobility limiting factor, ZnO FET devices were fabricated with different metal contacts. The transfer characteristics of 50 nm Ti-70 nm Au contact FETs are compared with 100 nm Al contacted FETs in Fig. 6.9. The device with Ti-Au contacts showed lower ON current even with 20 V drains voltage as compared with the Al

contact device at 1 V drain voltage. The corresponding values of estimated linear mobility were 2.27 x 10^{-4} cm^2/V.s for the Ti-Au device and 1.08 x 10^{-2} cm^2/V.s for the Al device. This increase in mobility may be attributed to lower work function of Al, which is more suitable for electron injection as well as clean ZnO-Al interface as compared with the ZnO-Ti interface. Moreover, the higher amount of hysteresis was also evident in Ti-Au contacted device.

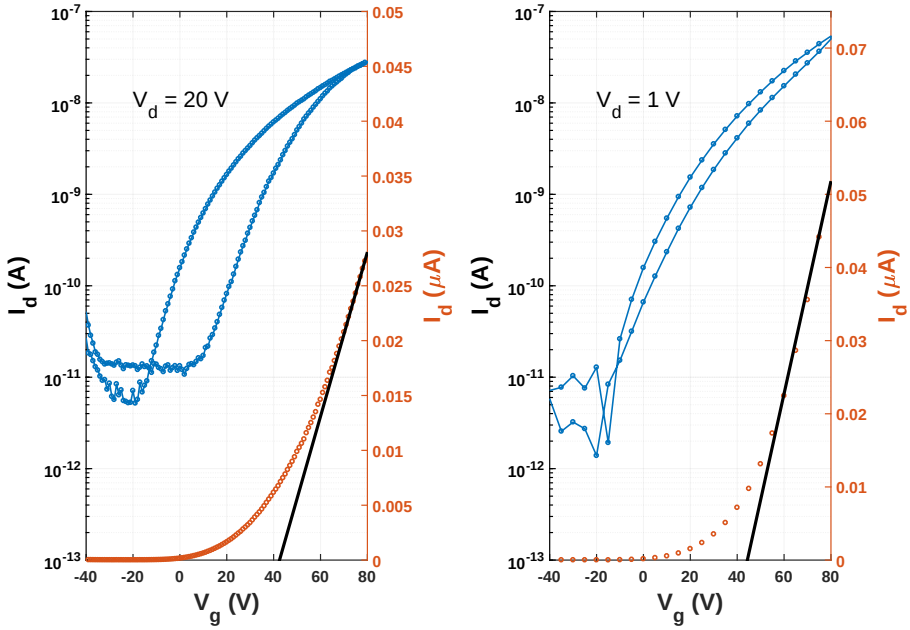

(a) 50 nm Ti + 70 nm Au as contact metal (b) 100 nm Al as contact metal

Fig. 6.9 Comparison of transfer characteristics acquired from ZnO FETs with different contact metal schemes (a) 50nm Ti-70nm Au (b) 100 nm Al.

6.4 Fabrication method using photolithography

While writing large-scale features of metal electrodes, PMMA-based EBL, although suitable, requires much longer processing time. Moreover, residue left by PMMA after lithography may cause device instabilities and contact resistance issues in devices. For this reason EBL was henceforth used only for crosslinking and patterning zinc precursors and metal electrodes were fabricated using the conventional photolithography process. Fig. 6.10a depicts the process flow for the fabrication of ZnO FETs for the remainder of the study.

In order to ensure alignment between the ZnO and electrode layer, prefabricated markers were used, as discussed in earlier section. Fig. 6.10b presents an example image of local

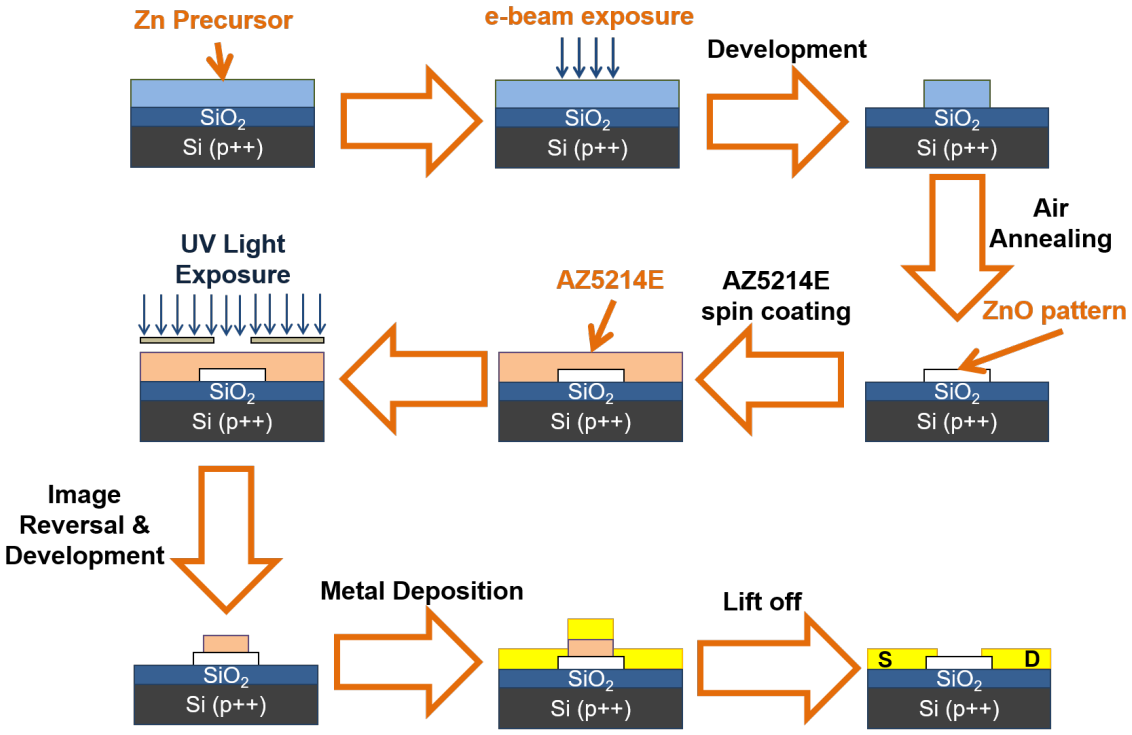

(a)

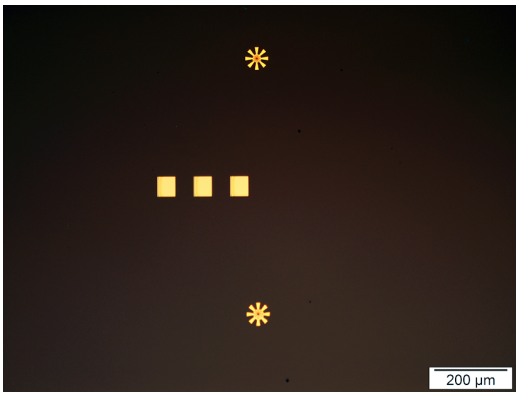

(b)

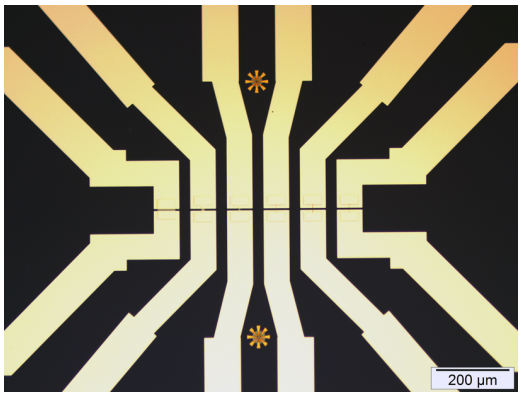

(c)

Fig. 6.10 (a) Processing steps for fabrication of ZnO FETs using direct-write EBL (b) example of 50 μm square patterns fabricated using aligned EBL (c) example of aligned photolithography after metal deposition and lift- off.

alignment markers and ZnO micro-patterns fabricated using aligned EBL. After the formation of ZnO micro/nano patterns by direct-write EBL and annealing (as described in previous section), samples were rinsed in acetone-IPA and dried under compressed nitrogen. Prior to spin coating photoresist, samples were baked at 200 °C for 10 min. AZ5214E was spin coated on at 6000 rpm for 60 sec with 2000 rpm/sec ramp rate. Resist thickness was estimated using surface profilometer to be 1 μm. Immediately after spin coating, samples were placed on a 115 °C hotplate for 1 min to evaporate excess solvent.

SUSS MJB4 mask aligner with 365 nm UV source was then used to align the samples prior to exposure. The negative image of the electrode pattern was exposed through a chrome mask on soda-lime glass. First exposure of 10 mJ/cm^2 was used to activate the photo-initiator which causes crosslinking within exposed regions after 2 min post exposure (reversal) bake. Finally, 250 mJ/cm^2 flood exposure was applied to make uncrosslinked regions soluble in developer. 25 sec of development was conducted in AZ 726 MIF followed by water rinse to stop the development. Samples were then immediately loaded into the Lesker thermal evaporator and 100 nm aluminium was evaporated at 10^{-6} mbar vacuum using tungsten boats. The lift-off process was carried out in a manner similar to that described in previous section. The metal electrodes thus fabricated using aligned photolithography are shown in Fig. 6.10c.

6.5 ZnO micro-FETs from zinc neodecanoate

Although TGA analysis of zinc neodecanoate suggests complete decomposition of organic species at $\sim$ 350 °C, after electron-beam-induced crosslinking it was necessary to investigate the quality of converted zinc oxide. After spin-coating zinc neodecanoate on Si-SiO_2 substrates, an area of 4.8 mm x 4.8 mm was exposed with an electron beam. A 100 nA beam current and 1200 μm x 1200 μm exposure field was used with 60 nm step size to expose to 5 mC/cm^2 dose. Samples were then developed in toluene for 30 sec and annealed for 1 hr at 500 °C. Photoluminiscence spectroscopy was then employed using 266 nm laser excitation to investigate the quality of ZnO formed.

Acquired PL spectra is presented in Fig. 6.11. A sharp near band edge (NBE) peak clearly seen at $\sim$375 nm wavelength, in agreement with previous reports [191, 192]. Interestingly, the ratio of NBE emission to deep level emission is significantly improved as compared with ZnO films prepared without e-beam irradiation (Fig. 4.8). Such reduction in the defects suggests higher quality of ZnO formation after e-beam irradiation and can be

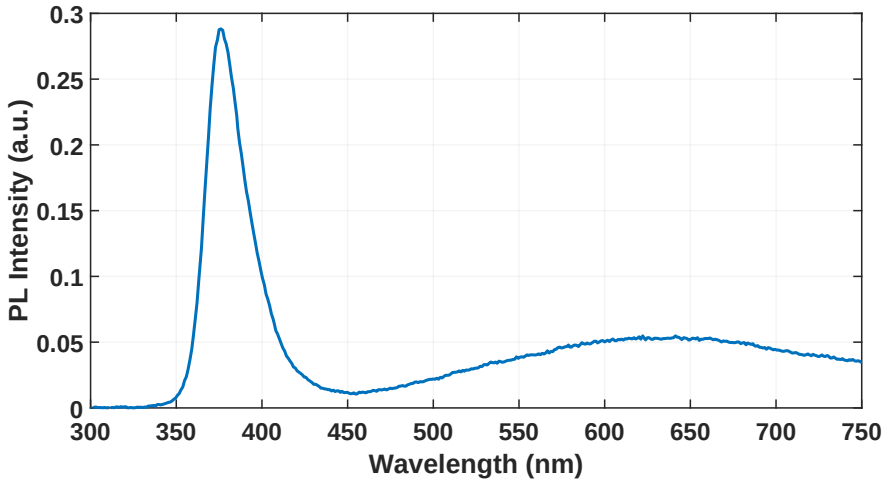

Fig. 6.11 Photoluminiscence spectra of zinc oxide films prepared from EBL-patterned 15 % zinc neodecanoate and annealed at 500 °C for 1 hr.

correlated with densification of the precursor layer during crosslinking which is similar to the photo-induced densification in zinc methacrylate under DUV irradiation [224].

Three concentrations of zinc neodecanoate were spin-coated on substrates with pre-fabricated alignment markers. Details of zinc neodecanoate dilution are presented previously in Table 4.1. In order to fabricate micro-FETs 50 μm x 50 μm regions were exposed with 20 nA beam current and 1200 μm x 1200 μm field size. An areal dose of 7.5 mC/cm^2 was used for the exposure. After 30 sec development in toluene and 1 hr annealing at 500 °C, source-drain electrodes were patterned with channel length of 5 μm.

AFM analysis was carried out to elucidate the surface morphology of the ZnO synthesised from difference precursor concentrations. Fig. 6.12 depicts the topography and phase images acquired by AFM measurements. At 5 % concentration, small ZnO grains can be seen. The film prepared from 15 % concentration shows an increase in grain size. From the AFM scans, values of ZnO thickness and RMS grain size were estimated and presented in Fig. 6.13. As expected, the thickness of ZnO patterns increases linearly with precursor concentration. However, the grain size seem to saturate at ∼24 nm for 15 % and 25 % concentrations, after initial increase from ∼20.4 nm for 5 % concentration.

Fig. 6.14 shows FET transfer curves acquired from three concentrations in linear regime with 1 V source-drain voltage. Devices fabricated from 5 % concentration showed hysteresis pointing to the presence of considerable deep-level defects. For both 15 % and 25 % concentrations a small amount of hysteresis was observed. 25 % concentration devices showed slightly lower ON current while the OFF current was increased by a small amount.

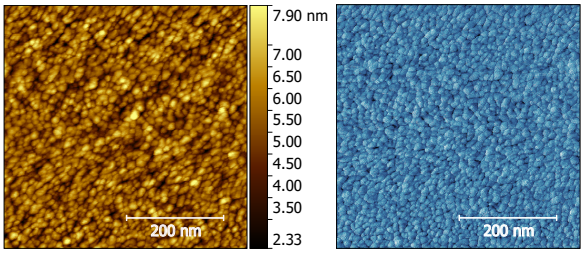

(a) Concentration 5 % R_{rms}= 0.89 nm

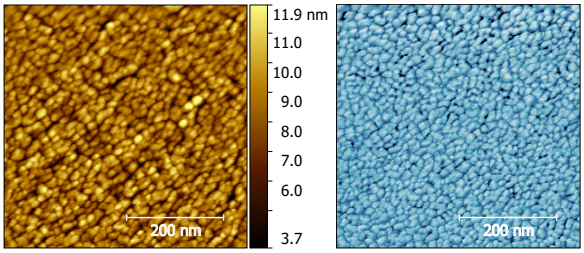

(b) Concentration 15 % R_{rms} =1.31 nm

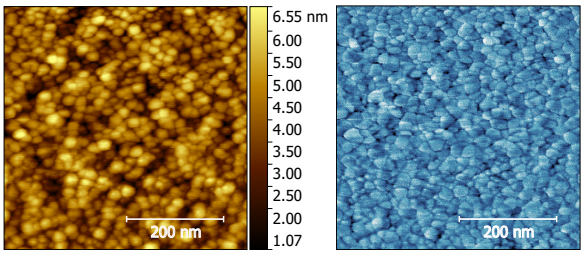

(c) Concentration 25 % R_{rms} = 0.77 nm

Fig. 6.12 Atomic Force Microscopy images showing Topography (left) and Phase (right) over 500 nm x 500 nm area of EBL-patterned 50 μm x 50 μm ZnO films prepared from different zinc neodecanoate concentrations and annealed at 500 °C for 1 hr.

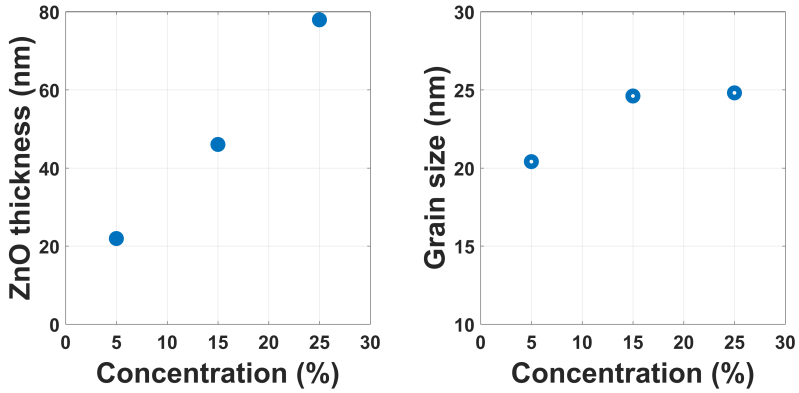

(a) (b)

Fig. 6.13 ZnO thickness (a) and grain size (b) estimated from AFM scans for micro-patterns written on different concentrations of zinc neodecanoate.

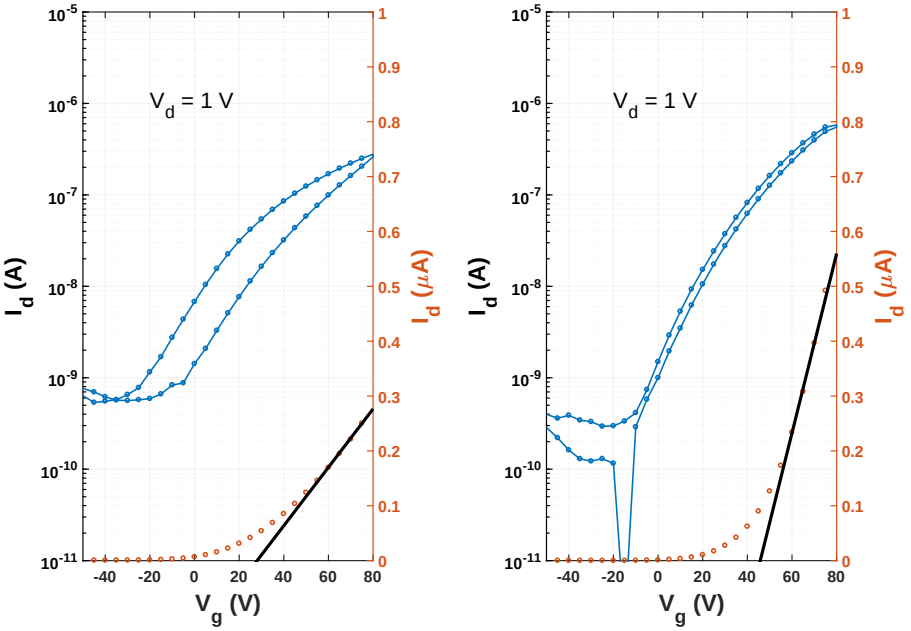

(a) Concentration 5 % **(b) Concentration 15 %**

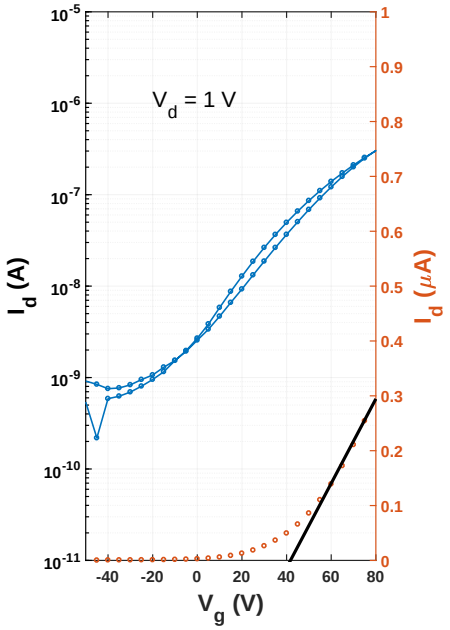

(c) Concentration 25 %

Fig. 6.14 Transfer Curves of ZnO FETs fabricated using different precursor concentrations of zinc neodecanoate with V_D = 1 V.

The output curves for 15 % and 25 % concentration devices can be seen in Fig. 6.15. While ohmic linear I-V characteristics can be seen at lower drain voltages, small deviation towards non-linearity is noticed at higher drain voltage.

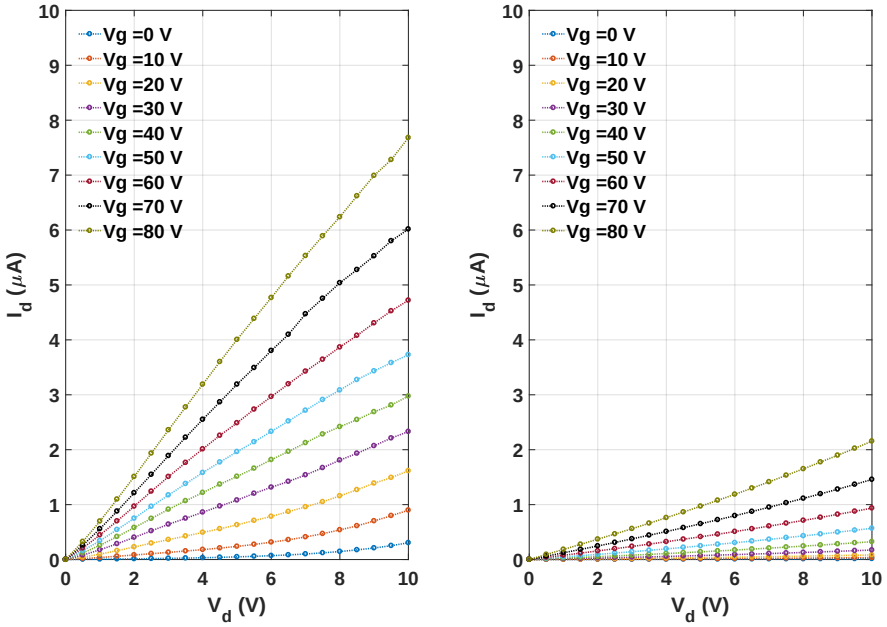

(a) Concentration 15 % **(b) Concentration 25 %**

Fig. 6.15 Output Curves of ZnO FETs fabricated using different precursor concentrations of zinc neodecanoate.

Linear mobility of the FET devices was calculated using equation

$$\mu_{lin} = \frac{L}{V_D W C_0} \left(\frac{\partial I_D}{\partial V_G} \right)$$

where L and W represents channel length and width respectively, C_0 is oxide capacitance per unit area and V_D is drain-source voltage. Gradient of I_D was calculated at each gate voltage (V_G) to estimate linear mobility (μ_{lin}) as a function of V_G. The maximum value of the μ_{lin} was used as a parameter of comparison. A straight-line fit was made where gradient of I_D is maximum and x-intercept was used to estimate the value of threshold voltage V_{th} . All the remaining transistor parameters were calculated in a similar way, as explained in section 4.4.1. Electrical characterisation of number of devices was carried out and calculated average values of transistor performance parameters which are summarised in Fig. 6.16.

The devices prepared with 15 % zinc neodecanoate concentration showed highest value of average linear mobility. The mobility value of 1.67 x 10^{-2} cm^2/V.s increased to 4.86

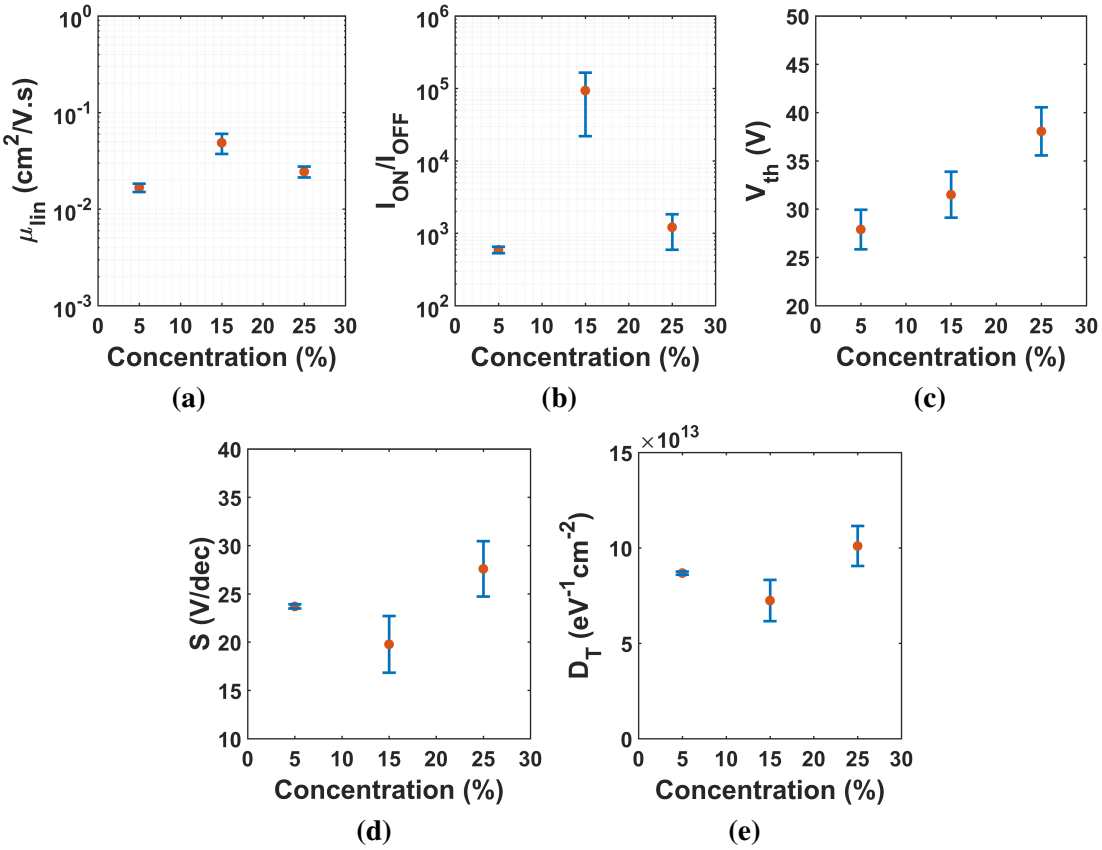

Fig. 6.16 Transistor parameters calculated for ZnO FETs from different concentrations of zinc neodecanoate.

x 10^{-2} cm^2/V.s when precursor concentration was increased from 5 % to 15 %. It can be seen from AFM analysis (shown in Fig. 6.13) that estimated ZnO thickness increased from 21.9 nm to 46 nm with small increase in grain size from 20.4 nm to 24.6 nm. This indicates to increased percolation pathways leading to higher mobility. Interestingly, the mobility variation with precursor concentration was less prominent than in the case of TFT devices discussed earlier in chapter 4. The densification of the precursor due to e-beam irradiation is most probably the cause of good transistor performance even in a 5 % precursor concentration device [224].

When the precursor concentration was increased from 15 % to 25 % a small decrease in mobility to 2.44 x 10^{-2} cm^2/V.s was observed. As presented in Fig. 6.13, the ZnO film thickness was increased from ∼46 nm to ∼77.9 nm while the grain size remained almost the same. Increased OFF current due to increased bulk conductivity as seen in Fig. 6.14c and increase in the interracial traps as seen from Fig. 6.16e combined may have been the cause of a small drop in the mobility. Our observation indicates that the best transistor

performance with mobility 4.86 x 10^{-2} cm^2/V.s, sub-threshold slope of $\sim$ 19.77 V/dec and traps concentration per unit energy of 7.24 x 10^{13} $eV^{-1}cm^{-2}$ were attained at 15 % concentrations.

6.6 ZnO micro-FETs from zinc naphthenate

Thermogravimetric analysis (TGA) was carried out on zinc naphthenate precursor to ascertain required annealing temperature. Fig. 6.17 displays percentage weight loss with temperature acquired during TGA run. A slow mass loss rate between ~175 °C and ~375 °C becomes steeper after ~400 °C. A peak in rate of mass loss at ~425 - 450 °C signifies decomposition of naphthenate molecules and formation of ZnO phase. Beyond ~450 °C a negligible mass loss can be observed, which can be attributed to completion of precursor conversion process.

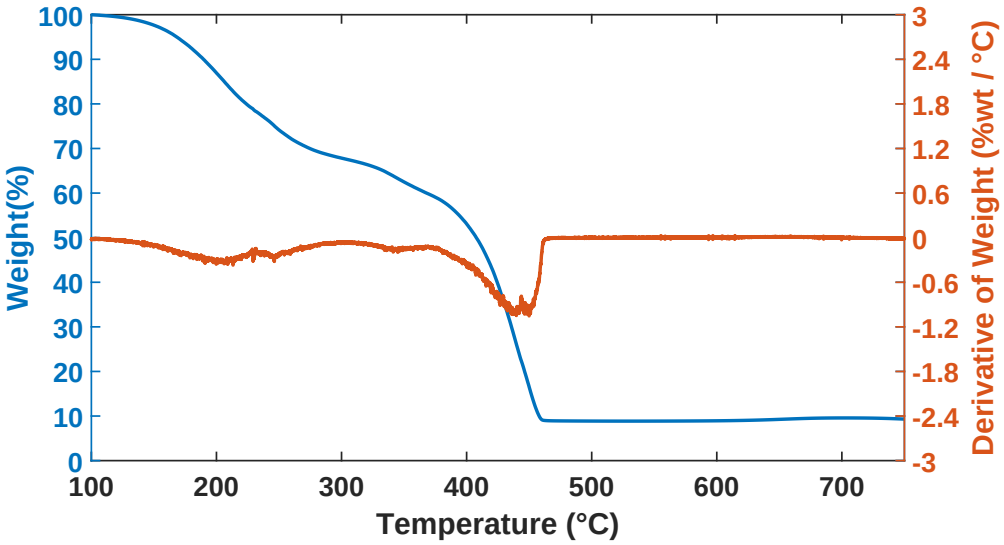

Fig. 6.17 Thermogravimetric analysis (TGA) of zinc naphthenate with percent weight loss (left axis) and rate of weight loss (right axis) performed in nitrogen flow of 20 ml/min with 10 °C/min starting with 43.15 mg. The material was held at 100 °C for 30 min prior to the final ramp up.

In order to ascertain the formation of crystalline ZnO, X-ray diffraction (XRD) measurements were carried out on ZnO film prepared by drop casting. A 25 % zinc naphthenate solution was drop cast on a cleaned Si-SiO_2 substrate and left overnight to evaporate the solvent. The substrate was then calcined at 500 °C for 1 hr and the resulting film was characterised using XRD (shown in Fig. 6.18). The peaks at 2θ angles of 32 °, 34.5 ° and 36.5

° correspond to (100), (002) and (101) crystal orientation of ZnO respectively, confirming the formation of polycrystalline zincite/wurtzite ZnO [180, 181]. The peak at 33 ° probably corresponds to contamination peak [182].

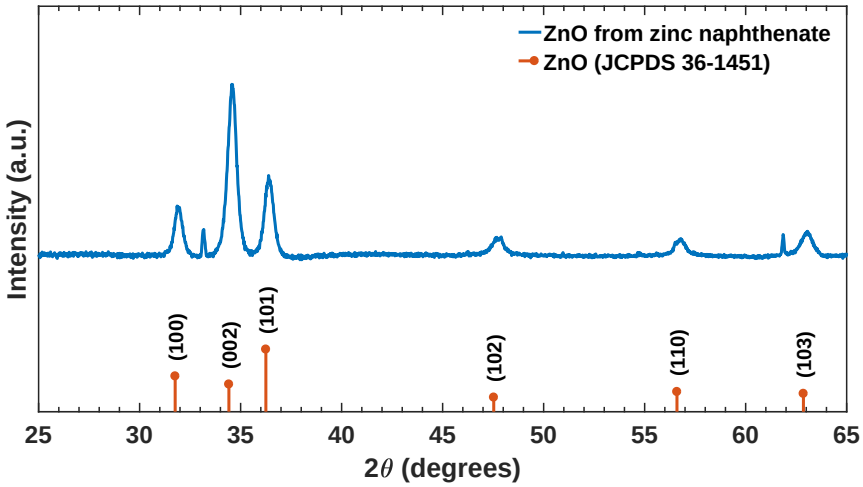

Fig. 6.18 X-ray diffraction measurements of ZnO films prepared by drop casting 25 % zinc naphthenate and annealed at 500 °C showing polycrystalline nature of the films. The peaks identified with polycrystalline wurtzite/zincite ZnO JCPDS card No. 36-1451 [180, 181], while the peak at 33 ° is probably a contamination peak [182].

Similar to zinc neodecanoate, PL spectroscopy was also conducted on 4.8mm x 4.8mm ZnO film prepared from zinc naphthenate to elucidate quality of ZnO formed. 100 nA e-beam current was used to expose 4x4 array of 1200 μm square exposure field patterned with 60 nm step size and exposure dose of 15 mC/cm^2. After 30 sec development in toluene substrate was annealed at 500 °C for 1 hr. As presented in Fig. 6.19, a ∼380 nm NBE peak due to free exciton recombination process is clearly visible. While NBE emission to defect emission ratio is smaller than in the case of zinc neodecanoate, the PL spectra still establishes good quality ZnO phase. A possible decrement in NBE emission than in the case of zinc neodecanoate can arise due to smaller zinc metal content in the naphthenate precursor. Nonetheless, on this evidence, annealing temperature of 500 °C was regarded as sufficient for further electrical characterisation.

In order to further explore optimal concentration of zinc naphthenate three precursor dilutions were prepared using quantities mentioned in Table 6.1. Due to the viscous nature of zinc naphthenate, the appropriate quantity was measured by weight instead of volume using zinc naphthenate density of 1.01 gm/cc. Each of the precursor concentrations was used to fabricate micro-FETs of W/L = 50 μm / 5 μm. 20 nA beam current and 1200 μm square field size with 60 nm beam step was used once again; however, 25 mC/cm^2 exposure

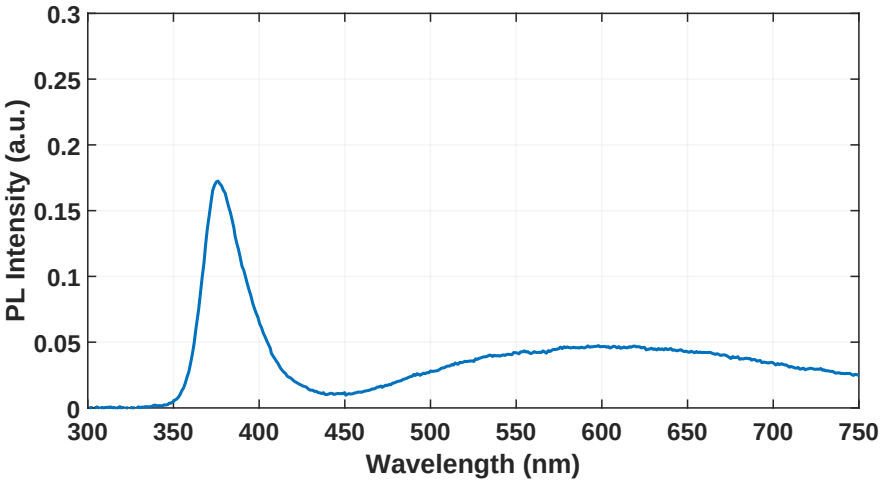

Fig. 6.19 Photoluminiscence Spectra of zinc oxide films prepared from EBL-patterned 25 % zinc naphthenate and annealed at 500 °C.

dose was used. The rest of the fabrication was carried out similarly to that described for zinc neodecanoate.

Table 6.1 Dilution of zinc naphthenate

Concentration	Toluene (ml)	Zinc Naphthenate (ml)	Zinc Naphthenate (gm)
5 %	15	0.75	0.76
15 %	15	2.25	2.27
25 %	15	3.75	3.79

Atomic force microscopy images of ZnO micro patterns obtained from different concentrations of zinc naphthenate are shown in Fig. 6.20. The RMS roughness values monotonously increase from 0.71 nm for 5 % concentration to 0.87 nm for 15 % concentration and finally to 0.92 nm for 25 % concentration. The corresponding increase in the grain size can also be clearly seen from the phase images.

Fig. 6.21 shows ZnO thickness and RMS grain size values estimated from AFM scans. A linear increase with precursor concentration can be seen in both thickness and grain size. Grain size of 16.8 nm for 11.2 nm thick ZnO prepared from 5 % zinc naphthenate points to insufficient percolation network available for carrier transport. The grain size and thickness increased to 18.6 nm and 27.3 nm, respectively, with the use of 15 % concentration, further increasing to 20.2 nm and 45.0 nm, respectively, for 25 % concentration.

FET characterisation was carried out for devices prepared from all three concentrations by applying 1 V source to drain voltage and sweeping gate voltage from -50 to 80 V. In

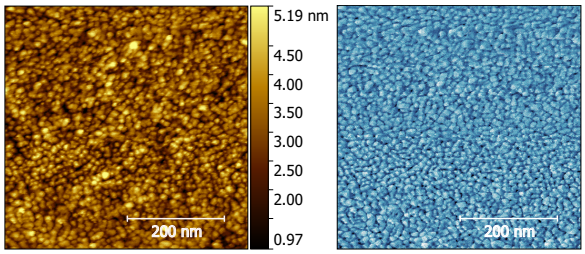

(a) Concentration 5 % R_{rms} = 0.71 nm

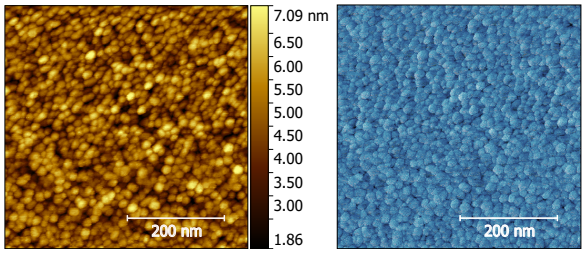

(b) Concentration 15 % R_{rms} = 0.87 nm

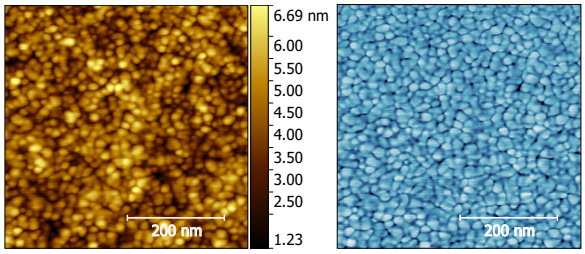

(c) Concentration 25 % R_{rms} = 0.92 nm

Fig. 6.20 Atomic Force Microscopy images showing Topography (left) and Phase (right) over 500 nm x 500 nm area of EBL patterned 50 μm x 50 μm ZnO films prepared from different zinc naphthenate concentrations and annealed at 500 °C.

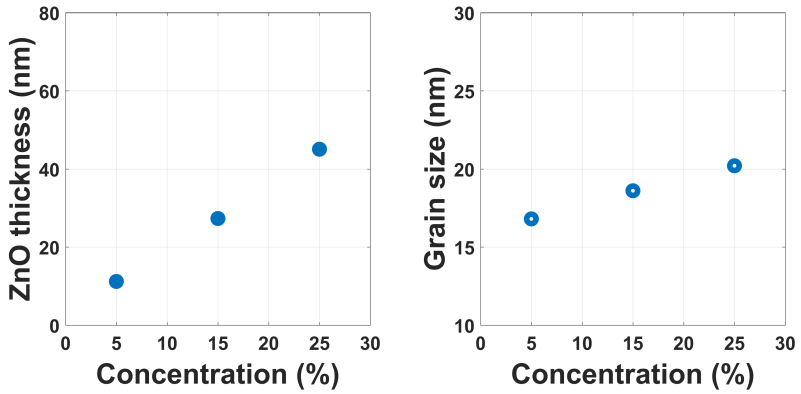

(a) **(b)**

Fig. 6.21 ZnO thickness (a) and grain size (b) for micro-patterns written on different concentrations of zinc naphthenate estimated from AFM scans.

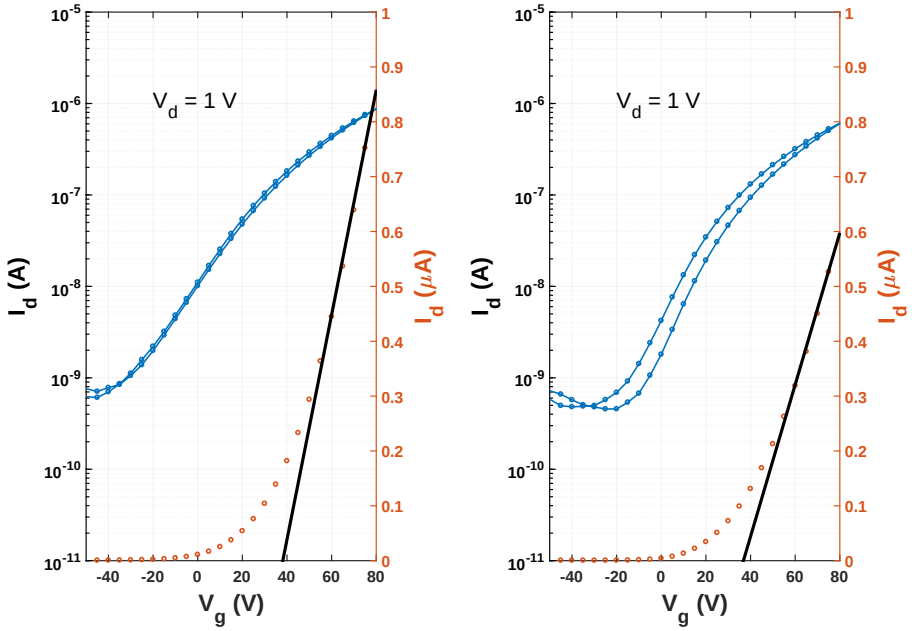

(a) Concentration 15 % **(b) Concentration 25 %**

Fig. 6.22 Transfer Curves of ZnO FETs fabricated using different precursor concentrations of zinc naphthenate.

contrast to zinc neodecanoate, no working transistor device could be found with 5 % zinc naphthenate precursor. Formation of ultra-thin ZnO layer at this concentration may have given rise to insufficient percolation in the channel region, which could be the cause behind non-functioning devices.

Fig. 6.22 shows the transfer characteristics of the devices prepared with 15 % and 25 % zinc naphthenate concentrations. Increase in the ON current with suppressed hysteresis indicates to increase in conduction pathways with channel thickness. A similar trend can also be seen in output curves depicted in Fig. 6.23, where a 25 % concentration precursor gives rise to a slightly higher drain current at given gate voltage. Linearity of I-V characteristics also suggests good quality ohmic contacts between ZnO and Al.

After electrical characterisation of a number of devices prepared from 15 % and 25 % zinc naphthenate concentrations, transistor parameters were extracted as explained for zinc neodecanote devices and presented in Fig. 6.24. Devices from both the concentrations showed I_{ON}/I_{OFF} ratio of $\sim 10^3$. The average linear mobility increased from 4.67 x 10^{-2} cm^2/V.s to 6.18 x 10^{-2} cm^2/V.s as precursor concentration was increased from 15 % to 25 %. This mobility increase can be explained by increased grain size providing increased percolation pathways and decreased grain boundary region decreasing carrier scattering.

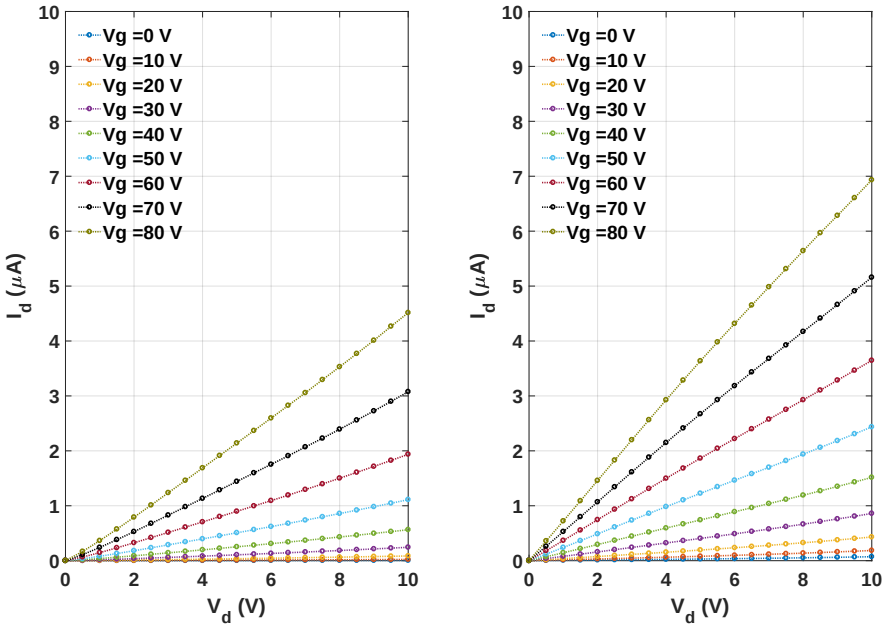

(a) Concentration 15 % **(b) Concentration 25 %**

Fig. 6.23 Output Curves of ZnO FETs fabricated using different precursor concentrations of zinc naphthenate.

On the other hand, the threshold voltage decreased from 39.6 V to 38.1 V, which may be attributed to higher bulk charge carrier concentration, and thus lesser gate voltage was required for turning the transistor ON[229].

6.7 Effect of Post-decomposition Annealing

In order to further improve the performance of the devices, post-decomposition annealing studies were conducted with ZnO micro-patterns prepared from 15 % zinc neodecanoate. Devices with W/L = 40 μm / 5 μm were fabricated. After precursor spin coating, all the substrates were subjected to an areal dose of 10 mC/cm^2 using a 20 nA e-beam current and 1200 μm x 1200 μm field size. Development was carried out in toluene for 30 sec and crosslinked zinc neodecanoate was decomposed with usual thermal treatment of 500 °C for 1 hr. After decomposition, one sample was post-annealed at 500 °C for 1 hr under 100 sccm Ar flow. Another sample was post-annealed at 500 °C for 1 hr under 10 sccm flow of 5 % H_2 in N_2 (forming gas).

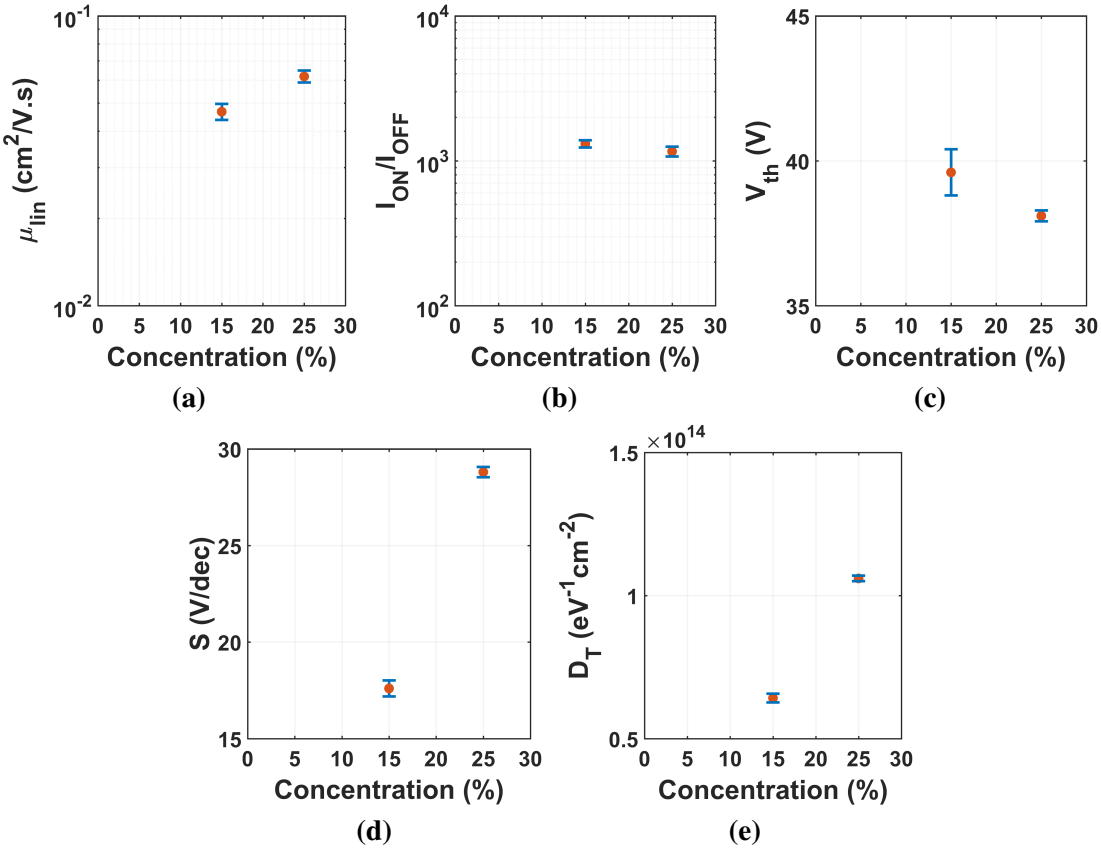

Fig. 6.24 Transistor parameters calculated for ZnO FETs from different concentrations of zinc naphthenate.

Deposition of 100 nm Al source-drain electrodes was then carried out with a photolithography process described earlier, on both of the post-annealed samples along with another sample without any post-treatment. Immediately before Al deposition, 15 sec Ar plasma treatment was carried out at 10 mbar pressure and 100 W power in an Oxford ICP-RIE system. Such surface treatment has been previously used by Kälblein *et al.* [230]. The purpose in using such a plasma treatment was twofold. Firstly, this treatment removes any possible resist residue left after the development (descum). Secondly, it renders the surface of ZnO slightly oxygen-deficient, and thus more conductive [231]. These increased oxygen vacancies at the surface increase surface-carrier concentration and improve charge injection from metal to ZnO [228]. Additionally, an oxygen-deficient ZnO surface decreases the possibility of Al_2O_3 barrier layer formation, which can compromise the stability of the device.

Electrical characterisation of all the samples was carried out and representative transfer curves are shown in Fig. 6.25. All the devices showed a current modulation I_{ON}/I_{OFF} ratio of $\sim 10^5$. The subthreshold slope was also found to be $\sim$2 V/dec, suggesting the different

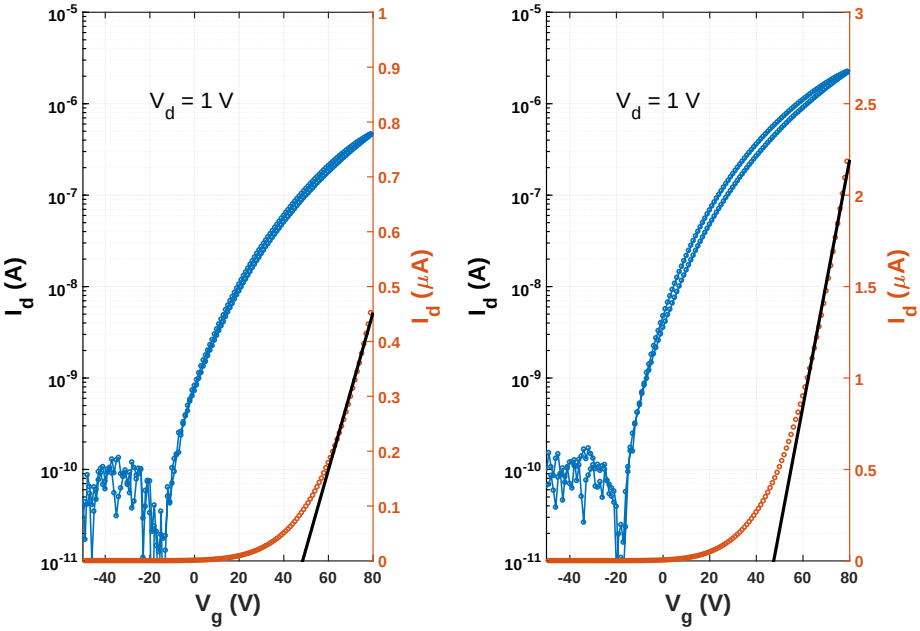

(a) As decomposed **(b) 1 hr in Ar**

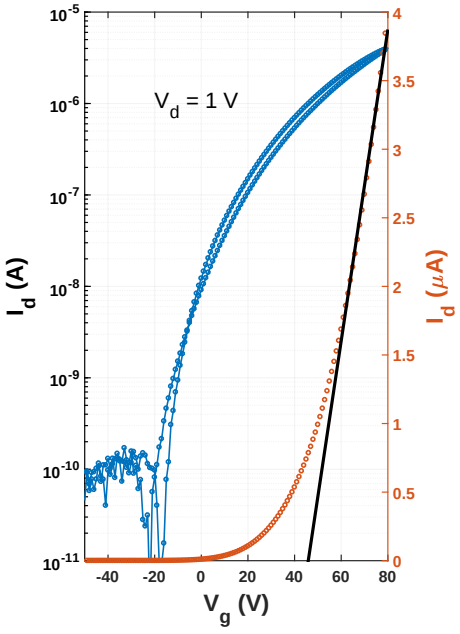

(c) 1 hr in forming gas (5 % H_2 in N_2)

Fig. 6.25 Transfer Curves of ZnO FETs after different post-decomposition annealing.

annealing conditions probably did not have any significant effect on the semiconductor-dielectric interface.

The device without any post-annealing treatment (Fig. 6.25a) showed slightly higher mobility of 0.068 cm^2/V.s, as compared with the devices presented earlier in section 6.5. This may be attributed to improved charge injection due to Ar plasma treatment prior to Al deposition. The device annealed in Ar (Fig. 6.25b) displayed increased drain current with linear mobility reaching 0.33 cm^2/V.s. This performance improvement may have been caused by generation of oxygen vacancies, which are considered to be shallow donors in ZnO.

The device annealed in forming gas (Fig. 6.25c) demonstrated further increment in drain current with linear mobility rising to 0.53 cm^2/V.s. The forming gas annealing is often used to passivate electronically active traps arising due to dangling bonds [232]. Additionally, it can act as source of hydrogen interstitials in ZnO crystal which are also considered shallow n-type dopants [233]. Similar mobility improvement in ZnO FETs, as a consequence of forming gas annealing, is also reported by Nam *et al.* [234]. The increased mobility achieved in forming gas-annealed devices is in close agreement with previous reports of ZnO FETs [225, 218].

Similar improvement is also observed in the threshold voltage of the ZnO devices. Upon post-decomposition annelaing treatement the threshold voltage decreased from 48.4 V to 47.4 V for an Ar annealed device, further dropping to 45.8 V with a forming gas annealed device. Such negative shift in threshold voltage means lower gate voltage was required to create charge depletion at the dielectric-semiconductor interface, which once again points to higher charge carrier concentration in ZnO channel [229]. It should be noted that the devices still show very high values of threshold voltage. Due to the linear operation regimes of the devices, a straight line fit to I_D curve was made to estimate threshold voltage. However, due to the presence of inter-band traps states the transistors do not show a sharp tuning on and I_D vs $V_(G)$ curve is non-linear. As a result, extracting $V_(th)$ using straight line fit, may have incurred errors in the estimation.

6.8 Scaling down ZnO FETs to nanoscale

After optimising the micro-FETs, direct-write EBL was further used to scale down the width of ZnO channel to 100 nm. In order to study the evolution of device performance with decreasing width, devices were fabricated with both the precursors 15 % zinc neodecanoate and 25 % zinc naphthenate. The precursor patterning was carried out in two steps. Firstly,

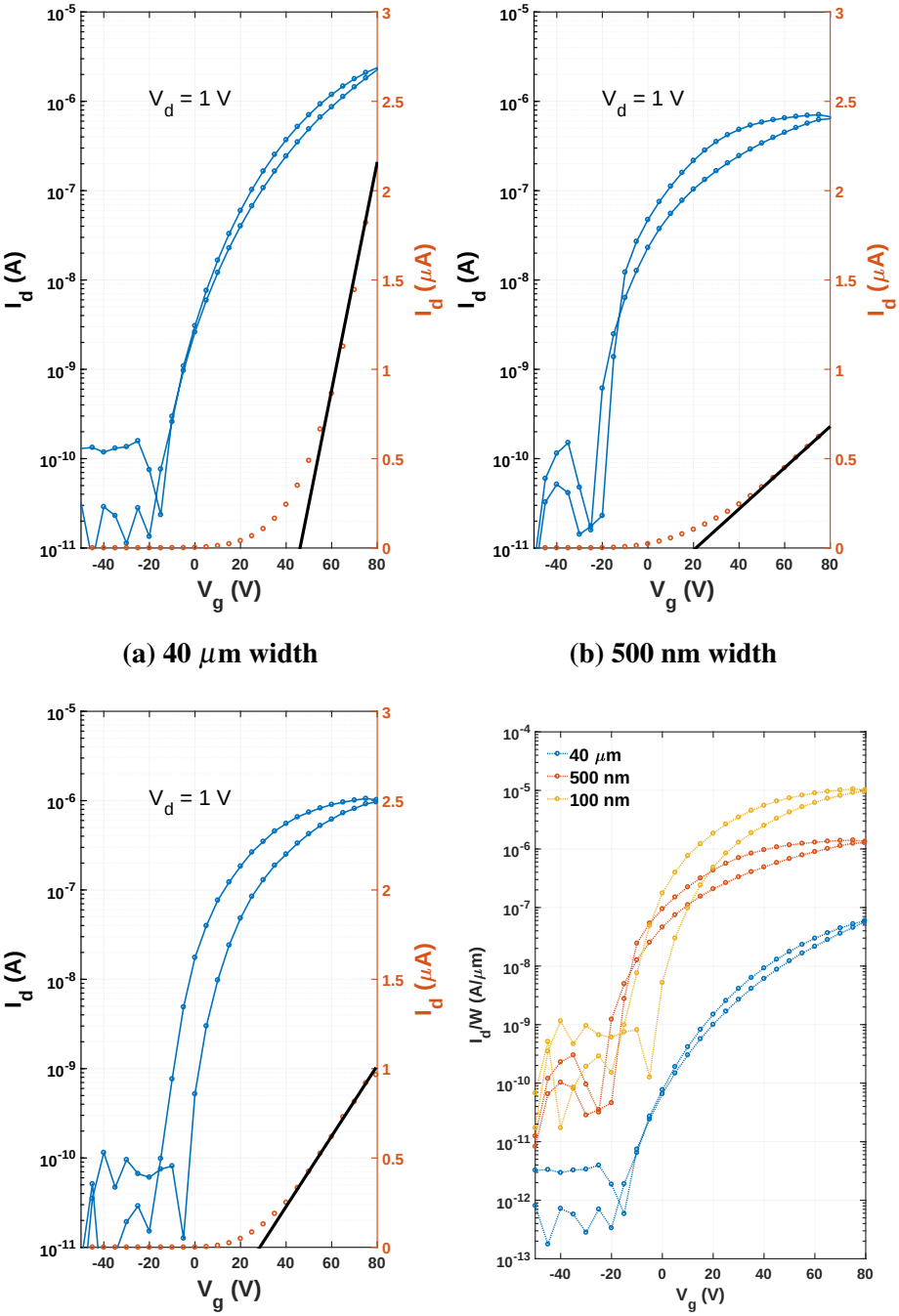

(a) 40 μm width **(b) 500 nm width**

(c) 100 nm width **(d) Width normalised**

Fig. 6.26 Width variation of ZnO FETs prepared from zinc neodecanoate.

micro-scale patterns, for both micro-devices as well as charge injection pads for nano-devices, were patterned using a 20 nA current and 1200 μm x 1200 μm field with 60 nm steps. The samples with zinc neodecanoate were subjected to an areal dose of 10 mC/cm^2 while zinc naphthenate samples were exposed with a 15 mC/cm^2 dose.

During the second step nano-scale pattern structures were exposed with a 1 nA current in order to get smaller beam diameter. A field size of 600 μm x 600 μm was used for exposure with 10 nm step size. The corresponding nano-channel regions were exposed to a 100 mC/cm^2 dose for both the precursors. The same set of pre-fabricated markers was exploited to ensure patterns from both EBL steps were aligned to each other. The samples were then subjected to earlier optimized annealing conditions with forming gas post-decomposition step and source-drain electrode deposition was carried out to achieve a 5 μm channel length.

The transfer characteristics of devices fabricated using zinc neodecanoate precursor at V_D = 1 V are depicted in Fig. 6.26. All the devices displayed $I_{ON}/I_{OFF} > 10^5$ with the 40 μm device exhibited linear mobility of 0.32 cm^2/V.s. On decreasing the device width to 500 nm the linear mobility increased by an order of magnitude reaching 3.6 cm^2/V.s. Furthermore, in the case of the 100 nm width device, another order of magnitude increment was observed in linear mobility with magnitude going up to a value of 33.7 cm^2/V.s. Additionally, the sub-threshold slope also demonstrated slight improvement, decreasing from 6.16 V/dec for 40 μm width to 5.31 V/dec for the 100 nm width device.

On the other hand, it should be noted that the hysteresis exhibited by the 40 μm device increased as device width was scaled down. As established during our initial experiments, this hysteresis may be attributed to oxygen adsorption on the ZnO surface caused by trapping charge carriers at the surface states. As the width of the device is decreased, the surface area-to-volume ratio increases, leading to greater oxygen adsorption. In order to illustrate increase in the current density with decreasing channel width, drain current was normalised by channel width. The plot of normalised drain current against gate voltage is presented in Fig. 6.26d. It can be seen that current density has increased in both ON and OFF states, with decreasing channel width.

A similar trend of mobility increment with scaling down of channel width was seen in devices prepared from zinc naphthenate. Transfer curves for these devices at V_D = 1 V are shown in Fig. 6.27. While $I_{ON}/I_{OFF} > 10^4$ was seen, a slight increase from 3.13 x 10^4 for 50 μm width devices to 5.16 x 10^4 for 500 nm and 7.24 x 10^4 for 100 nm device was observed. The estimated linear mobility of 0.1 cm^2/V.s increased to 3.23 cm^2/V.s with the device of 500 nm width. Furthermore, the device of 100 nm width demonstrated mobility of 21.38 cm^2/V.s. Width normalised I_D-V_G characteristics of these devices are also plotted in Fig.

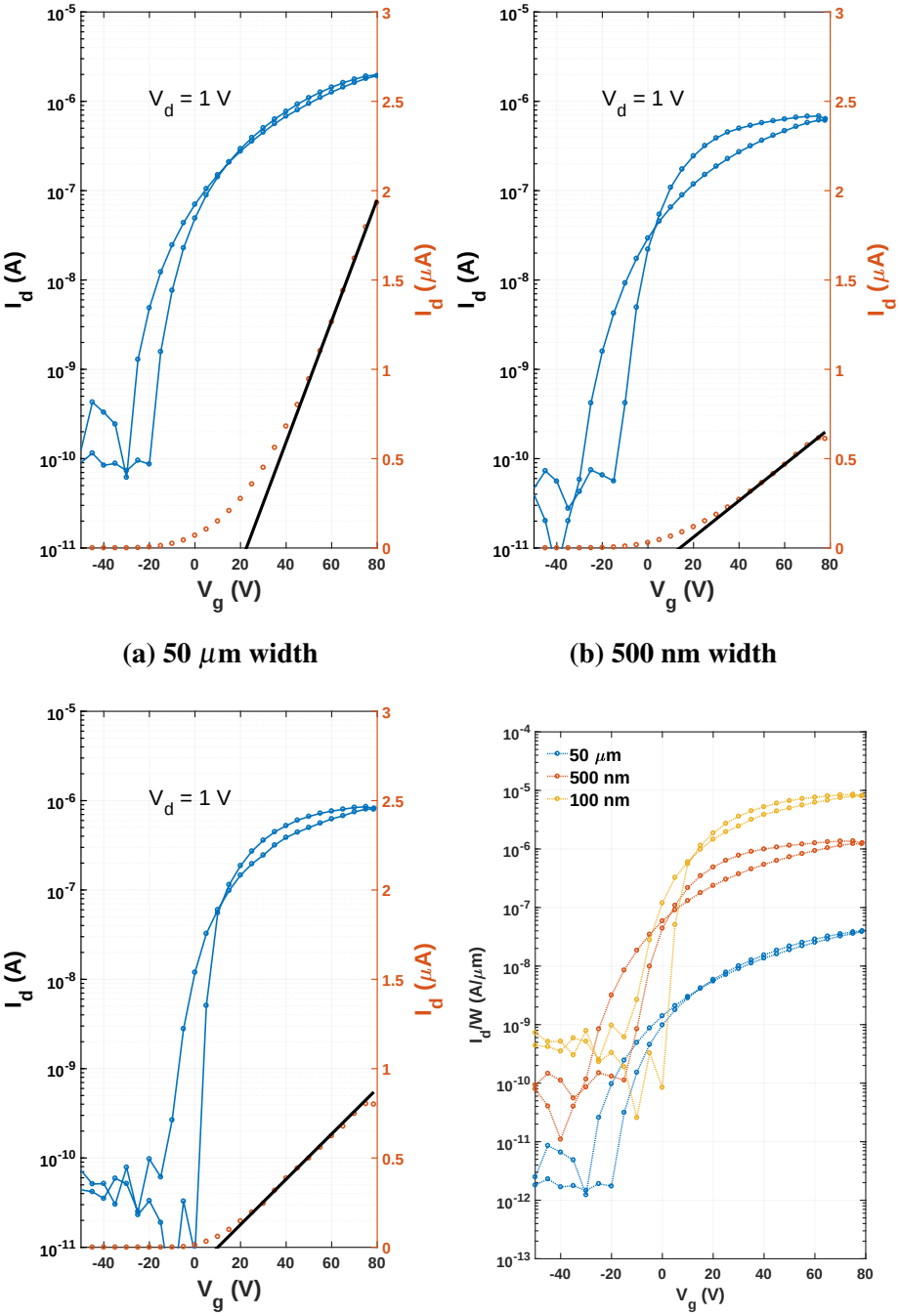

(a) 50 μm width **(b) 500 nm width**

(c) 100 nm width **(d) Width normalised**

Fig. 6.27 Width variation of ZnO FETs prepared from zinc naphthenate.

6.27d, clearly depicting higher current density as width of the ZnO channel was decreased from 50 μm to 500 nm and 100 nm.

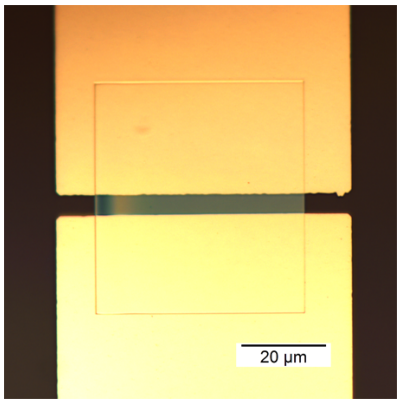

(a) 50 μm width device

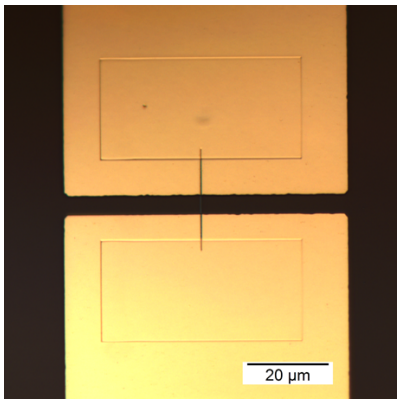

(b) 100 nm width device

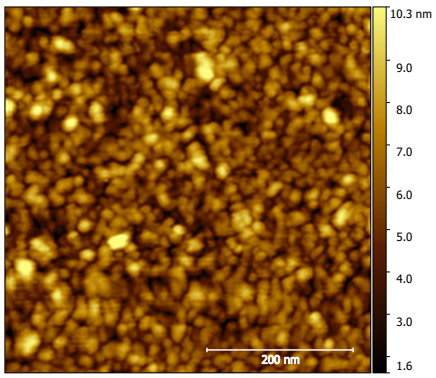

(c) 50 μm width AFM

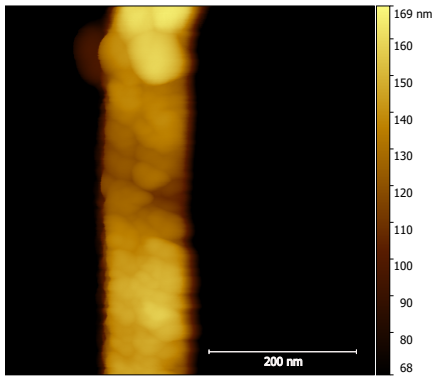

(d) 100 nm width AFM

Fig. 6.28 Optical microscope images (a), (b) and AFM topography images comparing grain structure (c), (d) for 50 μm width and 100 nm width ZnO patterns respectively, fabricated from 15 % zinc neodecanoate and annealed at 500 °C.

In order to investigate the cause of increased mobility with the scaling down of channel width, AFM analysis was conducted on 50 μm and 100 nm width ZnO devices prepared from 15 % concentration of zinc neodecanoate. AFM topography images of the two scans are presented in Fig. 6.28, where distinctively different grain structures can be observed. The 50 μm patterned ZnO showed much smaller grain size, that may be limiting percolating-conduction pathways. On the other hand, ZnO grains of 100 nm width are not only bigger but also much more tightly packed. Due to such closely packed grains, the grain boundary region, and thus grain-boundary scattering could be greatly suppressed in 100 nm patterns, leading to higher electron mobility.

Although the exact mechanism behind the grain evolution is not known, the difference in grain structure may be attributed to a number of factors. Firstly, higher surface-area-

to-volume ratio in nano-patterns would have assisted in more efficient removal of organic components of the precursor during decomposition. Secondly, unidirectional strain within the nano-pattern may have provided additional driving force for the grain coalescence. Moreover, slow ramp up and ramp down of the furnace during the annealing phase provided sufficient time for lattice rearrangement and grain boundary diffusion, leading to densely packed bigger grains [235].

The impeccable increase in the current density of the ZnO patterns as a consequence of decreasing the pattern widths from 50 μm to 100 nm is seen in width-normalised I_D-V_G plots, while using both zinc neodecanoate (Fig. 6.26d) and zinc naphthenate (Fig. 6.27d) as direct-write precursors. These measurements are also in good agreement with AFM images (Fig. 6.28) showing increased grain size and improved grain packing. However, it should be noted that the gradual-channel approximation for thin film transistor was used throughout to estimate and compare the field effect mobility values. Inherently, the edge effects due to fringing fields are neglected during this mobility calculation, which may lead to slight overestimation. In order to, accurately estimate the mobility of narrow-width devices and thus, to elucidate impact of narrow widths, further studies are needed to be carried out.

6.9 Concluding remarks

Direct-write electron beam lithography of zinc naphthenate and zinc neodecanoate has been implemented for fabrication of ZnO-FETs. During the initial experiments, it was established that oxygen and/or water adsorption is a major source of traps in ZnO FETs, giving rise to substantial hysteresis at slower scan speeds. It was also concluded that contact resistance between ZnO and source-drain metal is a significant mobility-limiting factor with Al contacts exhibiting the best device performance.

After trying different precursor concentrations for fabricating micro-FETs, it was found that devices fabricated with 15 % zinc neodecanoate and 25 % zinc naphthenate exhibit the best device performance, with a linear mobility of $\sim$0.05 cm^2/V.s for ZnO films of $\sim$50 nm thickness. Given a sharp NBE peak and low defect emission during PL measurements, 500 °C annealing temperature was considered optimal for device processing. Additionally, post-decomposition annealing was implemented to passivate traps within ZnO structure. In the case of post-decomposition annealing carried out in forming-gas atmosphere, hydrogen interstitials may get incorporated and act as shallow donors. Linear mobility as high as $\sim$0.5 cm^2/V.s was achieved in micro-FETs fabricated from 15 % zinc neodecanoate after post-decomposition annealing in the forming gas.

Size-dependant improvement in mobility was also reported as a result of decreasing patterned precursor width from 50 μm to 100 nm. Almost two orders of magnitude mobility enhancement was observed. AFM analysis revealed increase in the grain size as well as close packing in nanoscale ZnO as compared with micron sized patterns. Linear mobility as high as $\sim$33.7 cm^2/V.s was attained, which is one of the best reported values for direct-write patterned solution processed ZnO transistors.

Chapter 7

Polycrystalline ZnO nanowires for gas sensing application

7.1 Introduction

One of the widespread application areas for ZnO and its nanostructures lies in the domain of gas sensors. The two most common directions of research in the field have been the use of either single-crystal nanowires or polycrystalline thin films. The higher surface-to-volume ratio seen in single crystalline nanowire-based sensors leads to improved sensing response, due to increased surface depletion modulation. On the other hand, polycrystalline morphology consists of grain boundary regions, that are highly reactive. The change in surface depletion near the grain boundary regions can have a greater effect on sensor resistance. One of the motivations of this project is to combine these two aspects by implementing polycrystalline nanowire sensors. The direct-write top-down synthesis route creates polycrystalline ZnO nanowires and helps in achieving this goal. In the previous chapter optimisation of direct write patterned micro as well as nano FETs has been discussed in detail. The present chapter focuses on investigating their gas-sensing properties.

An overview of the detection mechanism in metal oxide gas sensors is presented in Chapter 2. The current chapter begins with discussion of the design of the in-house vapour-sensing measurement setup. The setup was then used to test the sensing response of direct-write patterned micro/nano ZnO devices to various solvent vapours. In a separate experiment a nano-patterned device is analysed for low concentration NO_2 detection. Finally, ongoing work related to silane functionalisation of ZnO gas sensors is briefly outlined.

7.2 Design of a gas-sensor characterisation system

7.2.1 Physical design of the setup

In order to properly analyse the gas-sensing response of ZnO devices to a variety of volatile organic compounds (VOC)s, a specialized system was built. Its design is explained in this section. The system was designed such that it could be made portable without much modification. Thus a PCB-based measurement was preferred. The system could be made portable by including a gas sampling unit, moisture getters, signal-conditioning and an analysis system on the PCB (also called daughterboard) and ultimately on the chip.

As shown in the schematic (Fig. 7.1) the system comprises a cylindrical medical-grade steel chamber of about 5 cm inner diameter and 2.5 cm depth. The gas delivery system is equipped with four mass flow controllers (MFC) and a four-channel readout system acquired from MKS. Two channels were dedicated to supplying carrier/dilution gas N_2 or dry air

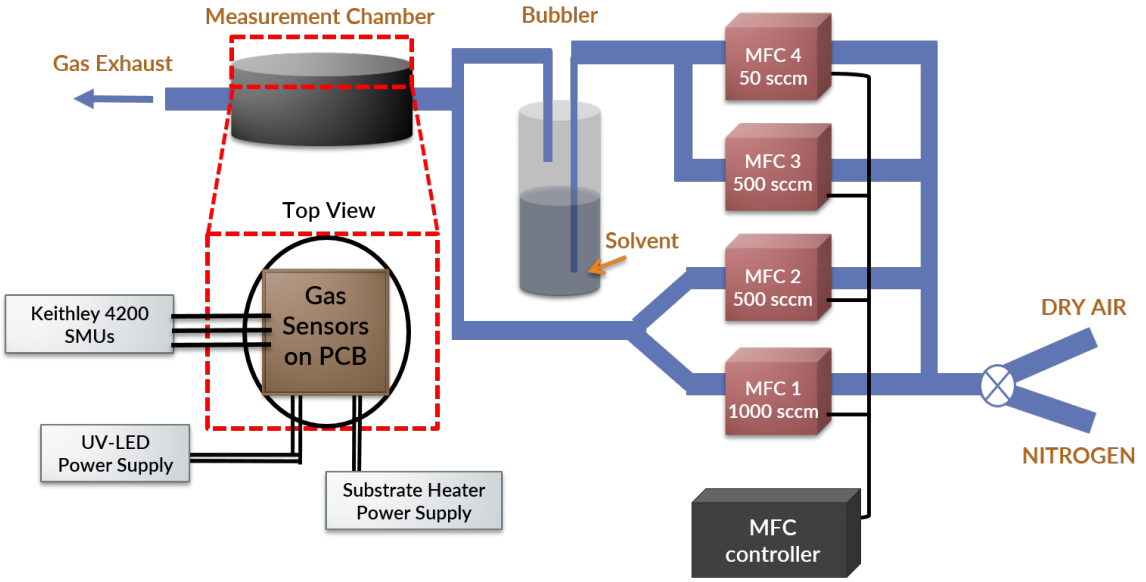

Fig. 7.1 Schematic diagram of the gas sensor characterisation setup for VOC detection. A carrier gas is bubbled through a sealed solvent container to drag solvent vapour along with it. Further dilution is achieved by additional carrier gas flow before the final mixture enters the sensing chamber. A gas sensor is loaded on PCB and measurements are performed with Keithley 4200.

directly. The other two channels insert the carrier gas into a glass bubbler. A carrier gas, flowing through the bubbler, carries a proportional amount of solvent vapour, depending on the vapour pressure of the solvent. These vapours are then further diluted by a carrier gas before entering the sensing chamber. The mixture of analyte gas and carrier gas enters the chamber through the gas inlets. Finally the gases are extracted from the chamber through a line connected to the house exhaust. The entire constructed setup is displayed in Fig. 7.2a.

Gas flow rates through the MFCs are set using the readout system, which is in turn connected to a PC via RS 232 port. In order to control the flow through each of the MFCs for a specified duration, a LabVIEW based user interface was developed, with the help of fellow PhD student Juan Rubio-Lara. Once a required solvent is selected, the interface acquires the predefined flow rate value for each of the MFCs, necessary to generate different concentrations of the corresponding solvent. A characterisation recipe is then specified, which consists of concentration values and a time period for which they should be applied. The setup then employs the concentrations for the specified period. Once the sensor is loaded into the chamber the setup can thus cycle through various concentrations.

Gas sensor substrate is attached to a leadless chip carrier (LCC) package using silver-epoxy. The electrode bond-pads on the substrate are connected to the chip carrier pads using

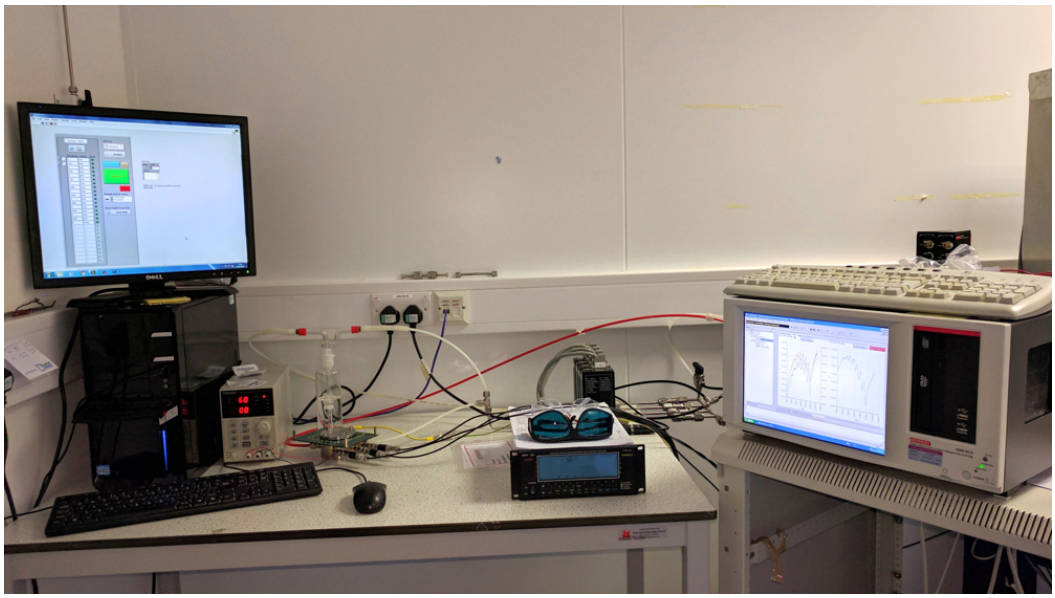

(a)

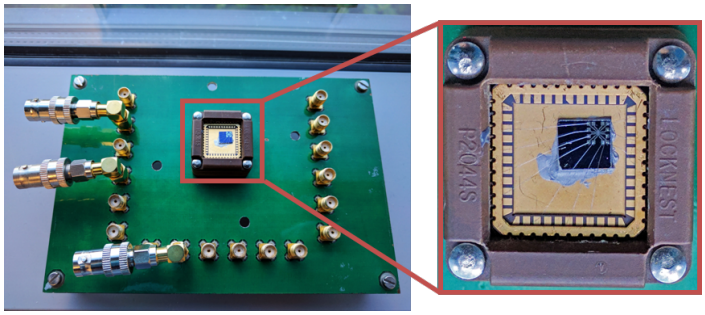

(b)

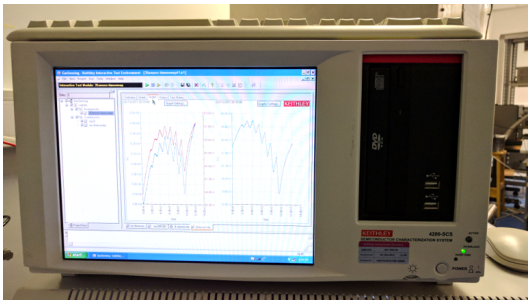

(c)

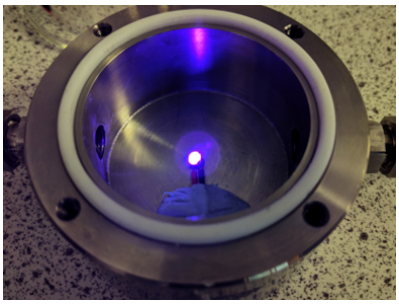

(d)

Fig. 7.2 (a) Construction of the setup showing gas delivery system, solvent bubbler, Labview PC, power supply for UV-LED, sensor PCB loaded into the chamber and Keithley 4200 (b) PCB board with zoomed-in image of the sensor substrate attached to a chip carrier and wire-bonded devices (c) Keithley 4200 running time-dependant measurements (d) inside of the sensing chamber with UV-LED.

wire bonding. These chip carriers are easily incorporated on universal PCBs (Fig. 7.2b), thus simplifying the electrical connections. SMU connectors on the PCB are connected to

the Keithley 4200 semiconductor parameter analyser. Typically drain current is measured at 5 sec interval, by turning on the drain voltage for a brief period of 0.1 sec. The baseline measurement is carried out in the carrier gas environment and the sensing response of the analyte gas is measured as a change in the drain current in the presence of the known amount of gas for a particular time period. Fig. 7.2c shows an example of Keithley 4200 running time-resolved measurement.

Since the optimum sensing response of a number of reported devices is observed at elevated temperature, gas sensor devices need to be heated up during the measurements. Although it is feasible to design on-chip micro-heaters integrated along with the gas-sensing devices, that route was not explored during this project because the main focus was on the synthesis and characterisation of ZnO devices. Thus a commercially available thin-film heater was used for characterisation. A small 8 mm x 8 mm heater was purchased from Watlow. The heater was attached on the back of the chip carrier and connected through the backside of the PCB. Initial measurements indicated device degradation at prolonged heating of up to $\sim$300 °C, leading to non-reproducible results. This thermal degradation was most likely caused due to diffusion of aluminium electrode metal. Therefore room temperature gas sensing in the presence of UV light was explored.

There have been a number of recent reports on UV-enhanced gas sensing using ZnO at relativey low temperatures [236] and even at room temperature [237–239]. A Nichia NCSU275T- U365 UV LED was installed within the sensing chamber (Fig. 7.2d) and connection feedthroughs were taken out of the chamber and sealed with silicon RTV also known as vacuum grease. The LED had a peak emission at 365 nm and was placed at a distance of $\sim$3 mm from the sensor. The intensity of $\sim$1.2 mW/cm^2 was measured at this distance.

7.2.2 Calculations for determining vapour concentrations

Since the goal of our sensing experiments was to deploy different solvent vapours as analytes, a simple bubbler-based system was installed for vapour delivery. A bubbler is essentially a sealed glass cylinder with two gas tubes. The purpose of one of the tubes is to supply carrier gas directly into the liquid and thus it needs to be dipped into the liquid. The other tube extracts the mixture of carrier gas and liquid vapours.

The amount of vapour coming out of the bubbler depends on the vapour pressure of the liquid. For the purpose of our measurements, it was assumed that the pressure within the bubbler is equal to atmospheric pressure and the temperature of the liquid remains at $\sim$25

°C. At equilibrium the ratio of mole fraction of vapour (x_v) and carrier gas (x_c) can be related to their partial pressures respectively using expression

$$\frac{x_v}{x_c} = \frac{P_v}{P_c}$$

where P_v and P_c are partial pressures of vapour and carrier gas, respectively. According to Dalton's Law of partial pressures, total pressure (P_t) inside the bubbler can be expressed as

$$P_t = P_v + P_c$$

Thus the above expression becomes

$$\frac{x_v}{x_c} = \frac{P_v}{P_t - P_v}$$

On the assumption that the pressure inside the bubbler is equal to the atmospheric pressure, P_t = 760 mmHg. The flow from the bubbler will have the same composition as the vapour within the headspace of the bubbler. At the same time the total flow from the the bubbler should be the same as the total flow going in. Thus the flow rate of the vapours coming out of the bubbler can be estimated by

$$F_v^{out} = F_c^{in}\, x\, \frac{P_v}{760 - P_v}$$

where F_c^{in} is the flow rate of carrier gas going into the bubbler and F_v^{out} is the flow rate of vapour coming out of the bubbler. The vapour-carrier gas mixture can be further diluted using additional carrier gas and the concentration of the vapour entering the sensing chamber can be calculated as

$$x_{v,final} = \frac{F_v^{out}}{F_c^{total}}$$

Table 7.1 Volatile Organic Compounds analysed for gas sensing

Vapour	Vapour Pressure (mmHg)	Min Concentration analysed (ppm)
Acetone	231	500
Ethanol	59.3	250
IPA	45.4	250
Toluene	28.4	100
MIBK	19.9	75
Anisole	3.54	25

While the working of the system described here was fairly straightforward, it imposes a limitation on the concentration of vapours generated. As a result fairly low concentrations can be produced for low vapour pressure solvents. However, for high vapour pressure solvents the system is limited to larger concentrations. Throughout the experiments a total flow of 500 sccm was employed. On the other hand, the lowest range MFC used 50 sccm. Thus the minimum carrier gas flow into the bubbler that could be reliably produced was $\sim$1 sccm and vapour coming out of the bubbler could only be diluted a further 500 times at the maximum. Table 7.1 presents different solvents analysed during the experiments with their vapour pressures and minimum concentrations that were used for the measurements. All the vapour pressure values used for the calculations were obtained from https://pubchem.ncbi.nlm.nih.gov/.

7.3 ZnO width dependence on VOC sensing

A number of volatile organic compounds (VOC)s are constituents of human breath and are, thus, of particular interest for breath diagnostic applications. With this in mind, six of the general use solvents, which included ethanol, isopropyl alcohol (IPA), acetone, toluene, anisole and methyl-isobutyl ketone (MIBK), were selected as representative VOC analytes for studying sensing response of direct-write patterned ZnO devices. Sensing measurements were conducted using the custom-built in-house setup described in the earlier section.

During each sensing run, measurements were simultaneously performed on three devices. One of the device was a 50 μm width micro-channel ZnO device. The other two devices were fabricated with a grating type of structure as depicted in Fig. 5.14. The 500 nm device consisted of 50 ZnO nano-lines of 500 nm width and 1μm pitch. On the other hand, the 100 nm device included 100 ZnO nano-lines of 100 nm width and 500 nm pitch. The electrode fabrication was carried out as per the optimized protocol discussed in Chapter 6.

The sensing measurements were carried out under constant UV irradiation. After loading the sensors into the chamber and sealing it, the sensors were exposed to 1 hour of UV irradiation in constant flow of 500 sccm dry air and 1 V voltage bias, which allows the sensors to stabilize before starting the sensing measurements. During the measurements a 1 V voltage bias was periodically applied every 5 sec for 0.1 sec and the source-drain current was measured. Such pulsed-biasing method was chosen to avoid probable bias-induced degradation of the device under testing. Different concentrations of analyte VOC were introduced to the chamber for 10 min, followed by 10 min of dry air flow to recover the sensor before introducing the next concentration.

The acquired time-resolved measurements demonstrated a positive drift in the sensor resistance over the measurement period. While the precise cause of the sensor drift was unclear, stronger drift was observed with higher bias voltage. A baseline fitting was performed on the time-resolved data using the sensor resistance at the point of insertion of the analyte. Subsequently, the change in sensor resistance was estimated by subtraction of the baseline from the time-resolved resistance data.

The concentration of ethanol was varied from 250 ppm to 5000 ppm over the course of the measurement. The change in sensor resistance (after baseline subtraction) as response to different concentrations of ethanol is shown in Fig. 7.3a. Even at concentration of 250 ppm, a small change in resistance can be seen, especially for the 100 nm device. Negative values of the resistance change as a response to ethanol indicates reducing nature of the ethanol vapours. Such decrease in sensor resistance due to ethanol is in accordance with the previous reports on ZnO nanowire [240, 57] and SnO_2 [241] sensors at elevated temperatures.

Before discussing the ethanol detection mechanism it is important to understand the effect of the UV irradiation on ZnO. In an ambient atmosphere oxygen molecules are adsorbed onto the ZnO surface and capture conduction electrons from ZnO to turn negatively charged species [239]. The underlying reaction at temperatures below 100 °C can be expressed a [240],

$$O_{2(g)} + e^- \longrightarrow O^-_{2(ad)}$$

Due to the thermal stability of these chemisorbed O_2^- species at room temperature they are not easily desorbed by reducing gas. Thus sensor response is extremely small at room temperature. Under the presence of the UV light, however, electron-hole pairs are generated at first instance.

$$h\nu \longrightarrow h^+ + e^-$$

Subsequently the photogenerated holes can accept electrons from the adsorbed O_2^- species, causing them to be desorbed.

$$h^+ + O^-_{2(ad)} \longrightarrow O_{2(g)}$$

At the same time ambient oxygen may also react with photogenerated electrons and generate $O^-_{2(h\nu)}$ ions as per the equation,

$$O_{2(g)} + e^-_{(h\nu)} \longrightarrow O^-_{2(h\nu)}$$

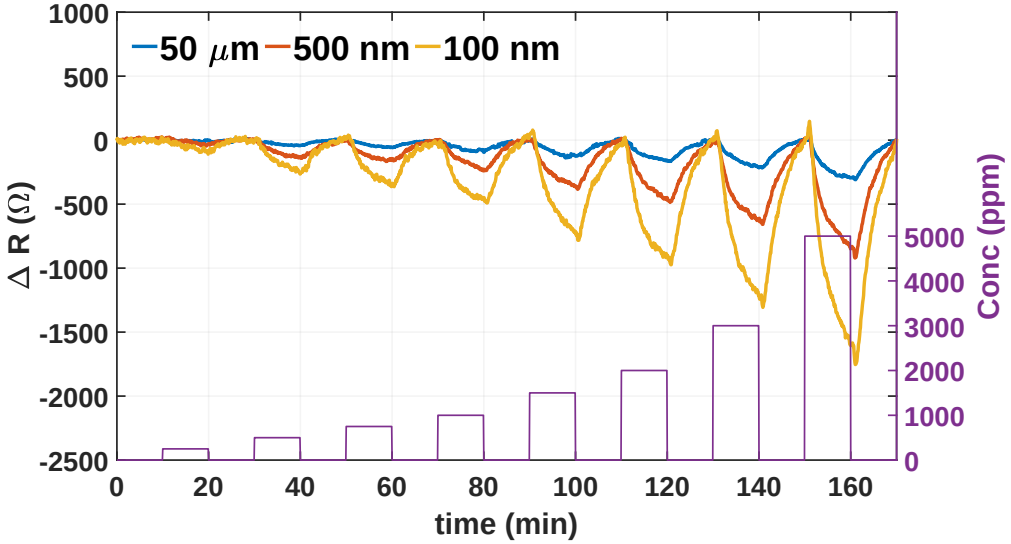

(a)

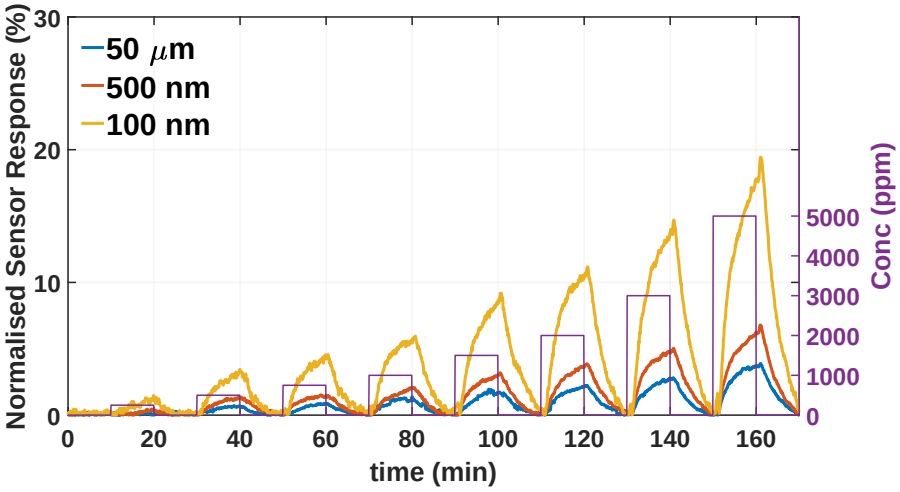

(b)

Fig. 7.3 Room temperature time-resolved response of ZnO sensors subjected to different concentrations of ethanol. Change in sensor resistance (a) and normalised sensor response (b) demonstrating improvement in sensing with decreased ZnO pattern width.

Although a small increase in resistance is caused by increase in surface depletion, the resistance and surface depletion is much smaller than in dark conditions. These photoinduced $O^-_{2(h\nu)}$ ions are relatively loosely bound to the ZnO surface and thus easier to remove when a reducing gas to introduced in the surroundings [238, 242, 243].

When ethanol vapours are introduced in the sensors ambient, ethanol molecule can then react with $O^-_{2(h\nu)}$ species and release the electron back into the ZnO conduction band. As a result the charge carrier density is increased, decreasing the width of the surface depletion region. A drop in the ZnO sensor resistance can therefore be observed. The reaction between photoinduced oxygen ion and ethanol molecule can be represented as [242],

$$C_2H_5OH + 3O^-_{2(h\nu)} \longrightarrow 2CO_2 + 3H_2O + 3e^- \tag{7.1}$$

Another interesting observation from Fig. 7.3a is the width dependence of the resistance change for a given ethanol concentration. For almost all the measured concentrations the higher change in resistance is observed as the width of the ZnO channel is decreased. Such improvement in sensor response can be attributed to the increased surface-to-volume ratio as the width of the ZnO region is scaled down from 50 μm to 100 nm. Consequently a higher surface area is available for the analyte interaction in smaller patterns, and hence the relative change in the surface depletion region can be much higher. Improved sensor response of ZnO nano-wires as compared with thin film devices has been also observed in solution processed ZnO devices fabricated using soft-EBL by Fan *et al.* [239, 238] and in ALD fabricated ZnO devices with the help of nanoscale spacer lithography by Ra *et al.* [131].

The relative sensor response was calculated using formula

$$Sensor\ Response = \frac{\Delta R}{R} = \frac{|R_{air} - R_{gas}|}{R_{air}}\, X100 \tag{7.2}$$

The value of the baseline, which accounts for the drift within the sensor, was extracted from the original time-resolved response data and used for R_{air} during the calculations.

The areal coverage of the sensing region also affects the sensor response. If the sensing region is spread over a wider area, the probability of an analyte molecule coming in contact with the sensor surface increases. Therefore, in order to accurately analyse the effect of patterning on sensing response, normalisation of the projection area was performed. All the devices had a channel length of 5 μm. The projection area of a 50 μm patterned device was straightforward, 50 μm x 5 μm. In the case of nano-patterned devices, however, the projection area was smaller. For 500 nm devices, 50 ZnO lines of 500 nm width were patterned, making the total projection area 25 μm x 5 μm. On the other hand, for a 100 ZnO lines of 100 nm width were patterned for a 100 nm devices. Thus the total projection area in this case was 10 μm x 5 μm. A normalised value of the sensor response was thus determined by multiplying the value calculated by Equation 7.2 with a factor of 2 for a 500 nm device

and with factor of 5 for a 100 nm device. The resulting time-resolved normalised sensor response for ethanol is plotted in Fig. 7.3b.

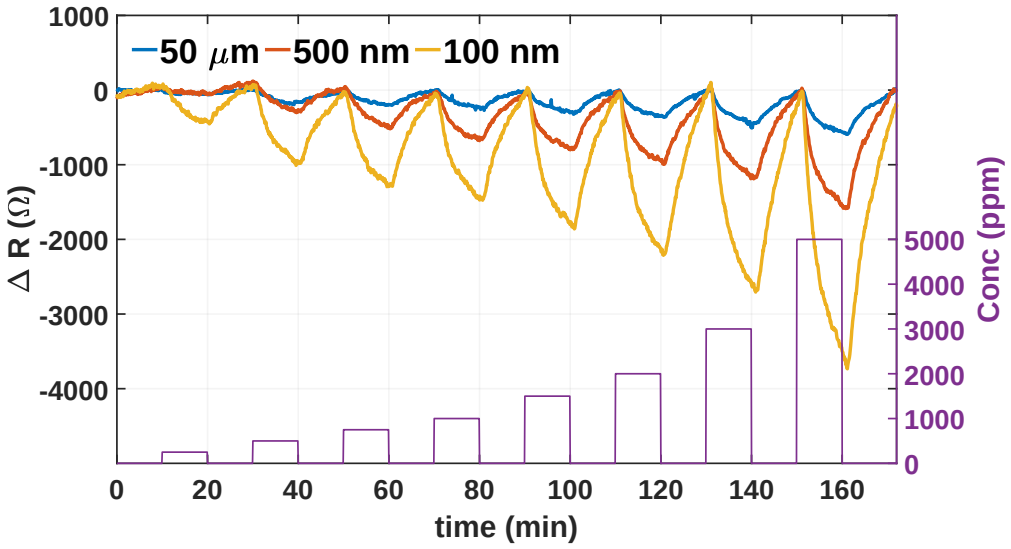

(a)

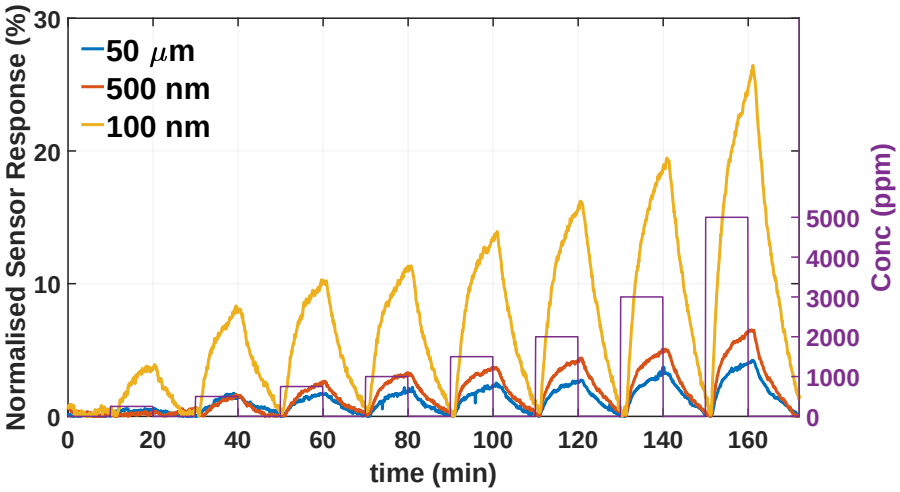

(b)

Fig. 7.4 Room temperature time-resolved response of ZnO sensors for different concentrations of isopropyl alcohol (IPA). Change in sensor resistance (a) and normalised sensor response (b) showing that the smaller ZnO pattern width causes improvement in sensing performance.

The response of ZnO devices was also characterised against different concentrations of isopropyl alcohol (IPA). The concentration was varied from 250 ppm to 5000 ppm. The time-resolved sensor resistance change, subject to different IPA concentrations, is presented

in Fig. 7.4a. The percentage sensor response was also calculated using Equation 7.2 and normalised in the same way as explained in the case of ethanol measurements, as shown in Fig. 7.4b. Reaction between IPA molecules and photoinduced oxygen species can be expressed as

$$2CH_3CHOHCH_3 + 9O^-_{2(h\nu)} \longrightarrow 6CO_2 + 8H_2O + 9e^- \tag{7.3}$$

The pattern width dependence on response of the sensor can also be observed with IPA. Both the change in sensor resistance and the normalized percent response show an increase in sensitivity as the pattern width is decreased. The 100 nm device showed an excellent signal-to-noise ratio even at 250 ppm, suggesting that even lower concentrations can be detected. However, as shown in Table 7.1, in our home-made setup, it was not possible to reproducibly generate lower concentrations of IPA. The response of 50 μm and 500 nm devices at 250 ppm was close to the signal noise and thus, indistinguishable. At 500 ppm both 50 μm and 500 nm devices demonstrated an almost identical response. However, from 750 ppm and beyond, the 500 nm device produced a higher response than the 50 μm device.

Similarly to ethanol and IPA, time-resolved sensing measurements were also carried out for different concentrations of acetone, toluene, MIBK and anisole. Detection as low as 500 ppm acetone, 250 ppm toluene, 25 ppm anisole and 100 ppm MIBK was also achieved under the UV irradiation at room temperature. The normalised sensing response of all the VOCs tested are compared in Fig. 7.5. It can be seen that, except for very low concentrations, the normalised sensor response was increased as the pattern width was narrowed.

It is worth noting that the sensor response of the 100 nm device was higher for IPA (Fig. 7.5b) than for ethanol (Fig. 7.5a) at any given concentration. For 50 μm as well as 500 nm device, the response to IPA was slightly better than ethanol for lower concentrations. However, at higher concentrations the devices showed nearly the same response, possibly because the device started to saturate. According to the Equation 7.3 each molecule of IPA would release more electrons into the ZnO channel than ethanol (Equation 7.1), which would explain the higher sensitivity to IPA. However, at higher concentrations,the number of oxygen ions available may limit the reaction, causing the sensor response to saturate.

Interestingly, all the devices showed overall much higher response to toluene (Fig. 7.5b) than both ethanol and IPA. In comparison with IPA, the 100 nm device showed a lower response to toluene at concentrations below 1000 ppm, whereas, the trend was reversed at higher concentrations. At 1000 ppm the response to both IPA and toluene was nearly equal. However, with further increase in concentration, the response to toluene increased faster than to IPA and became nearly twice at 5000 ppm. The cause of such behaviour may be saturation

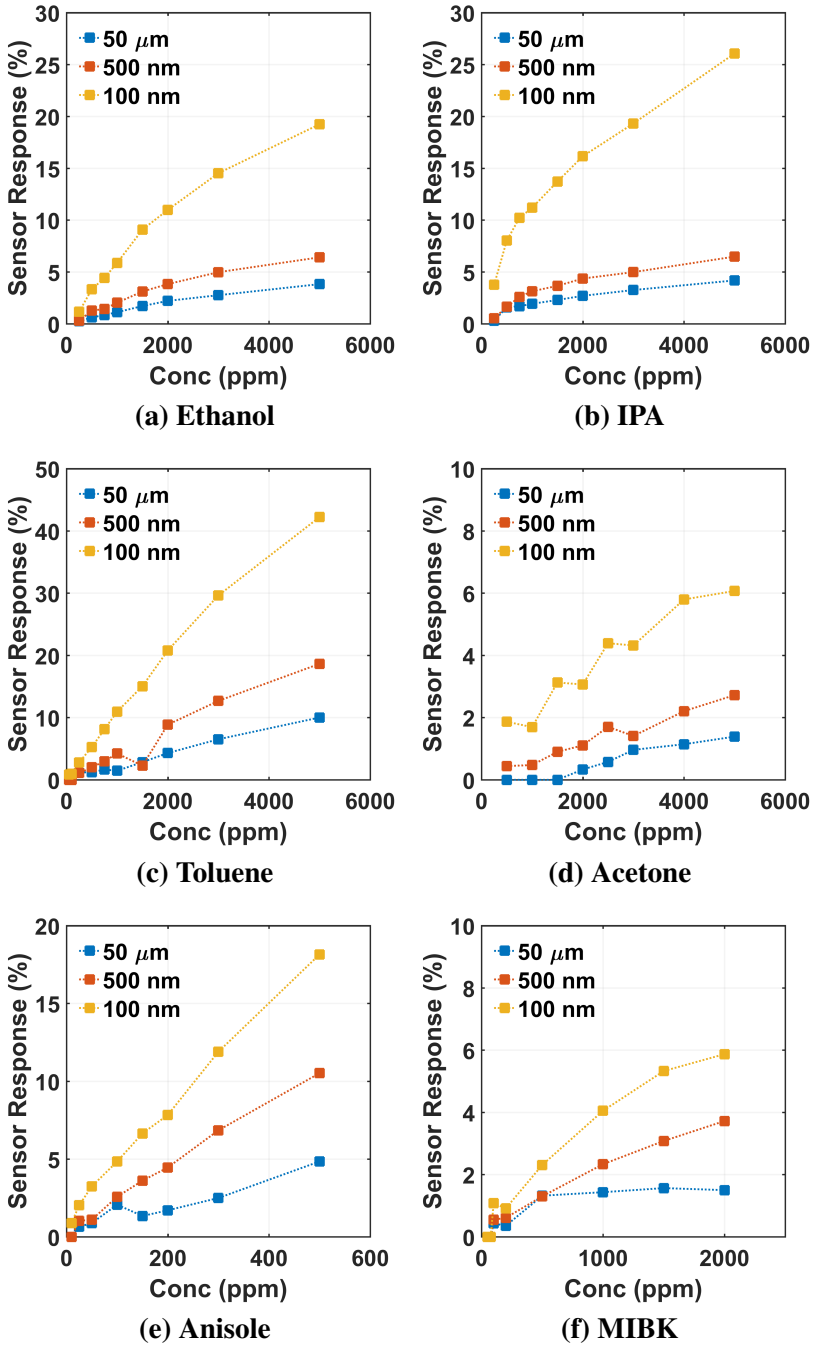

Fig. 7.5 Normalised sensing response of direct-write EBL fabricated ZnO sensors with three pattern widths against the VOC concentration at room temperature.

of sensor response to IPA, contrary to the linear increase in sensor response to toluene. In the case of 50 μm and 500 nm devices the response to toluene was higher than to IPA over the entire concentration range.

The sensor response to anisole was primarily measured for relatively lower concentrations. All three sensors showed linear increase in response with concentrations. At 500 ppm concentration the response of all the devices was highest to anisole, in comparison to the rest of the VOCs. The 100 nm device, for example, showed normalised response as high as $\sim$18 %, whereas response to IPA was $\sim$8 % and for rest of the VOCs it was below 5 %. Thus it appears that the direct-write patterned ZnO device may be implemented for selective detection of anisole vapours.

The response of all three sensors was markedly lower to acetone and MIBK over all the concentration ranges. While concentrations as low as 500 ppm acetone and 100 ppm MIBK were detected with the 100 nm device, the normalised sensor response was only $\sim$1 %. Even at concentrations as high as 5000 ppm of acetone and 2000 ppm of MIBK, the sensor showed little over 5 % normalised response. Such low response may be attributed to the presence of ketone functional group in both acetone and MIBK.

Since the detection mechanism of various VOCs essentially involves the corresponding VOC getting oxidised, the observed trends in the sensitivity may be explained based on susceptibility of the VOC towards oxidation. Acetone and MIBK, both contain an oxygen atom doubly bonded to a carbon atom. Thus, they might be less prone to further oxidation, hence sensors showed poor response towards them. On the other hand, toluene does not contain any oxygen, which may cause toluene molecules to get readily oxidised and sensors showing very high sensitivity. Interestingly, anisole, in spite of having an oxygen atom, showed highest response at 500 ppm. Although, the reason behind this behaviour is unclear, presence of -OCH_3 might be activating other sites on the phenyl ring for getting readily oxidised. Ethanol and IPA both contain oxygen atom attached to a carbon and a hydrogen and where sensors showed intermediate sensitivity.

7.4 NO_2 detection with polycrystalline ZnO nanowires

The device, consisting of the grating pattern of 100 ZnO nanowires of 100 nm width, was also subjected to NO_2 sensing experiments. The time-resolved gas-sensing response to different concentrations of NO_2 was measured with the help of Dr. Stephen Hodge at the Cambridge Graphene Centre. The ZnO sensor substrate was attached to a LCC package and wire-bonded to chip carrier pads. After loading the chip carrier into the sensing chamber, metal probes were used to make contact with the chip carrier pads and the chamber was sealed. Before starting the measurements, the chamber was pumped for 15 min to remove ambient air and humidity while the substrate chuck was heated to the required temperature.

After this the dry air was introduced to the chamber. The system reached atmospheric pressure and was left to stabilise for 30 more min. Consequently different concentrations of NO_2 were sent into the chamber for 5 min and dry air was flushed for 10 min in between each concentration. Throughout the measurement the sensor was biased with 0.1 V and current was continuously measured. The drift in the sensor resistance during the time-resolved measurements was removed by baseline subtraction in order to extract the change in resistance at each concentration.

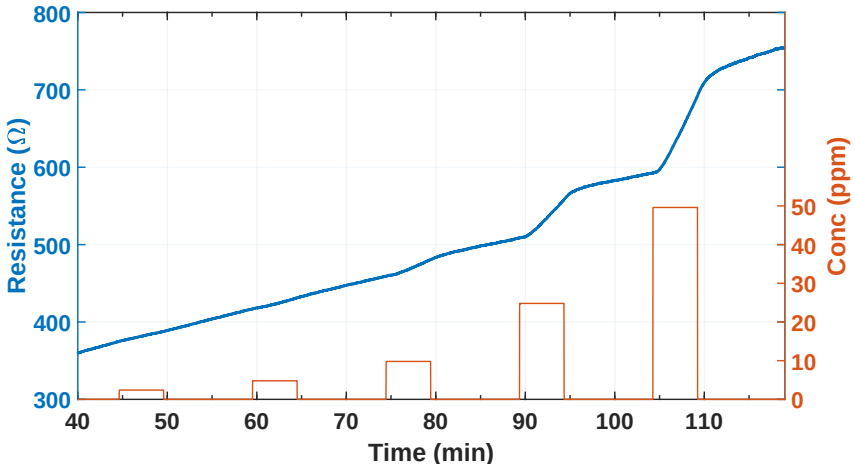

(a)

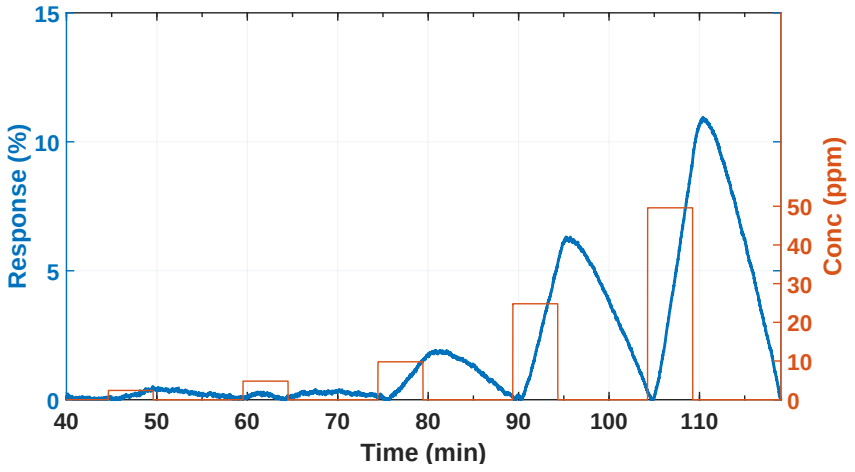

(b)

Fig. 7.6 Time-resolved plot showing variation in sensor resistance as a function of time (a) and percent sensing response (b) for 100 nm device subjected to different NO_2 concentrations at room temperature.

The variation in sensor resistance at different concentrations of NO_2, under room temperature ($\sim$25 °C) conditions, is shown in Fig. 7.6a. A positive drift in sensor resistance

can be seen, which is probably due to the insufficient recovery of the sensor. Percent sensor response as a function of time, calculated as per Equation 7.2 is shown in Fig. 7.6b. At 2.5 ppm and 5 ppm, negligible response is seen. However, the sensor showed a 1.9 % response at 10 ppm, increasing to 6.3 % and 10.9 % at 25 ppm and 50 ppm, respectively. Thus NO_2 detection down to 10 ppm is feasible with the direct-write EBL patterned 100 nm ZnO devices at room temperature.

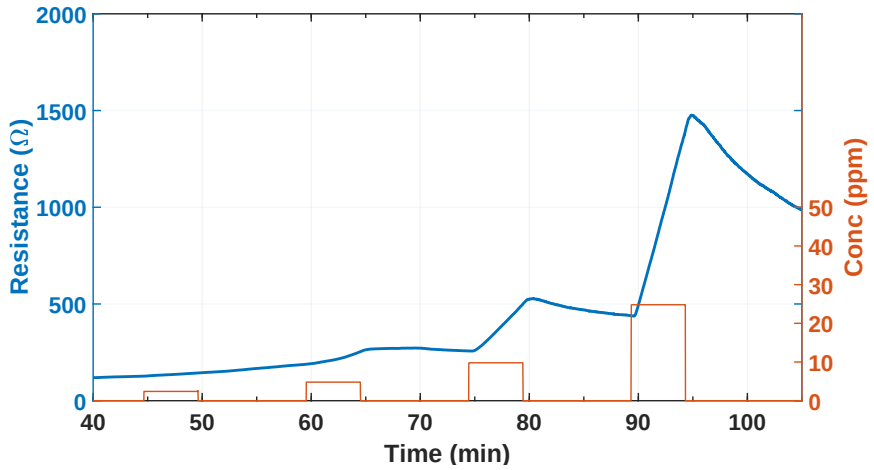

(a)

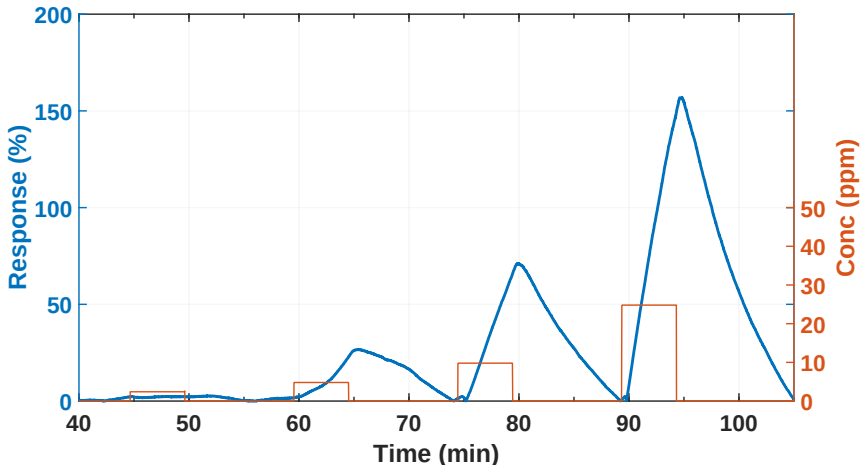

(b)

Fig. 7.7 Time-resolved plot showing variation in sensor resistance as a function of time (a) and percent sensing response (b) for 100 nm device subjected to different NO_2 concentrations at room temperature under UV illumination.

The change in sensor resistance in the presence of NO_2 is due to the oxidising nature of NO_2 and is in close agreement with the previous reports [239, 244, 237]. When a NO_2 molecule comes in contact with the ZnO surface, it accepts an electron from the ZnO

conduction band and resulting species get adsorbed onto ZnO surface. Such a pinning of conduction electron to a surface state, widens the surface depletion at the ZnO surface. It decreases the number of available free charge carriers and consequently, an increase in the sensor resistance is observed. The underlying reaction involving NO_2 interaction can be expressed as [137],

$$NO_{2(g)} + e^- \longleftrightarrow NO^-_{2(ads)} \tag{7.4}$$

$$NO_{2(g)} + e^- \longleftrightarrow NO_{(g)} + O^-_{(ads)} \tag{7.5}$$

On removal of the NO_2 gas, the captured electrons are returned to the ZnO conduction band, thus decreasing the surface depletion. Consequently the resistance of the sensor is decreased.

The 100 nm ZnO sensor device was also subjected to different concentrations of NO_2 under UV light irradiation at room temperature. It can be seen in time-resolved measurements shown in Fig. 7.7a that the positive drift is still exhibited in the sensor resistance. However, here the change in sensor resistance, due to the presence of NO_2, is much larger than in the measurements carried out without UV illumination. A similar observation has also been reported in the case of ZnO nanosheets by Mun *et al.* [237]. Fig. 7.7b presents percent sensor response of ZnO sensor under UV illumination as a function of time. It can clearly be seen that the sensor is able to detect as low as 5 ppm NO_2 giving 26.4 % response. The response increased to 70 % for 10 ppm and 156.9 % for 25 ppm. This phenomenon can be attributed to a larger number of free electrons being available than is the case in the dark. Under UV illumination photo-generation of electron-hole pairs takes place. NO_2 gas being an acceptor of electrons, as the number of electrons available for the NO_2 molecules to capture is increased, the change in the charge-carrier density is larger. Therefore the change in sensor resistance is increased [237].

The response and recovery of ZnO sensors to NO_2 improves with temperature to a certain extent [124]. Thus the 100 nm ZnO device was also exposed to different concentrations of NO_2 at 100 °C. Sensor resistance after exposing it to various NO_2 concentrations is plotted in Fig. 7.8a and the corresponding percent sensor response is shown in Fig. 7.8b. The time-resolved sensor resistance shows only a small drift as compared with the room temperature measurements. This decrease in sensor drift may be attributed to the near full recovery of the sensor due to desorption of NO_2 molecules. Excellent signal-to-noise ratio can be seen at concentration as low as 2.5 ppm, with sensor response of 16.4 %. Evidently much lower concentrations of NO_2 can be detected at moderately low sensor temperature of 100 °C. The response increases to 200 % at 25 ppm and 300 % at 50 ppm.

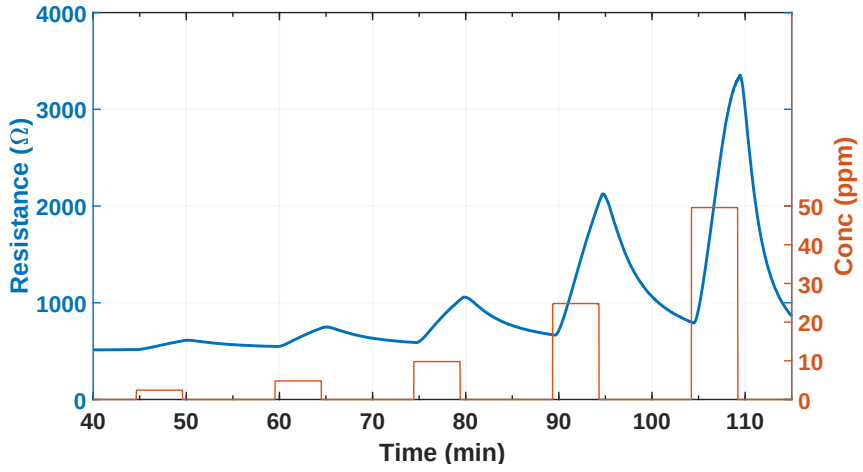

(a)

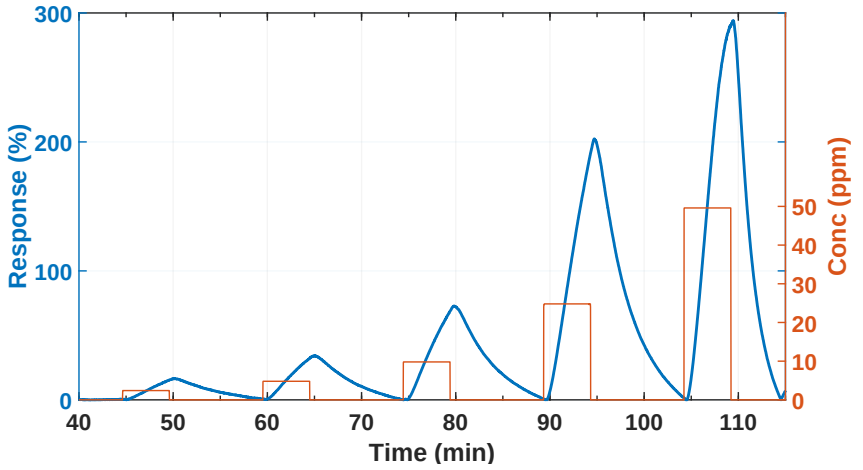

(b)

Fig. 7.8 Time-resolved plot showing variation in sensor resistance as a function of time (a) and percent sensing response (b) for 100 nm device subjected to different NO_2 concentrations at 100 °C.

The response of the sensor was further increased when measurements were carried out at 100 °C under UV illumination. Time-dependent sensor response measurements are shown in Fig. 7.9. It is clearly seen that response was increased well beyond that produced in dark conditions. At 10 ppm the response in UV light changes by three orders of magnitude. However, after about 90 min the UV LED inserted in the sensing chamber was burnt, due to prolonged heating at 100 °C and the device was found to have degraded. Therefore reliable measurements could only be achieved up to 10 ppm.

Percent response of the 100 nm ZnO device is shown against NO_2 concentration in Fig. 7.10, in order to compare all the conditions under which the NO_2 sensing measurements

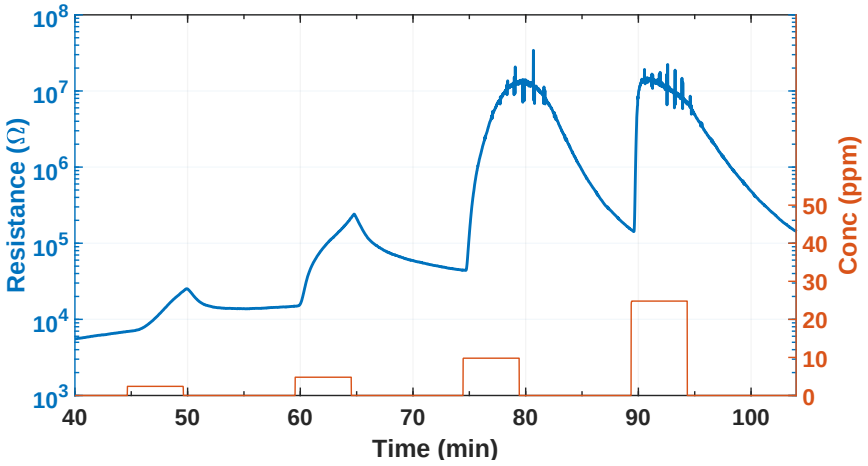

Fig. 7.9 Time-resolved plot showing variation in sensor resistance as a function of time for 100 nm device subjected to different NO_2 concentrations at 100 °C under UV illumination.

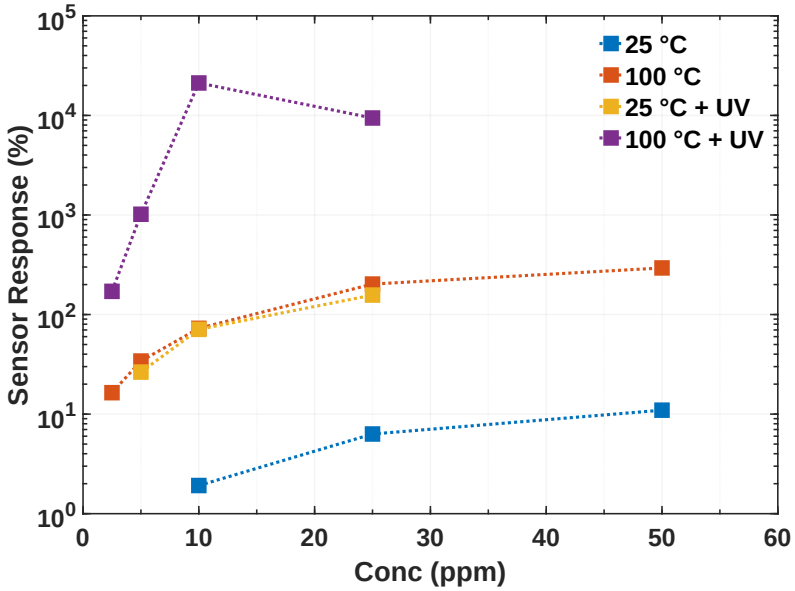

Fig. 7.10 Comparison of percent sensor response against NO_2 concentrations for 100 nm device at ∼25 °C (room temperature) and 100 °C.

were carried out. More than order of magnitude increase in response is observed at 100 °C as compared with room temperature measurements. This improvement in sensor response and recovery can be attributed to the lowering of the activation energy barrier for NO_2 adsorption and desorption, respectively. The measurements under UV illumination at room temperature also showed the sensing response as good as measurements at 100 °C. However, in spite of UV irradiation, concentration below 5 ppm was not detected at room temperature.

The measurements at 100 °C under the UV illumination showed dramatically high sensor response. Even for 2.5 ppm concentration, the sensor response was ∼171 %, which suggests that these sensors can easily detect sub-ppm levels of NO_2 gas. The response was further increased to ∼1000 % for 5 ppm and 2.1 x 10^4 % for 10 ppm.

7.5 Silane SAM functionalisation for sensing VOCs

The ability of the direct-write EBL-patterned ZnO devices to detect a number of VOCs has been demonstrated in section 7.2. However, a similar order of response from these devices to different VOCs limits the selectivity. Thus a self-assembled monolayer (SAM)-based functionalisation using organosilanes was also investigated to impart variability to the sensing response of the ZnO devices. The difference in the length of the organosilane and functional group tail could alter the reactivity of the ZnO surface. The resulting sensor response of the functionalised sensors, along with the response of unfunctionalised sensors discussed in section 7.2, can be analysed with multivariate analysis, such as PCA, in order to distinguish between the different vapours.

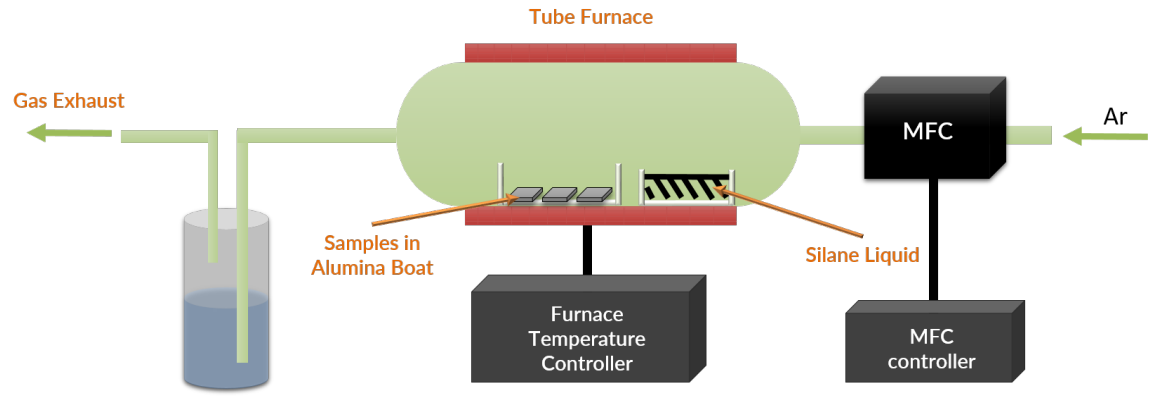

Fig. 7.11 Schematic of vapour phase silanisation setup for functionalising ZnO devices with different organosilanes.

One of the issues arising during the SAM functionalisation is the intercrosslinking of the organosilane molecules, leading to deposition of a thick layer on ZnO. This would be detrimental to the gas-sensing response of the ZnO devices. It is therefore critical to ensure the formation of a silane monolayer on ZnO surface. Thus a vapour phase silane deposition setup was built by adapting conventional tube furnace. The schematic of the setup is shown Fig. 7.11. The device samples, freshly rinsed with acetone and IPA to clean the ZnO surface and dried with compressed nitrogen, were placed in an alumina boat and loaded into the

furnace worktube. Subsequently a small quantity of the required organosilane liquid was placed in another smaller alumina boat and also loaded into the furnace. A constant flow of 100 sccm Ar was maintained through the furnace to create a small pressure gradient. The other end of the tube was connected to a water bubbler to filter the unreacted silane and preventing it from entering the house exhaust. The furnace was heated to $\sim$100 °C for 1 hr and then allowed to cool down. The increased temperature dehydrates device substrates and evaporates silane liquid. The silane molecules in vapour form are then carried by the Ar gas to the sample surface, where SAM layer formation takes place. When the process is complete the increase in water contact angle of the Si-SiO_2 control substrate, processed concurrently with ZnO device, is observed to ensure silane layer formation.

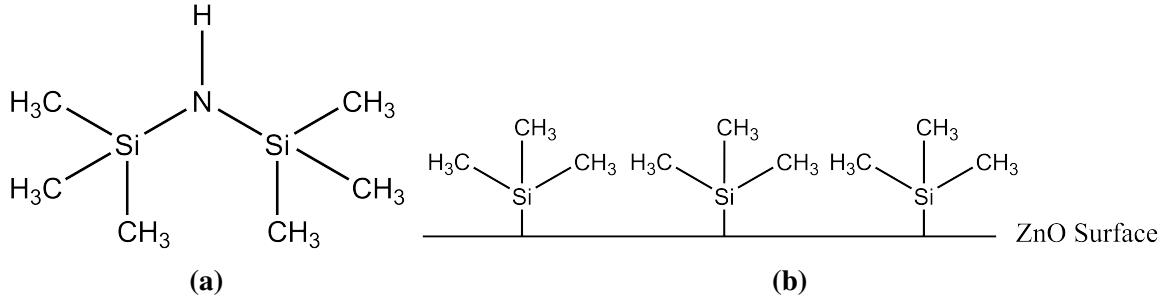

Fig. 7.12 Structure of HMDS molecule (a) and ZnO surface after self assembled monolayer formation (b).

The structure of the hexamethyldisilazane (HMDS) molecule is shown in Fig. 7.12a. The ZnO surface after HMDS SAM layer formation is illustrated in Fig. 7.12b. VOC sensing measurements were carried out on HMDS functionalised ZnO devices in the same way as on unfunctionalised devices. The normalised sensing response of the HMDS functionalised ZnO devices to different VOCs is presented in Fig. 7.13. In comparison with unfunctionalised devices, the functionalised 100 nm device showed a small increase in response to ethanol, while the response of the 50μm and 500 nm device was nearly the same. Interestingly, sensor response to all the other VOCs was less than was the case with the unfunctionalised devices. The response to IPA and anisole was decreased by a factor of 2 and 3 respectively.

On the other hand, almost an order of magnitude change was seen in the case of toluene. The lower response of acetone and MIBK, in the case of unfunctionalised devices, was further degraded with HMDS monolayer. The response to acetone was nearly halved, whereas, due to the extremely poor signal-to-noise ratio for MIBK measurements, accurate estimation of the sensor response was not possible.

A precise mechanism pertaining to the effect of a monolayer on gas sensing is not known. However, the overall trend of decreased sensor response for VOCs with three or

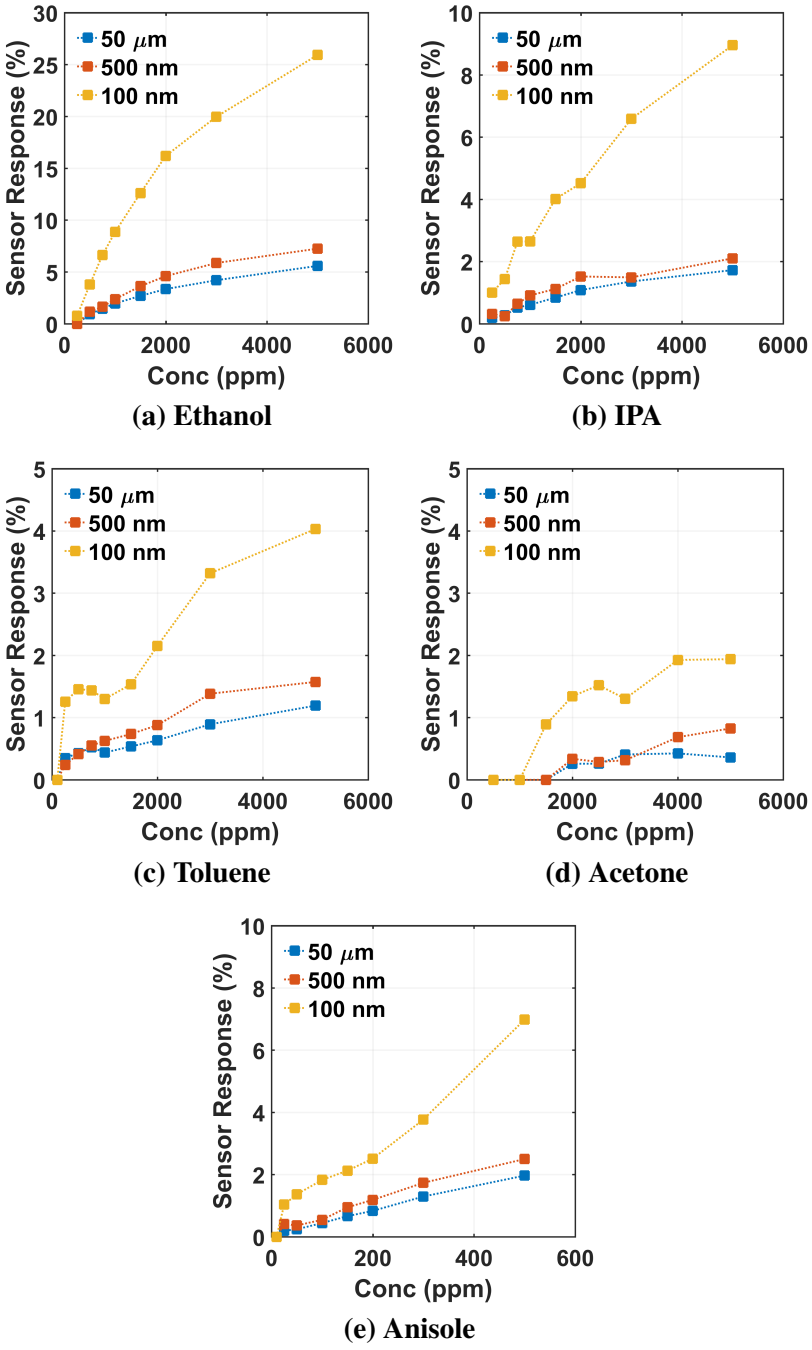

Fig. 7.13 Normalised sensing response of HMDS functionalised direct-write EBL fabricated ZnO sensors with three different pattern widths against the VOC concentration at room temperature.

more carbon atoms may be attributed to the steric effect caused by the three methyl groups present in the SAM layer. The sensing response for the given set of VOCs suggests that it may be possible to improve the selectivity of the ZnO devices to ethanol sensing by HMDS

functionalisation. However, more in-depth investigation is required in order to elucidate the underlying mechanism of the HMDS functionalised ZnO gas sensing.

7.6 Concluding remarks

An in-house gas-sensor characterisation setup was built for VOC detection measurements. A bubbler-based vapour delivery system was included in the setup along with UV irradiation capability for enhancing the sensor response at room temperature. Six VOCs were tested using this setup to characterise ZnO sensors. Three pattern widths (50 μm, 500 nm and 100 nm) of direct-write ZnO devices were characterised for gas-sensing application.

Photoinduced oxygen ions, generated as a consequence of UV light stimulus, are loosely bound to a ZnO surface, unlike the chemisorbed oxygen ions in dark conditions. Their easier removal by reducing gas gives rise to a room-temperature sensing response [238, 242, 243]. The response of the ZnO devices was found to have dependence on the pattern width. Smaller, nano-scale patterned devices showed sensing response greater than that of wider micro-scale patterned devices. This phenomenon may be attributed to the higher surface-to-volume ratio in smaller, nanoscale devices. As a result 100 nm width devices were found to show the best sensing performance. The minimum concentrations of various VOCs detected with good signal-to-noise ratio using direct-write ZnO devices and the sensing response of a 100 nm device are summarised in Table 7.2.

Table 7.2 Comparison of lowest concentrations of VOCs detected and their sensing response at lowest detected concentration as well as at 500 ppm

Vapour	Min concentration detected (ppm)	Normalised response at min concentration (%)	Normalised response at 500 ppm (%)
Acetone	500	1.87	1.87
Ethanol	250	1.17	3.33
IPA	250	3.78	8.04
Toluene	250	2.80	5.25
MIBK	100	1.08	2.31
Anisole	25	2.02	18.15

The 100 nm device was also subjected to NO_2 sensing measurements. Detection down to 10 ppm was achieved at room temperature without any external stimulus of UV light. However, the sensor showed positive drift, possibly due to the insufficient recovery of the

sensor. By contrast, at the moderate temperature of 100 °C, a much improved response and almost full recovery was seen. As low as 2.5 ppm NO_2 was detected. The effect of UV stimulus on NO_2 sensing still needs to be explored.

Finally, to improve the selectivity of ZnO gas sensors, organosilane-based SAM layer functionalisation is being investigated. A vapour-based SAM deposition is employed using a home-built setup for this purpose. It is found that after HMDS functionalisation ZnO devices showed improved sensitivity to ethanol, while the sensitivity of other VOCs was degraded. Further work is called for, using functionalisation with different silane layers and multivariate analysis of the sensor response from functionalised as well as unfunctionalised ZnO devices.

Chapter 8

Summary and Future Work

8.1 Thesis Summary

This thesis has explored the use of novel solution based precursors zinc neodecanoate and zinc naphthenate in scaling down ZnO field effect transistors (FET) to nanoscale. Two transistor fabrication approaches have been investigated, conventional thin film transistors and direct-write EBL patterned transistors. Finally, the sensing capabilities of direct patterned devices have been studied for their response to various VOCs and NO_2.

ZnO thin films were fabricated using zinc neodecanoate solution precursor. Optical characterisation of the prepared films revealed excellent transmittance in the visible region. The bandgap of $\sim$ 3.2 eV was estimated using Tauc plot. In agreement with previous reports, near bad edge (NBE) emission peak was observed at $\sim$ 380 nm during PL spectroscopy. The NBE to deep-level emission ratio improved with increasing annealing temperature, suggesting enhancement in crystallinity and decrease in grain boundary disorder.

TFT fabrication was carried out on Si/SiO_2 substrates. Al source-drain electrodes with 5 μm channel length and 500 μm width were deposited on ZnO thin films using photolithography. Electrical characterisation of the fabricated devices was carried out in back-gate configuration by acquiring transfer and output curves and analysed in terms of various transistor parameters such as saturation mobility, I_{ON}/I_{OFF} ratio, threshold voltage, subthreshold slope along with trap density estimation.

A 15 % precursor dilution in toluene produced $\sim$20 nm thick ZnO film after annealing and was found to show optimal device performance. The increase in decomposition temperature led to improvement in the device performance. The best performance was

attained from devices with ZnO films annealed at 700 °C. Saturation mobility as high as 0.1 cm^2/V.s was obtained with I_{ON}/I_{OFF} ratio of $\sim 10^7$ and subthreshold swing of 2.26 V/dec. Based on the analytical model, it was established that trap-limited conduction (TLC) is the dominant transport mechanism in ZnO TFTs. However, the devices annealed at 700 °C showed transition from TLC transport to percolation limited transport at higher gate voltages. Moreover, the presence of deep traps was estimated, based on activation energy extracted from an Arrhenius plot, at lower annealing temperature. The trap levels tend to become shallower after annealing at higher temperature.

Negative tone electron beam lithography (EBL) based direct-write approach was then developed as a top-down synthesis route, using zinc naphthenate and zinc neodecanoate resists. Various exposure tests were conducted to ascertain the optimal dose for structures of different length scales. Exposure dose curves were extracted from AFM topography measurements conducted on dose tests for 2.5 μm square patterns. Resist parameters were estimated in accordance with these dose curves. Resist sensitivity of 16.7 mC/cm^2 and 4.4 mC/cm^2 was exhibited by zinc naphthenate and zinc neodecanoate respectively; whereas a contrast of 6.2 and 6.4 was calculated for zinc naphthenate and zinc neodecanoate, respectively. Furthermore, 25 μm long nanoscale patterns down to 50 nm linewidth were demonstrated using both the resist precursors.

ZnO patterns produced using direct-write EBL were employed for fabrication of FET devices. Firstly, transfer characteristics of micron-scaled ZnO FETs were acquired while exposed to different atmospheres, namely ambient air and vacuum. It was established that in ambient atmosphere, oxygen and/or water adsorption causes hysteresis in ZnO FETs. It was also ascertained that Al source-drain contacts impart best performance to the devices, due to their favourable work function for ZnO.

Crosslinked zinc naphthenate and zinc neodecanoate were subjected to 500 °C temperature annealing. PL measurement revealed sharp NBE peak near 380 nm and low defects emission, thus confirming good quality of prepared ZnO. It was found that $\sim$50 nm thick ZnO fabricated from both the precursors demonstrated best device performance, albeit precursor concentrations of 15 % and 25 % were required in the case of zinc neodecanoate and zinc naphthenate, respectively. ZnO FETs with W/L = 50 μm/5 μm revealed linear mobility as high as $\sim$0.05 cm^2/V.s and I_{ON}/I_{OFF} ratio of $\sim 10^5$. Post-decomposition annealing was used to passivate electronically active traps and also to incorporate shallow donors such as hydrogen interstitials. An order of magnitude enhancement in the linear mobility was observed with forming gas annealing reaching $\sim$0.5 cm^2/V.s.

Interestingly, two orders of magnitude mobility increment was discovered on decreasing ZnO FET channel width from 50 μm to 100 nm with the use of direct-write EBL. Devices with 100 nm channel width exhibited linear mobility values up to $\sim$33.7 cm^2/V.s, which is one of the highest attained values among direct-write patterned ZnO transistors. This performance enhancement with decreasing channel width was attributed to suppressed grain boundary scattering as a result of grain-size increase and tighter grain packing at smaller pattern widths. Most of the FETs exhibited drain current $\sim$1 μA and I_{ON}/I_{OFF} ratio of $\sim 10^4$-10^5 under 1 V drain bias.

The sensing response of direct-write EBL ZnO devices was characterised using an in-house built setup, consisting of an automated bubbler-based vapour delivery system and UV sensitisation facility. In agreement with recent results, ZnO devices exhibited room-temperature detection of six different VOCs with UV stimulus. Relatively easier removal of photoinduced oxygen ions by reducing gas, as compared with chemisorbed oxygen ions in dark conditions, is probably the underlying cause of room temperature sensor response.

The width-normalised sensor response demonstrated dependence on ZnO pattern width. Higher surface-to-volume ratio imparted by nanoscale ZnO resulted in improvement in sensing response with decreasing pattern width. Detection of concentrations as low as 250 ppm of ethanol, IPA and toluene, 500 ppm of acetone, 100 ppm of MIBK and 25 ppm of anisole was attained at room temperature.

A small degree of selectivity was also observed during the measurements. Sensors indicated higher response to aromatic compounds, such as toluene and anisole, than aliphatic alcohols ethanol and IPA. On the other hand, response to VOCs consisting of ketone group, namely acetone and MIBK, was found to be extremely small. The HMDS functionalisation manifested selectivity to ethanol, by suppressing response to other VOCs tested. Further work is called for with organosilane functionalisation of ZnO devices and multivariate analysis of sensor response.

High performance NO_2 sensing was also demonstrated using 100 nm ZnO devices. Time-dependant sensing measurements revealed detection of 10 ppm levels of NO_2 at room temperature. With the help of UV sensitisation, enhancement of response was attained, leading to a 5 ppm level of detection at room temperature. On increasing the temperature to a moderate 100 °C, much larger improvement in response and recovery of the sensors was observed, which was further enhanced by UV stimulus. ZnO sensors exhibited a sensing response as great as 171 % to 2.5 ppm levels of NO_2 at 100 °C under UV illumination. An excellent signal-to-noise ratio during the measurements clearly suggested the possibility of sub-ppm levels of NO_2 detection using direct-write EBL patterned ZnO nanowires.

8.2 Future Work

Over the course of this thesis, direct-write EBL technique is developed for fabrication of ZnO micro-nano devices and their application in FETs and gas sensors. Several future directions are outlined in this section.

8.2.1 Low temperature processing of ZnO TFTs

Due to higher decomposition temperatures of zinc neodecanoate and zinc naphthenate, temperatures of 500 °C or higher are used for the fabrication of ZnO devices. However, such higher temperature limits the use of these precursors for wider device substrates such as flexible polymers. A few reports have been made on combustion synthesis technique using fuel and oxidiser additives in order to decrease the processing temperatures [245, 246, 215]. Use of such approach may be helpful in bringing down the required annealing temperatures of zinc neodecanoate and zinc naphthenate-based fabrication.

8.2.2 Direct-write patterned oxide transistors

The primary focus of this thesis has been on ZnO based devices. However, doping the zinc oxide matrix with various materials such as In, Ga, Sn, Al can be further explored to improvise the device characteristics. In and Ga additions are widely used for decreasing the off state current of the FETs, whereas, Sn doping is being explored in order to improve their stability. In contrast, Al incorporation provides metal like characteristics, which can be then used as low contact resistance electrode fabrication in opto-electronic devices. To the best of our knowledge there has not been any report of naphthenate and neodecanoate based scheme in either TFT or direct-write route for doped ZnO and may be an interesting avenue for building high performance devices.

In addition, copper and nickel naphthenate have previously been reported for sub-10 nm metal line fabrication using direct-write EBL [214] by decomposing them in highly reducing environment. There may be a possibility of fabricating p-type semiconductors such as copper oxide and nickel oxide using these precursors, with the help of annealing in air or high oxygen environment.

8.2.3 Oxide semiconductor based gas sensors and electronic nose

ZnO nanowires provide excellent gas sensing response due to their interaction with range of gases through adsorption-desorption of oxygen. In this thesis, high sensitivity gas sensing response of ZnO based devices has been demonstrated to six VOCs and NO_2. However, various other metal oxides also possess gas sensitivity, SnO_2 being the most widely used in commercial gas sensors. The direct-write EBL approach may also be implemented for the fabrication of nanoscale oxide gas sensors based on SnO_2, CuO, NiO, VO_2, In_2O_3 etc using metal salts of neodecanoic and naphthenic acids. The sensor based on different metal oxides would show varied response to the gases and VOCs under investigation. This variability in the response can be exploited to distinguish between the gaseous species by conducting multivariate analysis such as PCA or LDA.

In a collaborative research, we have also developed a core-shell electrospinning method for fabrication of ZnO nanofibres using zinc neodecanoate and demonstrated their excellent gas sensing capability (manuscript in preparation). This technique can also be expanded for other metal oxides and further exploited for building an e-nose system.

SAM-based sensor functionalisation has been briefly explored during this project. However, it is of paramount importance to elucidate the precise effect of chain length and functional tail-end groups on the gas sensing performance. Therefore a systematic variation in the organosilanes and correlating them to the gas sensing response is necessary. Additionally, functionalisation with noble metal nanoparticles such as Pt, Pd and Au can also be implemented in order to bring variability in the sensor response. They can be deployed either from colloidal suspension or with the use modified of atomic layer deposition.

Sensors with each functionalisation can be fabricated on separate substrates and analysed together as an array. However, the ultimate goal remains to design and fabricate an one-chip e-nose sensor array. This would require a number of devices with each type of functionalisation and a good spatial separation of the sensor array to facilitate selective functionalisation. Based on the combination of functionalisation methods that need to be employed, a combined fabrication process would need to be formulated. Some of the ways for achieving selective functionalisation could be the use of precision micro-dropper for dispersing liquid solutions at required location on the substrate or developing microfludic channel network. Furthermore, for a portable sensor platform integration of micro-heaters and UV-LED would also be require to provide thermal and radiation sensitisation respectively.

References

[1] "International technology roadmap for semiconductors: 2012 update overview." http://www.itrs2.net/2012-itrs.html, 2012. Last Accessed: 01-Nov-2017.

[2] C. Thelander, P. Agarwal, S. Brongersma, J. Eymery, L. Feiner, A. Forchel, M. Scheffler, W. Riess, B. Ohlsson, U. Gösele, and L. Samuelson, "Nanowire-based one-dimensional electronics," *Materials Today*, vol. 9, pp. 28–35, oct 2006.

[3] D. Panda and T.-Y. Tseng, "One-dimensional ZnO nanostructures: fabrication, optoelectronic properties, and device applications," *Journal of Materials Science*, vol. 48, pp. 6849–6877, oct 2013.

[4] X. Chen, C. K. Y. Wong, C. A. Yuan, and G. Zhang, "Nanowire-based gas sensors," *Sensors and Actuators, B: Chemical*, vol. 177, pp. 178–195, feb 2013.

[5] "Strategic research agenda - european nanoelectronics initiative advisory council." http://www.eniac.eu/web/downloads/SRA2007.pdf, 2007. Last Accessed: 01-Nov-2017.

[6] A. Gurlo, "Nanosensors: towards morphological control of gas sensing activity. SnO2, In2O3, ZnO and WO3 case studies.," *Nanoscale*, vol. 3, no. 1, pp. 154–65, 2011.

[7] A. D. Wilson and M. Baietto, "Advances in electronic-nose technologies developed for biomedical applications," *Sensors*, vol. 11, no. 1, pp. 1105–1176, 2011.

[8] B. Buszewski, M. Kęsy, T. Ligor, and A. Amann, "Human exhaled air analytics: biomarkers of diseases," *Biomedical Chromatography*, vol. 21, pp. 553–566, jun 2007.

[9] D. Hill and R. Binions, "Breath Analysis for Medical Diagnosis.," *International Journal on Smart Sensing and Intelligent Systems*, vol. 5, no. 2, pp. 401–440, 2012.

[10] D. Guo, D. Zhang, N. Li, L. Zhang, and J. Yang, "A novel breath analysis system based on electronic olfaction," *IEEE Transactions on Biomedical Engineering*, vol. 57, no. 11, pp. 2753–2763, 2010.

[11] A. D. Wilson, "Future applications of electronic-nose technologies in healthcare and biomedicine," *Wide Spectra of Quality Control*, pp. 267–290, 2011.

[12] S. H. K. Park, C. S. Hwang, H. Y. Jeong, H. Y. Chu, and K. I. Cho, "Transparent ZnO-TFT Arrays fabricated by atomic layer deposition," *Electrochemical and Solid State Letters*, vol. 11, no. 1, pp. H10–H14, 2008.

[13] S. W. Cho, D. E. Kim, W. J. Kang, B. Kim, D. H. Yoon, K. S. Kim, H. K. Cho, Y.-H. Kim, and Y. Kim, "Chemical durability engineering of solution-processed oxide thin films and its application in chemically-robust patterned oxide thin-film transistors," *J. Mater. Chem. C*, vol. 5, no. 2, pp. 339–349, 2017.

[14] C. Klingshirn, "ZnO: From basics towards applications," *physica status solidi (b)*, vol. 244, pp. 3027–3073, sep 2007.

[15] A. B. Djurišić, X. Chen, Y. H. Leung, and A. Man Ching Ng, "ZnO nanostructures: growth, properties and applications," *Journal of Materials Chemistry*, vol. 22, no. 14, p. 6526, 2012.

[16] L. Schmidt-Mende and J. L. MacManus-Driscoll, "ZnO - nanostructures, defects, and devices," *Materials Today*, vol. 10, no. 5, pp. 40–48, 2007.

[17] N. Izyumskaya, V. Avrutin, Ü. Özgür, Y. I. Alivov, and H. Morkoç, "Preparation and properties of ZnO and devices," *physica status solidi (b)*, vol. 244, pp. 1439–1450, may 2007.

[18] Z. L. Wang, "ZnO nanowire and nanobelt platform for nanotechnology," *Materials Science and Engineering: R: Reports*, vol. 64, pp. 33–71, apr 2009.

[19] Z. L. Wang, "Zinc oxide nanostructures: growth, properties and applications," *Journal of Physics: Condensed Matter*, vol. 16, pp. R829–R858, jun 2004.

[20] Ü. Özgür, Y. I. Alivov, C. Liu, A. Teke, M. A. Reshchikov, S. Doğan, V. Avrutin, S.-J. Cho, and H. Morkoç, "A comprehensive review of ZnO materials and devices," *Journal of Applied Physics*, vol. 98, p. 041301, aug 2005.

[21] C. Klingshirn, J. Fallert, H. Zhou, J. Sartor, C. Thiele, F. Maier-Flaig, D. Schneider, and H. Kalt, "65 years of ZnO research - old and very recent results," *physica status solidi (b)*, vol. 247, pp. 1424–1447, apr 2010.

[22] C. Wang, L. Yin, L. Zhang, D. Xiang, and R. Gao, "Metal Oxide Gas Sensors: Sensitivity and Influencing Factors," *Sensors*, vol. 10, pp. 2088–2106, mar 2010.

[23] S. M. Kanan, O. M. El-Kadri, I. A. Abu-Yousef, and M. C. Kanan, "Semiconducting Metal Oxide Based Sensors for Selective Gas Pollutant Detection," *Sensors*, vol. 9, pp. 8158–8196, oct 2009.

[24] I. D. Kim, A. Rothschild, and H. L. Tuller, "Advances and new directions in gas-sensing devices," *Acta Materialia*, vol. 61, no. 3, pp. 974–1000, 2013.

[25] S. Sharma and M. Madou, "A new approach to gas sensing with nanotechnology," *Philosophical Transactions of the Royal Society A: Mathematical, Physical and Engineering Sciences*, vol. 370, pp. 2448–2473, may 2012.

[26] A. Wei, L. Pan, and W. Huang, "Recent progress in the ZnO nanostructure-based sensors," *Materials Science and Engineering: B*, vol. 176, pp. 1409–1421, nov 2011.

[27] M. M. Arafat, B. Dinan, S. A. Akbar, and A. S. M. A. Haseeb, "Gas Sensors Based on One Dimensional Nanostructured Metal-Oxides: A Review," *Sensors*, vol. 12, pp. 7207–7258, may 2012.

[28] J. Huh, J. Park, G. T. Kim, and J. Y. Park, "Highly sensitive hydrogen detection of catalyst-free ZnO nanorod networks suspended by lithography-assisted growth," *Nanotechnology*, vol. 22, p. 085502, feb 2011.

[29] M. Guo, C. Yang, M. Zhang, Y. Zhang, T. Ma, X. Wang, and X. Wang, "Effects of preparing conditions on the electrodeposition of well-aligned ZnO nanorod arrays," *Electrochimica Acta*, vol. 53, no. 14, pp. 4633–4641, 2008.

[30] M. H. Wong, A. Berenov, X. Qi, M. J. Kappers, Z. H. Barber, B. Illy, Z. Lockman, M. P. Ryan, and J. L. MacManus-Driscoll, "Electrochemical growth of ZnO nano-rods on polycrystalline Zn foil," *Nanotechnology*, vol. 14, no. 9, pp. 968–973, 2003.

[31] Z. Wang, X.-F. Qian, J. Yin, and Z.-K. Zhu, "Large-Scale Fabrication of Tower-like, Flower-like, and Tube-like ZnO Arrays by a Simple Chemical Solution Route," *Langmuir*, vol. 20, pp. 3441–3448, apr 2004.

[32] Z. Chen and L. Gao, "A facile route to ZnO nanorod arrays using wet chemical method," *Journal of Crystal Growth*, vol. 293, no. 2, pp. 522–527, 2006.

[33] I. C. Yao, P. Lin, S. H. Huang, and T. Y. Tseng, "Electrical properties and reliability of ZnO-based nanorod current emitters," *IEEE Transactions on Components, Packaging and Manufacturing Technology*, vol. 2, no. 7, pp. 1143–1150, 2012.

[34] Q. Li, V. Kumar, Y. Li, H. Zhang, T. J. Marks, and R. P. H. Chang, "Fabrication of ZnO nanorods and nanotubes in aqueous solutions," *Chemistry of Materials*, vol. 17, no. 5, pp. 1001–1006, 2005.

[35] I.-C. Yao, P. Lin, and T.-y. Tseng, "Field Emission Properties and Reliability of ZnO Nanorod, Nanopagoda, and Nanotip Current Emitters," *IEEE Transactions on Nanotechnology*, vol. 11, pp. 746–750, jul 2012.

[36] I.-C. Yao, P. Lin, and T.-Y. Tseng, "Nanotip fabrication of zinc oxide nanorods and their enhanced field emission properties.," *Nanotechnology*, vol. 20, no. 12, p. 125202, 2009.

[37] O. Lupan, G. A. Emelchenko, V. V. Ursaki, G. Chai, A. N. Redkin, A. N. Gruzintsev, I. M. Tiginyanu, L. Chow, L. K. Ono, B. Roldan Cuenya, H. Heinrich, and E. E. Yakimov, "Synthesis and characterization of ZnO nanowires for nanosensor applications," *Materials Research Bulletin*, vol. 45, no. 8, pp. 1026–1032, 2010.

[38] B. Q. Cao, X. L. Hu, H. M. Wei, and H. Y. Xu, "Radial and axial nanowire heterostructures grown with ZnO nanowires as templates," in *TENCON 2010 - 2010 IEEE Region 10 Conference*, pp. 986–989, IEEE, nov 2010.

[39] S.-W. Kim, S. Fujita, and S. Fujita, "ZnO nanowires with high aspect ratios grown by metalorganic chemical vapor deposition using gold nanoparticles," *Applied Physics Letters*, vol. 86, no. 15, p. 153119, 2005.

[40] G. Zhang, A. Nakamura, T. Aoki, J. Temmyo, and Y. Matsui, "Au-assisted growth approach for vertically aligned ZnO nanowires on Si substrate," *Applied Physics Letters*, vol. 89, no. 11, pp. 1–4, 2006.

[41] V. E. Sandana, D. J. Rogers, F. H. Teherani, R. McClintock, M. Razeghi, H.-J. Drouhin, M. C. Clochard, V. Sallet, G. Garry, and F. Fayoud, "MOCVD growth of ZnO nanostructures using Au droplets as catalysts," in *Proc. of SPIE* (F. H. Teherani and C. W. Litton, eds.), vol. 6895, p. 68950Z, feb 2008.

[42] W. I. Park, D. H. Kim, S. W. Jung, and G. C. Yi, "Metalorganic vapor-phase epitaxial growth of vertically well-aligned ZnO nanorods," *Applied Physics Letters*, vol. 80, no. 22, pp. 4232–4234, 2002.

[43] H. W. Kim, N. H. Kim, J.-H. Shim, N.-H. Cho, and C. Lee, "Catalyst-free MOCVD growth of ZnO nanorods and their structural characterization," *Journal of Materials Science: Materials in Electronics*, vol. 16, no. 1, pp. 13–15, 2005.

[44] Z. Z. Ye, J. Y. Huang, W. Z. Xu, J. Zhou, and Z. L. Wang, "Catalyst-free MOCVD growth of aligned ZnO nanotip arrays on silicon substrate with controlled tip shape," *Solid State Communications*, vol. 141, no. 8, pp. 464–466, 2007.

[45] M. H. Huang, "Room-Temperature Ultraviolet Nanowire Nanolasers," *Science*, vol. 292, no. 5523, pp. 1897–1899, 2001.

[46] X. Wang, J. Song, P. Li, J. H. Ryou, R. D. Dupuis, C. J. Summers, and Z. L. Wang, "Growth of uniformly aligned ZnO nanowire heterojunction arrays on GaN, AlN, and Al0.5Ga0.5N substrates," *Journal of the American Chemical Society*, vol. 127, no. 21, pp. 7920–7923, 2005.

[47] J. Song, X. Wang, E. Riedo, and Z. L. Wang, "Systematic study on experimental conditions for large-scale growth of aligned ZnO nanwires on nitrides," *Journal of Physical Chemistry B*, vol. 109, no. 20, pp. 9869–9872, 2005.

[48] X. Wang, J. Song, C. J. Summers, J. H. Ryou, P. Li, R. D. Dupuis, and Z. L. Wang, "Density-controlled growth of aligned ZnO nanowires sharing a common contact: A simple, low-cost, and mask-free technique for large-scale applications," *Journal of Physical Chemistry B*, vol. 110, no. 15, pp. 7720–7724, 2006.

[49] S. Xu, C. Lao, B. Weintraub, and Z. L. Wang, "Density-controlled growth of aligned ZnO nanowire arrays by seedless chemical approach on smooth surfaces," *Journal of Materials Research*, vol. 23, no. 08, pp. 2072–2077, 2008.

[50] S. Xu, Y. Wei, M. Kirkham, J. Liu, W. Mai, D. Davidovic, R. L. Snyder, and L. W. Zhong, "Patterned growth of vertically aligned ZnO nanowire arrays on inorganic substrates at low temperature without catalyst," *Journal of the American Chemical Society*, vol. 130, no. 45, pp. 14958–14959, 2008.

[51] Y. Qin, R. Yang, and Z. L. Wang, "Growth of Horizonatal ZnO Nanowire Arrays on Any Substrate," *The Journal of Physical Chemistry C*, vol. 112, pp. 18734–18736, dec 2008.

[52] N. D. Khoang, H. S. Hong, D. D. Trung, N. V. Duy, N. D. Hoa, D. D. Thinh, and N. V. Hieu, "On-chip growth of wafer-scale planar-type ZnO nanorod sensors for effective detection of CO gas," *Sensors and Actuators, B: Chemical*, vol. 181, pp. 529–536, may 2013.

[53] Y.-J. Lin and C.-L. Tsai, "Comment on "Threshold voltage control of oxide nanowire transistors using nitrogen plasma treatment" [Appl. Phys. Lett. 97, 203508 (2010)]," *Applied Physics Letters*, vol. 98, no. 17, p. 176101, 2011.

[54] W. Lin, A. A. Seshia, C.-C. Wu, and Y.-C. Lin, "Catalyst-free synthesis of zinc oxide nanostructures by microheaters in the ambient environment," in *2011 6th IEEE International Conference on Nano/Micro Engineered and Molecular Systems*, vol. 12, pp. 897–900, IEEE, feb 2011.

[55] P. K. Guha, S. Santra, J. A. Covington, F. Udrea, and J. W. Gardner, "Zinc oxide nanowire based hydrogen sensor on SOI CMOS platform," *Procedia Engineering*, vol. 25, pp. 1473–1476, 2011.

[56] S. Santra, S. Z. Ali, P. K. Guha, P. Hiralal, H. E. Unalan, S. H. Dalal, J. A. Covington, W. I. Milne, J. W. Gardner, and F. Udrea, "CMOS alcohol sensor employing zno nanowire sensing films," *AIP Conference Proceedings*, vol. 1137, pp. 119–122, 2009.

[57] S. Santra, P. K. Guha, S. Z. Ali, P. Hiralal, H. E. Unalan, J. A. Covington, G. A. J. Amaratunga, W. I. Milne, J. W. Gardner, and F. Udrea, "ZnO nanowires grown on SOI CMOS substrate for ethanol sensing," *Sensors and Actuators, B: Chemical*, vol. 146, pp. 559–565, apr 2010.

[58] S. Santra, P. K. Guha, S. K. Ray, F. Udrea, and J. W. Gardner, "SOI CMOS integrated zinc oxide nanowire for toluene detection," in *2013 IEEE 5th International Nanoelectronics Conference (INEC)*, pp. 119–121, IEEE, jan 2013.

[59] P.-C. Chang and J. G. Lu, "ZnO Nanowire Field-Effect Transistors," *IEEE Transactions on Electron Devices*, vol. 55, no. 11, pp. 2977–2987, 2008.

[60] Y. Y. S. Huang, T. Oppenheim, E. Terentjev, S. Lacour, and M. Welland, "Direct-write conductive fibres for soft electronics," *Proceedings of the IEEE Conference on Nanotechnology*, pp. 2–3, 2012.

[61] Z. Fan, D. Wang, P. C. Chang, W. Y. Tseng, and J. G. Lu, "ZnO nanowire field-effect transistor and oxygen sensing property," *Applied Physics Letters*, vol. 85, no. 24, pp. 5923–5925, 2004.

[62] W. I. Park, J. S. Kim, G.-C. Yi, M. H. Bae, and H.-J. Lee, "Fabrication and electrical characteristics of high-performance ZnO nanorod field-effect transistors," *Applied Physics Letters*, vol. 85, pp. 5052–5054, nov 2004.

[63] Z. Fan and J. G. Lu, "Electrical properties of ZnO nanowire field effect transistors characterized with scanning probes," *Applied Physics Letters*, vol. 86, no. 3, pp. 1–3, 2005.

[64] D.-J. Kim, J.-H. Hyung, D.-W. Seo, D.-I. Suh, and S.-K. Lee, "Dual-Gate Multiple-Channel ZnO Nanowire Transistors," *Journal of Electronic Materials*, vol. 39, pp. 563–567, may 2010.

[65] J. R. LaRoche, Y. W. Heo, B. S. Kang, L. C. Tien, Y. Kwon, D. P. Norton, B. P. Gila, F. Ren, and S. J. Pearton, "Fabrication approaches to ZnO nanowire devices," *Journal of Electronic Materials*, vol. 34, no. 4, pp. 404–408, 2005.

[66] K. Keem, J. Kang, C. Yoon, D. Yeom, D. Y. Jeong, B. M. Moon, and S. Kim, "A fabrication technique for top-gate ZnO nanowire field-effect transistors by a photolithography process," *Microelectronic Engineering*, vol. 84, no. 5-8, pp. 1622–1626, 2007.

[67] H.-J. Kim, C.-H. Lee, D.-W. Kim, and G.-C. Yi, "Fabrication and electrical characteristics of dual-gate ZnO nanorod metal–oxide semiconductor field-effect transistors," *Nanotechnology*, vol. 17, pp. S327–S331, jun 2006.

[68] D. I. Suh, S. Y. Lee, J. H. Hyung, T. H. Kim, and S. K. Lee, "Multiple ZnO nanowires field-effect transistors," *Journal of Physical Chemistry C*, vol. 112, no. 4, pp. 1276–1281, 2008.

[69] H. T. Ng, J. Han, T. Yamada, P. Nguyen, Y. P. Chen, and M. Meyyappan, "Single crystal nanowire vertical surround-gate field-effect transistor," *Nano Letters*, vol. 4, no. 7, pp. 1247–1252, 2004.

[70] G. A. J. Amaratunga, A. S. Teh, S. N. Cha, G. W. Ho, J. E. Jang, Y. Yang, Y. Choi, K. B. K. Teo, S. H. Dalal, D. J. Kang, N. L. Rupesinghe, W. I. Milne, D. Hasko, M. E. Welland, and J. M. Kim, "Nanotube and nanowire transistors," *Proceedings of the International Semiconductor Conference, CAS*, vol. 1, pp. 3–8, 2005.

[71] S. Cha, J. Jang, Y. Choi, G. Ho, D.-J. Kang, D. Hasko, M. Welland, and G. Amaratunga, "High performance ZnO nanowire field effect transistor," *Proceedings of 35th European Solid-State Device Research Conference, 2005. ESSDERC 2005.*, no. 1, pp. 217–220, 2005.

[72] S. N. Cha, J. E. Jang, Y. Choi, G. A. J. Amaratunga, G. W. Ho, M. E. Welland, D. G. Hasko, D. J. Kang, and J. M. Kim, "High performance ZnO nanowire field effect transistor using self-aligned nanogap gate electrodes," *Applied Physics Letters*, vol. 89, no. 26, pp. 10–13, 2006.

[73] S. W. Lee, M. H. Ham, J. P. Kar, W. Lee, and J. M. Myoung, "Selective alignment of a ZnO nanowire in a magnetic field for the fabrication of an air-gap field-effect transistor," *Microelectronic Engineering*, vol. 87, no. 1, pp. 10–14, 2010.

[74] K. Keem, D. Y. Jeong, S. Kim, M. S. Lee, I. S. Yeo, U. I. Chung, and J. T. Moon, "Fabrication and device characterization of omega-shaped-gate ZnO nanowire field-effect transistors," *Nano Letters*, vol. 6, no. 7, pp. 1454–1458, 2006.

[75] Y. W. Heo, L. C. Tien, Y. Kwon, D. P. Norton, S. J. Pearton, B. S. Kang, and F. Ren, "Depletion-mode ZnO nanowire field-effect transistor," *Applied Physics Letters*, vol. 85, no. 12, pp. 2274–2276, 2004.

[76] W. K. Hong, D. K. Hwang, I. K. Park, G. Jo, S. Song, S. J. Park, T. Lee, B. J. Kim, and E. A. Stach, "Realization of highly reproducible ZnO nanowire field effect transistors with n -channel depletion and enhancement modes," *Applied Physics Letters*, vol. 90, no. 24, pp. 1–4, 2007.

[77] G. Jo, W. K. Hong, J. Maeng, M. Choe, W. Park, and T. Lee, "Logic inverters composed of controlled depletion-mode and enhancement-mode ZnO nanowire transistors," *Applied Physics Letters*, vol. 94, no. 17, pp. 1–4, 2009.

[78] S. Roy and Z. Gao, "Direct-write fabrication of a nanoscale digital logic element on a single nanowire.," *Nanotechnology*, vol. 21, no. 24, p. 245306, 2010.

[79] C. Yim, D. Jeon, K. Kim, and G. Kim, "Electrical properties of the ZnO nanowire transistor and its analysis with equivalent circuit model," *Journal of the Korean . . .*, vol. 48, no. 6, pp. 1565–15691569, 2006.

[80] Y. Yoon, J. Lin, S. J. Pearton, and J. Guo, "Role of grain boundaries in ZnO nanowire field-effect transistors," *Journal of Applied Physics*, vol. 101, no. 2, 2007.

[81] S. Ju, K. Lee, D. B. Janes, M. H. Yoon, A. Facchetti, and T. J. Marks, "Low operating voltage single ZnO nanowire field-effect transistors enabled by self-assembled organic gate nanodielectrics," *Nano Letters*, vol. 5, no. 11, pp. 2281–2286, 2005.

[82] S. Ju, K. Lee, D. B. Janes, R. C. Dwivedi, H. Baffour-Awuah, R. Wilkins, M. H. Yoon, A. Facchetti, and T. J. Mark, "Proton radiation hardness of single-nanowire transistors using robust organic gate nanodielectrics," *Applied Physics Letters*, vol. 89, no. 7, 2006.

[83] S. Ju, D. B. Janes, G. Lu, A. Facchetti, and T. J. Marks, "Effects of bias stress on ZnO nanowire field-effect transistors fabricated with organic gate nanodielectrics," *Applied Physics Letters*, vol. 89, no. 19, 2006.

[84] S. Ju, K. Lee, M.-H. Yoon, A. Facchetti, T. J. Marks, and D. B. Janes, "High performance ZnO nanowire field effect transistors with organic gate nanodielectrics: effects of metal contacts and ozone treatment," *Nanotechnology*, vol. 18, no. 15, p. 155201, 2007.

[85] Y.-J. Kim, C.-H. Lee, Y. J. Hong, G.-C. Yi, S. S. Kim, and H. Cheong, "Controlled selective growth of ZnO nanorod and microrod arrays on Si substrates by a wet chemical method," *Applied Physics Letters*, vol. 89, no. 16, p. 163128, 2006.

[86] T.-H. Moon, M.-C. Jeong, B.-Y. Oh, M.-H. Ham, M.-H. Jeun, W.-Y. Lee, and J.-M. Myoung, "Chemical surface passivation of HfO 2 films in a ZnO nanowire transistor," *Nanotechnology*, vol. 17, no. 9, pp. 2116–2121, 2006.

[87] P.-C. Chang, Z. Fan, C.-J. Chien, D. Stichtenoth, C. Ronning, and J. G. Lu, "High-performance ZnO nanowire field effect transistors," *Applied Physics Letters*, vol. 89, no. 13, p. 133113, 2006.

[88] W.-K. Hong, S. Song, D.-K. Hwang, S.-S. Kwon, G. Jo, S.-J. Park, and T. Lee, "Effects of surface roughness on the electrical characteristics of ZnO nanowire field effect transistors," *Applied Surface Science*, vol. 254, no. 23, pp. 7559–7564, 2008.

[89] J. Song, X. Wang, J. Liu, H. Liu, Y. Li, and Z. L. Wang, "Piezoelectric potential output from ZnO nanowire functionalized with p-type oligomer," *Nano Letters*, vol. 8, no. 1, pp. 203–207, 2008.

[90] S. Nedic, *Zinc oxide nanowire field effect transistors*. PhD thesis, University of Cambridge, 2013.

[91] W.-K. Hong, J. I. Sohn, D.-K. Hwang, S.-S. Kwon, G. Jo, S. Song, S.-M. Kim, H.-J. Ko, S.-J. Park, M. E. Welland, and T. Lee, "Tunable Electronic Transport Characteristics of Surface-Architecture-Controlled ZnO Nanowire Field Effect Transistors," *Nano Letters*, vol. 8, no. 3, pp. 950–956, 2008.

[92] W.-K. Hong, B.-J. Kim, T.-W. Kim, G. Jo, S. Song, S.-S. Kwon, A. Yoon, E. A. Stach, and T. Lee, "Electrical properties of ZnO nanowire field effect transistors by surface passivation," *Colloids and Surfaces A: Physicochemical and Engineering Aspects*, vol. 313-314, pp. 378–382, 2008.

[93] J. Maeng, G. Jo, S. S. Kwon, S. Song, J. Seo, S. J. Kang, D. Y. Kim, and T. Lee, "Effect of gate bias sweep rate on the electronic properties of ZnO nanowire field-effect transistors under different environments," *Applied Physics Letters*, vol. 92, no. 23, pp. 10–13, 2008.

[94] J. I. Sohn, W.-K. Hong, M. J. Lee, T. Lee, H. Sirringhaus, D. J. Kang, and M. E. Welland, "The influence of surface chemical dynamics on electrical and optical properties of ZnO nanowire field effect transistors.," *Nanotechnology*, vol. 20, no. 50, p. 505202, 2009.

[95] D. Weissenberger, D. Gerthsen, A. Reiser, G. M. Prinz, M. Feneberg, K. Thonke, H. Zhou, J. Sartor, J. Fallert, C. Klingshirn, and H. Kalt, "Influence of the measurement procedure on the field-effect dependent conductivity of ZnO nanorods," *Applied Physics Letters*, vol. 94, no. 4, 2009.

[96] M. Choe, W. Park, J.-w. Kang, S. Jeong, W.-K. Hong, B. H. Lee, S.-J. Park, and T. Lee, "Investigation of threshold voltage instability induced by gate bias stress in ZnO nanowire field effect transistors," *Nanotechnology*, vol. 23, no. 48, p. 485201, 2012.

[97] W.-K. Hong, G. Jo, S.-S. Kwon, S. Song, and T. Lee, "Electrical Properties of Surface-Tailored ZnO Nanowire Field-Effect Transistors," *Ieee Transactions On Electron Devices*, vol. 55, pp. 3020–3029, nov 2008.

[98] S. Song, W. K. Hong, S. S. Kwon, and T. Lee, "Passivation effects on ZnO nanowire field effect transistors under oxygen, ambient, and vacuum environments," *Applied Physics Letters*, vol. 92, no. 26, pp. 3–5, 2008.

[99] S. Y. Lee, "Controllability of threshold voltage of ZnO nanowire field effect transistors by manipulating nanowire diameter by varying the catalyst thickness," *Transactions on Electrical and Electronic Materials*, vol. 14, no. 3, pp. 156–159, 2013.

[100] H.-W. Ra and Y.-H. Im, "Effect of chemically reactive species on properties of ZnO nanowires exposed to oxygen and hydrogen plasma," *Nanotechnology*, vol. 19, no. 48, p. 485710, 2008.

[101] Z.-M. Liao, Y. Lu, H.-C. Wu, Y.-Q. Bie, Y.-B. Zhou, and D.-P. Yu, "Improved performance of ZnO nanowire field-effect transistors via focused ion beam treatment," *Nanotechnology*, vol. 22, no. 37, p. 375201, 2011.

[102] W. Park, W.-K. Hong, G. Jo, G. Wang, M. Choe, J. Maeng, Y. H. Kahng, and T. Lee, "Tuning of operation mode of ZnO nanowire field effect transistors by solvent-driven surface treatment," *Nanotechnology*, vol. 20, no. 47, p. 475702, 2009.

[103] W.-k. Hong, G. Jo, J. I. Sohn, W. Park, M. Choe, G. Wang, Y. H. Kahng, M. E. Welland, and T. Lee, "Tuning of the Electronic Characteristics of ZnO Nanowire Field Effect Transistors by Proton Irradiation," *ACS Nano*, vol. 4, no. 2, pp. 811–818, 2010.

[104] M. Choe, W. K. Hong, W. Park, J. Yoon, G. Jo, T. Kwon, M. E. Welland, and T. Lee, "UV photoconductivity characteristics of ZnO nanowire field effect transistor treated by proton irradiation," *Thin Solid Films*, vol. 520, no. 9, pp. 3624–3628, 2012.

[105] J. Maeng, W. Park, M. Choe, G. Jo, Y. H. Kahng, and T. Lee, "Transient drain current characteristics of ZnO nanowire field effect transistors," *Applied Physics Letters*, vol. 95, no. 12, 2009.

[106] B. Xiang, P. Wang, X. Zhang, S. A. Dayeh, D. P. R. Aplin, C. Soci, D. Yu, and D. Wang, "Rational synthesis of p-type zinc oxide nanowire arrays using simple chemical vapor deposition," *Nano Letters*, vol. 7, no. 2, pp. 323–328, 2007.

[107] L. Ming, Z. Hai-Ying, G. Chang-Xin, X. Jing-Bo, F. Xiao-Jun, and C. Pu-Feng, "Characterization of ZnO nanowire field-effect transistors exposed to ultraviolet radiation," *Chinese Physics B*, vol. 18, pp. 5020–5023, nov 2009.

[108] G. D. Yuan, W. J. Zhang, J. S. Jie, X. Fan, J. A. Zapien, Y. H. Leung, L. B. Luo, P. F. Wang, C. S. Lee, and S. T. Lee, "p-type ZnO nanowire arrays," *Nano Letters*, vol. 8, no. 8, pp. 2591–2597, 2008.

[109] J. Kang, K. Keem, D. Y. Jeong, and S. Kim, "Electrical characteristics of ZnO nanowire-based field-effect transistors on flexible plastic substrates," *Japanese Journal of Applied Physics, Part 1: Regular Papers and Short Notes and Review Papers*, vol. 46, no. 9 B, pp. 6227–6229, 2007.

[110] S. Ju, A. Facchetti, Y. Xuan, J. Liu, F. Ishikawa, P. Ye, C. Zhou, T. J. Marks, and D. B. Janes, "Fabrication of fully transparent nanowire transistors for transparent and flexible electronics.," *Nature nanotechnology*, vol. 2, no. 6, pp. 378–384, 2007.

[111] Y.-Y. Noh, X. Cheng, H. Sirringhaus, J. I. Sohn, M. E. Welland, and D. J. Kang, "Ink-jet printed ZnO nanowire field effect transistors," *Applied Physics Letters*, vol. 91, no. 4, p. 043109, 2007.

[112] S. H. Ko, I. Park, H. Pan, N. Misra, M. S. Rogers, C. P. Grigoropoulos, and A. P. Pisano, "ZnO nanowire network transistor fabrication on a polymer substrate by low-temperature, all-inorganic nanoparticle solution process," *Applied Physics Letters*, vol. 92, no. 15, pp. 3–5, 2008.

[113] M. Liu, "Synthesis of ZnO Nanowires and Applications as Gas Sensors," *Science*, vol. 1, no. 9, 2010.

[114] S. J. Pearton, F. Ren, Y. L. Wang, B. H. Chu, K. H. Chen, C. Y. Chang, W. Lim, J. Lin, and D. P. Norton, "Recent advances in wide bandgap semiconductor biological and gas sensors," *Progress in Materials Science*, vol. 55, no. 1, pp. 1–59, 2010.

[115] K. J. Choi and H. W. Jang, "One-dimensional oxide nanostructures as gas-sensing materials: Review and issues," *Sensors*, vol. 10, no. 4, pp. 4083–4099, 2010.

[116] N. Barsan, D. Koziej, and U. Weimar, "Metal oxide-based gas sensor research: How to?," *Sensors and Actuators, B: Chemical*, vol. 121, pp. 18–35, jan 2007.

[117] T. Anderson, F. Ren, S. Pearton, B. S. Kang, H. T. Wang, C. Y. Chang, and J. Lin, "Advances in hydrogen, carbon dioxide, and hydrocarbon gas sensor technology using GaN and ZnO-based devices," *Sensors (Switzerland)*, vol. 9, no. 6, pp. 4669–4694, 2009.

[118] B. S. Kang, H.-T. Wang, L.-C. Tien, F. Ren, B. P. Gila, D. P. Norton, C. R. Abernathy, J. Lin, and S. J. Pearton, "Wide Bandgap Semiconductor Nanorod and Thin Film Gas Sensors," *Sensors*, vol. 6, no. 6, pp. 643–666, 2006.

[119] X.-J. Huang and Y.-K. Choi, "Chemical sensors based on nanostructured materials," *Sensors and Actuators B: Chemical*, vol. 122, pp. 659–671, mar 2007.

[120] G. Di Francia, B. Alfano, and V. La Ferrara, "Conductometric gas nanosensors," *Journal of Sensors*, vol. 2009, 2009.

[121] J. Huang and Q. Wan, "Gas sensors based on semiconducting metal oxide one-dimensional nanostructures," *Sensors*, vol. 9, no. 12, pp. 9903–9924, 2009.

[122] J. S. Wright, W. Lim, D. P. Norton, S. J. Pearton, F. Ren, J. L. Johnson, and A. Ural, "Nitride and oxide semiconductor nanostructured hydrogen gas sensors," *Semiconductor Science and Technology*, vol. 25, no. 2, p. 024002, 2010.

[123] H. Gu, Z. Wang, and Y. Hu, "Hydrogen Gas Sensors Based on Semiconductor Oxide Nanostructures," *Sensors*, vol. 12, pp. 5517–5550, apr 2012.

[124] A. Z. Sadek, S. Choopun, W. Wlodarski, S. J. Ippolito, and K. Kalantar-zadeh, "Characterization of ZnO nanobelt-based gas sensor for H2, NO2, and hydrocarbon sensing," *IEEE Sensors Journal*, vol. 7, pp. 919–924, jun 2007.

[125] H. U. Lee, K. Ahn, S. J. Lee, J. P. Kim, H. G. Kim, S. Y. Jeong, and C. R. Cho, "ZnO nanobarbed fibers: Fabrication, sensing NO2 gas, and their sensing mechanism," *Applied Physics Letters*, vol. 98, no. 19, pp. 2011–2014, 2011.

[126] B. Kang, Y. Heo, L. Tien, D. Norton, F. Ren, B. Gila, and S. Pearton, "Hydrogen and ozone gas sensing using multiple ZnO nanorods," *Applied Physics A*, vol. 80, pp. 1029–1032, feb 2004.

[127] T. J. Hsueh, C. L. Hsu, S. J. Chang, and I. C. Chen, "Laterally grown ZnO nanowire ethanol gas sensors," *Sensors and Actuators, B: Chemical*, vol. 126, pp. 473–477, oct 2007.

[128] D. Zhang, S. Chava, C. Berven, S. K. Lee, R. Devitt, and V. Katkanant, "Experimental study of electrical properties of ZnO nanowire random networks for gas sensing and electronic devices," *Applied Physics A*, vol. 100, pp. 145–150, jul 2010.

[129] M. Yin, M. Liu, and S. Liu, "Development of an alcohol sensor based on ZnO nanorods synthesized using a scalable solvothermal method," *Sensors and Actuators, B: Chemical*, vol. 185, pp. 735–742, aug 2013.

[130] L. Liao, H. B. Lu, M. Shuai, J. C. Li, Y. L. Liu, C. Liu, Z. X. Shen, and T. Yu, "A novel gas sensor based on field ionization from ZnO nanowires: moderate working voltage and high stability.," *Nanotechnology*, vol. 19, no. 17, p. 175501, 2008.

[131] H. W. Ra, K. S. Choi, J. H. Kim, Y. B. Hahn, and Y. H. Im, "Fabrication of ZnO nanowires using nanoscale spacer lithography for gas sensors," *Small*, vol. 4, no. 8, pp. 1105–1109, 2008.

[132] J. Y. Son, S. J. Lim, J. H. Cho, W. K. Seong, and H. Kim, "Synthesis of horizontally aligned ZnO nanowires localized at terrace edges and application for high sensitivity gas sensor," *Applied Physics Letters*, vol. 93, no. 5, pp. 1–4, 2008.

[133] S.-W. Choi, J. Y. Park, and S. S. Kim, "Synthesis of SnO2-ZnO core-shell nanofibers via a novel two-step process and their gas sensing properties.," *Nanotechnology*, vol. 20, p. 465603, 2009.

[134] J. Y. Park, S.-W. Choi, and S. S. Kim, "A model for the enhancement of gas sensing properties in SnO2 –ZnO core–shell nanofibres," *Journal of Physics D: Applied Physics*, vol. 44, p. 205403, may 2011.

[135] S. Park, S. An, Y. Mun, and C. Lee, "UV-Enhanced NO2 Gas Sensing Properties of SnO2-Core/ZnO-Shell Nanowires at Room Temperature," *ACS Applied Materials and Interfaces*, vol. 5, pp. 4285–4292, may 2013.

[136] H.-W. Ra, R. Khan, J. T. Kim, B. R. Kang, and Y. H. Im, "The effect of grain boundaries inside the individual ZnO nanowires in gas sensing," *Nanotechnology*, vol. 21, no. 8, p. 85502, 2010.

[137] S. Park, S. An, H. Ko, C. Jin, and C. Lee, "Synthesis of Nanograined ZnO Nanowires and Their Enhanced Gas Sensing Properties," *ACS Applied Materials and Interfaces Interfaces*, vol. 4, pp. 3650–3656, jul 2012.

[138] J. Chu, X. Peng, Z. Wang, and P. Feng, "Sensing performances of ZnO nanostructures grown under different oxygen pressures to hydrogen," *Materials Research Bulletin*, vol. 47, no. 12, pp. 4420–4426, 2012.

[139] Y. Zhang, J. Xu, P. Xu, Y. Zhu, X. Chen, and W. Yu, "Decoration of ZnO nanowires with Pt nanoparticles and their improved gas sensing and photocatalytic performance.," *Nanotechnology*, vol. 21, no. 28, p. 285501, 2010.

[140] L. C. Tien, H. T. Wang, B. S. Kang, F. Ren, P. W. Sadik, D. P. Norton, S. J. Pearton, and J. Lin, "Room-Temperature Hydrogen-Selective Sensing Using Single Pt-Coated ZnO Nanowires at Microwatt Power Levels," *Electrochemical and Solid-State Letters*, vol. 8, no. 9, p. G230, 2005.

[141] L. C. Tien, P. W. Sadik, D. P. Norton, L. F. Voss, S. J. Pearton, H. T. Wang, B. S. Kang, F. Ren, J. Jun, and J. Lin, "Hydrogen sensing at room temperature with Pt-coated ZnO thin films and nanorods," *Applied Physics Letters*, vol. 87, no. 22, pp. 1–3, 2005.

[142] T. J. Hsueh, S. J. Chang, C. L. Hsu, Y. R. Lin, and I. C. Chen, "Highly sensitive ZnO nanowire ethanol sensor with Pd adsorption," *Applied Physics Letters*, vol. 91, no. 5, 2007.

[143] L.-L. Xing, C.-H. Ma, Z.-H. Chen, Y.-J. Chen, and X.-Y. Xue, "High gas sensing performance of one-step-synthesized Pd-ZnO nanoflowers due to surface reactions and modifications.," *Nanotechnology*, vol. 22, p. 215501, 2011.

[144] K. V. Gurav, P. R. Deshmukh, and C. D. Lokhande, "LPG sensing properties of Pd-sensitized vertically aligned ZnO nanorods," *Sensors and Actuators, B: Chemical*, vol. 151, pp. 365–369, jan 2011.

[145] H. T. Wang, B. S. Kang, F. Ren, L. C. Tien, P. W. Sadik, D. P. Norton, S. J. Pearton, and J. Lin, "Hydrogen-selective sensing at room temperature with ZnO nanorods," *Applied Physics Letters*, vol. 86, no. 24, pp. 1–3, 2005.

[146] N. S. Ramgir, P. K. Sharma, N. Datta, M. Kaur, A. K. Debnath, D. K. Aswal, and S. K. Gupta, "Room temperature H2S sensor based on Au modified ZnO nanowires," *Sensors and Actuators, B: Chemical*, vol. 186, pp. 718–726, sep 2013.

[147] S.-J. Chang, T.-J. Hsueh, I.-C. Chen, and B.-R. Huang, "Highly sensitive ZnO nanowire CO sensors with the adsorption of Au nanoparticles," *Nanotechnology*, vol. 19, no. 17, p. 175502, 2008.

[148] Z. Fan and J. G. Lu, "Gate-refreshable nanowire chemical sensors," *Applied Physics Letters*, vol. 86, no. 12, pp. 1–3, 2005.

[149] Q. H. Li, Y. X. Liang, Q. Wan, and T. H. Wang, "Oxygen sensing characteristics of individual ZnO nanowire transistors," *Applied Physics Letters*, vol. 85, no. 26, pp. 6389–6391, 2004.

[150] P. C. Chen, G. Shen, and C. Zhou, "Chemical sensors and electronic noses based on 1-D metal oxide nanostructures," *IEEE Transactions on Nanotechnology*, vol. 7, no. 6, pp. 668–682, 2008.

[151] a.D Wilson and M. Baietto, "Applications and advances in electronic-nose technologies.," *Sensors*, vol. 9, no. 7, pp. 5099–5148, 2009.

[152] A. P. Turner and N. Magan, "Innovation: Electronic noses and disease diagnostics," *Nature Reviews Microbiology*, vol. 2, no. 2, pp. 161–166, 2004.

[153] F. Röck, N. Barsan, and U. Weimar, "Electronic nose: Current status and future trends," *Chemical Reviews*, vol. 108, no. 2, pp. 705–725, 2008.

[154] J. W. Gardner and P. N. Bartlett, "A brief history of electronic noses," *Sensors and Actuators: B. Chemical*, vol. 18, no. 1-3, pp. 210–211, 1994.

[155] D. J. Strike, M. G. H. Meijerink, and M. Koudelka-Hep, "Electronic noses - A mini-review," *Fresenius' Journal of Analytical Chemistry*, vol. 364, no. 6, pp. 499–505, 1999.

[156] A. Berna, "Metal oxide sensors for electronic noses and their application to food analysis," *Sensors*, vol. 10, no. 4, pp. 3882–3910, 2010.

[157] A. A. Tomchenko, G. P. Harmer, B. T. Marquis, and J. W. Allen, "Semiconducting metal oxide sensor array for the selective detection of combustion gases," *Sensors and Actuators, B: Chemical*, vol. 93, pp. 126–134, aug 2003.

[158] M. Martí, O. Busto, J. Guasch, and R. Boqué, "Electronic noses in the quality control of alcoholic beverages," *TrAC Trends in Analytical Chemistry*, vol. 24, pp. 57–66, jan 2005.

[159] C. Wongchoosuk, A. Wisitsoraat, A. Tuantranont, and T. Kerdcharoen, "Portable electronic nose based on carbon nanotube-SnO2 gas sensors and its application for detection of methanol contamination in whiskeys," *Sensors and Actuators, B: Chemical*, vol. 147, pp. 392–399, jun 2010.

[160] K. Arshak, E. Moore, G. Lyons, J. Harris, and S. Clifford, "A review of gas sensors employed in electronic nose applications," *Sensor Review*, vol. 24, no. 2, pp. 181–198, 2004.

[161] D. James, S. M. Scott, Z. Ali, and W. T. O'Hare, "Chemical sensors for electronic nose systems," *Microchimica Acta*, vol. 149, no. 1-2, pp. 1–17, 2005.

[162] M. K. Baller, H. P. Lang, J. Fritz, C. Gerber, J. K. Gimzewski, U. Drechsler, H. Rothuizen, M. Despont, P. Vettiger, F. M. Battiston, J. P. Ramseyer, P. Fornaro, E. Meyer, and H. J. Güntherodt, "A cantilever array-based artificial nose," *Ultramicroscopy*, vol. 82, no. 1-4, pp. 1–9, 2000.

[163] H. P. Lang, M. K. Baller, R. Berger, C. Gerber, J. K. Gimzewski, F. M. Battiston, P. Fornaro, J. P. Ramseyer, E. Meyer, and H. J. Güntherodt, "An artificial nose based on a micromechanical cantilever array," *Analytica Chimica Acta*, vol. 393, no. 1-3, pp. 59–65, 1999.

[164] H. P. Lang, J. P. Ramseyer, W. Grange, T. Braun, D. Schmid, P. Hunziker, C. Jung, M. Hegner, and C. Gerber, "An Artificial Nose Based on Microcantilever Array Sensors," *Journal of Physics: Conference Series*, vol. 61, pp. 663–667, 2007.

[165] P.-C. Chen, F. N. Ishikawa, H.-K. Chang, K. Ryu, and C. Zhou, "A nanoelectronic nose: a hybrid nanowire/carbon nanotube sensor array with integrated micromachined hotplates for sensitive gas discrimination.," *Nanotechnology*, vol. 20, no. 12, p. 125503, 2009.

[166] M. Castro, B. Kumar, J. F. Feller, Z. Haddi, A. Amari, and B. Bouchikhi, "Novel e-nose for the discrimination of volatile organic biomarkers with an array of carbon nanotubes (CNT) conductive polymer nanocomposites (CPC) sensors," *Sensors and Actuators, B: Chemical*, vol. 159, pp. 213–219, nov 2011.

[167] Y. Hu, H. Lee, S. Kim, and M. Yun, "A highly selective chemical sensor array based on nanowire/nanostructure for gas identification," *Sensors and Actuators, B: Chemical*, vol. 181, pp. 424–431, may 2013.

[168] V. V. Sysoev, E. Strelcov, M. Sommer, M. Bruns, I. Kiselev, W. Habicht, S. Kar, L. Gregoratti, M. Kiskinova, and A. Kolmakov, "Single-Nanobelt Electronic Nose: Engineering and Tests of the Simplest Analytical Element," *ACS Nano*, vol. 4, pp. 4487–4494, aug 2010.

[169] S. MacNaughton, S. Sonkusale, S. Surwade, S. Ammu, and S. Manohar, "Electronic nose based on graphene, nanotube and nanowire chemiresistor arrays on silicon," *Proceedings of IEEE Sensors*, pp. 125–128, 2011.

[170] W. Ko, N. Jung, M. Lee, M. Yun, and S. Jeon, "Electronic nose based on multipatterns of zno nanorods on a quartz resonator with remote electrodes," *ACS Nano*, vol. 7, no. 8, pp. 6685–6690, 2013.

[171] J. Chen, H. Su, and W. Zhou, "Gas discrimination by ZnO nanowire arrays with different metal oxide coatings," in *2011 11th IEEE International Conference on Nanotechnology*, pp. 34–37, IEEE, aug 2011.

[172] H. Su, J. Chen, K. Wang, A. A. Ayyad, and W. Zhou, "The Electronic Nose : The Effect of Metal Oxide Modifications to Well-Aligned ZnO Nanowire Arrays for Highly Sensitive and Selective Gas Detection," in *Proc. IMCS 2012 – 14th Int. Meet. Chem. Sensors*, no. 2, pp. 126–129, 2012.

[173] J. Chen, K. Wang, and W. Zhou, "Vertically Aligned ZnO Nanorod Arrays Coated with SnO2/Noble Metal Nanoparticles for Highly Sensitive and Selective Gas Detection," *IEEE Transactions on Nanotechnology*, vol. 10, pp. 968–974, sep 2011.

[174] B. Kateb, M. A. Ryan, M. L. Homer, L. M. Lara, Y. Yin, K. Higa, and M. Y. Chen, "Sniffing out cancer using the JPL electronic nose: A pilot study of a novel approach to detection and differentiation of brain cancer," *NeuroImage*, vol. 47, no. SUPPL. 2, pp. T5–T9, 2009.

[175] S. Dragonieri, R. Schot, B. J. A. Mertens, S. Le Cessie, S. A. Gauw, A. Spanevello, O. Resta, N. P. Willard, T. J. Vink, K. F. Rabe, E. H. Bel, and P. J. Sterk, "An electronic nose in the discrimination of patients with asthma and controls," *Journal of Allergy and Clinical Immunology*, vol. 120, no. 4, pp. 856–862, 2007.

[176] M. Phillips, S. C. Erzurum, T. Burch, D. Laskowski, P. J. Mazzone, T. Mekhail, C. Jennings, J. K. Stoller, R. F. Machado, J. Pyle, O. Deffenderfer, and R. A. Dweik, "Can the electronic nose really sniff out lung cancer?," *American Journal of Respiratory and Critical Care Medicine*, vol. 172, pp. 1060–1061, oct 2005.

[177] C. Di Natale, A. Macagnano, E. Martinelli, R. Paolesse, G. D'Arcangelo, C. Roscioni, A. Finazzi-Agrò, and A. D'Amico, "Lung cancer identification by the analysis of breath by means of an array of non-selective gas sensors," *Biosensors and Bioelectronics*, vol. 18, pp. 1209–1218, sep 2003.

[178] J. W. Gardner, H. W. Shin, and E. L. Hines, "Electronic nose system to diagnose illness," *Sensors and Actuators, B: Chemical*, vol. 70, pp. 19–24, nov 2000.

[179] S. Chen, Y. Wang, and S. Choi, "Applications and Technology of Electronic Nose for Clinical Diagnosis," *Open Journal of Applied Biosensor*, vol. 02, no. 02, pp. 39–50, 2013.

[180] D. Ledwith, S. C. Pillai, G. W. Watson, and J. M. Kelly, "Microwave induced preparation of a-axis oriented double-ended needle-shaped ZnO microparticles," *Chemical Communications*, no. 20, p. 2294, 2004.

[181] H.-H. Park, X. Zhang, K. W. Lee, K. H. Kim, S. H. Jung, D. S. Park, Y. S. Choi, H.-b. Shin, H. K. Sung, K. H. Park, H. K. Kang, H.-h. Park, and C. K. Ko, "Position-controlled hydrothermal growth of ZnO nanorods on arbitrary substrates with a patterned seed layer via ultraviolet-assisted nanoimprint lithography," *CrystEngComm*, vol. 15, no. 17, p. 3463, 2013.

[182] M. S. M. Saifullah, K. R. V. Subramanian, D. J. Kang, D. Anderson, W. T. S. Huck, G. A. C. Jones, and M. E. Welland, "Sub-10 nm high-aspect-ratio patterning of ZnO using an electron beam," *Advanced Materials*, vol. 17, pp. 1757–1761, jul 2005.

[183] G. Xiong, G. Jones, R. Rungsawang, and D. Anderson, "Non-aqueous solution processed ZnO thin film transistors," *Thin Solid Films*, vol. 518, pp. 4019–4023, may 2010.

[184] G. Adamopoulos, A. Bashir, W. P. Gillin, S. Georgakopoulos, M. Shkunov, M. A. Baklar, N. Stingelin, D. D. C. Bradley, and T. D. Anthopoulos, "Structural and electrical characterization of ZnO films grown by spray pyrolysis and their application in thin-film transistors," *Advanced Functional Materials*, vol. 21, no. 3, pp. 525–531, 2011.

[185] B. D. Viezbicke, S. Patel, B. E. Davis, and D. P. Birnie, "Evaluation of the Tauc method for optical absorption edge determination: ZnO thin films as a model system," *Physica Status Solidi (B)*, vol. 11, no. 8, pp. n/a–n/a, 2015.

[186] S. T. Tan, B. J. Chen, X. W. Sun, W. J. Fan, H. S. Kwok, X. H. Zhang, and S. J. Chua, "Blueshift of optical band gap in ZnO thin films grown by metal-organic chemical-vapor deposition," *Journal of Applied Physics*, vol. 98, no. 1, 2005.

[187] R. R. Ghimire, S. Mondal, and A. K. Raychaudhuri, "Synergistic ultraviolet photoresponse of a nanostructured ZnO film with gate bias and ultraviolet illumination," *Journal of Applied Physics*, vol. 117, no. 10, 2015.

[188] J. Lu, Z. Ye, L. Wang, J. Huang, and B. Zhao, "Structural, electrical and optical properties of N-doped ZnO films synthesized by SS-CVD," *Materials Science in Semiconductor Processing*, vol. 5, no. 6, pp. 491–496, 2002.

[189] M. F. Malek, M. H. Mamat, M. Z. Sahdan, M. M. Zahidi, Z. Khusaimi, and M. R. Mahmood, "Influence of various sol concentrations on stress/strain and properties of ZnO thin films synthesised by sol-gel technique," *Thin Solid Films*, vol. 527, pp. 102–109, 2013.

[190] V. Srikant and D. R. Clarke, "On the optical band gap of zinc oxide," *Journal of Applied Physics*, vol. 83, pp. 5447–5451, may 1998.

[191] Y. Chen, S.-k. Hong, H.-j. Ko, M. Nakajima, T. Yao, and Y. Segawa, "Plasma-assisted molecular-beam epitaxy of ZnO epilayers on atomically flat MgAl2O4(111) substrates," *Applied Physics Letters*, vol. 76, no. 111, pp. 245–247, 2000.

[192] Y. Chen, D. M. Bagnall, H.-j. Koh, K.-t. Park, K. Hiraga, Z. Zhu, and T. Yao, "Plasma assisted molecular beam epitaxy of ZnO on c -plane sapphire: Growth and characterization," *Journal of Applied Physics*, vol. 84, no. 7, p. 3912, 1998.

[193] K.-K. Kim, J.-H. Song, H.-J. Jung, W.-K. Choi, S.-J. Park, J.-H. Song, and J.-Y. Lee, "Photoluminescence and heteroepitaxy of ZnO on sapphire substrate (0001) grown by rf magnetron sputtering," *Journal of Vacuum Science & Technology A: Vacuum, Surfaces, and Films*, vol. 18, pp. 2864–2868, nov 2000.

[194] V. V. Khomyak, M. M. Slyotov, I. I. Shtepliuk, G. V. Lashkarev, O. M. Slyotov, P. D. Marianchuk, and V. V. Kosolovskiy, "Annealing effect on the near-band edge emission of ZnO," *Journal of Physics and Chemistry of Solids*, vol. 74, no. 2, pp. 291–297, 2013.

[195] S. Mridha and D. Basak, "Effect of thickness on the structural, electrical and optical properties of ZnO films," *Materials Research Bulletin*, vol. 42, pp. 875–882, may 2007.

[196] J. S. Lyu, K. S. Nam, and C. Lee, "Determination of the interface trap density in metal oxide semiconductor field-effect transistor through subthreshold slope measurement," *Japanese Journal of Applied Physics*, vol. 32, no. 10 R, pp. 4393–4397, 1993.

[197] S. Lee, S. Jeong, D. Kim, B. K. Park, and J. Moon, "Fabrication of a solution-processed thin-film transistor using zinc oxide nanoparticles and zinc acetate," *Superlattices and Microstructures*, vol. 42, no. 1-6, pp. 361–368, 2007.

[198] Y. H. Hwang, S.-J. Seo, and B.-S. Bae, "Fabrication and characterization of sol-gel-derived zinc oxide thin-film transistor," *Journal of Materials Research*, vol. 25, pp. 695–700, apr 2010.

[199] S. Jeong and J. Moon, "Low-temperature, solution-processed metal oxide thin film transistors," *Journal of Materials Chemistry*, vol. 22, no. 4, pp. 1243–1250, 2012.

[200] C.-s. Li, Y.-n. Li, Y.-l. Wu, B.-s. Ong, and R.-o. Loutfy, "Fabrication conditions for solution-processed high-mobility ZnO thin-film transistors," *Journal of Materials Chemistry*, vol. 19, pp. 1626–16341634, 2009.

[201] A. Bashir, P. H. Wöbkenberg, J. Smith, J. M. Ball, G. Adamopoulos, D. D. C. Bradley, and T. D. Anthopoulos, "High-Performance Zinc Oxide Transistors and Circuits Fabricated by Spray Pyrolysis in Ambient Atmosphere," *Advanced Materials*, vol. 21, pp. 2226–2231, jun 2009.

[202] S. Lee, K. Ghaffarzadeh, A. Nathan, J. Robertson, S. Jeon, C. Kim, I. H. Song, and U. I. Chung, "Trap-limited and percolation conduction mechanisms in amorphous oxide semiconductor thin film transistors," *Applied Physics Letters*, vol. 98, no. 20, pp. 98–101, 2011.

[203] Y.-H. Lin, H. Faber, K. Zhao, Q. Wang, A. Amassian, M. McLachlan, and T. D. Anthopoulos, "High-Performance ZnO Transistors Processed Via an Aqueous Carbon-Free Metal Oxide Precursor Route at Temperatures Between 80-180 °C," *Advanced Materials*, vol. 25, pp. 4340–4346, aug 2013.

[204] J. F. Cordaro, Y. Shim, and J. E. May, "Bulk electron traps in zinc oxide varistors," *Journal of Applied Physics*, vol. 60, no. 12, pp. 4186–4190, 1986.

[205] S. M. Sultan, K. Sun, M. R. R. De Planque, P. Ashburn, and H. M. H. Chong, "Top-down fabricated ZnO nanowire transistors for application in biosensors," *European Solid-State Device Research Conference*, no. c, pp. 137–140, 2012.

[206] K. K. Lee, Y. Luo, X. Lu, P. Bao, and A. M. Song, "Development of reactive-ion etching for ZnO-based nanodevices," *IEEE Transactions on Nanotechnology*, vol. 10, no. 4, pp. 839–843, 2011.

[207] K. Y. Yang, K. M. Yoon, K. W. Choi, and H. Lee, "The direct nano-patterning of ZnO using nanoimprint lithography with ZnO-sol and thermal annealing," *Microelectronic Engineering*, vol. 86, no. 11, pp. 2228–2231, 2009.

[208] M.-H. Jung and H. Lee, "Selective patterning of ZnO nanorods on silicon substrates using nanoimprint lithography.," *Nanoscale research letters*, vol. 6, p. 159, jan 2011.

[209] H.-B. Jo, K.-J. Byeon, H. Lee, M.-H. Kwon, and K.-W. Choi, "Fabrication of ZnO nano-structures using UV nanoimprint lithography of a ZnO nano-particle dispersion resin," *Journal of Materials Chemistry*, vol. 22, no. 38, p. 20742, 2012.

[210] S. Kim, D. O. Shin, D. G. Choi, J. R. Jeong, J. H. Mun, Y. B. Yang, J. U. Kim, S. O. Kim, and J. H. Jeong, "Graphoepitaxy of block-copolymer self-assembly integrated with single-step ZnO nanoimprinting," *Small*, vol. 8, no. 10, pp. 1563–1569, 2012.

[211] V. Auzelyte, H. Sigg, B. Schmitt, and H. H. Solak, "Direct formation of ZnO nanostructures by chemical solution deposition and EUV exposure," *Nanotechnology*, vol. 21, no. 21, p. 215302, 2010.

[212] M. S. M. Saifullah, K. R. V. Subramanian, D. Anderson, D.-J. Kang, W. T. S. Huck, G. A. C. Jones, and M. E. Welland, "Sub-10-nm high aspect ratio patterning of ZnO in a 500 μm main field," *Journal of Vacuum Science and Technology B: Microelectronics and Nanometer Structures*, vol. 24, no. 3, p. 1215, 2006.

[213] J. van Kan, A. Bettiol, S. Chiam, M. Saifullah, K. Subramanian, M. Welland, and F. Watt, "New resists for proton beam writing," *Nuclear Instruments and Methods in Physics Research Section B: Beam Interactions with Materials and Atoms*, vol. 260, pp. 460–463, jul 2007.

[214] M. Nedelcu, M. S. M. Saifullah, D. G. Hasko, A. Jang, D. Anderson, W. T. S. Huck, G. A. C. Jones, M. E. Weiland, D. J. Kang, and U. Steiner, "Fabrication of sub-10nm metallic lines of low line-width roughness by hydrogen reduction of patterned metal-organic materials," *Advanced Functional Materials*, vol. 20, pp. 2317–2323, jun 2010.

[215] Y. S. Rim, H. S. Lim, and H. J. Kim, "Low-temperature metal-oxide thin-film transistors formed by directly photopatternable and combustible solution synthesis," *ACS Applied Materials and Interfaces*, vol. 5, pp. 3565–3571, may 2013.

[216] A. Olziersky, P. Barquinha, A. Vilà, L. Pereira, G. Gonçalves, E. Fortunato, R. Martins, and J. R. Morante, "Insight on the SU-8 resist as passivation layer for transparent Ga2O3–In2O3–ZnO thin-film transistors," *Journal of Applied Physics*, vol. 108, p. 064505, sep 2010.

[217] H. H. Hsieh and C. C. Wu, "Amorphous ZnO transparent thin-film transistors fabricated by fully lithographic and etching processes," *Applied Physics Letters*, vol. 91, no. 1, pp. 23–26, 2007.

[218] S. M. Sultan, O. D. Clark, T. B. Masaud, Q. Fang, R. Gunn, M. M. A. Hakim, K. Sun, P. Ashburn, and H. M. H. Chong, "Remote plasma enhanced atomic layer deposition of ZnO for thin film electronic applications," *Microelectronic Engineering*, vol. 97, pp. 162–165, 2012.

[219] S. M. Sultan, N. J. Ditshego, R. Gunn, P. Ashburn, and H. M. Chong, "Effect of atomic layer deposition temperature on the performance of top-down ZnO nanowire transistors," *Nanoscale Research Letters*, vol. 9, no. 1, p. 517, 2014.

[220] N. A. B. Ghazali, M. Ebert, N. M. J. Ditshego, M. R. R. De Planque, and H. M. H. Chong, "Top-down fabrication optimisation of ZnO nanowire-FET by sidewall smoothing," *Microelectronic Engineering*, vol. 159, pp. 121–126, 2016.

[221] H. S. Lim, Y. S. Rim, and H. J. Kim, "Photoresist-free fully self-patterned transparent amorphous oxide thin-film transistors obtained by sol-gel process.," *Scientific reports*, vol. 4, p. 4544, 2014.

[222] Y. S. Rim, H. Chen, Y. Liu, S. H. Bae, H. J. Kim, and Y. Yang, "Direct light pattern integration of low-temperature solution-processed all-oxide flexible electronics," *ACS Nano*, vol. 8, no. 9, pp. 9680–9686, 2014.

[223] H.-C. Lin, F. Stehlin, O. Soppera, H.-W. Zan, C.-H. Li, F. Wieder, A. Ponche, D. Berling, B.-H. Yeh, and K.-H. Wang, "Deep ultraviolet laser direct write for patterning sol-gel InGaZnO semiconducting micro/nanowires and improving field-effect mobility," *Scientific reports*, vol. 5, no. April, p. 10490, 2015.

[224] C. C. Yeh, H. C. Liu, M. Y. Chuang, J. Denzer, D. Berling, H. W. Zan, and O. Soppera, "Controllable Formation of Zinc Oxide Micro- and Nanostructures via DUV Direct Patterning," *Advanced Materials Interfaces*, vol. 3, no. 19, p. 1600373, 2016.

[225] Y. J. Jeong, T. K. An, D. J. Yun, L. H. Kim, S. Park, Y. Kim, S. Nam, K. H. Lee, S. H. Kim, J. Jang, and C. E. Park, "Photo-Patternable ZnO Thin Films Based on Cross-Linked Zinc Acrylate for Organic/Inorganic Hybrid Complementary Inverters," *ACS Applied Materials and Interfaces*, vol. 8, pp. 5499–5508, mar 2016.

[226] G. A. C. Jones, G. Xiong, and D. Anderson, "Fabrication of nanoscale ZnO field effect transistors using the functional precursor zinc neodecanoate directly as a negative electron beam lithography resist," *Journal of Vacuum Science and Technology B: Microelectronics and Nanometer Structures*, vol. 27, no. 6, p. 3164, 2009.

[227] L.-l. Chua, J. Zaumseil, J.-f. Chang, E. C.-W. Ou, P. K.-H. Ho, H. Sirringhaus, and R. H. Friend, "General observation of n-type field-effect behaviour in organic semiconductors," *Nature*, vol. 434, pp. 194–199, mar 2005.

[228] L. J. Brillson and Y. Lu, "ZnO Schottky barriers and Ohmic contacts," *Journal of Applied Physics*, vol. 109, no. 12, 2011.

[229] J.-S. Park, J. K. Jeong, Y.-G. Mo, H. D. Kim, and C.-J. Kim, "Control of threshold voltage in ZnO-based oxide thin film transistors," *Applied Physics Letters*, vol. 93, p. 033513, jul 2008.

[230] D. Kälblein, H. Ryu, F. Ante, B. Fenk, K. Hahn, K. Kern, and H. Klauk, "High-Performance ZnO Nanowire Transistors with Aluminum Top-Gate Electrodes and Naturally Formed Hybrid Self-Assembled Monolayer/AlO x Gate Dielectric," *ACS Nano*, vol. 8, pp. 6840–6848, jul 2014.

[231] H. W. Ra, K. S. Choi, C. W. Ok, S. Y. Jo, K. H. Bai, and Y. H. Im, "Ion bombardment effects on ZnO nanowires during plasma treatment," *Applied Physics Letters*, vol. 93, no. 3, pp. 1–4, 2008.

[232] H. Qian, Y. Wang, Y. Fang, L. Gu, R. Lu, and J. Sha, "High-performance ZnO nanowire field-effect transistor with forming gas treated SiO 2 gate dielectrics," *Journal of Applied Physics*, vol. 117, p. 164308, apr 2015.

[233] A. Janotti and C. G. Van de Walle, "Fundamentals of zinc oxide as a semiconductor," *Rep Prog Phy*, vol. 72, p. 126501, dec 2009.

[234] C.-Y. Nam, A. Stein, K. Kisslinger, and C. T. Black, "Electrical and structural properties of ZnO synthesized via infiltration of lithographically defined polymer templates," *Applied Physics Letters*, vol. 107, p. 203106, nov 2015.

[235] V. P. Dravid, ""Controlling" internal microstructure of nanopatterned oxides via soft electron beam lithography (soft-eBL)," *Journal of Materials Chemistry*, vol. 19, no. 25, p. 4295, 2009.

[236] C.-S. Chou, Y.-C. Wu, and C.-H. Lin, "Oxygen sensor utilizing ultraviolet irradiation assisted ZnO nanorods under low operation temperature," *RSC Adv.*, vol. 4, pp. 52903–52910, oct 2014.

[237] Y. Mun, S. Park, S. An, C. Lee, and H. W. Kim, "NO2 gas sensing properties of Au-functionalized porous ZnO nanosheets enhanced by UV irradiation," *Ceramics International*, vol. 39, no. 8, pp. 8615–8622, 2013.

[238] S. W. Fan, A. K. Srivastava, and V. P. Dravid, "UV-activated room-temperature gas sensing mechanism of polycrystalline ZnO," *Applied Physics Letters*, vol. 95, no. 14, pp. 2007–2010, 2009.

[239] S. W. Fan, A. K. Srivastava, and V. P. Dravid, "Nanopatterned polycrystalline ZnO for room temperature gas sensing," *Sensors and Actuators, B: Chemical*, vol. 144, no. 1, pp. 159–163, 2010.

[240] S. Santra, A. De Luca, S. Bhaumik, S. Z. Ali, F. Udrea, J. W. Gardner, S. K. Ray, and P. K. Guha, "Dip pen nanolithography-deposited zinc oxide nanorods on a CMOS MEMS platform for ethanol sensing," *RSC Adv.*, vol. 5, no. 59, pp. 47609–47616, 2015.

[241] Z. Dai, L. Xu, G. Duan, T. Li, H. Zhang, Y. Li, Y. Wang, Y. Wang, and W. Cai, "Fast-response, sensitivitive and low-powered chemosensors by fusing nanostructured porous thin film and IDEs-microheater chip," *Scientific reports*, vol. 3, p. 1669, 2013.

[242] Z. Q. Zheng, J. D. Yao, B. Wang, and G. W. Yang, "Light-controlling , flexible and transparent ethanol gas sensor based on ZnO nanoparticles for wearable devices," *Scientific reports*, vol. 5, no. May, p. 11070, 2015.

[243] P. Wang, Y. Fu, B. Yu, Y. Zhao, L. Xing, and X. Xue, "Realizing room-temperature self-powered ethanol sensing of ZnO nanowire arrays by combining their piezoelectric, photoelectric and gas sensing characteristics," *J. Mater. Chem. A*, vol. 3, no. 7, pp. 3529–3535, 2015.

[244] M. W. Ahn, K. S. Park, J. H. Heo, D. W. Kim, K. J. Choi, and J. G. Park, "On-chip fabrication of ZnO-nanowire gas sensor with high gas sensitivity," *Sensors and Actuators, B: Chemical*, vol. 138, pp. 168–173, apr 2009.

[245] M.-G. Kim, M. G. Kanatzidis, A. Facchetti, and T. J. Marks, "Low-temperature fabrication of high-performance metal oxide thin-film electronics via combustion processing," *Nature Materials*, vol. 10, pp. 382–388, may 2011.

[246] K. K. Banger, Y. Yamashita, K. Mori, R. L. Peterson, T. Leedham, J. Rickard, and H. Sirringhaus, "Low-temperature, high-performance solution-processed metal oxide thin-film transistors formed by a 'sol–gel on chip' process.," *Nature materials*, vol. 10, no. 1, pp. 45–50, 2011.